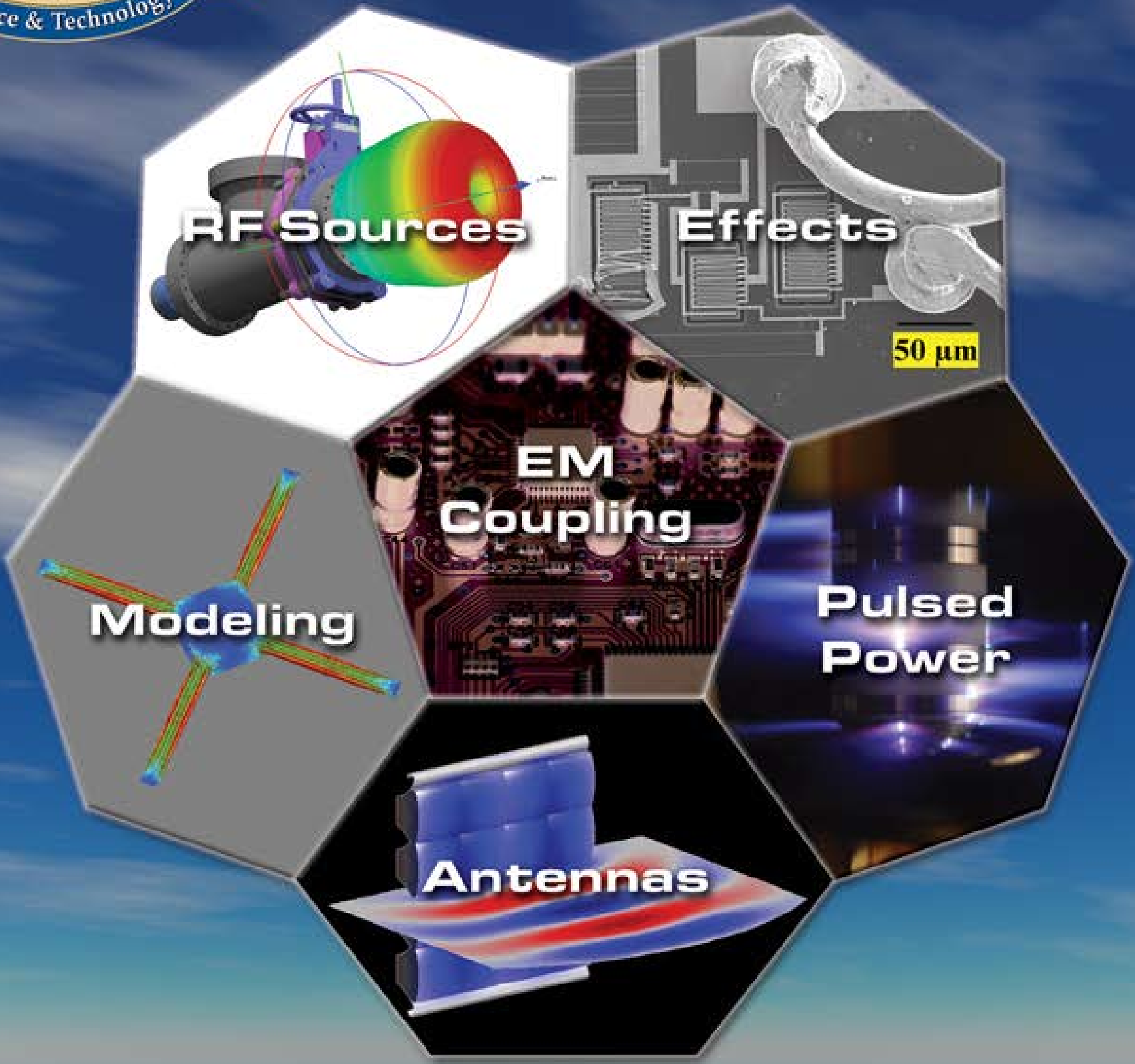

DIRECTED ENERGY WEAPONS (DEW)
HIGH POWER MICROWAVE (HPM)
6.1 PROGRAMS
FY19 ANNUAL REPORT

Mr. Ryan Hoffman, Program Manager

DISTRIBUTION STATEMENT A. Approved for public release; distribution is unlimited.
DCN#: 43-7462-20

Directed Energy Weapons (DEW) High Power Microwave (HPM) Program Annual Report for FY19

Table of Contents

Introduction

Program Officer
Ryan Hoffman, Office of Naval Research

The Directed Energy Weapons (DEW) Program of ONR was initiated in response to the rapid development and growing threat of directed energy technologies by adversaries. Directed energy weapons are defined as electromagnetic systems capable of converting chemical or electrical energy to radiated energy and focusing it on a target, resulting in physical damage that degrades, neutralizes, defeats, or destroys an adversarial capability. The U.S. Navy uses HPM to gain and sustain tactical, operational, and strategic advantage in the arena of EM Maneuver Warfare and Integrated Defense for U.S. forces across the full range of military operations, including power projection and integrated defense missions. The ability to focus radiated energy reliably and repeatedly at range, with precision and controllable effects, while producing measured physical damage, is the measure of DEW system effectiveness. In anticipation of DEW advancements, the ONR HPM Program comprises a portfolio of initiatives and research projects which seek to provide the science and engineering basis for means and methodologies to provide the Navy advanced HPM technologies, systems, and techniques enabling a new class of weapons that will be highly effective in the battlespace. The goal is to be the most effective steward of DEW systems.

Asymmetric threats are proliferating worldwide and likely will continue to do so until such time as effective countermeasures are deployed. Often enough, Rules of Engagement will restrict kinetic engagement with asymmetric threats contingent on the particulars of the scenario. DEW systems – or more specifically for this report, HPM weapons – are expected to allow Naval commanders significantly more flexible responses to a number of asymmetric threats, including various small surface craft and unmanned aerial vehicle (UAV) threats. This flexibility is possible since the restrictions on engaging targets might be removed or reduced based on recognition of 1) the low collateral damage and 2) the non-lethal and reversible effects associated with HPM weapons.

HPM weapons create pulses of electromagnetic energy over a broad spectrum of known radio and microwave frequencies, causing either temporary or permanent results on electronics within targeted systems at scalable effects. HPM weapon systems can be used to disrupt, disable, or potentially destroy critical electronic circuitry in target systems, even in restricted scenarios, while also having the advantage of low cost per shot. HPM weapons deliver electromagnetic energy through coupling of the electromagnetic wave to target circuits through aperture or cable points of entry, thereby inducing currents in the circuitry capable of causing a variety of effects. Potential effects include erroneous signals, system lock-up, shutdown, loss of communications between systems, and physical damage.

As DEW falls within the Fundamental Research part of the broad ONR Science & Technology Investment Portfolio, projects funded are long-term initiatives, covering basic research or applied science. These investigations can have a five to twenty year horizon. Across the HPM technology thrust areas, research projects within the program include performers from academia, industry, government laboratories, and small businesses. Moreover, the program includes performers whose research is financed through Navy SBIR/STTR funding. In addition, science and technology solutions from an international technical community are afforded through ONR Global, which funds projects that foster cooperation in areas of mutual interest with global partners. The program encourages the cross-pollination of ideas and collaboration among performers worldwide, and offers an annual review where performers provide updates on the status of their research and present results to their DEW peers. Furthermore, data and facilities sharing are encouraged within the program. This approach contributes to increased success for the program and for the Navy.

Focus areas cover HPM sub-systems that optimize power and/or energy density at the electronic target for a variety of platform sizes and capabilities while minimizing size, weight, power and cost. Examples of related areas for S&T investment and research include supporting technologies such as power electronics, pulsed power drivers, power modulators, as well as frequency agile RF sources and antennas.

Additional research focus areas include research into electronic system coupling, interaction, and effects with the first goal of enabling development of predictive effects tools for current systems. A second goal of this work includes an exploration of in band and out of band coupling and interaction mechanisms. This exploration will exploit developing advances in frequency and bandwidth agility both to identify new potential weapon system possibilities as well as to achieve significant improvements in size, weight, power, and cost in new variants of existing systems.

Research Challenges and Opportunities

- RF coupling and modeling tools to capture complex EM wave interactions with electronics and associated enclosures, RF component disruption, along with novel techniques for experimental validation. Prediction of effects on electronics with improved techniques for HPM lethality testing and analysis. Analysis of HPM coupling mechanisms, electronic device interaction physics, and component level effects validated through experiment. Development of tools and techniques for more efficient identification and utilization of novel RF waveforms.
- Pulsed power/power electronics; including high energy density capacitors, power conditioning, high voltage switches, dielectric insulators, 3D printed/novel materials and power modulator pulse forming networks that enable higher duty cycle operation
- Solid state and vacuum electronic based HPM sources that provide frequency and waveform parameter tunability and are reconfigurable to adapt to changing requirements; computer codes for modelling HPM physics to enable the next generation of devices
- Wide bandwidth high power amplifiers that provide the ability of very rapid waveform adjustment.
- High power, low profile, or conformal antenna designs and capable radome materials, novel array concepts, high power beam steering techniques and distributed beam forming approaches.
- Novel HPM sensors, instrumentation and algorithms are of interest for measurement of waveforms and diagnosing system performance as well as applied to Electronic battle damage indication (eBDI).

RF Coupling Revisited

Grant No. N00014 -17-1-2932

Annual Summary Report for Fiscal year 2019

Period of Performance: October 1, 2018 to September 30, 2019

Prepared by:

Professor Anthony Caruso, Principal Investigator
University of Missouri, Kansas City, MO
Department of Physics and Astronomy
5110 Rockhill Rd.
Flarsheim Hall, Room 257
Kansas City, MO 64110
Tel: (816) 235-2505
Fax: (816) 235-5221
Email: carusoan@umkc.edu

DEPARTMENT OF THE NAVY
UNITED STATES MARINE CORPS

This work was sponsored by the Office of Naval Research (ONR), under grant number N00014 -17-1-2848. The views and conclusions contained herein are those of the authors only and should not be interpreted as representing those of ONR, the U.S. Navy or the U.S. Government.

Grant or Contract Number: N00014-17-1-2932
Date Prepared: 30 Jan 2020
Project Title: ONR Short Pulse Research, Evaluation and non-SWaP Demonstration for C-sUAV Study
Annual Summary Report: FY2019
Principle Investigator: Anthony Caruso, 816-235-2505, carusoan@umkc.edu, University of Missouri Kansas City

Section I: Project Summary

1. Overview of Project

Abstract:
Develop tunable High Power Microwave (HPM) sources and electronically steerable radiators whose wave-forms enable control over all levels of lethality on cUAV and similar targets, with the least power density.

Objective:
The OSPRES program is to map small unmanned aerial vehicle (sUAV) effects space, empirically and by simulation, as a function of high power microwave (HPM) waveform (power density, frequency, bandwidth, pulse repetition frequency, angle-of-incidence, polarization, pulse shape and pulse width). Then, use the waveform space(s) that enable control over the desired levels-of-lethality on sUAV and similar targets, with the least power density, to drive development of transitionable HPM sources and electronically steerable radiators. Effects measurement, HPM system development, and RF Coupling through simulation are the three signature areas of the program.

Introduction:
Small unmanned aerial systems (sUAS) continue to present an increasing asymmetric threat, from intelligence capture to payload transfer to kinetic airspace nuisance. This problem is considered a grand challenge begging for a comprehensive study of present- and future-art countermeasures, to identify the most optimal (including policy acceptable engagement) means of mitigating the sUAS threat with extrapolation to practical range, cost, delivery and integration. Solution categories include kinetic and non-kinetic tools; of the non-kinetic tools, the main classes are high energy laser (HEL) and high power microwave (HPM) weapons. Within the HPM space are long- and short-pulse, high-peak and high-average power technologies; short-pulse and high-average power is an important and relatively unexplored space, and the focus of this effort.

Within the OSPRES program are efforts to 1) identify the fundamental processes by which RF waveforms interact with the materials and components of UAVs, 2) further develop and understand the models and limitations of a variety of photoconductive solid state switch technologies, and 3) develop new electrically small antennas for the propagation of electromagnetic waveforms. By understanding how RF waveforms couple to components, HPM systems may be developed that are more efficient in terms of the radiated RF power to coupling and induced current on components. Investigation into PCSS technologies and electrically small antennas, aims to bring the cost and size of HPM counter UAV systems down so that they can compete with more established kinetic and non-kinetic systems.

Background:

The OSPRES project is broken into subareas of HPM system development, coupling studies, and antenna development. Within some of these areas are subareas which are listed below with a brief description of the research.

Positive feedback NLTL based soliton generator

Nonlinear transmission lines (NLTL) are used to generate high-power radio frequency (RF) signals using passive elements, and are primarily used for pulse sharpening. Traditionally, a continuous signal stream is required to generate sharpened RF signals at NLTL output. The objective of our research was to develop a compact high power RF signal generator using the combination of a laterally-diffused metal-oxide semiconductor (LDMOS) based push-pull power amplifier (PA) with a Schottky diode-based NLTL while a single pulse is used as a source. This compact self-sustaining soliton (high-frequency RF signal) generator can be used for low to medium power RF signal generation.

Development of PCSS power conditioning circuit

Photoconductive semiconductor switches (PCSS) are promising devices for compact, repetitive pulsed power generation due to their fast response time, negligible time jitter, precise synchronization, high repetition rate and optical electrical isolation. One of the methods to generate a high-power RF signal is charging a transmission line from a high-voltage (HV) DC power supply, and subsequent discharge through another transmission line by a rapid triggering of the PCSS. Traditional methods of charging (e.g., Direct DC charging, low-pass filter based charging) may cause the PCSS to experience high voltage and temperature stress during the entire period of operation. This phenomenon adversely affects the lifetime of the PCSS, therefore, the reliability of the overall system. In addition, high voltage stress across the PCSS and leakage current through it during the OFF-state leads to excessive power loss, thereby reducing system efficiency. The objective of our research is to design a solid-state switch-based power conditioning circuit that can efficiently keep the voltage across the PCSS close to zero during its OFF-state leading to mitigation of excess voltage and temperature stress across it.

Trade Space Analysis of a Phased Array of Electrically Small Antennas.

There are two distinct efforts involved: (a) investigations into electrically small antenna (ESA) characterization and (b) trade space studies/parametric analysis on down selecting a *phased array*. The ultimate goal is to explore options on how to finally integrate an ESA as an element in a phased array for realizing a desired performance as defined by the PCSS systems.

RF Coupling Modeling and Experimental Measurements

The RF coupling work is focused on developing computational electromagnetics models for predicting RF coupling to UAVs' wires and their various electronic components. Our approach involves building progressively more complex UAV systems, simulating the RF coupling for each system, and validating the simulations using innovative experimental measurements. We used the Characteristic Mode Analysis to quantify how RF coupling varies with parameters such as the direction, frequency, and characteristics of the incident excitation. The ultimate goal of this work is to develop a computational platform that can predict the excitation to generate the desired effect on a UAV.

High power ultrafast switching fundamentals, materials and figure of merit

To quantitatively evaluate the properties of semiconducting/semi-insulating materials and device topologies in the context of high power, fast-rise, high PRF capable switching to implement optimal source driver for HPM generation.

GaN:C Photoconductive Solid-state Switches (PCSS)

The purpose of the GaN:C PCSS project is to characterize and evaluate the performance and cost effectiveness of using GaN:C switches in pulsed power and HPM applications. While performing some device characterization and pulsed power testing.

2. Activities and Accomplishments

Positive feedback NLTL based soliton generator

We constructed a compact 16-section NLTL from reverse-biased 1200 V rated Schottky diodes featuring nonlinear capacitance, and 100 nH fixed inductors. An LDMOS (BLF188XR) based power amplifier (PA) was constructed with suitable matching networks to match the impedance of the NLTL and to sustain the generated RF signal in the NLTL by compensating for the signal attenuation. Broadband RF transformers with type-61 (NiZn) ferrite toroid core were built for the input and output matching sections of the PA. A high voltage (650 V) compact pulse generator was constructed from 650 V rated GaN FETs (TPH3206PSB) made by Transphorm and an isolated universal half-bridge gate driver (UCC21520) from Texas Instruments. The rationale for fabricating this high voltage pulse generator was to replace the commercially available bulky pulse generator with this GaN FET based compact system. We obtained pulses with rise and fall times close to 20 ns and minimum width at full width at half maximum (FWHM) close to 100 ns using the fabricated pulse generator prototype. An external trapezoidal pulse with 250 mV amplitude (peak-peak), 50 ns width, and rise and fall times of 8.9 ns generated by a function generator was used as the input pulse to the in-house pulse generator. A 50 V DC power supply was used at the FET side of the pulse generator, and the amplified output pulse (peak amplitude [40 V], and a width close to 200 ns, and rise and fall times close to 20 ns) generated from the pulse generator was applied to the NLTL. The output of the PA was connected to the NLTL, and the output of the NLTL was connected to the input of the PA, thereby forming a closed-loop configuration. As shown in Figure 1, continuous RF signals were observed across a 50 Ω resistive load connected to the 11th section of the NLTL.

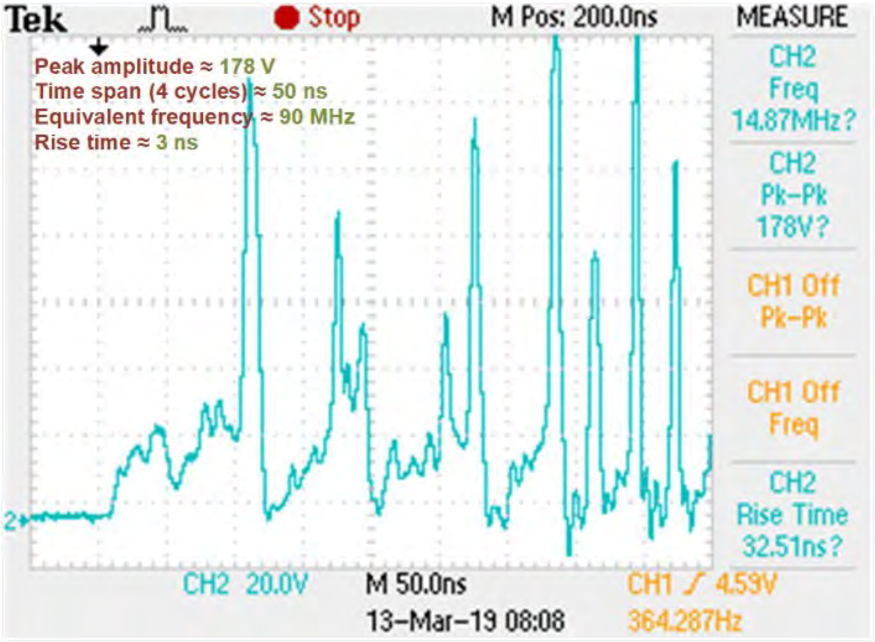

Figure 1: *Output across the 11th section of the 1200 V rated Schottky diode based NLTL coupled with UCC21520 based in-house pulse generator (V_{HVLINK}= 35 V, V_{DD} = 25 V, f = 2 MHz).*

Development of PCSS power conditioning circuit

We have tested different techniques to charge a transmission line connected to a PCSS. A MOSFET with low input capacitance and an IGBT have been alternatively used as the charge controller of the transmission line. Both series and shunt configurations of the solid-state switches have been interchangeably used to evaluate their impact on the charging and discharging profiles. The solid-state switch-based charging method was able to reduce the power loss across the PCSS compared to the traditional charging methods e.g., direct DC charging, low-pass filter based charging. At an input voltage of 40 V and a repetition frequency of 2 kHz, the energy loss across the PCSS over a full cycle has been reduced from 101 mJ (direct DC charging) to 18 mJ (MOSFET based charging). However, high *di/dt* occurring from the rapid switching of the PCSS (<10 ns) interacts with the stray inductance of the circuit and causes ringing in the transmission line. The ringing in the transmission line results in an unintended secondary pulse at the output. To minimize this undesirable effect, we have developed a commercial 14 kV rated Si HV switch-based power conditioning circuit connected in series with the PCSS. We have evaluated the board by triggering the PCSS at a supply voltage up to 2 kV and at a repetition frequency of 2 kHz. Using this board, we have been able to generate output pulses with a peak amplitude close to the theoretical value (half of the supply voltage) and minimal ringing in the charging transmission line after PCSS triggering. The experimental result at a supply voltage of 1 kV and at a repetition frequency of 1 kHz is shown in Figure 2.

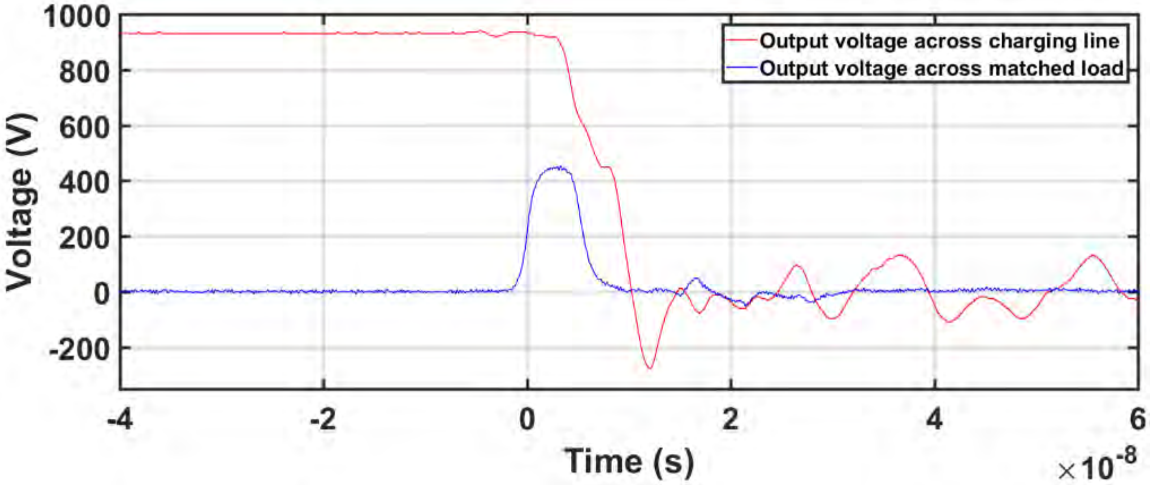

Figure 2: *Experimental result using a power conditioning board for a supply voltage of 1000 V, a repetition frequency of 1 kHz.*

We have tested the board using both positive and negative power supply. In both cases, we have obtained expected results, which confirmed that the board is suitable for different configurations of the transmission line. Using the power conditioning board, we were able to further reduce the energy loss across the PCSS to a value of 9.5 mJ. We conducted experiments using the board at a repetition frequency of 50 kHz up to a supply voltage of 2 kV. At 50 kHz, the HV Si switch operates in a burst mode to minimize excessive switching loss and protect the switch from physical damage due to thermal stress. We have been able to obtain up to 28 output pulses in a single burst at a repetition frequency of 50 kHz at a voltage up to 2 kV. The experimental result (supply voltage 700 V, repetition frequency 50 kHz) is shown in Figure 3.

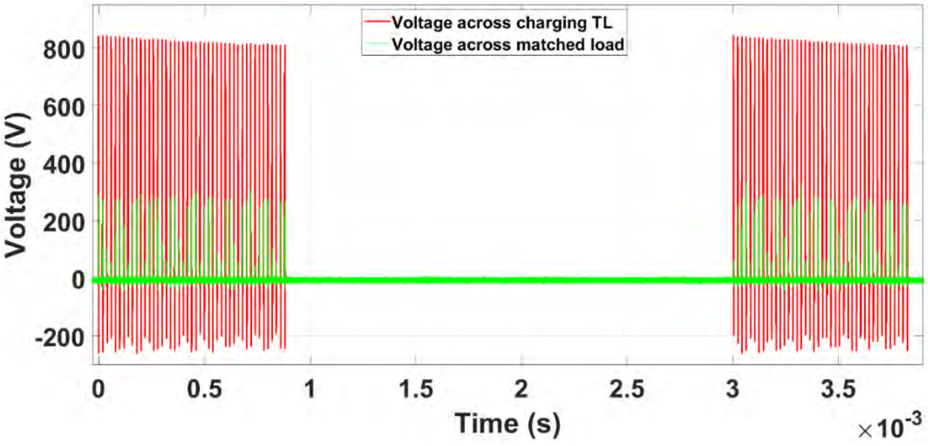

Figure 3: *Experimental results using HV switch for a supply voltage of 700 V at a repetition frequency of 50 kHz (zoomed out).*

Owing to their simple design, light weight, small size and tractable performance, coaxially fed microstrip patch antennas have been considered for the array element design. Contrary to common perception [1], it is possible to obtain >30% 2:1 VSWR bandwidth by strategically placing the probe at 2/3rd distance along the diagonal of a rectangular patch as shown in Figure 4.

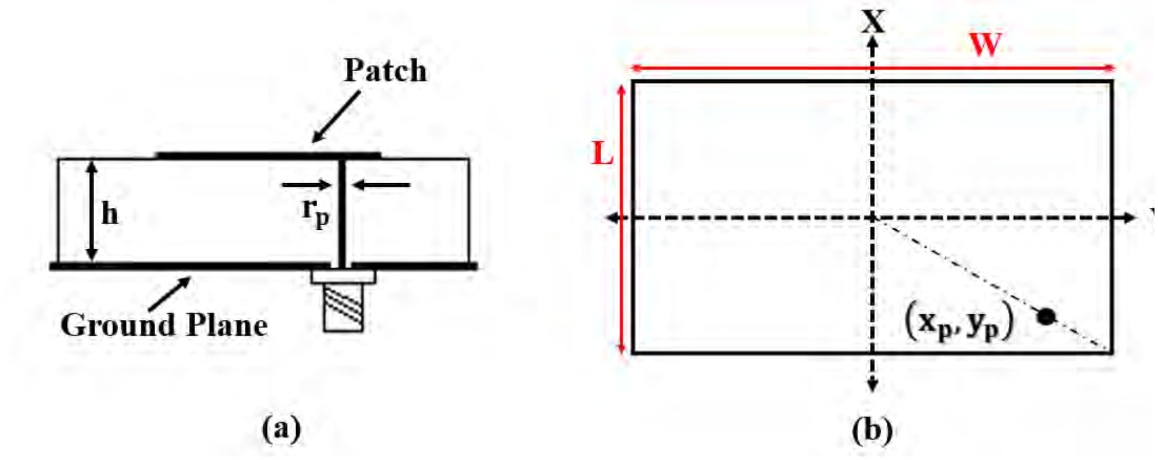

Figure 4. (a) Side view and (b) Top view of the designed coaxial probe fed microstrip patch antenna.

Element Optimization

A new multi-parameter element optimization technique, also known as the D/Q method [2], is currently being used for the performance optimization of the antennas. Here D is the Directivity (far field parameter) and Q is the Quality Factor (near field parameter). Using this technique it is possible to optimize both the far field as well as the near field parameters simultaneously. A comparison between the performance optimization of the designed antennas using the D/Q method and the well-known Characteristic Mode Analysis technique will be carried out in the future.

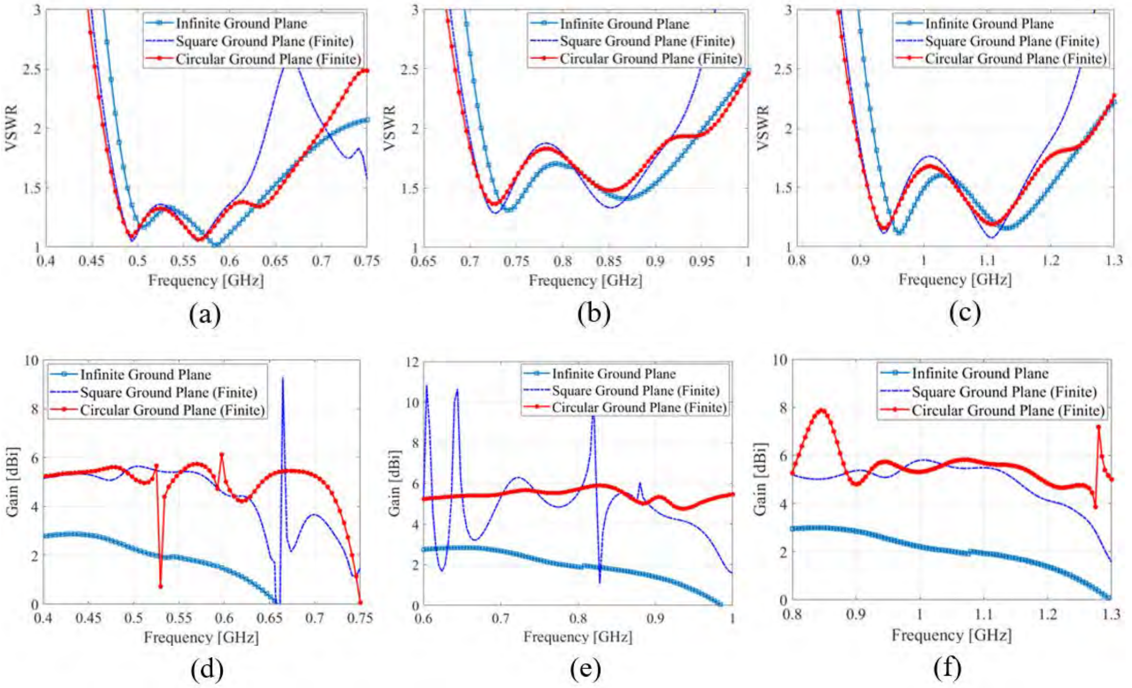

Figure 5. VSWR of (a) Antenna 1, (b) Antenna 2, (c) Antenna 3 and Gain of (d) Antenna 1, (e) Antenna 2, (f) Antenna 3 for different ground plane shapes.

GaN:C Photoconductive Solid-state Switches (PCSS)

Previously, testing was conducted using a N_2 gas laser with a pulse width of approximately 10-ns and the GaN:C PCSS were used to trigger simple 10-ns pulse forming transmission lines—both greater than the expected recovery time of the switch. However, the use of transmission-line based PFNs resulted in a time-dependent bias on the PCSS, obscuring measurements needed for recovery time and time-dependent on-state resistance. Since then, we have (1) acquired a 1064-nm Wedge-HB laser system delivering a 1-ns pulse width and a triple harmonic generation (THG) system for converting the 1064-nm pulse to 355 nm, (2) conducted a series of characterization studies using new pulse forming networks, and (3) began a manuscript for evaluating the cost-effectiveness of GaN manufacturing for high power applications.

GaN:C PCSS switching was characterized on two different test fixtures: (1) a parallel plate transmission line designed for the 70-ps pulse width of the NeoLASE 1064-nm laser with the THG setup, and, (2) a more compact PCB-based pulse forming network (PFN) to allow for a more compact fixture and ease in switching out circuit components.

Both setups allowed for the output voltage to equal the charge voltage on the line and more accurate characterization of time-dependent on-state resistance. While originally designed for the 70-ps pulse width of the NeoLASE laser, the pulse width was too short GaN:C devices were not able to be fully activated (in part due to the THG system), and continued characterization was conducted using the 1-ns pulse width Wedge-HB with the THG system.

To understand the trade-space between low on-state resistance, breakdown, and laser energy cost, we measured the on-state resistance as a function of gap length (distance between the contacts) and incident energy. Initial measurements swept through a range of charge voltage while increasing the incident laser energy. The laser energy was measured using an Ophir energy meter, but ultimately the energy was limited by the damage threshold of the THG system and beam shaping optics. The on-state resistances calculated from the output pulse voltage, charge voltage, load resistance are shown in Figure 6. However, some error exists due to inaccuracies in the charge voltage used in the calculations, but the trends extrapolated from the data hold.

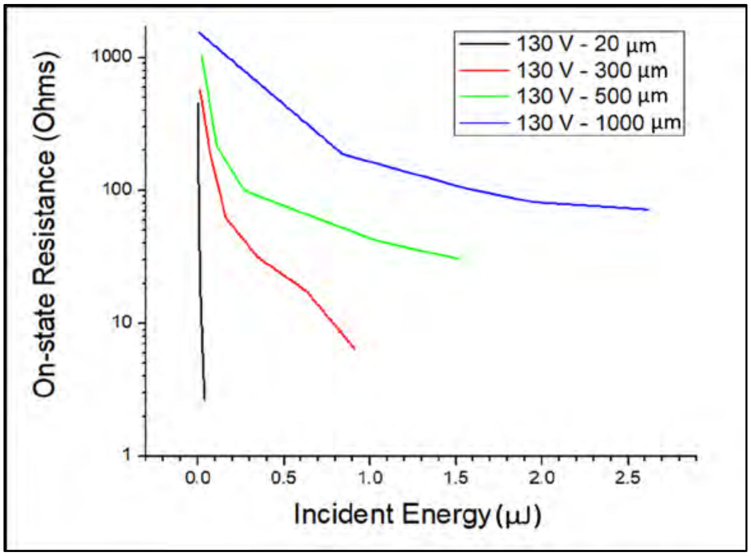

Figure 6: *On-state resistance as a function of incident energy for various gap lengths of GaN:C devices. Minimum on-state resistance was not achieved due to limited laser energy.*

As shown in Figure 6, the trend follows the expectation of larger gap lengths requiring more incident energy to reduce on-state resistance than smaller gap lengths. The plot is shown using a log y-axis to show that on-state resistance can be further minimized by using higher incident energies.

To minimize the on-state resistance, new optics were purchased and installed. Pulse waveforms were then collected on a 500 μm GaN:C PCSS, and the peak voltage and on-state resistance were calculated, shown in Figure 7, at a charge voltage ranging from 100–800 V. At 900 V, the charge resistors failed, ending the study.

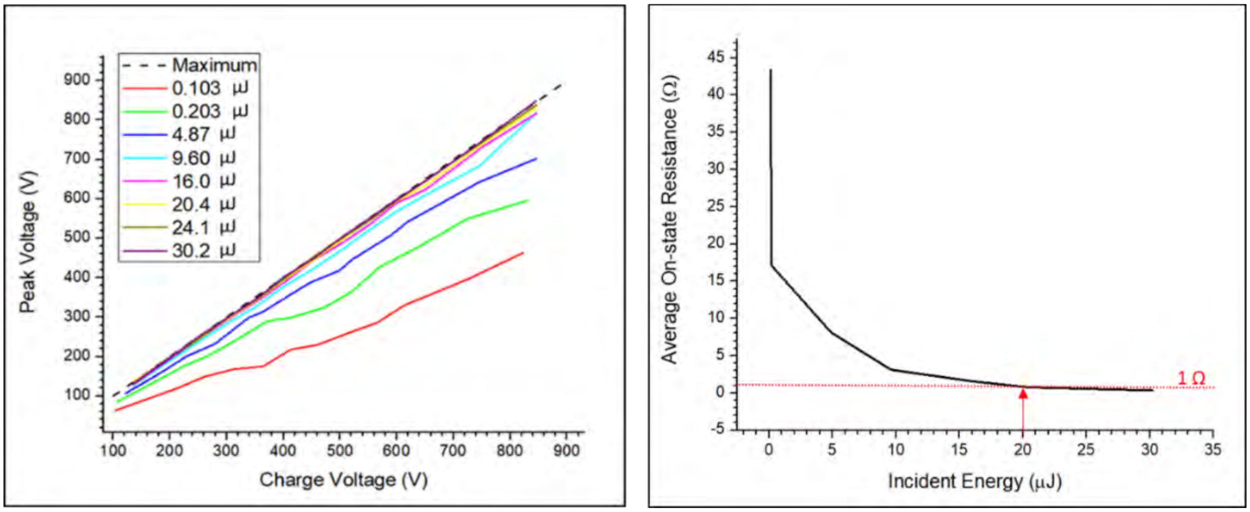

Figure 7: *(left) Peak output voltage as a function of charge voltage for different incident energies on a 500 μm GaN:C PCSS showing the approximately linear relationship between charge voltage and peak output voltage across a range of incident energies. (right) Average (over all charge voltages tested) on-state resistance as a function of incident energy for a 500 μm GaN:C PCSS with maximum output ($V_{out} \approx V_{in}$) occurring with ~20 μJ of incident energy.*

The expected relationship between incident energy and lower on-state resistances was confirmed, as shown in Figure 7 (a) and (b). The gain (V_{out}/V_{charge}) was constant over charge voltage and increased with incident energy increases to a maximum of 1 (occurring at approximately 20 μJ), indicating a switch resistance of much less than 50 Ohms (the load resistance). The linear gain lends itself for extrapolation of expected device behavior at voltages outside of those measured. Further studies are needed to determine the incident energy required for sub-Ohm on-state resistance at additional gap lengths.

High power ultrafast switching fundamentals, materials and figure of merit

In the previous year, semiconducting/semi-insulating materials with photo- and electro- stimulated device topologies were studied to evaluate high-power, ultra-fast transient capabilities for source driver implementation alongside UMKC's active efforts with Si-DSRDs, Si-, SiC- and GaN:C-PCSS. A two-stage evaluation was implemented, 1) evaluate device topologies based on their transient response, jitter, pulse repetition rate (PRF), and power density for both modes of stimulation along with circuit level implementation and 2) evaluate semiconducting/semi-insulating materials optimal for the selected topologies by extending and tailoring figures of merit in prior art to specific topologies and application space. The metrics required for each device technology to be an optimal source driver were laid out and carrier drift limiting factors (joule heating, carrier scattering) at high fields and current densities were studied. The critical phenomena for switches—both for general and optically actuated considered in this study are provided in *Table 1*.

Table 1: *Critical phenomena affecting properties of high power devices at a micro and macro levels.*

General Switches		**PCSS-Specific**	
Macro parameters	**Micro parameters**	**Macro parameters**	**Micro parameters**
-Rise-time	- Generation	-Incident energy	-Absorptivity
-Voltage hold-off	- Recombination	-Contact Pattern	-Direct/Indirect Abs.
-Recovery	-Defect States	-AR coatings	-State transitions
-Conductance	-Scattering		
-Impedance	-Dopants		
-Dark current	-Carrier transport		
-Contacts	-Drift and diffusion		
-Geometry	-Injection		

The metrics required for each device technology to be an optimal source driver were laid out and carrier drift limiting factors (joule heating, carrier scattering) at high fields and current densities were studied. The critical phenomena for switches—both for general and optically actuated considered in this study are provided in *Table 1*.

Because device performance and losses are highly dependent on the circuits in which they are used, we selected a representative model of a class-E amplifier for initial modeling. In the circuit, a switch was driven by a 1.2-kV pulses with a 50% duty cycle. The rise and fall time of the pulse was 1-ns, and a constant 3-kV bias was applied to the circuit. In the on-state, the switch resistance (voltage controlled) was set to decrease to micro-Ohms. Because the class-E's zero voltage switching (ZVS) minimizes the power losses during turn-on, turn-off losses in the switch were readily isolated and evaluated. This behavior can be seen in Figure 2 in which the excitation pulse rise (green) initiates when the switch voltage reaches (blue) zero volts. However, due to the arbitrary voltage-control of this of this model, our focus shifted to generating a general FoM for high power switches.

Focusing on a more applicable FoM, we reviewed efforts by Baliga, Johnson, Keyes, Kim, Shigekane, Wang, Huang and Shenai [1], and hierarchically classified the materials for electrically-actuated devices. A major issue with existing figures of merit is their basis on electrically-actuated devices; no such FoM existed for optically-actuated devices. To resolve this, we narrowed the power dissipation model to the on-off transition and on state—the switching state being of particular importance due losses peaking while switching under load, further exacerbated at high power and PRF—and derived a new FoM for linear PCSS, based on photo-generation and recombination.

Starting with Nunnally's equations for carrier generation and device resistance, we created MATLAB script considering the cases of Si, SiC and GaN, while varying their geometry and incident light intensity. Materials 500-µm thick were modeled when illuminated with an optical pulse energy of 600-mJ. All material recombination times were set to 1-µs, and the resulting carrier generation and resistance are shown in Figure 8. The resistance of each switch declined with carrier generation, but the 1-µs recombination time was not representative of SiC and GaN, as their recombination times are generally one-to-two orders of magnitude less. However, this represented an initial application of Nunnally's equations and laid the foundation for generating a PCSS-specific FoM.

Expanding on the carrier generation model, parameters from Table A1 were incorporated into a power loss equation including, but not limited to: breakdown field, saturation velocity, carrier-generation, transport and recombination, e-h mobility, geometry, incident energy, and thermal conductivity. During the on-state, the derived power loss is given by Equation 1.

$$P_{on} = \frac{E_C^2 L^4 h\vartheta}{(R_{on}+R_{Load})^2 q\mu_T t_r I_0} \qquad \text{Eq. (1)}$$

However, because the resistance is time dependent during the switching state, calculating the corresponding power losses is more complex, requiring the time-dependent device resistance (R_{device}), current (i), and net carriers generated (n), given by Equations 2, 3, and 4, respectively.

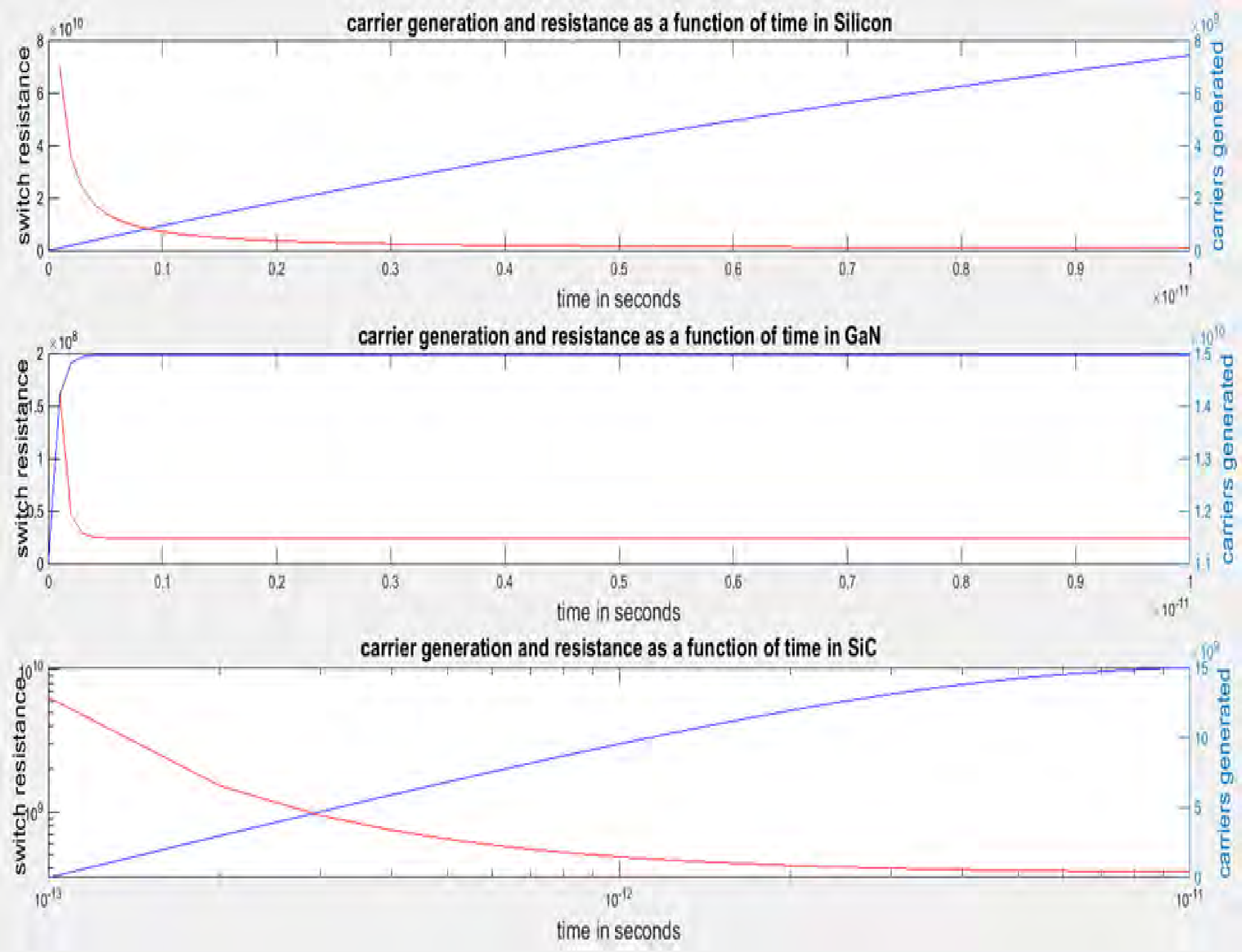

Figure 8: *Carrier generation (blue) and switch resistance (red) as a function of time for Si, GaN and SiC.*

$$R_{device}(t) = \frac{L^2\ h\upsilon}{qIT_{net}\mu_T(1-e^{-\frac{t}{T_{net}}})} \qquad \text{Eq. (2)}$$

$$i(t) = \frac{E_c Ldwq\ \mu_T n(t)}{R_L dwq\mu_T n(t)+L} \qquad \text{Eq. (3)}$$

$$n(t) = \frac{I}{h\upsilon\ dwL} T_{net}\ * [1 - e^{-\frac{t}{T_{net}}}] \qquad \text{Eq. (4)}$$

Where:

E_c – critical field
L – Thickness of the device (switch gap)
d,w – length and width of the device
hυ – Energy carried in each photon
*I – I_0*exp (-2.77$(t/T_{FWHM})^2$)*
I_0 – peak optical intensity
R_{on} – On-state resistance
R_{Load} – load resistance
q – Charge of the electron
μ_T – Mobility of holes and electrons
t_r – inherent device recombination time
t_T– transit time of carriers
*T_{net} – t_r*t_T/ (t_r + t_T)*

The incident optical pulse was modeled by a temporal Gaussian with a FWHM of 2-ns and wavelength equivalent to the material's bandgap. The resulting on-state losses (Eq. 1) for Si are shown in Figure A3 as a function of optical energy and device length (i.e., thickness). Those for SiC and GaN, were also calculated but are not included in this report. These plots show the on-state power loss accounting for mobility of the generated carriers and the recombination time into account as shown in Equation (1). The recombination time used was held constant for all materials. By comparing the plots for Si, GaN and SiC, we notice SiC has relatively higher on-state losses.

Figure 9: *Si on-state losses as a function of path length and optical power. GaN and SiC losses were calculated, but omitted from this report.*

For switching transition, we derived the power dissipation omitting size approximations as shown in equations (6) and (7), while equation (5) shows the time varying device resistance. The power dissipated in the device during these stages of operation adds heat to the lattice and drives device damage at high peak powers and repetition rates. Equations (6) and (7) will be quantitatively analyzed with time-varying Gaussian laser profiles, geometric variations, recombination, and dopant dependent mobility

$$R_{device}(t) = \frac{\frac{\mathrm{E}_{\lambda} L}{w}}{\mathrm{q}\mu_{\mathrm{T}}(\mathrm{t})(1-\mathrm{r})\mathrm{I}_0 \mathrm{T}_{\mathrm{net}}[1-\mathrm{e}^{-\frac{\mathrm{t}}{\mathrm{Tnet}}}]} \qquad \text{Eq. (5)}$$

$$\mathrm{P}_{\text{turn-on}} = \frac{\mathrm{E_c}^2\mathrm{L}^3}{\mathrm{R_{Load}I_0}} \int_{t_1}^{t_2} \frac{\left(1-exp\left(-\frac{t}{Tnet}\right)\right)}{\exp\left(-2.77\left(\frac{t}{t_p}\right)^2\right)\left[2+\frac{R_{Load}\, q\, \mu_{\mathrm{T}} I0 T_{net}}{h\upsilon\ L}\right] - 2R_{Load}\, q\, \mu_{\mathrm{T}} \mathrm{I_0 T_{net}} [\exp(-5.54 \left(\frac{t}{t_p}\right)^2 - (\frac{t}{T_{net}}))\ ] /(h\upsilon\ L)}\, dt \quad \text{Eq. (6)}$$

$$\mathrm{P}_{\text{turn-off}} = \mathrm{I_0 T_{net} q \mu_T E_c{}^2 L^3} \int_{t_3}^{t_4} \frac{\left[\exp\left(-2.77\left(\frac{t}{t_p}\right)^2 - \frac{t}{T_{net}}\right)\right]}{\mathrm{h\upsilon} L^3 + 2R_{Load}\, q\mu_{\mathrm{T}}\, I_0 T_{net}\, exp\left(-2.77\left(\frac{t}{tp}\right)^2 - \frac{t}{T_{net}}\right)}\, dt \qquad \text{Eq. (7)}$$

Where:
E_c *– critical field*
L – Thickness of the device (switch gap)
d, w – length and width of the device
hv – the energy carried in each photon
R_{Load} *– load resistance*
q – Charge of the electron
μ_T *– mobility of holes and electrons*
t_r *– inherent device recombination time*
t_T *– transit time of carriers*
t_p *– FWHM duration of the laser pulse*
*Tnet – tr*tT/ (tr+tT)*
I_0 *– peak optical intensity*

Considering only the power dissipation calculations, the FoM is inconclusive. For example, although SiC showed the greatest power losses, in reality this may be overcome by its higher thermal conductivity, allowing for greater dissipation of losses. Therefore, the materials' specific heat and thermal conductivities necessary for a realistic FoM.

Another caveat to this FoM arises from the demands of specific applications. While some applications require maximum power or pulse energy at low repetition rates, others require less at greater repetition rates. Thus, depending on application, power losses may not be the most critical factor in performance. To compensate for these difference, future analysis will be conducted through the lens of SWaP-C^2 to provide cost-effective, application-specific solution(s) for high power switches.

RF Coupling Modeling and Experimental Measurements

Quantifying the electromagnetic response of sUAVs is complicated by the wide variety of their shapes, sizes, and material compositions. A wide range of electronics, subsystems and components can also be featured in sUAVs. During the first year of the project we reviewed common sUAV shapes, sizes, material compositions, and electronics and used Characteristic Mode Analysis (CMA) to computationally quantify electromagnetic coupling and interference to UAV frames over the L-band and S-band. Over the second year of the project, we have studied how the relative location and height of wires above dielectric UAV frames affect RF coupling, used Characteristic

Mode Analysis (CMA) to computationally quantify electromagnetic coupling and interference to practical wires and PCB distributions above dielectric UAV frames over the L-band and S-band, studied how to develop simpler models for the UAV frame that reduce the computational time but yield the same RF coupling values, developed new experimental setups and validated the CMA coupling predictions using measurements conducted in our facilities at UMKC, and applied time-domain electromagnetic analysis, guided by CMA, to study RF coupling to UAVs using time-domain short pulses of different shapes. This work is ongoing and continuing to evolve, more detailed information expected in the next 6 months of the project.

[1] R. Garg, P. Bhartia, I. Bahl, and A. Ittipibon, Microstrip Antenna Design Handbook, Boston, USA: Artech House, 2001.

[2] M. Gustafsson, *et al*, "Physical limitations on antennas of arbitrary shape," *Proceedings of the Royal Society A: Mathematical, Physical and Engineering Sciences,* vol. 463, issue 2086, 2007, pp. 2589-2607.

[3] Baliga, B J. 1989. “Power Semiconductor Device Figure of Merit.” *IEEE Electron Device Letters* 10 (10): 455–57.

[4] W. C. Nunnally and R. B. Hammond, “Optoelectronic switch for pulsed power”, *edited by Chi. H. Lee, Orlando, Florida: Academic Press, Inc., 1984.*

3. Findings and Conclusions

4. Plans and Upcoming Events

Further work on the project will include designing a power conditioning board based on an HV SiC MOSFET. This is due to SiC MOSFETs have lower ON-resistance compared to Si MOSFETs, the new solution can reduce the switching loss in the system compared to Si MOSFET based solutions. Work on improving the thermal management of the HV switch and the PCSS to perform continuous operation at a high voltage (≥ 10 kV) and high repetition frequency (≥ 50 kHz). The RF coupling effort will perform an exhaustive statistical analysis of coupling to complex wire systems mounted on top of or inside UAV frames and couple the Singularity Expansion Method (SEM) with CMA to predict the coupling current to UAV wire systems in the time domain. Further refinements of the PCSS modeling and simulation tools will be refined and compared to experimental pulsed power and characterization data. An electrically small antenna design will be applied to linear and 3x3 arrays for modeling, prototype arrays will be constructed and characterized for performance. Experimental data from the arrays will be compared to calculations for refinement of models and optimization of array designs. Continued development of PCSS theoretical models will begin to simulate operation of silicon based PCSS in pulsed power operation and begin to be expanded to GaN:C in PCSS applications.

Recommendations for Future Work:

5. Transitions and Impacts

6. Collaborations

7. Personnel

Principal investigator
    Anthony Caruso, 3, No
Co-investigator or Co-PI
    Ahmed Hassan 3, No
    Deb Chatterjee, 3, No
    Faisal Khan, 3, No
    Travis Fields, 3, No
Team Members
    Joseph Crow, 12, No
    Eliot Myers, 12, No
    Jonathan Smith, 6, No
    Leta Moler, 12, No
    Johnathan Lancaster, 6, No
    James Currie, 6, No

8. Students 14

9. Technology Transfer

UMKC Invention Disclosure and USPTO Provisional Patent: High-efficiency High-power Microwave Generation using Multipass Non-linear Network Topologies

10. Products, Publications, Patents, License Agreements, etc.

Publications resulting from this project:

Hassan, Chatterjee both have some conference papers and possibly some peer reviewed full journal articles.

<u>Conference Papers</u>

a. Sustaining High Power RF Signal Generation in a Positive Feedback Network
b. A. N. M. Wasekul Azad, and F. Khan
c. *2019 IEEE Pulsed Power and Plasma Science Conference*
d. Conference Date
e. Orlando, FL
f. awaiting publication
g.
h.
i.
j. Yes

a. Analytical Models for L-Probe fed Microstrip Antennas
b. B. Barman, D. Chatterjee, & A. N. Caruso
c. 2019 IEEE International Symposium on *Antennas and Propagation and USNC-URSI Radio Science Meeting*
d. July 7-12 2019
e. Atlanta, GA
f. published
g.
h.
i.
j. Yes

a. Some Investigations into Mutual Coupling Analysis for Trade Space Studies of Linear Arrays
b. B. Barman, D. Chatterjee, & A. N. Caruso
c. *2019 IEEE International Symposium on Phased Array Systems and Technology*
d. Oct 15-18 2019
e. Waltham, MA
f. published
g.
h.
i.
j. Yes

a. Characteristic Mode Analysis of a straight and an L-probe fed Microstrip Patch
b. B. Barman, D. Chatterjee, & A. N. Caruso
c. *2nd Indian Conference on Antennas and Propagation (InCAP2019)*
d. Dec 19-22 2019
e. Ahmedabad, India
f. published
g.
h.
i.
j. Yes

a. Characteristic Mode Analysis of the Effect of the UAV Frame Material on Coupling and Interference
b. M. Hamdalla, A. N. Caruso, A. M. Hassan
c. *IEEE International Symposium on Antennas and Propagation and USNC-URSI Radio Science Meeting at Atlanta*
d. July 7-12 2019
e. Atlanta, GA
f. published
g.
h.
i.
j. Yes

a. Electromagnetic Interference of Unmanned Aerial Vehicles: A Characteristic Mode Analysis Approach
b. M. Hamdalla, J. Hunter, Y. Liu, V. Khilkevich, D. Beetner, A. Caruso, A. M. Hassan
c. *IEEE International Symposium on Antennas and Propagation and USNC-URSI Radio Science Meeting at Atlanta*
d. July 7-12 2019
e. Atlanta, GA
f. published
g.
h.
i.
j. Yes

a. Electromagnetic Coupling Analysis of Printed Circuit Board Traces using Characteristic Mode Analysis
b. K. Durbhakula, J. Lancaster, J. Hunter, Y. Liu, D. Beetner, V. Khilkevich, D. Chatterjee, A. Caruso, A. M. Hassan
c. *IEEE International Symposium on Antennas and Propagation and USNC-URSI Radio Science Meeting at Atlanta*
d. July 7-12 2019
e. Atlanta, GA
f. published
g.
h.
i.
j. Yes

a. Scalable characteristic mode analysis using big data techniques
b. K. Alsultan, P. Rao, A. N. Caruso, and A. M. Hassan
c. *International Symposium on Electromagnetic Theory (EMTS 2019)*
d. May 27-31 2019
e. San Diego, CA
f. published
g.
h.
i.
j. Yes

a. Characteristic Mode Analysis of Electromagnetic Coupling to Wires with Realistic Shapes
b. M. Hamdalla, W. Al-Shaikhli, J. Lancaster, J. D. Hunter, L. Yuanzhuo, V. Khilkevich, D. G. Beetner, A. N. Caruso, and A. M. Hassan
c. *International Symposium on Electromagnetic Theory (EMTS 2019)*
d. May 27-31 2019
e. San Diego, CA
f. published
g.
h.
i.
j. Yes

Patents

Other Products: Identify any other significant products that were developed under this project. Describe the product and how it is being shared.

11. Point of Contact in Navy

Matthew McQuage, NSWCDD

Phillip Meyerhofer, NRL

12. Acknowledgement/Disclaimer

This work was sponsored by the Office of Naval Research (ONR), under grant number N00014-17-1-2932. The views and conclusions contained herein are those of the authors only and should not be interpreted as representing those of ONR, the U.S. Navy or the U.S. Government.

Electrochemical Prime Power Supply for a Repetitively Operated High-Power Marx Generator

Grant No. N00014-17-1-2847

Annual Report for Fiscal Year 2019

Period of Performance: October 1, 2018 to September 30, 2019

Prepared by:

Professor David Wetz, Principal Investigator
Associate Professor Electrical Engineering Department
University of Texas at Arlington
Department of Electrical and Computer Engineering
416 Yates Street, Rm. 537
Arlington, TX 76019
Tel: (817) 272-0719
Email: wetz@uta.edu

UNIVERSITY OF
TEXAS
ARLINGTON
COLLEGE OF ENGINEERING

DEPARTMENT OF THE NAVY
UNITED STATES MARINE CORPS

This work was sponsored by the Office of Naval Research (ONR), under grant number N00014 -17-1-2848. The views and conclusions contained herein are those of the authors only and should not be interpreted as representing those of ONR, the U.S. Navy or the U.S. Government.

Grant or Contract Number: N00014-17-1-2847
Date Prepared: 8/31/2019
Project Title: Electrochemical Prime Power Supply for a Repetitively Operated High Power Marx Generator
Annual Summary Report: September 1, 2018 to August 31, 2019
Principle Investigator: [PI David Wetz, 5127880848, wetz@uta.edu, University of Texas at Arlington (UTA), Arlington, Texas, 76019

Section I: Project Summary

1. Overview of Project

Abstract:

The US Navy has several active research projects aimed at bringing electrically powered weaponry to the fleet, typically referred to as directed energy weapons (DEW) systems. Though many technical advances are being made, most of these efforts are still in the research phase with many unanswered questions still to be answered before they will be deployed. Once deployed, the load can only be as effective as the power supply that drives it. Though every DEW power supply is different, two common elements that many share are the prime power supply and the intermediate energy storage, respectively. Regardless of whether the DEW is deployed on a ship or on a smaller, more mobile, platform, it must have a reliable and resilient power source from which to draw its prime power. The prime power supply may directly drive the DEW load, or it may feed energy to an intermediate energy storage device supplies high power to the load. A power supply that operates on its own or in some sort of hybrid fashion with the platform's existing power source is required. Energy storage in the form of ultracapacitors (UCs) and lithium-ion batteries (LIBs) hold a great deal of promise for use as a prime power source for DEWs. These supplies must source high power in as compact a form factor as possible so there is still a great deal of research to be performed to understand how these devices will operate, age, and fail when operated at high power so that they can be properly considered and sized. Limited references are available for pulsed power engineers to use when designing a prime power supply and a portion of the research performed here has been focused on developing empirically derived sizing tools they can use when considering LIBs and UCs, respectively. Though high voltage intermediate energy storage capacitors are technologically more mature and documented, there are still research challenges to overcome. Discharging them and recharging them at high current in a repetitive manner has been found to be hard on them and there is a need to research what could cause failure in this mode of operation. The remaining research performed this year has been focused on designing, constructing, and commissioning a high voltage testbed, as high as 80 kV, on which to study high voltage capacitors at rates of charge and discharge. The progress made on each of these efforts will be discussed in the report presented here.

Objective:

During this reporting period, there were two primary objectives to complete. The first was to advance the development of an empirically based sizing tool that can be used to size lithium-ion battery (LIB) and/or ultracapacitor (UC) based prime power supplies for directed energy applications. Tools such as Excel and MATLAB/SIMULINK® are being used to accomplish this task. The second objective was to setup a high voltage testbed that can be used to study the ability of high voltage pulsed power capacitors (HVPPCs) to be charged and discharged at high current rates in a controllable temperature environment. The progress made on both objectives will be discussed here.

Introduction:

Abbreviation List: DEW: Directed Energy Weapon, UC: Ultracapacitor, LIB: Lithium-ion Battery, COTS: Commercial-Off-the-Shelf, DE: Directed Energy, EDLC: Electric Double Layer Capacitor, UTA: University of Texas at Arlington, PPEL: Pulsed Power and Energy Laboratory, HVPPC: High Voltage Pulsed Power Capacitor, CC: Constant Current, NN: Neural Network, CLC: Capacitive-Inductive-Capacitive, VI: Virtual Instrument, cDAQ: Compact Data Acquisition, and EMI: Electromagnetic Interference

Task 1: Electrochemical Energy Storage Sizing Tool Development

Electrochemical energy storage is being studied across the US Navy to fulfill the electrical power requirements that have arisen in their effort to become a more electric fleet. Many different chemistries are available commercially off the shelf and each has unique properties with respect to its voltage, power, energy, impedance, and size characteristics, among many others. This makes choosing the correct energy storage for any application difficult and unfortunately there is no one-size-fits-all approach that can be taken. Energy storage manufacturers often design cells specifically for an application when approached by a customer. Even though they are designed for a specific application, the manufacturers often make them available commercially to other customers once fabricated, meaning that cells of countless geometries are available with very few industry standards available. This only increases the challenges faced when sizing energy storage for an application using COTS devices. When choosing a chemistry, there are many factors that should be considered. Those that are often considered first are the power density, energy density, impedance, and of course safety. Figure 1 presents a Ragone chart that demonstrates the range of power and energy density available from multiple energy storage chemistries.

The high power density of lithium-ion batteries (LIBs) and ultracapacitors (UCs) makes them attractive for use in DE applications since they demand a compact power supply that can supply high power transiently. UCs are also referred to as electric double layer capacitors (EDLCs) for reference. UCs make sense in applications that require a power supply with high power, long life, and high safety but not high energy store. When higher energy stored is required, a LIB is likely a better choice, but they come with many tradeoffs that must be considered. Within the LIB category, there are many different chemistries to choose from, most of which have not been studied significantly under high power operation. These vast choices make the design of a prime power supply for DE applications a non-trivial task. The intent of the research being performed here is to research the present state of the art UC and LIB technologies and assess their operation and usable capacity at high power. Because these technologies are rarely used at the power levels required by DE applications, little is understood about how they perform, age, fail, and how to properly size them for a high power applications. In the second year of this three year effort, progress has been made to advance the development of a MATLAB/SIMULINK® based sizing tool that can be used to assist pulsed power engineers with the design of compact prime power supplies.

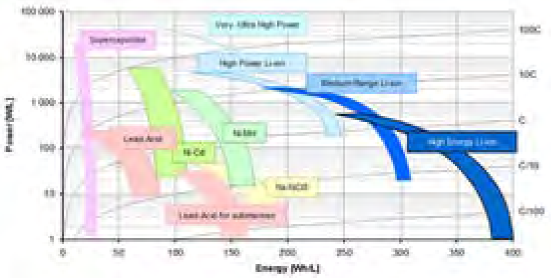

Figure 1. Ragone chart displaying the power and energy density (with respect to volume) for several energy storage chemistries.

Task 2: Study of High Voltage Pulsed Power Capacitors (HVPPCs) at High Charge and Discharge Rates

In many DE power supplies, the prime power supply referenced in Task 1 is used to transfer energy into an intermediate energy storage element that is used to supply high peak power to the load. In many cases, HVPPCs are used as the intermediate energy storage. Electrostatic dielectric film capacitors with self-healing electrodes have proven to be the most reliable for pulsed power applications where short pulse discharges are required. In the work being performed here, a capacitor manufacturer has provided a capacitor that they have had trouble with when attempting to recharge them quickly between repetitive discharges. The capacitors are proprietary and not a great deal is known about their construction or any special design features. It is assumed that the capacitor being studied is a polypropylene metallized film capacitor. The capacitor has a rated capacitance of just under 30 nF and voltage rating of 100 kV. The capacitor is being used as storage within a multi-staged Marx generator driving a DE load. In order to study its performance and lifetime in an emulated operational scenario that involves a high rate discharge, high rate recharge, and a second high rate discharge, a testbed has been designed and assembled. Commissioning of the testbed is still in progress as of this writing. The design and construction of the testbed will be presented here.

Background:

Since 2010, the University of Texas at Arlington’s (UTA’s) Pulsed Power and Energy Laboratory (PPEL) has been supporting the Office of Naval Research (ONR) in its study of electrochemical energy storage devices and systems. In the work performed here, the PPEL has assisted ONR with the development of a sizing tool for sizing prime power supplies that can be used in low energy, repetitively operated, 100 Hz, Marx generator. LIBs and UCs have been considered technologies with potential in these applications. A Microsoft Excel based sizing tool has been improved upon for future use in studying how different LIB and UC technologies compare with respect to power supply size and weight. Time was spent this FY redesigned the sizing tool using the MATLAB/SIMULINK® environment so that iterative processing can be achieved. In order to ensure its accuracy, the sizing tools have been developed using data that is experimentally collected at the high power rates required of a compact DE prime power supply. The power rates they are studied at are rarely published by the manufacturer making the work performed by the PPEL critical to understanding what is achievable using these COTS energy storage devices. The tool has only been partially validated with more work to be done in the future. Toward the middle of the year, effort was redirected towards designing and setting up a testbed on which HVPPCs could be studied at high rates of discharge and recharge, respectively. The testbed is needed to study the performance and eventual failure mechanisms of the types of metalized film capacitors used in repetitive rate Marx generators.

2. Activities and Accomplishments

During this reporting period, two tasks were executed and partially completed. The first was to improve a Microsoft Excel based energy storage sizing tool that can be used to accurately design a prime power supply for DE and other Navy applications. The results of the Excel development will not be presented here as it is not significantly different from last year. Shortcomings of the Excel were identified in late FY19, primarily the lack of iterative processing, that prompted the tool to be redesigned using MATLAB/SIMULINK® and time was spent this FY making that possible. A simple flowchart describing the sizing tool’s functionality is presented in

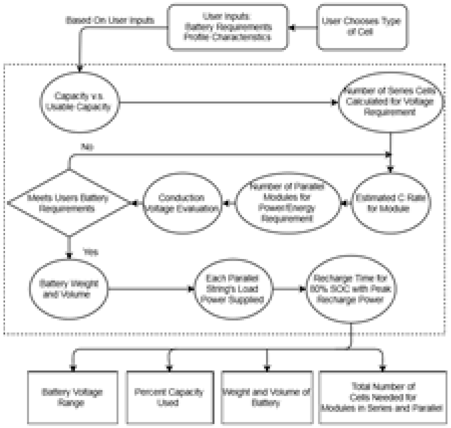

Figure 2. Flowchart describing the battery sizing tool operation.

Figure 2. Because LIBs have a nearly constant discharge curve, the power they can supply is quite consistent and utilization of Excel was found to be relatively enough for sizing a high rate prime power supply. UCs on the other hand have a conduction voltage that linearly decreases and as a result their power decreases linearly as well assuming a constant current (CC) discharge. Since Excel is not able to iteratively solve a problem easily, an environment such as MATLAB/ SIMULINK® is advantageous. The sizing tool is designed for the user to enter a profile and power level and tool uses both datasheet and empirically collected values, respectively, to provide the user with an estimate of the minimum number of series/parallel cells needed to meet the application constraints. The tool takes the cell's maximum discharge rate and conduction voltage into account such that it keeps the voltage above the minimum voltage requirement in its calculation of the minimum number of cells needed. Temperature, usable capacity, and usable energy could be implemented in later iterations of the sizing tool. Results from the sizing tool are seen in Figure 3 that show how the conduction voltage changes with each module that is added in parallel.

Because UCs are easier to model than LIBs, a SIMULINK® model was introduced into the UC sizing tool for further validation. Figure 4 shows a simulation result, again based off a user's input requirements, that is model level validation of the sizing tool's optimized sizing result. In the figure, the simulation results show the energy supplied to the load, the power supply's conduction voltage, the supplied current, and the output power are all presented. Though not easy to read, the intent of the figure is to demonstrate the simulation capability of the UC sizing tool.

Though not introduced into the sizing tool yet, time was also spent this year studying the utilization of neural networks (NNs) to fill in voltage versus capacity data that is not captured empirically. When experimentally cycling energy storage devices, there are only so many rates that the devices can be feasibly cycled at to obtain a full idea of what they are capable of. The ability to use NNs to more accurately predict data that is not measured experimentally would be very beneficial from time and accuracy perspectives. A NN using thirty hidden

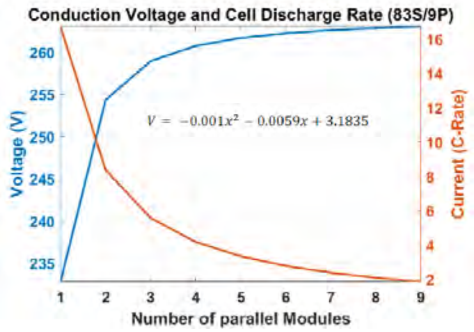

Figure 3. Battery sizing tool results showing how the conduction voltage & discharge rate changes as the number of parallel modules increases.

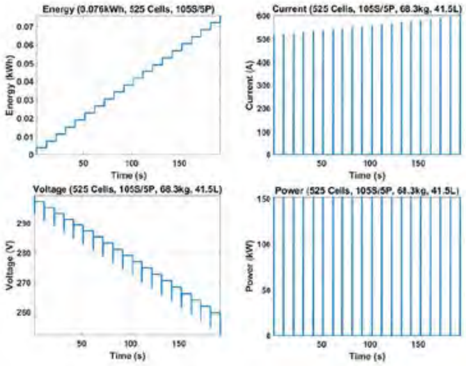

Figure 4. UC sizing tool simulation results.

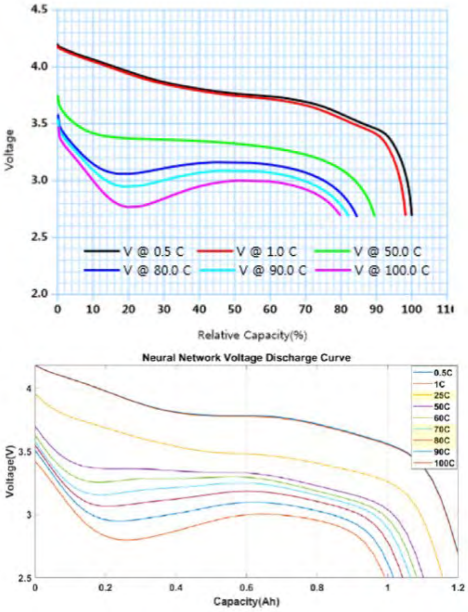

Figure 5. Kokam KMX16003 datasheet discharge curves (above) and NN simulated results (below). The rates highlighted in yellow are predictions made by the trained NN.

layers was created that estimates battery voltage curves based off selected points input from either the datasheet or experimentally collected data by the user. The original manufacturer datasheet (above) as well as results obtained from the trained NN (below) are shown in Figure 5. To evaluate the NN, discharge rates for which data was not obtained were run through the NN. As shown, the discharge curves of the NN based battery model mimic the datasheet very closely. The estimated curves the NN was not trained on, highlighted in yellow, appear to make sense but need still need to be validated against electrical data. These results are promising and suggest that if the NN can be introduced into the battery sizing tool, the results could be improved with respect to accuracy6. of estimating the usable capacity as a function of discharge and recharge current rate.

National Instruments Control and Data Acquisition

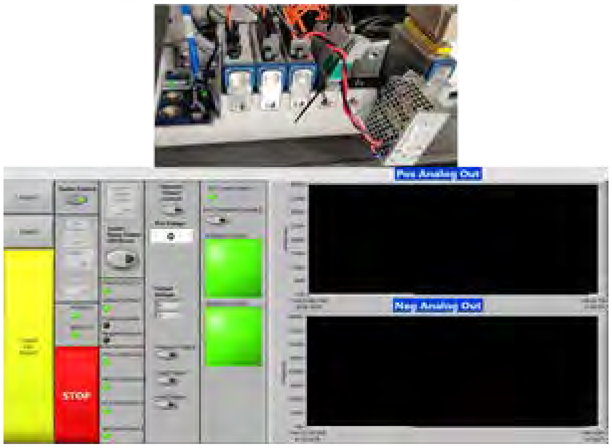

Figure 10. cDAQ chassis (top), and VI (below).

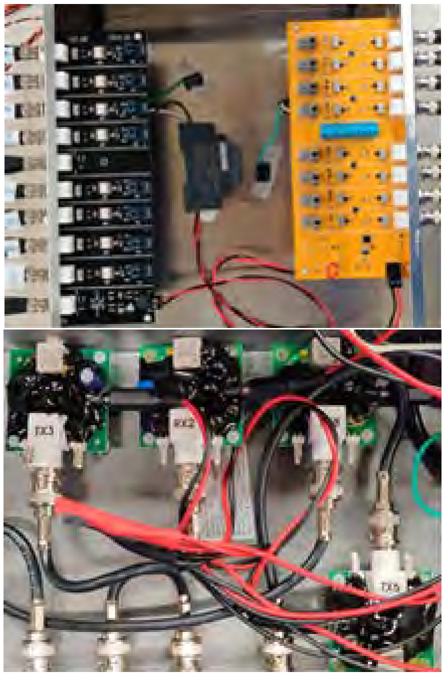

Figure 11. Digital/fiber converter boards (top) and analog/fiber converter boards (bottom)

The second task executed this FY was to design, construct, commission, and utilize a testbed for studying HVPPCs subjected to high current pulsed charge and discharge currents. As previously written, a HVPPC manufacturer has experimentally found problems when attempting to repetitively charge and discharge capacitors at high pulsed currents. To assist in better understanding what is causing the failure, a capacitive-inductive-capacitive (CLC) testbed has been designed, constructed, and partially commissioned this FY. A schematic diagram of the testbed is shown in Figure 6. Simply described, two 40 kVDC power supplies, of opposing polarity, are used to charge two 80 nF HVPPCs that act as an intermediate energy storage device. The unit under test is 28.3 nF capacitor labeled UUT. Initially the two 80 nF capacitors are charged using the power supplies and Ross Relays labeled 'DC_Charge' are used to isolate the power supplies from the system after charging.

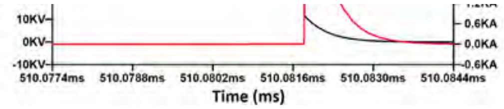

c.

Figure 7. Simulated results of the CLC circuit during

. The unit under test is also charged up differentially to 80 kV. To prevent back and forth resonant charging between the UUT and the two 80 nF capacitors; two diode stacks labeled 'D5' and 'D7' were implemented. Once charged, 'Sparkgap2' is triggered causing the unit under test to discharge its current into the 2 Ω load, made up of several large water resistors connected in parallel. This is designed to produce a 5.8 kA pulse that is roughly 300 ns wide, as shown in the upper Figure 7.

Roughly 10 ms after the first discharge, ‘Sparkgap’ is triggered connecting the common ground of the two 80 nF capacitors and bringing them into the circuit. Once this happens, the 28.3 nF capacitor is rapidly recharged by the pulsed current supplied by the two 80 nF capacitors connected in series through the series inductance placed between the high and low sides of the capacitor. The 50 µs wide recharge pulse, with a roughly 36 A amplitude, is shown in the middle plot in Figure 7. Since the circuit is an underdamped CLC circuit, it wants to oscillate however the intent is to retrigger ‘Sparkgap2’ once the first voltage peak is reached causing it to again discharge a 300 ns pulse into the 2 Ω load, shown in the lower plot of Figure 7. This operational scenario mimics one type of scenario the 28.3 nF capacitor under test may be expected to perform under in a DE application.

Photographs of the testbed are shown in Figure 8. The high voltage components are all contained within an aluminum enclosure that is lined with a pan liner and then filled with transformer oil for dielectric insulation. The 80 nF capacitors, the capacitor under test, and the spark gaps were all provided by the sponsors. The charging inductors were contracted out for assembly. The spark gaps are triggered using the circuit shown in Figure 9. Simply described, a 47 µF capacitor is charged to 480 V and then discharged through a step-up transformer using a high-side SCR. The secondary steps up the voltage to roughly 24 kV to break down the switch. Three of these circuits have been assembled and are connected to the data acquisition and control system, seen in Figure 10, fiber optically for galvanic isolation. A National Instruments (NI) cDAQ chassis is used to control the system as well as sample and digitize some of the data. A custom Virtual Instrument (VI) panel, seen in the lower part of Figure 10, was created to interact with the power supplies and control the whole process. To isolate the NI controller from the high voltage system; fiber optic circuit boards, seen in Figure 11, were designed and fabricated to interface the digital signals of the two systems. To interface the analog signals, analog/fiber converters, seen in Figure 11, were procured by a company called AA Labs.

As of this writing, the CLC testbed has been constructed and partially commissioned with many hurdles overcome along the way. Early in the commissioning, arcing occurred between one of the charge relays and the dump relay that took out a portion of the data acquisition. Once that was solved, electromagnetic interference (EMI) started to be observed during the charge sequence that was crashing the VI and severely affecting other experiments operating in the lab. To date the effect of EMI on the VI has been able to be overcome but it is still affecting other hardware in the lab and that is being solved so that experimentation can begin. It is anticipated that evaluation of the capacitors of interest will begin in November 2019.

3. Findings and Conclusions

As documented here, two main tasks have been worked on during this FY. The first was incremental improvements made to the LIB and UC sizing tool, which was redeveloped using MATLAB/SIMULINK® in place of Excel. The tool has been validated partially, for both LIBs and UCs with more work to come in the next FY when time permits. Though not introduced into the sizing tool, time was spent evaluating the use of NNs for more accurate prediction of usable battery capacity as a function of discharge and recharge rate. The goal would be to integrate NNs into the sizing tool such that it can more accurately estimate the required number of cells a battery needs to meet the user’s needs. The results were quite accurate with minimal effort placed on it so there is confidence that this can be improved further if time permits in the next FY. Finally, time was spent on a second task designing and constructing a testbed on which HVPPCs can be evaluated under high rates of charge and discharge. As shown in the simulation results presented here, a CLC circuit is being used to emulate a discharge-recharge-discharge scenario for the capacitors of interest. The testbed has been constructed and partially commissioned though there have been challenges encountered that have prevented progress from being as quickly as anticipated. The primary challenges involve reliable triggering of the spark gaps and reduction in EMI that is causing problems within the testbed itself and the surrounding experiments. These problems are being worked on and it is anticipated that they will be overcome soon.

4. Plans and Upcoming Events

In the next FY, the focus will be on getting the CLC testbed working more reliably and evaluating multiple capacitors of interest under different experimental conditions. The goal is to more fundamentally understand high voltage capacitor aging and failure under high rates of charge and discharge in varying environmental conditions. If time allows, additional time will be spent improving the MATLAB/SIMULINK® sizing tool. UTA will work with researchers at NSWC Dahlgren, Sandia National Laboratories, and Air Force Research Laboratories - Kirtland to facilitate this testing.

5. Transitions and Impacts

To date the knowledge gained can be transitioned on to any team performing work in the directed energy (DE) area any groups interested in designing compact prime power systems utilizing electrochemical energy storage would benefit from the knowledge gained to date It is our understanding that many laser, high power microwave, and electromagnetic railgun programs are ongoing that are considering batteries as their prime power systems who may benefit.

6. Collaborations

We have collaborated with:

Jordan Chapparo – NSWC-DD, Yeong-Jer Chen – NSWC-DD, Frank Hegeler – Naval Research Laboratories (NRL), Dale Coleman – Sandia National Laboratories, Emily Schrock – Sandia National Laboratories, Josh Gilbrech – Air Force Research Laboratories – Kirtland, and Mark Schneider – General Atomics

7. Personnel

Principal investigator: Dr. David Wetz – 2.5 months (400 hours), National Academy Member (N)
Business Contact: Jeremy Forsberg, ogcs@uta.edu
Team Members: Listed as students below
Subs: None

8. Students

Jacob Sanchez: EE PhD Candidate (Graduated in May 2019), Blake Adams: EE Undergraduate Student (Graduated in December 2018), Bradley Pipes: EE Undergraduate Student (Graduated in December 2018), David Dodson: EE PhD Candidate (Graduated in May 2019), Chris Martinez – EE MS Candidate (will graduate in December 2019), Cameron Johnston: EE Undergraduate Student.

9. Technology Transfer

None

10. Products, Publications, Patents, License Agreements, etc.

One conference presentation was given at the 2019 IEEE International Pulsed Power Conference in June 2019 and another was given at the 2019 Pacific Symposium on Pulsed Power and Applications. Monthly reports were compiled and delivered to ONR. A status brief was given at the DE Program Review in Washington DC in April 2019.

11. Point of Contact in Navy

Ryan Hoffman – ONR PM (contacted on multiple occasions)
Matthew McQuage – NSWC-DD (contacted on multiple occasions)
Frank Hegeler – NRL (contacted on multiple occasions)
Yeong-Jer Chen - (contacted on multiple occasions)
Jordan Chapparo - (contacted on multiple occasions)

12. Acknowledgement/Disclaimer

This work was sponsored by the Office of Naval Research (ONR), under grant number N00014-17-1-2847. The views and conclusions contained herein are those of the authors only and should not be interpreted as representing those of ONR, the U.S. Navy or the U.S. Government.

Efficient, Insulators for High Power Radio Frequency Devices

Grant No. N00014 -17-1-2848

Annual Report for Fiscal year 2019

Period of Performance: October, 1, 2018 to September 30, 2019

Prepared by:
Professor Jane Lehr, Principal Investigator
University of New Mexico
Department of Electrical and Computer Engineering
MSC 01 1100
Albuquerque NM 87131-0001
Tel: (505) 277-1749
Fax: (505)277-1439
Email: jmlehr@unm.edu

This work was sponsored by the Office of Naval Research (ONR), under grant number N00014 -17-1-2848. The views and conclusions contained herein are those of the authors only and should not be interpreted as representing those of ONR, the U.S. Navy or the U.S. Government.

Grant or Contract Number: N00014-17-1-2848
Date Prepared: 31 Jan 2020
Project Title: EFFICIENT INSULATORS FOR HPRF DEVICES
Annual Summary Report: CY2019
Principle Investigator: Jane Lehr
University of New Mexico, Electrical and Computer Engineering
(505) 277-1749; jmlehr@unm.edu

Section I: Project Summary

1. Overview of Project

Abstract: In the design of directed energy and high power radio frequency (HPRF) sources, high power electrical pulses are generated in a volume filled with high dielectric strength fluids while the directed energy source typically operates in vacuum. The two sections, then, require an insulating barrier that is subject to very high electric fields and susceptible to electrical breakdown. This insulating barrier is, by far, the most likely component to fail within the system. Electrical breakdown is overwhelmingly more likely to occur along a solid immersed in the fluid (called a surface flashover) and the mechanism of its development remains only marginally understood. The system implications of failure of this barrier is critical: not only does the flashover prevent power flow to the directed energy load, but the reflected power results in a large, repetitive voltage reversal which either degrades (or destroys) the pulsed power driver resulting in complete system failure. This research effort is intent on improving the voltage withstand capability of an insulating barrier efficiently – that is, without introducing new reactance. This is accomplished by utilizing a high gradient insulator geometry, surface contouring to control the electric field components driving the discharge and investigating the origins of surface flashover in vacuum through coupled modeling and experiment.

Objective: Our objective is to experimentally demonstrate an insulating barrier in vacuum with a factor of two improvement in withstand capability over the current state-of-the-art, preferably with a vacuum compatible material. To accomplish this goal, the relative importance of secondary electron emission material properties, triple points, surface shape, insulator length and high gradient insulator design will be investigated.

Introduction: Insulating barriers separating vacuum sections from fluid insulated sections occur across many vacuum applications, such as vacuum circuit breakers, pulsed power devices, high power microwave (HPM) dielectric window, high energy physics and other vacuum electronic devices. For such a vacuum-solid insulation system, discharge preferentially occurs along the solid surface, developing to flashover. The applied electric field for surface flashover occurs at a frustratingly lower level than the bulk breakdown strength of either the solid or vacuum gap of the same length and typical values of ~ 5% are used. For example, the critical bulk breakdown field for vacuum is about 350 kV/cm, and ~300 kV/cm for high purity alumina ceramics, while it is only a few tens of kV/cm when flashover occurs in a vacuum-alumina solid insulation system. The vacuum-insulator interface is affected by the high electric field and complex environment, including exposure to charged particles, ultraviolet and x-rays, which will lead to surface insulation modification and create pulsed flashover failure. The voltage withstand should be as high as possible to ensure energy delivery to the target. Thus, surface flashover is the limitation on both the size weight and power, reliability and power flow.

Generally, for high power radiofrequency (HPRF) vacuum electronics, the insulator separating the pulsed power driver from the directed energy source is in an axial stack as shown below. The geometry adds significant inductance and size to the device. Using high gradient insulators, UNM has proposed a radial insulating stack to hold off voltages on the order of 750 kV in a 10cm diameter tube in vacuum, resulting in great savings of space and inductance. The proposed design requires a tangential component of the electric fields to be 70 kV/cm to meet the design constraints. UNM's insulating stack converts the logarithmic dependence of the electric field in concentric cylinders to be both uniform and close to the mean electric using high gradient insulators.

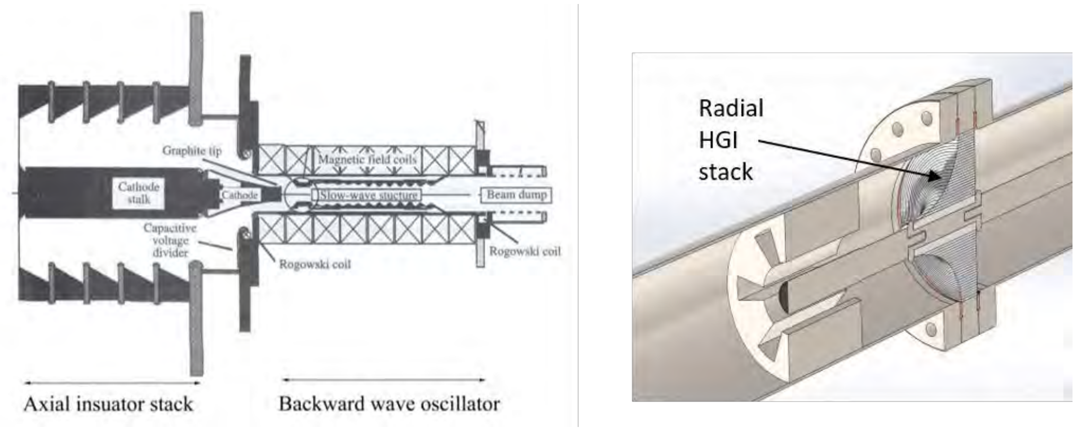

Figure 1 The conventional insulator technology and the radial design.

According to the predominant theory of surface flashover in vacuum, the Saturated Secondary Electron Emission Avalanche Theory (SSEEA), shorter vacuum insulators are able to endure higher electric field gradients. Eoin Gray first proposed alternating layers of insulator and metals - now commonly referred to a high gradient insulators (HGI) - to take advantage of this phenomenon to increase the withstand voltage for larger structures. Elizondo suggested that the maximum thickness of the dielectric layers should be less than the expected electron range, so that electrons were intercepted by a metal layer before they could collide with the dielectric surface and produce secondaries. HGIs designed following these guidelines usually have dielectric layers in the order of 500μm thickness, interspersed with much thinner metal layers that protrude beyond the dielectric, like vanes. However, experiments showed that HGIs with protruding vanes did not perform differently to those without protruding vanes except for the difficulty in fabrication so most recently built HGIs are assembled with metal layers nominally flush with the dielectric surface. Sampayan found that an ultra-high gradient insulator could greatly increase surface insulation strength by a factor of four over the conventional cylindrical insulators.

Another mechanism for HGIs proposed by Leopold et al was that the periodic electric field perpendicular to HGI surface might be able to interrupt the SEEA by sweeping electrons away from insulator surface if the geometry was properly designed. Numerical calculations of electron orbits showed that the electric field in HGI assemblies had the favorable property of sweeping charged particles away from the surface, and that electron multiplication on the surface was suppressed when $I/M<3$, where I is the axial length of an insulating layer and M the length of a metal layer. Compared with conventional insulators, a much better performance was observed for HGIs when $I/M<3$, but somewhat worse when $I/M>3$. By the calculation and analysis of the electric field, Ren also verified that the electric field of a structure beginning with a half-layer of metal could sweep electrons generated from cathode away from HGI surface. The surface features of HGIs significantly affect the electrical performance. However, extremely high level of preparation technologies is required in the machining and processing of HGIs, such as film coating technology, high temperature heating technology, and ultrasonic grinding technology.

UNM and Sienna are using a polycrystalline form of the machinable ceramic aluminum nitride (AlN) as the insulator for its many attractive properties. Aluminum Nitride is a man-made material that has high vacuum compatibility. Sienna Technologies makes several different formulations and have measured the secondary electron emission yield (SEE) of each. The metal layers were made from primarily from copper and molybdenum.

2. Activities and Accomplishments

A baseline holdoff flashover voltage for monolithic AlN insulators was measured in order to compare to previous results reported for a similar type of insulator. Six total straight wall cylindrical samples were tested and the average electric field holdoff was used for the comparison.

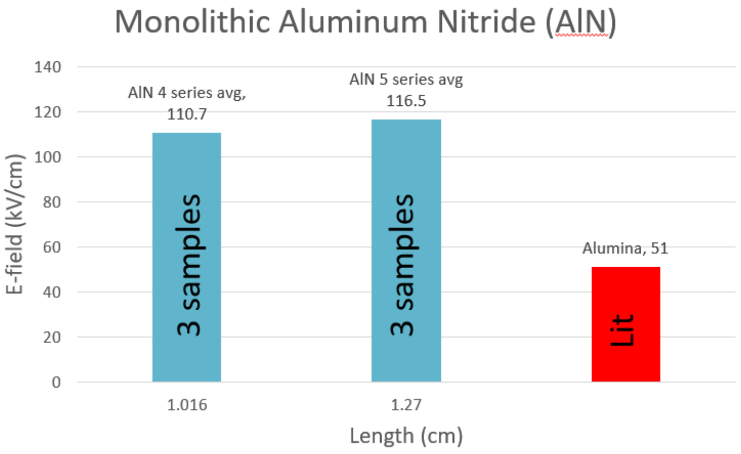

Figure 2 Comparison of monolithic AlN and monolithic alumina insulators.

Figure 2 compares the average electric field the samples were able to holdoff of two different sizes of monolithic AlN insulators to that of the of an alumina insulator. The alumina samples height was not given; however, the assumption is that the sample length is between 1.6 - 2cm from commentary in the publication. Figure 2 shows that the average AlN insulator had an electric field holdoff over double the alumina insulator.

Conical AlN Insulators: Conical insulators with varying angled slopes have larger holdoff voltages compared to straight wall insulators due to the behavior of the electric field at the triple point [3]. Similar results have been found with the AlN insulator samples. The tested conical AlN samples include two different sizes and two different angles as seen in Figure 3.

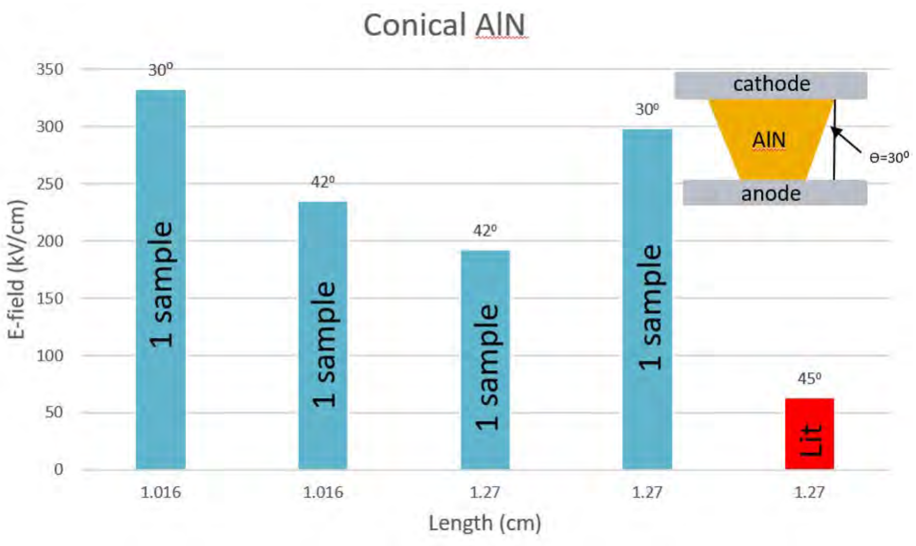

Figure 3: The results of the conical AlN testing. Blue bars were tested at UNM. Red bar was taken from O. Milton, (IEEE Trans. Elect. Insul. Vol EI-7, No. 1. March 1972).

The red bar denotes the measured results of a coated alumina sample found in the literature [4]. AlN insulators are able to holdoff a much larger electric field. However, it should be noted that a 2μs voltage pulse was used in the coated alumina experiment. It is not a direct comparison, however that data implies that the conical AlN may to holdoff more voltage compared to alumina. The results indicate that a 30 degree sample held off the largest electric field, however, more testing should be done to determine an average holdoff electric field. These four data points are taken from four different samples. Therefore, there may have been some variation between samples due to surface anomalies or other factors.

High Gradient Insulator The high gradient insulators tested were primarily made from aluminum nitrate (AlN) insulating ceramic and molybdenum (Mo) conductor, however in some cases copper (Cu) was used as the conducting material. Due to ease of manufacturing the thin layered samples were made using copper; however future experimentation should be done using thin layered molybdenum. Leopold et al reported that HGI's will have the largest holdoff field when the insulator to metal ratio (I/M) approached a value of 3 when testing with a fixed cell length. However, the Livermore group reported that an I/M ratio approaching infinity is optimal while using thinner cell lengths. A key differences in the two methods is the amount of layers in the insulator, and the overall size of material per layer. The results indicate that if thin/many layers are used, a larger I/M will have a higher holdoff. If thick/few layers are used, the highest holdoff approached 3. Our results agree with both authors; however having a thin/many layered sample will holdoff the largest electric field.

Leopold suggested that a conducting layer needs to be thicker in order to modify the electric field next to the surface enough to push electrons away from the surface. To verify that this dependence is associated with the I/M ratio and not the length of a metal layer Figure 4. was made. This graph shows that the thinnest metal layer withstood the largest electric field and as the metal layer got larger no trend in decline in performance can be seen.

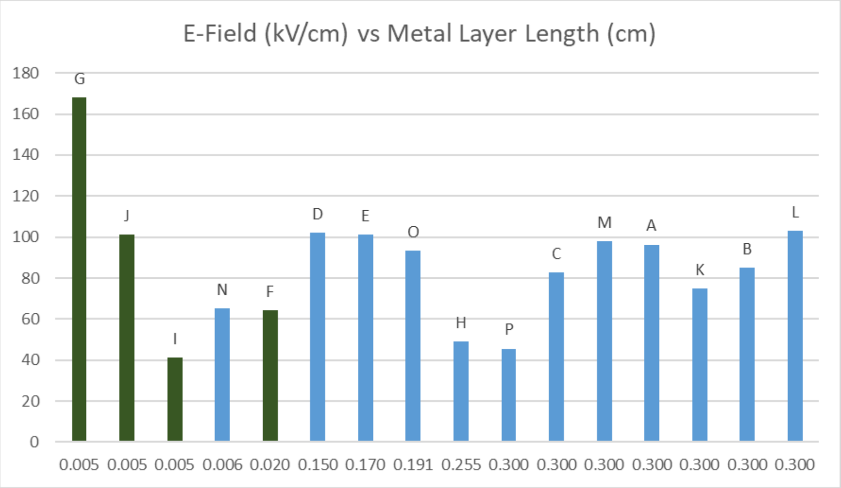

Figure 4: **This graph shows the sustained electric field vs the length of the metal layers of the HGI sample. The largest sustained electric field came from the sample with the smallest metal layer length. The green bars represent HGI samples with thin layers. The blue bars represent thick layers.**

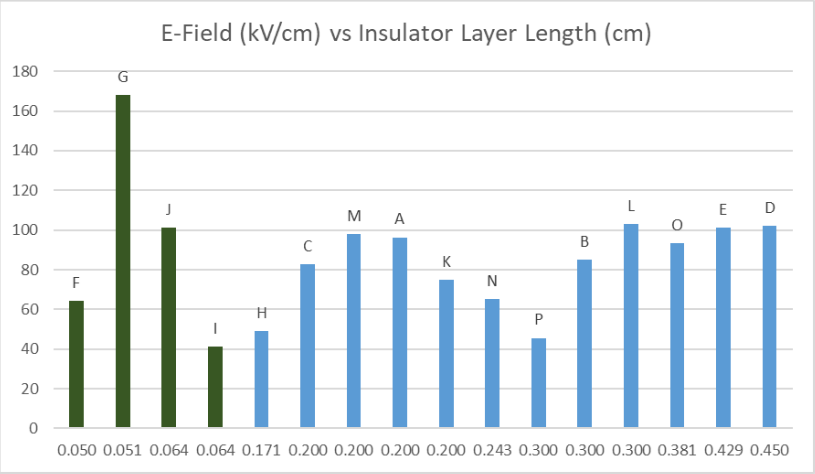

Figure 5: **The holdoff electric field for flashover vs the length of insulating layers. The largest flashover field came from the 2nd smallest length of insulator. The green bars represent HGI samples with thin layers. The blue bars represent thick layers.**

The $\frac{1}{\sqrt{L}}$dependence suggests that the smaller the insulator the lager the holdoff electric field will be higher. If HGIs are many insulators stacked on top of each other and the $\frac{1}{\sqrt{L}}$is applicable, the largest field should be expected to also have the smallest insulator layer length. Figure 4.9 shows that the smallest insulator did not holdoff the largest electric field, however the second smallest insulator sample did. Looking at the remaining data, no trend is clear. The $\frac{1}{\sqrt{L}}$ dependence should not be ruled out. HGI samples can be difficult to make, it is possible that sample F had surface anomalies that encouraged vacuum surface flashover. Also samples L, O, E, and D all performed about as well as sample J, this is a problem for the $\frac{1}{\sqrt{L}}$ trend**.**

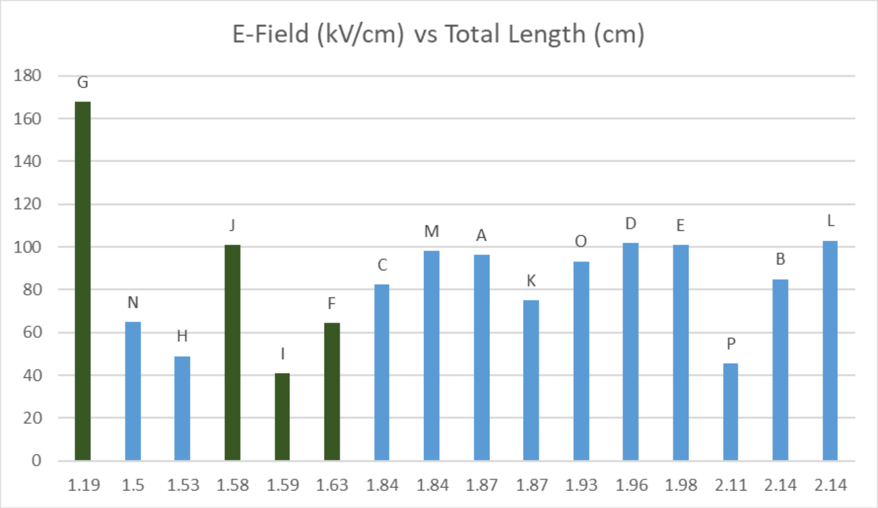

Figure 6: **This graph shows the holdoff electric field vs the total length of the HGI. The largest sustained field came from the smallest sample. Sample L heldoff an electric field of 103 kV/cm. This is the second largest holdoff. The green bars represent HGI samples with thin layers. The blue bars represent thick layers.**

Figure 7evaluates the holdoff electric field versus the total length of the HGI. Sample G was the smallest insulator and had the largest holdoff field. Sample L was the largest sample and had the second largest holdoff electric field. It should be noted that most thick/few layered HGIs heldoff an electric field around 100 kV/cm.

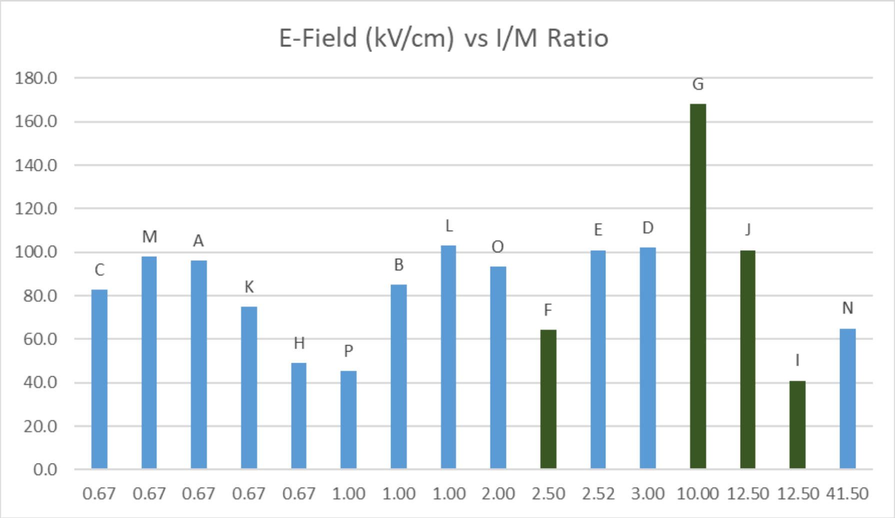

Figure 7: **This graph shows the holdoff electric field for each I/M ratio. It can be seen that as the ratio approaches 3 there is an increase in performance. However, samples M and L perform about as well as samples D and E. Sample G has an I/M ratio of 10 and was the only sample with an I/M > 3 to holdoff a much larger electric field. The green bars represent HGI samples with thin layers. The blue bars represent thick layers.**

Livermore proposed that HGI samples will continue to improve as the I/M ratio approached infinity (some point before the sample is monolithic)[]. Livermore used samples that had thin conducting and insulating layers. Sample G is a Livermore style insulator and had the largest holdoff electric field as seen in figure 4.11. Sample F is a Livermore style many thin layered model, however the I/M ratio approaches 3 and the sample did not perform well. Leopold used thick conducting and insulating layers and proposed that the optimal I/M ratio approaches 3[]. Sample D is a Leopold style HGI and was able to holdoff 101kV/cm. This result agrees with the results that Leopold gathered. Sample N is made of thick insulating layers and thin conducting layers resulting in an I/M ratio of 41.5. This sample did not perform well. It is difficult to draw conclusions on the thin HGIs. More data should be taken; however it should be noted that sample G had the largest electric field holdoff with a margin of 60kV/cm over the next highest performing sample.

3. Findings and Conclusions

This effort is comprised of two innovations. One is demonstrating the high gradient insulator concepts and its feasibility in a radial geometry. Because of fabrication limitations, the radial geometry cannot be achieved with polymers due to the hot-pressing requirement. The other innovation is optimizing the surface flashover potential by controlling the interface geometry. We have demonstrated significantly high electric fields using a ceramic comprised of a polycrystalline form of aluminum nitride. In seeking the optimum high gradient insulator, we are somewhat hampered by the lack of understanding of the physical mechanism that forms the basis of the high gradient insulator premise as well as the scaling of surface flashover potential with length. It is not widely known that both volume breakdown and surface flashover have a length dependence. This became apparent as we viewed our data across a number of samples. We intend to test the validity of the presumed dependence on the square root of the sample length. Our other hypothesis is that we can split the electric field into a coordinate system relative to the surface. The electric field component that drives the surface discharge is the tangential electric field. We will do some testing with conical samples to verify this hypothesis. In this calculation, refraction of the electromagnetic wave is ignored.

In the design of components for compact systems, design criteria are sparse. One reason is the variability of the surrounding atmosphere- and this is especially true in vacuum. That said, there have been remarkable accomplishments using physics-based design approaches. This year we have challenged two: first is the deconstruction of the surface flashover into the reference plane of the surface, and the other is the assumed scaling as the inverse of the square-root of the sample length.

The physical basis of changing the coordinate system is the rationale that along the surface, the electric field component tangential to the surface is the force driving the electron discharge that initiates the electrical breakdown. As a practical matter, the normal component should be managed so that it is “not too large.” To test this hypothesis, we tested several formulations of AlN in cylinders and in cones.

Surface flashover in vacuum is typically the limiting factor in high voltage experiments. Using different insulator materials or geometries have shown to increase the holdoff voltage. Depending on application, conical samples are not always ideal and high gradient insulators should be considered. A high gradient insulator was able to holdoff an electric field of $168\frac{kV}{cm}$. This is an increase of $50\frac{kV}{cm}$ compared to monolithic AlN insulators of similar size.

4. Plans and Upcoming Events

The PI will use this research effort as the basis for an IEEE Distinguished Lecturer award sponsored by IEEE's Nuclear and Plasma Sciences Society. Two talks are already planned: Purdue University's Nuclear Engineering Department and the local Joint IEEE Chapter.

Experimentally, we are approaching some significant results. Some, such as the verification of the scaling with length will be good to verify against Milton's results and remind the community that the scaling exists. More significantly, this scaling forms the basis for the HGI concept. If it is verified that will provide clear guidance for future testing. Testing regarding the importance of the ratio of insulator to metal lengths has shown that there is likely to be competing mechanisms such as electron deflection, that can work.

We are currently reviewing our large quantity of data with normalization. It is very clear from both our data as well as the Milton data that the SSEEA model is seriously flawed. Specifically, because materials that outgas (i.e. acrylic, polycarbonate) have a higher flashover potential that ones that do not (AlN, BN, alumina).

While we have made great progress and demonstrated the high gradient insulator architecture can work with vacuum compatible ceramics, the theory on how to design them for performance has not yet been determined. In particular, the dependence on the length of insulator is a key determination. We will design a test matrix where the length of insulator is tested for a given length of metal section and length.

An obligation to our collaborative subcontractor has not yet been released.

Recommendations for Future Work:
The pre-breakdown phase of surface flashover can be considered to have two distinct phases: initiation at the triple points and charge carrier multiplication along the surface. To date we have ignored the triple point issue by making a simple contact between the surface. By addressing the triple point, it would allow a procedure to separate out the initiation mechanism from the propagation development. It will be very illuminating to determine how much benefit (in terms of withstand voltage) can be achieved by addressing the triple points. Such an experiment has never been performed in monolithic or high gradient insulator geometries and thus would be unique. This is especially important for the high gradient insulator technology because, in some constructions, triple points are introduced at every layer.

The physics of triple points offer another opportunity for future research since the mechanism of electron emission is unknown. Typically, the phenomenon is attributed to enhanced field emission resulting from the singularity at the intersection of the dielectric-metal-vacuum boundary. Jordan (2007) showed computationally that the electron emission was too high to be explained purely by field enhancement. Research into this topic would be both scientifically interesting and have wide and important practical applications.

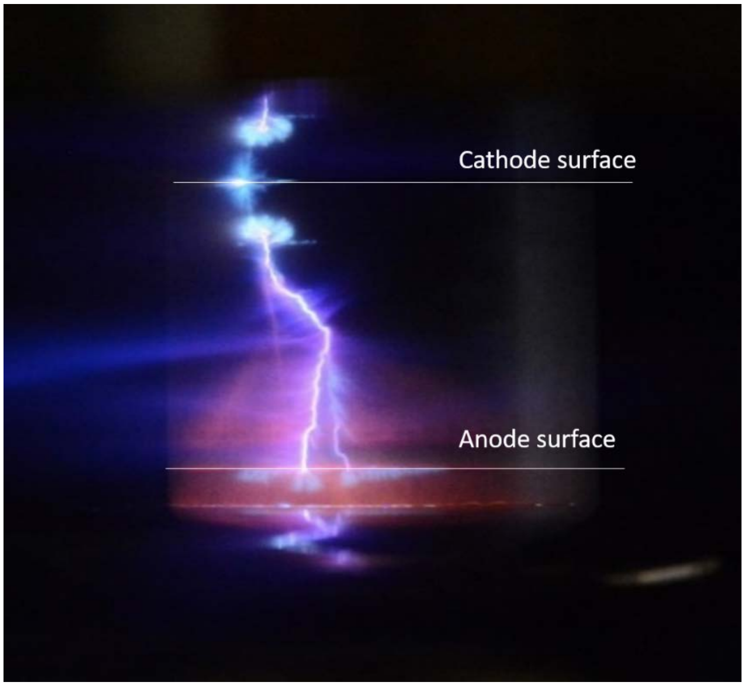

Figure 8. A time resolved photo of a surface flashover showing initiation at the cathode. Researchers have long devised techniques to minimize the effect of triple points empirically but the mechanism is not well understood and long suspected of being complex.

We have identified a flaw in the widely accepted theory of surface flashover. It would be essential to push the state of the art to determine material choice for performance.

Two approaches of high gradient insulator were explored in this work. The first approach (Leopold) used a few thick layers of insulating and conducting material and the second approach (Livermore) used many thin layers of the materials. Each approach suggested a different I/M ratio and had experimental results to support their claims and have been verified in our effort.

In this effort, we have not addressed the triple points – the junction between the insulator, metal and vacuum. Triple points are widely thought to be the results of electric field intensification (purely) which is unprovable because of the singularity. Open shutter photos of our data indicate that the discharge initiates at the cathode at the triple point. Future work could incorporate shielding techniques which would allow a separation of the effects of triple point from that of the discharge development. Moreover, a team at the University of Michigan proposed that the current of the electron emission at the triple point was too large to be purely the result of field enhancement. Measurements and theory regarding the physics of the triple point and mitigation techniques would have wide applications across the navy – not only for directed energy but for power electronics and electric ship applications.

The Air Force Research Laboratories Directed Energy Directorate has expressed interest in utilizing the results of this research in their nearly completed, anti-drone prototype HPM system. Their system uses an axial vacuum stack and recognize that a radial stack would increase reliability and performance due to reduced reactance.

5. Transitions and Impacts

Student J. Cameron Pouncey is a Smart Scholar slated for NSWC Dahlgren and spends summers in Virginia working on HPRF systems for Jacob Walker. He will aid in transitioning the results of this research into their devices.

Student Leonardo Rossetti has joined the Naval Research Laboratory's Electromagnetic Effects Section with PI Zachary Drikas (202-767-6629 / zachary.drikas@nrl.navy.mil).

The Air Force Research Laboratory' Directed Energy Directorate (POC Brad Hoff) has indicated strong interest in the technology. The Program Manager for THOR has cited the surface flashover of the insulator as the single biggest threat to system reliability and it interested in transitioning this technology to fieldable systems.

6. Collaborations

The Naval Surface Warfare Center- Dahlgren Division keeps in close contact regarding this effort.

Prof. David Wetz and I are in discussion regarding future collaborations.

Dr. Allen Gardner has been to visit UNM.

The Air Force Research Laboratory's Directed Energy Directorate and their contractor Leidos have expressed interest in transitioning this work into deployable systems.

7. Personnel

Principal investigator	Prof. Jane Lehr/ 0.5 person month/ National Academy: N
Co-investigator	N/A
Business Contact	N/A
Team Members	Dr. Lisa Fisher/ 3 person months/ National Academy: N Dr. Andrew Fierro, 2 person months/ National Academy: N
Subs	Dr. Ender Savrun/ / 0.25 person months/ National Academy: N

8. Students

Graduate Students:	J. Cameron Pouncey, Cameron Harjes, Leonardo Rossetti, Justin K. Smith
Undergraduates:	Ken Le, Brad Maynard, Isaac Garcia, Nikita Dougan (Freshman, Fall'19)
High School students:	Nikita Dougan, Joseph DiDomenicis

All of these students are US citizens.

9. Technology Transfer

The Air Force Research Laboratory’s Directed Energy Directorate (researcher Brad Hoff) has expressed interest in incorporating into fieldable devices.

NRL Principal Investigator Frank Hegeler has expressed strong interest in this research for implementation into the wide array of Navy applications involving high power.

NSWC Dahlgren will use this technology in future systems. They are also interested in a utilizing thermoplastics as potential lightweight insulators.

10. Products, Publications, Patents, License Agreements, etc.

Publications resulting from this project:

Archival Publications (publication reference information (article title, authors, journal, date, volume, issue) can be automatically entered using a DOI)

a. Article Title Erection of Compact Marx Generators
b. Journal IEEE Transactions on Plasma Science
c. Authors Jon Cameron Pouncey, Jane Lehr and David Giri
d. Keywords compact pulsed power, Marx generator, spark gaps, triggering
e. Distribution Statement: Unlimited distribution
f. Publication Status published
g. Publication Identifier Type: DOI: 10.1109/TPS.2019.291503
h. Publication Identifier: The unique identifier for the publication
i. Publication Date June 2019
j. Volume 47
k. Issue 6
l. First Page Number 2902
m. Publication Location: New Jersey USA
n. Acknowledgement of Federal Support? Yes
o. Peer Reviewed? Yes

Article Title; Measurement of Photoionization Rates in Air
b. Journal IEEE Trans. on Plasma Science, *Special Issue on Invited and Plenary Talks*
c. Authors Justin Smith, Lisa Fisher and Jane Lehr
d. Keywords photoionization, electrical breakdown
e. Distribution Statement: Unlimited distribution
f. Publication Status accepted for publication
g. Publication Identifier Type:
h. Publication Identifier:
i. Publication Date
j. Volume
k. Issue
l. First Page Number
m. Publication Location: New Jersey USA
n. Acknowledgement of Federal Support? Yes
o. Peer Reviewed? Yes

Conference Papers

a. Title: Insulator Technologies to Achieve Maximum Electric Field Holdoff
b. Authors Cameron Harjes, Lisa Fisher, Jon Cameron Pouncey, Ender Savrun, Isaac Garcia, Jane Lehr
c. Conference Name IEEE Int. Pulsed Power and Plasma Sciences Conference
d. Conference Date: June 23-28, 2019
e. Conference Location: Orlando, FL, USA
f. Publication Status: accepted
g. Publication Date
h. Publication Identifier Type
i. Publication Identifier
j. Acknowledgement of Federal Support? Yes

Books N/A

Book Chapter N/A

Theses

a. Identification of the Corona Point in Point-to-Plane Geometries in Atmospheric Air
b. University of New Mexico
c. Leonardo Rossetti
d. Completion Date: August 2019
e. Acknowledgement of Federal Support? Yes

a. Inhibiting Surface Flashover in Vacuum with High Gradient Insulators
b. University of New Mexico
c. Cameron Harjes
d. Completion Date: December 2019
e. Acknowledgement of Federal Support? Yes

a. Measurement of Photoionization Rates in Air*
b. University of New Mexico
c. Justin K. Smith
d. Completion Date: December 2019
e. Acknowledgement of Federal Support? Yes
* with Distinction

Websites N/A

Patents N/A

Other Products: Identify any other significant products that were developed under this project. Describe the product and how it is being shared.

a. Advanced Instrumentation Course Curricula
b. Graduate course is being developed to advance skills in various instrumentation – high precisions digitizers, network analyzers, advanced optical diagnostics for advanced graduate students.

11. Point of Contact in Navy

Yeong-Jer (Jack) Chen
NSWCDD, E13
Date of last contact: January 27, 2020

Matt McQuage
NSWCDD,
Date of last contact: January 28, 2020

Dr. Frank Hegeler
Naval Research Laboratory
Date of last contact: September 10, 2019

12. Acknowledgement/Disclaimer

This work was sponsored by the Office of Naval Research (ONR), under grant number N00014 - 17-1-2848. The views and conclusions contained herein are those of the authors only and should not be interpreted as representing those of ONR, the U.S. Navy or the U.S. Government.

Fundamental Studies for Nanoscale Vacuum Electronic Emission Devices

Grant No. N00014-18-1-2382

First Annual Report for Fiscal year 2019

Period of Performance: October, 1, 2018 to September 30, 2019

Prepared by:
Professor Ravi P Joshi, Principal Investigator
Texas Tech University
Department of Electrical and Computer Engineering
2500 Broadway MS 3102/Campus
Lubbock TX 79424
Tel: 806-834-7979
Email: ravi.joshi@ttu.edu

This work was sponsored by the Office of Naval Research (ONR), under grant number N00014 -17-1-2848. The views and conclusions contained herein are those of the authors only and should not be interpreted as representing those of ONR, the U.S. Navy or the U.S. Government.

Grant Number: N00014-18-1-2382
Date Prepared: December 31, 2019
Project Title: Fundamental Studies for Nanoscale Vacuum Electronic Emission Devices
Annual Summary Report: CY2019
Principle Investigator: Ravi P Joshi, 806-834-7979, Email: ravi.joshi@ttu.edu
Texas Tech University, Lubbock, TX 79424

Section I: Project Summary

1. Overview of Project

Abstract: The goals and objectives of this research are focused on theoretical studies, simulations and basic research on electron emission from nanostructures for vacuum electronics and other high power applications. This includes not just electrons, but also outgassing of desorbates that can potentially alter the space-charge of high power microwave (HPM) systems in the vicinity of emitting electrodes. In addition, evaluations of absorption of gaseous species (with hydrogen as a specific example) in metal electrodes (with copper as a representative metal) were carried out based on Molecular Dynamics (MD) simulations. Such evaluations are important to advance the fundamental physics-based understanding of vacuum field emission in nanoscale emitters, their photoemission characteristics, analyze surface physics including effects due to incident ion impact, and probe the role of proximity effects in nanoemitter arrays with regards to screening, field enhancements and safe operating ranges.

Objectives: Cathode emitters are important components contributing to the overall successful development of high power microwave devices. For example, in the magnetically insulated transmission line oscillators (MILOs), use of cathode arrays or field shaper cathodes have been demonstrated to affect the beam quality (i.e., the uniformity, stability, the cathode plasma expansion velocity, etc.) and thus, influence the performance. Given that there is interest in MILO development both at Texas Tech University (TTU) and the Navy, this proposed effort would also help MILO work with regards to: (a) understanding the electron emission that is the source of microwave power, (b) achieving better electric field uniformity on the cathode surfaces for suppressing potential cathode flare formation, (c) focusing on emitter arrays for scalable increases in current and design of optimal spacing, and (d) in evaluating the potential for outgassing that can degrade the efficiency of HPM systems.

Introduction: The project has begun analyses for electron emission including secondary emission, atomic ejection and has also carried out some analyses to probe outgassing for HPM in systems characterized by low pressure. Outgassing has been probed based on MD techniques. Our results of temperature dependent diffusion coefficients for hydrogen in copper, agree well with experimental reports over a wide range spanning 300 K to 1330 K. Separate results were also obtained for transport of hydrogen to ascertain whether a grain-boundary would facilitate channeled transport or work to impede flow by clustering the gas atoms. Finally, the use of a tungsten overlayer on copper is evaluated as a material-based strategy for mitigating outgassing. Collaborative efforts with Drs. A. Garner (Purdue University) and J. Mankowski (TTU) have brought synergies. Monte Carlo simulations of electron transport prior to emission from the metal surface have also been carried out.

Background: Study of emission from cathodes is important and is being studied at the multiple levels: (a) Electron emission from surface emitters based on self-consistent calculations of quantum tunneling that include interface barriers and wavefunctions modified by electric fields and photoexcitation, (b) Local heating due to incident photons and/or energetic charged particles that modify the surface temperature and create nonequilibrium distributions, (c) Out-gassing driven by temperature-dependent increases in diffusion that can affect space-charge in HPM systems above the emitting surface, with supporting Molecular Dynamics (MD) analysis (d) Modifications in electric fields due to proximity and screening effects based on both three-dimensional simulations based on software tools (e.g., CST Microwave Studio) and Linear Charge Models (LCMs). Higher order charge models have also been used to better represent the emitter geometry. Some of the results (e.g., outgassing rates) could be fed as input parameters to PIC codes that are already capable of HPM analysis (e.g., Dr. Luginsland, Confluent Sciences).

2. Activities and Accomplishments

(A) Probing Electron Emission from Laser Excitation in Presence of DC Field

Introduction: Ultrafast, laser-driven electron emission from metal nanostructures is of interest for free electron lasers and as sources of electrons in high power microwave devices. Applications range from photoelectron injectors for accelerators and free electron lasers [1], and even has relevance to time-resolved imaging of fundamental processes in solid state physics [2, 3], chemistry [4], and biology [5]. Applying strong electric fields to a metallic tip with nanometer sharpness enables electron emission via tunneling, producing continuous electron beams with high brightness and coherence [6, 7]. Furthermore, illumination of such tips by femtosecond laser pulses, in combination with a moderate dc voltage applied to the tip, has realized pulsed field emission with femtosecond and nanometer resolution. This has opened up avenues for both basic research and new applications like time-resolved electron microscopy, spectroscopy, holography, and free-electron lasers [8]. Photoemission from lasers with small pulse-widths affords tightly bunched bursts having low emittance.

Here, while electron emission driven by both a strong DC applied bias and a strong laser field was examined, as was done previously by Zhang and Lau [12], the role of heating by the laser to create dynamic, nonequilibrium electron distributions was additionally incorporated. Field screening in multi-emitter arrays was also discussed. Results for the emission current as a function of time, at different DC fields and AC intensities were first obtained. The role of electron heating on the photoemission was then also probed. While the emission currents are predicted to follow the AC oscillations over the femtosecond range, the hot carrier population persists much longer to yield a more gradual decay in the emission current. The numerical results were then extended to an emitter array, since the latter configurations are of interest from the standpoint of obtaining high current outputs. As might be expected, the role of screening and decreases in electric field due to proximity between adjacent emitters arise, and are treated and discussed here on the basis of equivalent charge models.

Model Details for Time Dependent Transmission Coefficients: Details of the model and its implementation have been reported in the archival literature [13]. The time-dependent transmission coefficient can be obtained from a solution of the time-dependent Schrodinger wave equation. A solution to this problem involving both DC and AC electric fields was originally reported by Truscott [14] and Wagner [15], and more recently discussed by Zhang and Lau [12] that included multiphoton processes. Hence, only an outline of the inherent formulation is included here.

Outside the metal, the wavefunction $\psi(z,t)$ is given by:

$$\psi(z,t) = T_0\, G_0(z,t)\, \exp(-i\omega t)\, \exp[i(k_x x+k_y y)]\, \exp[i\{qzF_1 \sin(\omega t)\}/(\hbar\omega) - \\ - iq^2 F_0F_1 \sin(\omega t)\}/(\hbar m\omega^3) + iq^2 F_1^2 \sin(2\omega t)\}/(8\hbar m\omega^3)] \ , \quad z \geq 0 \qquad (1)$$

where T_0 is the transmission coefficient, and G_0 given by the following expression:

$$G_0 = Ai(-\eta_0) - i\, Bi(-\eta_0) \ . \qquad (2)$$

In eqn. (1) above, F_0 and F_1 are the magnitudes of the DC and AC fields, ω the angular frequency of the optical excitation, $\hbar$ the reduced Planck's constant, m the electron effective mass, z the coordinate normal to the metal-air interface, and t the time. In addition, $\eta_0 = \{E_0/(q\, F_0) + \xi\}\, (2qmF_0/\hbar^2)^{1/3}$, with $E_0 = E - E_F - W - U_p$, $\xi = z + \{q\, F_1/(m\, \omega^2)\} \cos(\omega t)$, and $U_p = q^2\, F_1^2/(4m\, \omega^2)$. In the above, the workfunction is denoted by W, while E_F represents the Fermi energy. Finally, in Eqn. (1), k_x, and k_y denote wavevectors in the transverse direction.

Inside the metal, the wavefunction is given by:

$$\psi(z,t) \ = \ \exp(-i\omega t)\, \exp[i(k_x x+k_y y)] + R_0 \exp(-i\omega t)\, \exp[i(k_x x+k_y y-k_z z)] \ . \qquad (3)$$

where R_0 is the reflection coefficient. Continuity of the wavefunction and its derivative at the interface ($z=0$), then yields solutions for T_0 and R_0. The transmittance coefficient $D(k_z,t)$, after some algebra, then works out to:

$$D(k_z,t) \ = |T_0|^2\, [k_e/(\pi k_z) + (p(t)/k_z)\, \{(Ai)^2 + (Bi)^2\}] \ . \qquad (4)$$

The emission current density, J_{tran}, transmitted from the metal can then be obtained from knowledge of $D(k_z,t)$ as:

$$J_{tran} \ = \ \iiint q\, v_z\, D(k_z)\, [1/(2\pi)^3]\ 2\, k_{//}\, dk_{//}\, d\theta\, dk_z\, f(k_{//},k_z) \qquad , \qquad (5)$$

once the distribution function $f(k_{//},k_z)$ for the electrons inside the metal is known.

Model Details for Electron Distribution Function With Heating: The electron distribution function needed for the current density calculation was computed in a dynamic fashion, based on rate equations that embody energy exchanges between the electron and phonon sub-systems. In the process, energy gain by the electrons from the incident optical radiation, which deposits energy onto the metal, is taken into account. This is offset by energy losses from the electron sub-system through electron-phonon interactions which represent relaxation processes. A single lumped electron-phonon coupling constant has been assumed. Furthermore, for simplicity, the decay of phonons via the anharmonic phonon-phonon coupling has been modeled on the basis of an effective phonon lifetime Γ_{ph}. The coupled rate equations provide a time-dependent lattice temperature $T_e(t)$, involving the following rate equations:

$$P_{abs} - G\,[\,T_e(t) - T_L(t)] \;=\; C_e\, dT_e(t)/dt \;, \qquad (6a)$$

and, $$G\,[\,T_e(t) - T_L(t)] \;=\; C_L\,[\,dT_L(t)/dt + \{T_L(t) - T_0\}/\Gamma_{ph}\,] \;, \qquad (6b)$$

where G is the electron-phonon coupling constant (taken to be $4\text{x}10^{16}$ W/m^3/K as a typical value for copper), C_e and C_L are the electronic and lattice heat capacities. These values, based on the literature have been taken here to be: C_e = 71.5 J/m^3/K^2 T_e, with Γ_{ph} = 7 ps and C_L = $3.5\text{x}10^6$ J/m^3/K [16]. Also, $T_e(t)$ and $T_L(t)$ are the effective temperatures of the electrons and the host (copper) lattice, t denotes the time, and P_{abs} is the power density (in Watts/m^3). Finally, T_0 denotes the ambient lattice temperature, while Γ_{ph} is the phonon lifetime of 7 ps due to anharmonic decay [17]. The input power was related to the field strength F_I of incident optical signal. The coupled set of equations (6) were solved using the fourth-order Runge-Kutta method.

For the electron system, the distribution function $f_e(t)$ was taken to comprise of two parts given by:

$$f_e(T_e,\, t) \;=\; f_{e\text{-}NT}(t) + f_{e\text{-}T}(T_e, t) \;, \qquad (7)$$

where $f_{e\text{-}NT}(t)$ and $f_{e\text{-}T}(t)$ denote the non-thermal and thermal components. The thermal part of the electron distribution was taken to be the usual Fermi-Dirac, but at an elevated, time-dependent temperature $T_e(t)$. The non-thermal part of the distribution $f_{e\text{-}NT}(t)$, was obtained at each time t and energy E based on the following relation:

$$\begin{aligned} f_{e\text{-}NT}(E,t+dt) \;=\; & f_{e\text{-}NT}(E,t) \;-\; f_{e\text{-}NT}(E,t)\,\{[E - E_f\,]/E_f\,\}^2\, dt/\Gamma_0 \;+ \\ & +\;[P_{abs}\, dt/(\hbar\omega)][(E-\hbar\omega)/E]^{1/2}\; T\,/\,\{exp[(E-\hbar\omega-E_f)/(kT_e(t))]+1\} \;. \qquad (8) \end{aligned}$$

where, $$T \;=\; \frac{1}{\int_{E_F-\hbar\omega}^{E_F}\left[\dfrac{\sqrt{E}}{exp\frac{(E-E_F)}{kT_e(t)}}\right]dE} \;.$$

The time-dependent, nonequilibrium electron distribution function was next used to obtain the emission current based on the following expression:

$$J_{tran} = \iiint q\, v_z\, D(k_z)\, [1/(2\pi)^3]\; 2\, k_{//}\, dk_{//}\, d\theta\, dk_z\, f(k_{//},k_z) \quad , \qquad (9)$$

where $f(k_{//},k_z)$ denotes the equilibrium probability function for the occupancy of state k_z, and $D(E_z)$ represents the transmission coefficient at energy E_z.

Results Obtained: Simulation results were obtained based on the theory discussed above, and were recently published in the literature [13]. The time-dependent evolution of the electron temperature obtained in response to an incident power input from a constant laser source is shown in Figure 1a. The energy density was taken to be 2×10^{13} W/m^2. A sharp rise to about 2×10^4 ˚K is predicted within about 1.5 ps, followed by a more gentle rise. This heating of the electrons affects the overall distribution. As might be expected, the temperature reaches a saturating value at a point in time when the losses from the electron subsystem begin to equal the energy gain from the input laser. However, in practice, such a laser cannot be sustained for long periods, and so a finite duration laser pulse presents a more reasonable waveform. Taking a 100 fs pulse, the temperature evolution $T_e(t)$ was obtained for two different AC field intensities (F_1) of 0.1 V/nm and 0.15 V/nm, respectively. The results are given in Figure 1(b). The peak electron temperatures of 2563 ˚K and 5391 ˚K for the two AC field strengths are predicted at the end of the 100 fs pulse.

Based on the above time-dependent electron temperature $T_e(t)$ formulation, the combined distribution $f_e(T_e, t)$ comprised of both the thermal and nonthermal components was obtained for $F_1 = 10^8$ V/m. This value is quite large, but does help demonstrate the nonequilibrium changes and disparities in the distribution function. Later, smaller and more reasonable values of F_1 have been chosen. The distribution at four different time instants of 50 fs, 100 fs, 200 fs, and 500 fs are shown in Figure 2. Due to the heated, nonequilibrium, nonthermal contribution, the $f_e(T_e, t)$

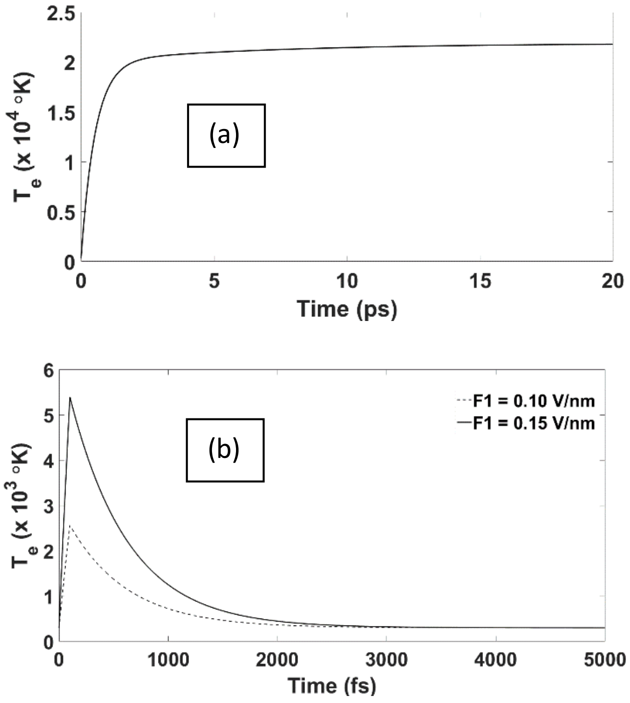

Figure 1. Effective electron temperatures as a function of time following two different incident laser excitation waveforms on a copper electrode. (a) Response to a unit step function, and (b) a 100 fs laser excitation.

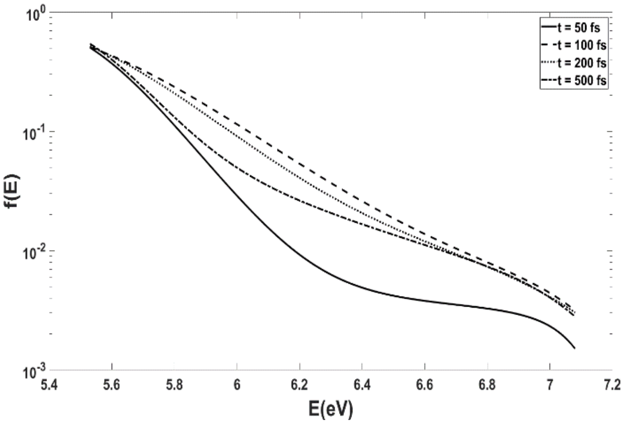

Figure 2. Snapshots of the overall combined distribution function *$f_e(T_e, t)$* as a function of electron energy at four time instants of 50 fs, 100 fs, 200 fs, and 500 fs.

curve exhibits a relative "shoulder" at the 100 fs instant with elevated values at the higher energies. Beyond the 100 fs time, the distribution function is predicted to gradually fall and evolve towards its equilibrium state.

The emission current densities resulting from combined fields (i.e., both F_0 and F_1) can be expected to naturally exhibit undulations because of the superimposed AC component in the driving excitation. The values over a few cycles, as obtained from the calculations, are shown in Figure 3 for $F_0 = 7\text{x}10^9$ V/m, $F_1 = 10^7$ V/m, and incident laser power of $1.33\text{x}10^{11}$ W/m^2. Upon termination of the laser pulse, the oscillations in the current density cease, and the values exhibit a slow but gradual decrease over time. The latter, almost imperceptible over the time scales shown, is the result of the slow relaxation of the distribution function as the electron cool in the presence of on-going interactions with the phonons. Upon taking the average over last cycle prior to laser termination, at different DC biasing levels, the field dependent behavior shown in Figure 4 for the current density (J_{tran}) emerged. For comparison, values of J_{tran} for the equilibrium Fowler-Nordheim (F-N) case are also shown in the figure. The two consequences apparent in the curves of Figure 4 are: (i) higher predicted currents for the non-equilibrium case as compared to the F-N levels because of the highly energetic distribution function which reduces transmission probabilities for a larger fraction of the electrons, and (ii) reduced threshold fields for the start of non-negligible currents.

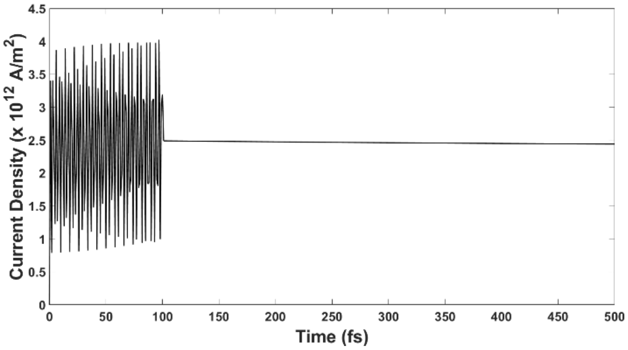

Figure 3. Simulation results of the time-dependent electron emission current density in response to a 100 fs laser pulse with inclusion of electron temperature increases and evolution of a nonequilibrium distribution function.

Thus, electron emission driven by both a strong DC applied bias and a superimposed laser field was examined, with inclusion of the heating that can create dynamic, nonequilibrium electron distributions. The evolution of the electron temperatures and the energy distribution was obtained on the basis of dynamic rate equations to ensure energy balance. While the emission currents are predicted to follow the AC oscillations over the femtosecond range, the hot carrier population persists much longer to yield a more gradual decay in the emission current beyond termination of the laser. Much higher emission currents were predicted due to the heating produced by the photoexcitation.

Finally, the above modifications to the emission current density were probed for the case of multiple emitters in an array. For such analysis it is crucial to first determine the electric fields in the vicinity of the emitting tips. As is well known, the presence of multiple emitters in close proximity to each other leads to a screening effect with reductions in the peak electric field magnitudes [18]. As shown in the recent past, such effects can conveniently and simply be probed on the basis of Line Charge Models (LCMs) which approximate the surface of an ungated, large aspect ratio field emitter tip by appropriate equipotentials above a dipole line charge [19]. The advantage of the LCM, and similar models [20-22], is that they facilitate the study of key array parameters, such as emitter height, tip radius, and array geometry, while invoking conceptual simplicity. These models yield quick solutions to the potentials and electric field distributions for a nanoemitter array, and are designed to provide an equivalent structure consisting of a line charge and its image, to replace the actual nanoprotrusion. Simple analytic expressions are then made available as a result, instead of having to solve a three-dimensional problem with the affiliated boundary conditions.

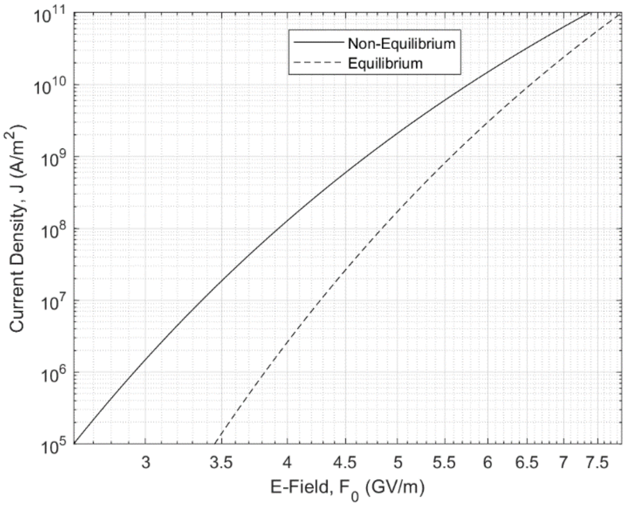

Figure 4. Emitted electron current density as a function of electric field, based on assumptions of equilibrium and nonequilibrium electron distribution functions.

However, as pointed out recently by Biswas et al. [22], the LCM generically mimics ellipsoidal emitters rather than a Cylindrical-Post-with-an-Ellipsoidal-Tip (CPET) that is typical of nanowires. An ellipsoidal emitter would be governed by the following equation in cylindrical co-ordinates: $z^2/z_1^2 + r^2/(a_1 z_1) = 1$, with the radius of curvature at the tip of the major axis (the emitter tip, essentially) equal to a_1. Charge densities beyond the linear regime, for example a quadratic charge distribution, would allow for modeling shapes that are closer to a CPET. Here, in order to address such aspects, higher-order charge density distributions from multiple rings were used in determining the electric fields and the screening effects in multi-emitter arrays. For example, the equipotential contours were improved in going from a three-ring to a nine-ring model, as shown in Fig. 5. For these calculations of Fig. 5, emitters of 1500 μm height and tip radius of 47.43 um were used to ensure a high aspect ratio. The distribution of charges for the two cases is listed in Table I. The use of multiple rings can be seen to improve the potential profiles. For example, the slight undulation near the emitter surface at a height of ~1400 μm in Fig. 5(a) is smoothened out in Fig. 5(b). In the present scheme, a charged ring was first set up close to the tip. Next, numerous other charge rings were added sequentially at different locations to ensure that the resulting equipotential contour from the emitter top to its base remained straight. Thus, the placement of an additional N^{th} ring was governed by the need to smooth out the occurrence of any undulation in the potential profile from the collective effect of the *N-1* rings and their images, over any region.

The nine-ring model was applied to multi-emitter arrays to probe screening in arrays. The predicted electric field values at the emitter tip as a function of emitter spacing (delta) for various numbers of emitters in an array are shown in Fig. 6. The peak field is predicted to reduce down to about 79% of the value for an isolated emitter at a 100 μm separation. Furthermore, the screening effect is predicted to almost disappear when separations equal the emitter height.

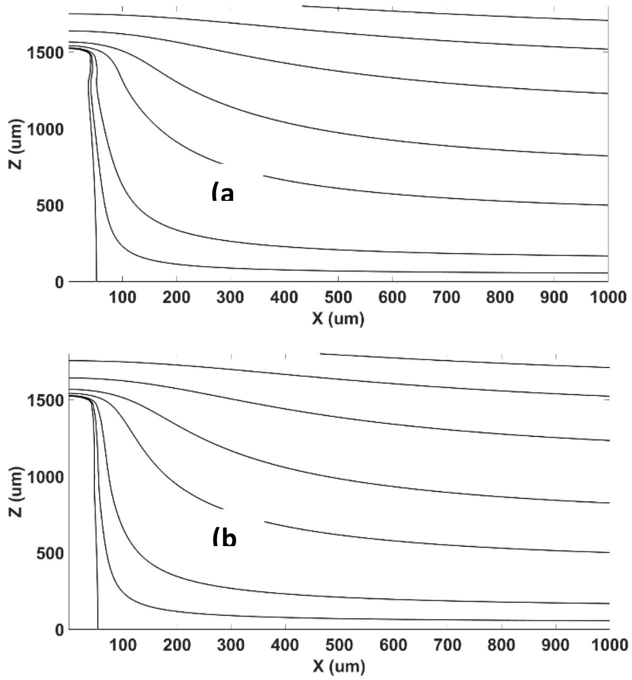

Figure 5. Equipotential profiles near a single emitter of 1500 μm height and 47.43 μm tip radius based on a linear charge model (LCM) with: (a) three charged rings, and (b) nine charged rings.

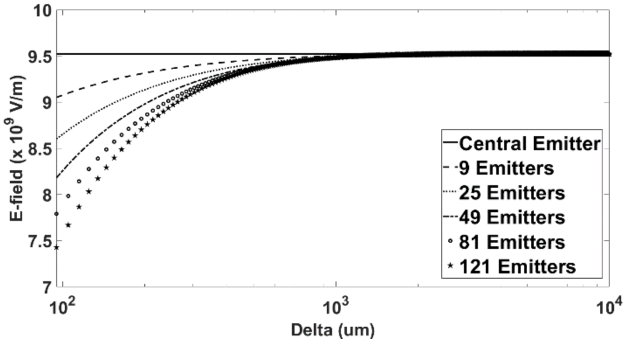

Figure 6. Predicted electric field values at the emitter tip as a function of emitter spacing (delta) for various numbers of emitters in the array.

In actual practice, the electron emission from the metal would depend on details of the internal scattering governed by both electron-electron, electron-phonon, and electron-plasmon interactions. This would fashion the characteristics, such as the energies, velocities, angular directions etc. of the emergent electron swarm. These aspects would be important for assessing the coherence and emittance of the electron source. The details could be treated by Monte Carlo transport techniques.

(B) Monte Carlo Simulations for Electron Distribution Following Photoexcitation

Introduction: Simulations of electron emission from electrodes were also carried out taking careful account of the internal scattering of electrons within the metal. For evaluating the laser excited photoemission currents, a population of electrons was first created at varying depths in the metal. A simple schematic of the laser photoemission process is given below in Figure 7. Laser excitation in copper was assumed to generate electrons at an energy $\hbar\omega$ (=1.55 eV in the present case). The location of the mobile electrons was chosen based on the Beer-Lambert law. Hence, an exponential profile of electrons was assumed to be present within the copper following laser excitation.

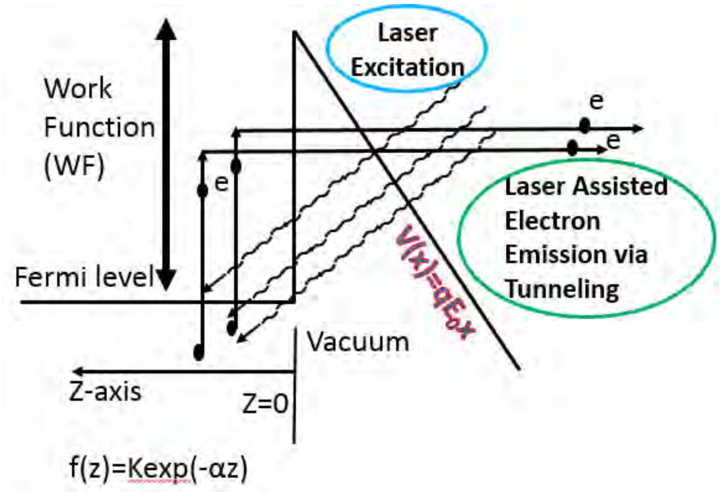

Figure 7. Simple schematic of laser photoexcitation for electron emission.

Both the elastic and inelastic scattering processes of electrons within the metal were considered. A Monte Carlo implementation of this process involves assigning initial velocities (v_{ix}, v_{iy}, v_{iz}) and angular directions (θ_i, φ_i) for the photogenerated electrons. This was done as:

$$|v_i| = (2\,E_i/m_0)^{1/2} \;;\; v_{ix} = |v_i|\cos(\theta_i) \;;\; v_{ix} = |v_i|\sin(\theta_i)\cos(\varphi_i) \;;\; v_{iy} = |v_i|\sin(\theta_i)\sin(\varphi_i)\,, \qquad (10)$$

where $\varphi_i = 2\pi r_i$, $\theta_i = \cos^{-1}[1-2r_i]$.

The position of the photogenerated electrons were chosen randomly along the transverse (x-y plane) and according to the Beer-Lambert law along the depth in the z-axis as:

$$x_i = L_x r_i \; ; \; y_i = L_y r_i \, , \; z_i = (-1/\alpha) \, Ln[1 - r_i + r_i \exp(-\alpha L_z) \; , \qquad (11)$$

where L_x, L_y and L_z were the dimensions of the Monte Carlo simulation box chosen in the x-, y-, and z-directions.

The position and velocity of each photogenerated electron was tracked and updated. Both elastic and inelastic scattering were applied to ascertain changes in momentum and energy. The energies and velocities of those electrons that might return and exit back out of the front face were recorded. This then enabled the tabulation and plotting of the energy (and perpendicular and lateral velocity) distributions of the electrons at the $z=0$ surface.

<u>Results</u>: Monte Carlo simulations were obtained for typical dimensional parameters of $L_x = 50$ microns, $L_y = 50$ microns, $L_z = 1$ microns and an absorption coefficient α of 7.5×10^7 m^{-1}. These results are shown in Figures 8(a)-8(c). The initial distribution of the photogenerated electrons is shown in Figure 8(a).

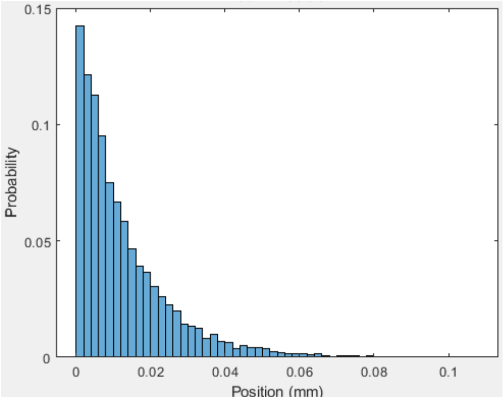

Figure 8(a). Initial spatial distribution of laser-generated electrons in the metal.

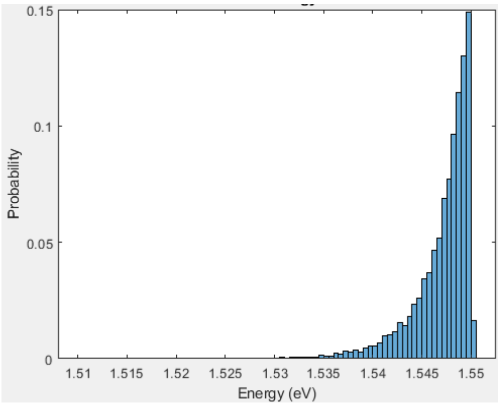

Figure 8(b). The energy distribution of outgoing (emitted) electrons from the metal.

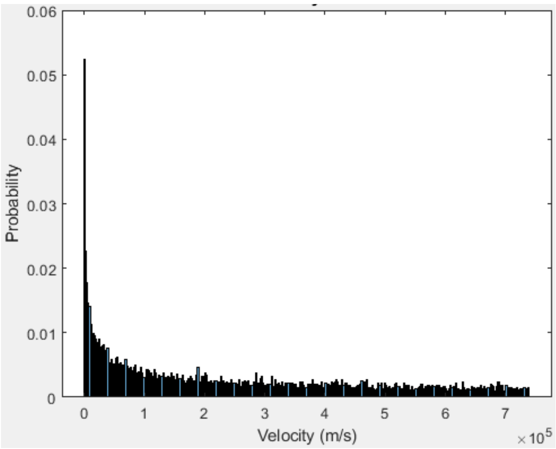

Figure 8(c). Velocity distribution of outgoing electrons reaching the metal surface.

Thus, the main conclusion of the detailed Monte Carlo analysis was that the energy spread from the initial 1.55 eV laser would not be very large. The relatively shallow absorption depth would preclude long and frequent interactions, leading to small energy losses and/or spreading.

(C) Simulations of Outgassing from Electrodes

Introduction: Gas desorption from materials can be an important factor in plasma formation in pulsed power and high power microwave systems. This phenomenon can then lead to breakdown, surface flashover, anode-cathode gap closure [19] and pulse shortening [20]. In the context of pulsed power devices, the monolayers of gas atoms that are usually adsorbed on the surface are likely to be liberated by direct electron impact. This can have downstream consequences such as the providing an additional source of neutrals for ionization and space-charge development. From an electrical standpoint, the operating conditions can then become dynamic, and affect the efficiencies of the operating devices, as pointed out by Haworth et al. [21]. Information of such out-gassing could, for example, be fed into particle-in-cell calculations for a more comprehensive analysis of High Power Microwave devices.

Simulation Method: Hydrogen diffusion in a copper lattice was simulated using the classical molecular dynamics (MD) scheme. In this technique, forces on any atom at a lattice site due to its many neighbors are evaluated based on semi-empirical interatomic potentials. In a sense, this approach allows one to pursue computational experiments by probing a variety of different configurations, and to include several species with their unique interactions at the molecular level. Its strength includes the ability to study fast non-equilibrium processes with atomic-level resolution. The limitations of the technique are well known. These include the inability to explicitly include electrons, the introduction of potential energy surfaces that are a function of atomic positions only (i.e., the Born-Oppenheimer approximation), and the treatment of potential energy surfaces through analytic functions that provide information as a function of atomic coordinates. Also, most approaches are based on classical Newtonian mechanics and ignore quantum effects and corrections. Furthermore, the computational complexity usually restricts the simulation length scales to tens or hundreds of nanometers; and time durations to the nanosecond regime. As the result of the finite size restrictions, deviations from the actual boundary conditions could also result.

Nonetheless, such simulations are a useful tool for analyzing and predicting defect properties, phase transformation mechanisms, kinetics and resultant structural evolutions, and dynamic behaviors of materials [22, 23]. In the present MD calculations, the interactions between Cu-Cu, H-H and Cu-H atoms were treated on the basis of the Bond-Order Potential. Bond order potentials (BOPs) which include the Finnis–Singlair and Tersoff formulations, are a class of empirical, analytical interatomic potentials that are often used, and have the advantage of describing several different bonding states of an atom, with the same parameters. The early version of the BOP potential [24] was improved to include distinct bond orders for sigma and pi-bonds [25]. Other developments include the adaptive intermolecular reactive empirical bond-order (AIREBO) potential [26] obtained from modifications to the Tersoff potential for covalent bonding. Finally, the modified embedded-atom method (MEAM) was created by modifying the EAM to consider the directionality of bonding. The MEAM represents the first interatomic treatment [28] capable of describing a wide range of elements (e.g., the fcc, bcc, hcp, diamond-structured and even gaseous elements) using a common formalism.

The interactions between W-W atoms were modeled here based on the MEAM. Molecular interactions between Cu-W and H-W are calculated using the truncated Lennard-Jones (6-12) potential $\Phi_{LJ}(r_{ij})$, in conjunction with the Lorentz-Berthelot mixing rule. The Lennard-Jones (L-J) potential has the form:

$$\Phi_{LJ}(r_{ij}) \;=\; 4\varepsilon\, [\{(\sigma/r_{ij})^{12} - (\sigma/r_{ij})^{6}\} - \{(\sigma/r_c)^{12} - (\sigma/r_c)^{6}\}] \;. \qquad (12)$$

In the above expression, the parameter r_c denotes a cut-off radius [28], while ε is the binding energy (depth of the potential) and σ is the molecular diameter. The values of σ for the Cu-Cu, H-H and W-W interactions were taken to be: 2.338 Å [29], 2.87 Å [30] and 3.2 Å [31], respectively; while the values of ε were found to be 9.43 kcal/mol [32], 0.0230 kcal/mol [33] and 0.05 kcal/mol [31], respectively. Using these parameters, the Lorentz-Berthelot mixing rule [32] was employed to calculate the Lennard-Jones parameters for the copper-tungsten and hydrogen-tungsten interactions.

The MD technique involves solving the equations of motion for interacting particles numerically, subject to appropriate initial and boundary conditions [33]. The open source LAMMPS code [34] with its library of potentials was used in the present calculations. Four structures were simulated: (i) a perfect copper lattice with no defects or inclusions. A face-centered cubic (fcc) structure was used for the copper with a lattice constant of 3.61 Å. This was thus effectively a rectangular box representing a slab of copper with atoms lying within it at the lattice points. The top surface above the box was taken to be vacuum. Atoms could escape the top surface, while periodic boundary conditions were applied at the remaining faces. (ii) A uniform copper slab having a small number of hydrogen atoms at interstitial sites. This was thus similar to the above geometry, but with some hydrogen atoms added to the copper mix. (iii) A copper slab containing a low-angle symmetric tilt grain boundary with hydrogen atoms included within the volume. The tilt grain boundary was created by defining two crystals having different orientations, and deleting the overlapping atoms at the common boundary. Specifically, the [0 0 1] crystallographic direction was taken to be parallel to the Z-axis, defined as the tilt axis. With the [1 0 0] crystallographic direction aligned with the X-axis, a grain boundary was formed around the middle plane by rotating lattices in the upper half part of the model around the tilt axis by a counterclockwise angle, while those in the lower half part of the model had a clockwise shift. (iv) Finally, to probe possible reductions in outgassing, a composite structure consisting of a 3 nm tungsten layer on top of the copper surface. A body-centered cubic (bcc) structure was used for the tungsten with a lattice constant of 3.16 Å. Hydrogen atoms were initially placed at the copper interstitial sites for this configuration, with escape possible only across the top tungsten surface.

The simulation box with a rectangular cross-section for the copper atoms was taken to have dimensions of 50 x 68.5 x 100 Å^3 with vacuum above the copper material. Hydrogen atoms were allowed to escape the top surface, while periodic boundary conditions were applied to the other surfaces to simulate infinite extensions. The target temperatures were created by assigning atomic speeds based on a Maxwellian distribution. In all simulations, the starting system configuration was initially relaxed by running the LAMMPS simulations up to 10 ns to achieve thermodynamic equilibrium and effectively minimize the overall energy. During the thermalization, the NPT (isobaric-isothermal) ensemble conditions were used with 29,568 copper atoms. Following relaxation, the operating temperature was maintained at a constant value for each of the simulations, and the NVT (canonical) ensemble conditions were used for the MD simulations. There was no scalar externally applied pressure in these simulations. The Langevin algorithm [35] was used to control pressure, with a damping parameter (P_{damp}) taken to be 0.5 ps. The Nose–Hoover thermostat [36, 37] was applied, and a 1 fs time-step was used [38]. Periodic boundary conditions were imposed, except at the outer surface for the outgassing evaluations.

The diffusion coefficient (D) of hydrogen gas trapped in the copper lattice was obtained by tracking the mean square displacement $<|r(t)|^2>$ of all the diffusing hydrogen atoms over a given period of time at each temperature. The mean square displacement (MSD) is related to time-dependent variations in position for an N-atom system as:

$$<|r(t)|^2> = \{{}^{N}\Sigma_{i=1}[\mathbf{r}_i(t)-\mathbf{r}_i(0)]^2\}/N \ , \qquad (13a)$$

where $\mathbf{r}_i(t)$ is the position vector of the i^{th} atom at time t. The MSD connects the diffusion coefficient through the relation [39]:

$$D = [d(<|r(t)|^2>)/dt]/6 \ . \qquad (13b)$$

Results: As a validity check of our MD implementation and as a preliminary assessment of our results of hydrogen diffusion in pure copper, MD simulations were first carried out to obtain the temperature-dependent diffusion coefficients. These initial calculations were aimed at facilitating simple comparisons with published experimental data. To ensure accuracy of results, three sets of simulations were performed for each case. The results were very similar, and the average is reported here. Results of hydrogen diffusion coefficient obtained from the simulations, along with various temperature-dependent data points reported in the literature, are shown in Fig. 9(a). A fairly good agreement between data and the calculations is evident. The experimental data points include reports by Perkins and Begeal [40], Eichenauer and Pebler [41], Sakamoto and Takao [42], Eichenauer et al. [43], Ishikawa and McLellan [44], and Katz et al. [45]. The diffusion coefficient was obtained from the slope of the mean square displacement versus time, with a representative MD simulation plot at 1000 K shown in Fig. 9(b). An Arrhenius type behavior naturally emerged from the calculations, with an activation energy of 0.41 eV and a pre-exponential factor of 6.108x10^{-7} m^2/s, which are comparable to other reports and other materials [46].

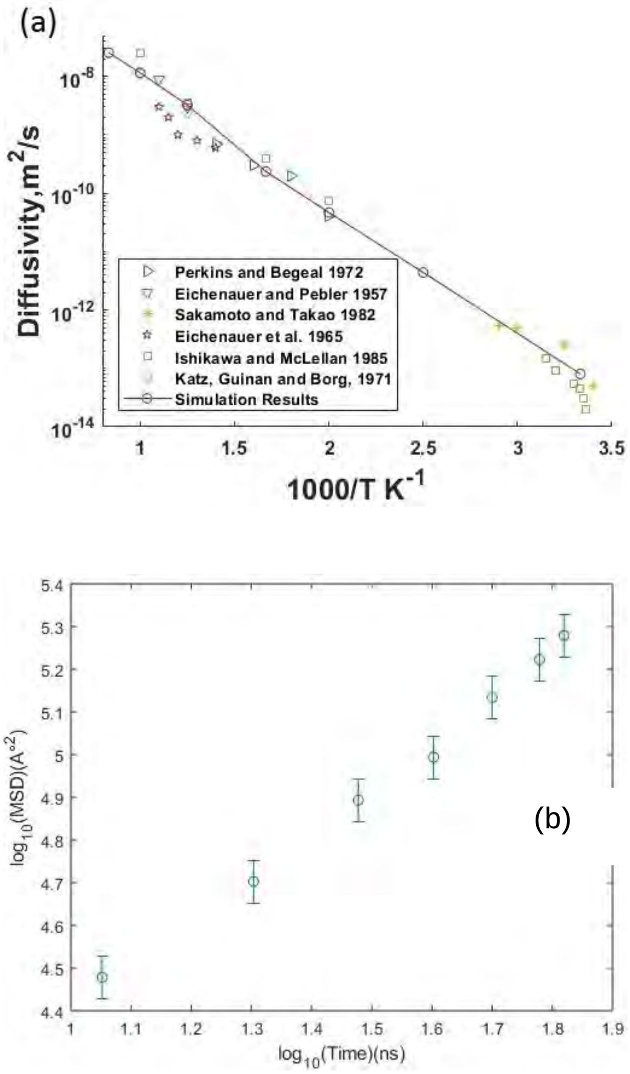

Figure 9. (a) Comparison between the temperature dependent diffusion coefficients for hydrogen obtained from the simulations and various data points reported in the literature. Good agreement between data and the calculations can be seen. (b) Representative result of the mean square displacement (MSD) versus time obtained from the MD simulations on log-log scale at 1000 K diffusion coefficient calculations.

Next, the role of a low-angle grain boundary on the out-diffusion of hydrogen atoms in copper was probed through MD simulations. A copper slab containing a grain boundary with hydrogen atoms initially included as random impurities at interstitial sites uniformly distributed throughout the volume, was considered. Initial thermalization and lattice relaxation was carried out for 10 ns. The NPT conditions with periodic boundaries were used to ensure the hydrogen atoms spread out and were effectively re-shuffled within the simulation space. Following this initial phase, an NVT ensemble was used and any hydrogen atom crossing out from a surface was eliminated from the simulation. This provided a count of the outgassing of hydrogen atoms from copper as a function of time. The outflow of hydrogen atoms parallel and perpendicular to the GB plane was tracked.

Results obtained at a temperature of 700 K are shown in Figure 10. One hundred fifty hydrogen atoms were inserted into the copper lattice to start with. A copper sample without any grain boundary (GB) was included to provide a baseline comparison. The results of Figure 10 show the structure losing atoms at the fastest rate for flow parallel to the grain boundary. The number of hydrogen atoms in the copper sample are predicted to reduce from 150 to about 112 in about 10 ns. By comparison, the flow perpendicular to the GB is very slowest, with about 141 of the starting 150 hydrogen atoms remaining in the copper sample. The transport without any grain boundary is seen to lie between these two limits. Roughly, 130 atoms are predicted to remain in the copper for the case without a grain boundary after 10 ns. This clearly shows the role played by grain boundaries with regards to transport and outgassing. A grain boundary can effectively provide a pathway to the surface and facilitate out-gassing. In the orthogonal direction, the same GB structure acts as a trap and could effectively suppress hydrogen flow. The qualitative trend obtained here in Figure 10 is similar to reports that grain boundaries in nuclear fuel materials provide fast transport paths in the absence of any porosity [47, 48]. In the context of nuclear materials, the role of grain boundary diffusion in fission gas release is well known and has been appropriately studied in the past. The atomistic results are qualitatively in keeping with the trends from the analytic model first developed by Fisher [49] who showed diffusion to occur along grain boundaries more rapidly than through the interior of crystals. This model has subsequently been embellished over the years [50].

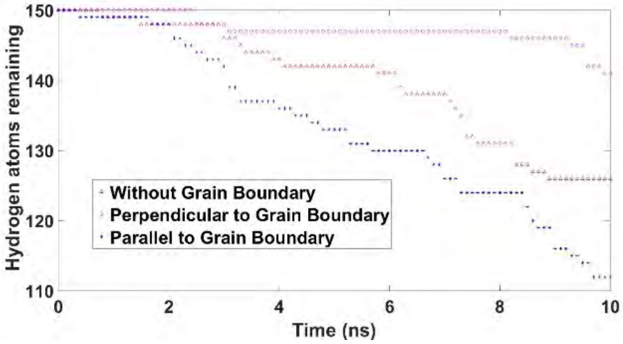

Figure 10. Simulation results showing the number of hydrogen atoms remaining in a copper slab as a function of time. Cases with and without a grain boundary (GB) were simulated, with the out-diffusion in directions both parallel and perpendicular to the GB plane.

Physically, the distortion of atoms in the GB region influences the diffusion of hydrogen atoms. Local deformations and variations within the GB core provide discrete paths for atomic hops. Spatial variability in the local energy near a grain boundary is well known [51], and one can expect deviations in the diffusive properties to be strongest at the GB core, though the core size variations were not examined here. In the perpendicular direction, the GB acts as a barrier (similar to a mountain range blocking normal flows), leading to very anisotropic transport. However, in an actual sample, diffusion via an interconnected network of grain boundaries can be expected to occur. Since neither the presence of various grain boundaries, nor their orientations can be controlled, it becomes impractical to only rely on GB-dependent transport to influence outgassing. Instead, a different, robust technique for impeding gas outflow becomes necessary.

One possibility to reduce gas out-diffusion might be to add a suitable thin material as a capping overlayer. Towards this goal of mitigating outgassing, and to test the effectiveness of an over-coating, a 30 Å thick tungsten layer was added to the simulation structure. The tungsten cap was placed on an open surface, at one end of the simulation box. Tungsten was chosen as a material for the overlayer, since diffusion of hydrogen in tungsten has been reported to be fairly low [52]. To validate and test this hypothesis of low hydrogen diffusivity in tungsten metal, the temperature dependent diffusion coefficient of hydrogen was first calculated in a pure, stand-alone tungsten slab. For this purpose, 50 Hydrogen atoms were added to a pure tungsten slab having 7000 metal atoms. The mean square displacement (MSD) versus time was obtained, and the diffusion coefficient was then extracted from the slope. The procedure and calculations were very similar to those for hydrogen in pure copper. Furthermore, a plot of diffusivity versus inverse temperature does not provide much information, until the activation energy and pre-exponential factor are extracted. For brevity, the diffusion versus inverse temperature results are not shown, and only the time-dependent out-diffusion at a fixed temperature of 1000 K is given in Figure 11. However, it must be mentioned that the MD simulations of hydrogen diffusion in tungsten at different temperatures yielded an activation energy of 0.42 eV and a pre-exponential factor of 6.918×10^{-7} m^2/s. The activation energy was similar to that reported by Frauenfelder [53]. From the results of Fig. 11, the value of the diffusion coefficient for hydrogen in tungsten was calculated to be 5.311×10^{-9} m^2/s. The reported value in the literature for hydrogen diffusion in tungsten is roughly 5.484×10^{-9} m^2/s [52] at 1000 K. Thus, these results for hydrogen diffusion in tungsten not only point to the validity of the calculations, but also underscore the much lower diffusivity in this material as compared to a copper host.

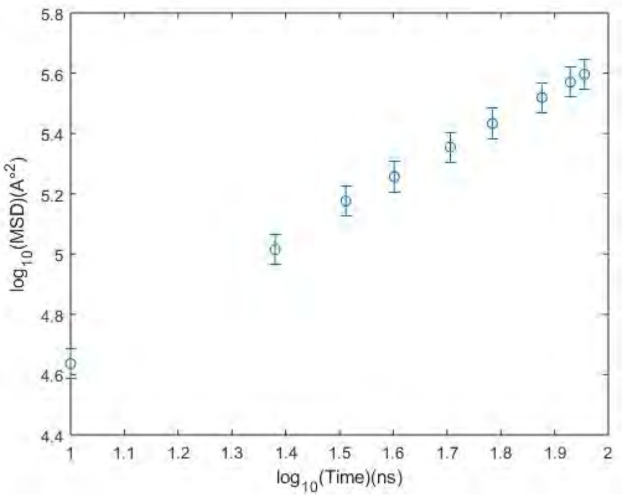

Figure 11. Mean square displacement (MSD) vs time plot for hydrogen atoms inserted at random interstitial sites in a tungsten slab. A temperature of 1000 K was used for the calculations. The diffusion coefficient was obtained from the slope of the above plot.

Finally, calculations of hydrogen outgassing from copper in the presence of a tungsten cap-layer were carried out. As with Fig. 10, a low-angle grain boundary was assumed in the copper. As before, the system was thermalized using the NPT ensemble for 10 ns. After shuffling all the atoms (i.e., hydrogen, copper and tungsten) during thermalization, the actual simulations were then performed for 30ns. The comparison of outgassing with and without the presence of a tungsten layer is shown in Figure 12 at a temperature of 700 K. In the results, the number of hydrogen atoms are predicted to reduce to around 110 from an initial number of 150, in about 10 ns. Rather than compare diffusion coefficients, the time-dependent populations escaping the metal system provide a more convenient and direct basis for comparison. In these simulations, there were no surface defects or trace impurities that might lead to surface recombination or trapping. With the added tungsten layer, the outgassing rate is seen to be much lower, with about 142 hydrogen atoms predicted to remain in the simulation box even after 30 ns. In Fig. 12, over a 10 ns duration, about 39 hydrogen atoms are predicted to leave the pure, homogeneous copper slab; while only 1 hydrogen atom escapes the metallic system with the tungsten cap layer. This is almost a factor of 40 reduction in the out-gassing rate. It is quite evident that the tungsten capping layer can work as a materials-based strategy to effectively mitigate outgassing.

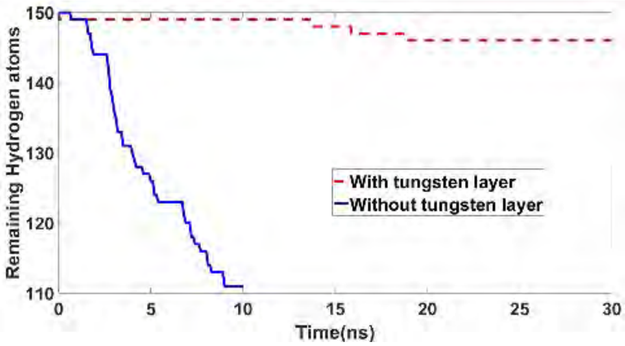

Figure 12. Comparison of outgassing rates with and without the tungsten over-layer.

The above calculations and results could form the basis for predictive analysis of gas emissions per unit area. For example, temperature dependent emission rates (or alternatively average lifetimes of the atomic gas) could be obtained from plots of the time-dependent decreases in the number of hydrogen atoms within copper at different temperatures. By knowing the surface area of the simulation box, the outflow rates per unit area could be estimated. For statistical accuracy though, averages over numerous simulation runs would be needed.

A practical validity test might then be to compare the predicted emission of hydrogen gas with measured increases of pressure within the test chambers. In these cases, the simulations would have to specifically assign the gas atoms within the top few monolayers of the surface.

Furthermore, an aspect not addressed here, but would be important for future work, in the context of charged particle incidence upon electrodes in pulsed power systems, would be the time dependent changes in temperature and associated spatial gradients. The latter could add a thermo-diffusive contribution to gas transport. In any event, a detailed analysis would require a three-step process of: (i) Initial calculations of the deposited energy from the incident particles, possibly through Monte Carlo calculations with energy-dependent Stopping Power and Mean Free Paths, (ii) Solutions of heat transport to obtain the evolutionary spatially variable temperature profiles, and (iii) Use of the spatially dependent temperatures thus obtained as inputs in the MD technique to naturally include thermal gradients.

(D) Simulations of Gas Flows at the Electrode Surface

The results for the number of outgoing hydrogen atoms versus time exhibited a near exponential-type response, which is characteristic of a first-order process. A decay constant was then extracted by fitting the data for the fall off in the hydrogen population within the copper, at each temperature. Results for the out-diffusion rate (or inverse time-constant) are shown in Figure 13 as a function of temperature.

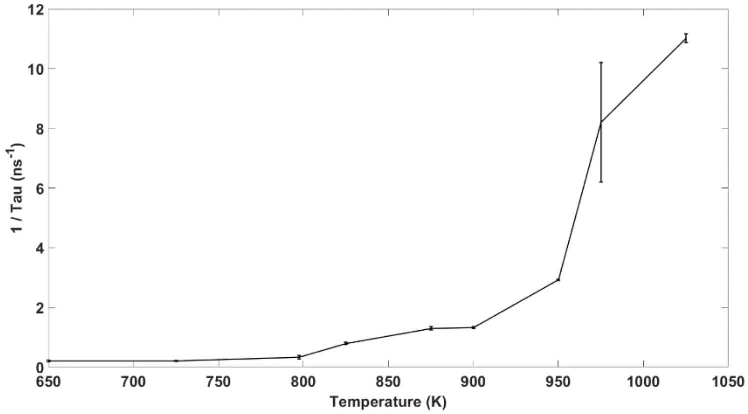

Figure 13. Temperature dependent outflow rate for hydrogen atoms from copper obtained from Molecular Dynamics simulations.

The results for the outflow rate *R(T)* could roughly be curve-fit by the following temperature (*T*) dependent expression:

$$R(T) = 9.503x10^{-6} \exp(0.01368\, T) \ . \qquad (14)$$

The above results were all obtained for a constant temperature inside the copper electrode. However, under actual operating conditions, it is very likely that the bombardment of ions on the metal would lead to their penetration. Subsequent energy losses in the copper through various inelastic collisions would create local temperature enhancements. Such a scenarios of incident ions impinging on the electrode had been simulated previously using a Monte Carlo scheme, and the internal temperature profiles obtained. Figure 14 shows a schematic of external ions impinging on the copper electrode, and depositing energy to heat up the copper and creating an internal thermal gradient. That internal temperature profile had also been reported in a previous monthly report. So now, those spatially nonuniform temperatures were used to gauge any differences or changes in hydrogen outflow.

Since MD is a computationally intensive technique, requiring the inclusion of actual atoms in a lattice, it is only possible to simulate very small length scales, which nonetheless will have a large number of atoms. So, a modest 10 nm thickness of copper with embedded hydrogen atoms was simulated, with the temperatures at the top and bottom surfaces being maintained at 790 K and 805 K, respectively, as shown in Figure 14. The temperature at the top surface and the gradient were taken from the previous Monte Carlo results.

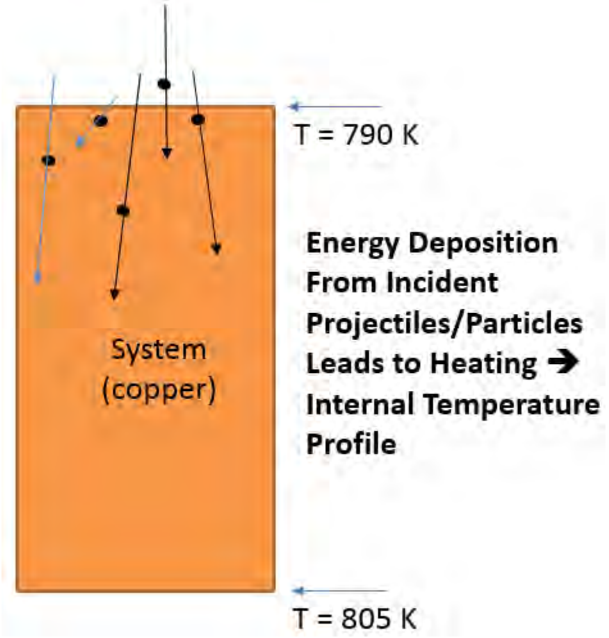

Figure 14. Schematic showing incident ions on copper electrode could lead to internal temperature increases and gradients.

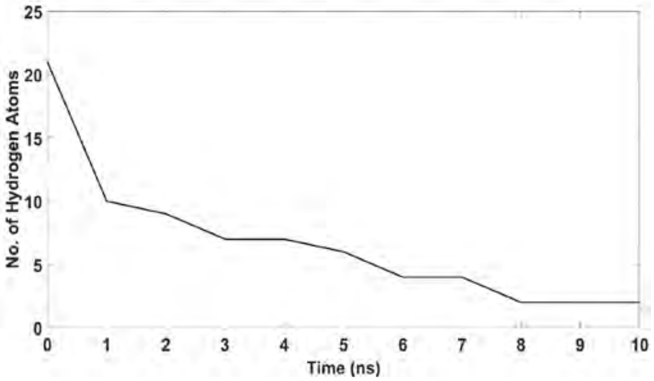

Figure 15. Molecular Dynamic results showing the decrease in hydrogen atoms within the copper over time, with the temperature gradient within the metal. The top and bottom surfaces were kept at 790 K and 805 K, respectively. The size of the simulated system was 25 Angstrom by 34.25 Angstrom by 101 Angstroms, with 7392 copper atoms and 21 hydrogen atoms.

The outflow rate for this case was nearly the same as the case where a uniform temperature at the average value of 797.5 K [= (805 K+790 K)/2] had been maintained. This result can probably be explained as the joint outcome of a lower surface temperature and a thermal gradient that provides a driving force. Thus, the 790 K surface temperature is lower than the 797.5 K value for the average value case. This would suggest lower outflow from the surface due to a smaller driving energy. However, the temperature gradient probably makes up for this by bringing more atoms to the surface from the depths. As a result, the overall outflow rate is predicted to remain almost unaffected. This shows, at least to a first-order, that temperature gradients may not have a strong effect in altered hydrogen outgassing, provided spatially averaged values were used.

While a metal electrode would give off hydrogen via out-gassing, there is also the finite probability that the gas within the hydrogen-rich environment outside the electrodes, could stick or embed into the electrode surface. Depending on the incident energy and angle, some hydrogen atoms impinging in the electrode would be reflected back from the metal, while others would go in the metal and be embedded.

The system was been set up and the MD calculations performed for the numerical study of atomistic inflow based on the LAMMPS software tool. A schematic of a simulation region consisting of copper atoms in a lattice at the bottom, with a lone hydrogen incident from the top, is shown in Figure 16. The incident hydrogen atom would have some energy, velocity, and angular direction. The particle would then slam into the copper below, and either be reflected immediately, or move for a short dostance into the metal before possibly going back out. The aim was to find the reflection and transmission coefficients in the copper electrode as a function of incident energy and angle.

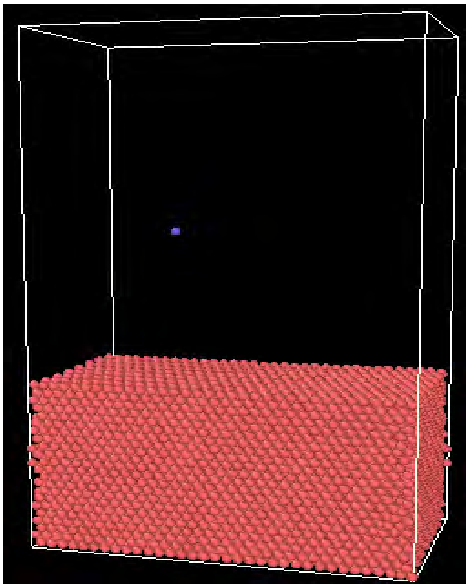

Figure 16. Schematic of the simulation set up for MD calculations of the sticking coefficient. An hydrogen in incident on a copper lattice at the bottom with a given energy and velocities. The aim was to find the reflection and transmission coefficients as a function of incident energy and angle.

The MD calculations performed used a simulation box with dimensions of 49.19 Å x 85.2118 Å x 50 Å containing copper atoms. The incident hydrogen atoms were generated at random locations in the x-y plane, and a height ″z″ that was 8 Å higher than the top surface of copper. The hydrogen atoms were launched downwards at the metal at different angles. In the calculations carried out so far, two distinct values of 15 and 30 degrees were used. (Here, 0-degrees with respect to the z – axis implies normal incidence onto the copper surface.)

The system was first thermalized to a temperature of 800K prior to the hydrogen atoms being launched at the copper lattice. This was carried out to yield a stable and well-bonded lattice structure prior to any external bombardment.
In the calculations shown below, the atoms were released down onto the copper target at a 30 degree angle to the normal. The initial location for each atom was a random variable with x- and y-coordinates . The release and simulated tracking of hydrogen atoms was done in batches of 10 particles at a time. This is unlike the previous simulations reported, when a larger number of particles were all released sequentially at the copper target. The reason for this change was to eliminate the possibility of distortions and defect creation in the copper material itself. The interaction of incident atoms with the copper substrate lead to possible ″knock-on″ collisions and the displacement of the host atoms. Consequently, it is likely that the copper lattice could have local defects and deviation for its original perfectly periodic structure. So, to avoid such large deviations, and restrict the possibility of cumulative effects, only 10 atoms were allowed to be incident on the lattice. After this batch of 10 sequentially incident atoms, a new thermalized and equilibrated copper lattice structure was used for the next batch of 10 simulations. In this manner, each batch of 10 atoms were made to target a new regular, undistorted lattice.

Each time for a batch of 10 ″*shots*″, the system was first thermalized to a temperature of 800K prior to the hydrogen atoms being launched at the copper lattice. This was carried out to yield a stable and well-bonded lattice structure prior to any external bombardment.

The results obtained are shown in Figure 17. At the lowest energy of 50 eV, the reflection coefficient is about 0.5, and monotonically reduces to 0.35 at 100 eV. This is qualitatively expected, since with higher energy, the incoming hydrogen would pack a larger punch, and be more likely to break-in, rather than bouncing away. The fraction of atoms that go through the copper are predicted to monotonically increase from about 0.13 at 50 eV to ~0.65 at 100 eV. These values are much lower than the corresponding fractions obtained previously for 50 Å sample. It can also evident that about 40% of the atoms are predicted to be absorbed within the 100 Å distance at the 50 eV energy. This compares to almost no predicted absorption in the last monthly report for the smaller 50 Å thickness. The absorbed fraction falls to about 0.12 at a 75 eV energy, and then to zero for 100 eV atoms. This is again qualitatively expected, since atoms with higher incident energies would be more likely to go past the 100 Å depth. Hence, at 100 eV energy, all the atoms go beyond 100 Å. This implies that for the higher energies (100 eV and beyond), any hydrogen taken up by the copper would likely reside deeper than 100 Å from the surface.

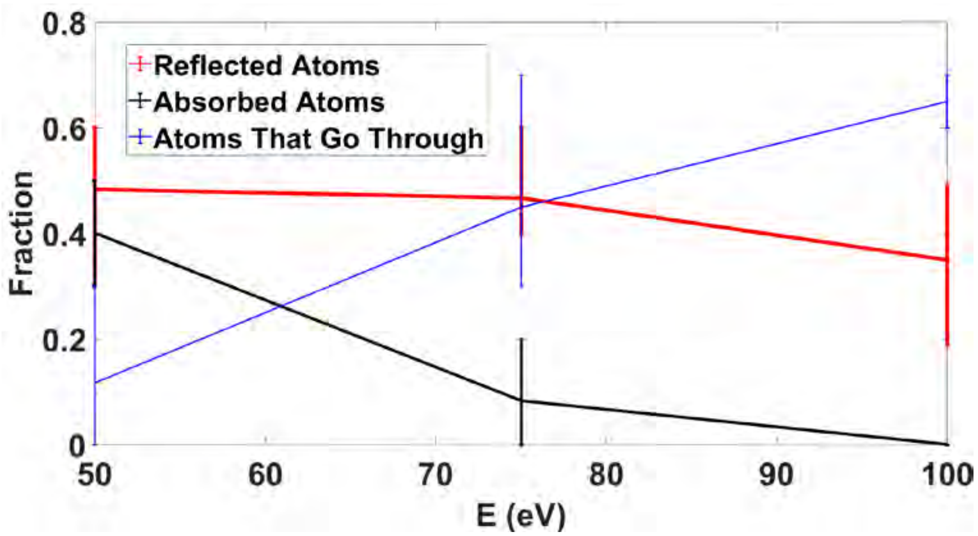

Figure 17. Plot showing the fraction of reflected and absorbed/embedded hydrogen atoms from MD simulations for a 100 Angstrom deep copper sample. The energy-dependent fraction of hydrogen atoms that go through the copper and are lost from the bottom face are also given. Error bars have also been shown.

3. Findings and Conclusions

The following results were obtained during the past twelve-month period, and are as given below.

(i) Model development along with supporting calculations for photoemission in the presence of an externally applied electric field. The total driving force for electron emission was thus a combination of both a DC field and the RF excitation of the incident laser; together with the photon energy input for transcending the workfunction barrier at the surface. Such photoemission is an important source for high density electron emitters.

(ii) Molecular Dynamics (MD) simulations of outgassing from electrodes were carried out successfully. Though there are many applications of interest to the Navy, one specific area that such calculation will support and aid is in the assessment of the design of cathodes for the magnetically insulated transmission line oscillator (MILO) devices. For example, recent research on this topic [21] based on particle-in-Cell (PIC) codes for MILO systems have assumed some level of gas. However, the specific role of outgassing, the resulting inhomogeneities in the concentration, and release rates have not been assessed. Hence, the evaluations of the system efficiency and perturbations in space-charge could change if more realistic and physically-based input to the PIC formulation was made available. The MD simulations are a step in the direction towards including outgassing from surface adsorbates.

Both of the above aspects are very germane and relevant to electron emitters for various high-density electron sources and other applications, to the Navy. Here it was shown that a tungsten overlayer can effectively curtail out-gassing from copper electrodes.

The MD simulations have also been used to get quantitative predictions on inflows into the metal at the surface in case gases may be present in the environment outside the metal. These have been obtained as a function of incident energy and angle.

(iii) The possibility of secondary electron emission (SEE) from copper was also studied through Monte Carlo simulations. Surface conditions are known to affect SEE. The role played by crystal orientation and a vacancy (which is a simple example of a surface defect) were probed through Monte Carlo simulations. The Monte Carlo simulations were in good agreement with previous experimental reports. The results indicated that the secondary electron yield for pure copper is the highest for the 110 orientation and the lowest for the 111 case, with a relatively higher differential predicted between a single vacancy and ideal copper for the 111 orientation. The results underscored the benefit of annealing or reducing inhomogeneities through laser or charged particle beam surface treatments.

References

[1] 1. V. Ayvazyan, N. Baboi, I. Bohnet, and R. Brinkmann, , Phys. Rev. Lett. **88**, 104802 (2002).
[2] 2. M. Merano, S. Sonderegger, A. Crottini, and S. Collin et al., Nature (London) **438**, 479 (2005).
[3] 3. B. J. Siwick, J. R. Dwyer, R. E. Jordan, and R. J. D. Miller, Science **302**, 1382 (2003).
[4] 4. H. Ihee, V. A. Lobastov, U. M. Gomez, B. M. Goodson, R. Srinivasan, C. Y. Ruan, and A. H. Zewail, Science **291**, 458 (2001).
[5] 5. V. A. Lobastov, R. Srinivasan, and A. H. Zewail, Proc. Natl. Acad. Sci. U.S.A. **102**, 7069 (2005).
[6] 6. G. Fursey, Field Emission in Vacuum Microelectronics (Kluwer Academic/Plenum Publishers, New York, 2003).
[7] 7. B. Cho, T. Ichimura, R. Shimizu, and C. Oshima, Phys. Rev. Lett. **92**, 246103 (2004).
[8] 8. H. Yanagisawa, C. Hafner, P. Doná, M. Klöckner, Phys. Rev. B **81**, 115429 (2010).
12. P. Zhang and Y. Y. Lau, Scientific Reports **6**, 19894, 2016.
13 D. Guo, S. N. Sami, and R. P. Joshi, AIP Advances **9**, 105302 (2019).
14. W. S. Truscott, Phys. Rev. Lett. **70**, 1900 (1993).
15. M. Wagner, Phys. Rev. Lett. **76**, 4010 (1996).
16. A. Majzoobi, R. P. Joshi, A. A. Neuber, and J. C. Dickens, AIP Advances **5**, 127237 (2015).
17. R. P. Joshi and D. K. Ferry, Phys. Rev B **39**, 1180 (1989).
18. M. T. Robinson, in Defects and Radiation Damage in Metals (Cambridge University Press, Cambridge, 1969).
19. A. Roy, R. Menon, S. Mitra, S. Kumar, V. Sharma, K. V. Nagesh, K. C. Mittal, and D. P. Chakravarthy, Physics of Plasmas **16**, 053103 (2009).
20. J. Benford and G. Benford, IEEE Trans. Plasma Sci. **25**, 311 (1997).
21. M. D. Haworth, K. L. Cartwright, J. W. Luginsland, D. A. Shiffler, and R. J. Umstattd, IEEE Trans. Plas. Sci. **30**, 992 (2002).
22. M. S. Daw, S. M. Foiles, and M. I. Baskes, Mater. Sci. Rep. **9**, 251 (1993).
23. B. J. Lee, J. Phase Equilib. and Diff. **30**, 509 (2009).
24. J. Tersoff, Phys. Rev. Lett. **56**, 632 (1986).
25. D. G. Pettifor and I. I. Oleinik, Phys. Rev. B. **59**: 8487 (1999).
26. S. J. Stuart, A. B. Tutein, J. A. Harrison, J. Chem. Phys. **112**, 6472 (2000).
27. M. I. Baskes, Phys. Rev. B **46**, 2727 (1992).
28. M. P. Allen and D. J. Tildesley, *Computer Simulation of Liquids* (Oxford, Clarendon Press, Oxford, 1987).
29. Q. C. Hsu, C.D. Wu and T. H. Fang, Computational Materials Science **34**, 314 (2005).
30. Y. Saito, N. Sasaki and T. Komatsu, IEEE Transactions on Magnetics **48**, 2009 (2012).
31. M. Wang, K. Mm Liechti, V, Srinivasan, J. M. White, P. J. Rossky and M. T. Stone, J. Appl. Mech **73**, 769 (2004).

32. P. M. Agrawal, B. M. Rice, and D. L. Thompson, Surf. Sci. **515**, 21 (2002).
33. B. J. Alder, and T. E. Wainright, J. Chem. Phys. **27**, 1207 (1957).
34. S. Plimpton, J. Comput. Phys. **117**, 1 (1995).
35. T. Schneider and E. Stoll, Phys. Rev. B **17**, 1302 (1978).
36. S. Nose, J. Chem. Phys. **81**, 511 (1984).
37. S. Nose, Mol. Phys. **100**, 191 (2002).
38. Z. Zhang, M. Giesselmann, J. Mankowski, J. Dickens, A. Neuber, and R. P. Joshi, Journ. Phys. D **50** 185202 (2017).
39. For example, R. Kubo, Rep. Prog. Phys. **29**, 255 (1966).
40. W. G. Perkins and D. R. Begeal, Berichte der Bunsengesellschaft **76**, 863 (1972).
41. W. Eichenauer and A. Pebler, Z. Metall. **48**, 373 (1957).
42. Y. Sakamoto and K. Takao, Journal of the Japan Institute of Metals **46**, 285 (1982).
43. W. Eichenauer, W. Löser, and H. Witte, Z. Metall. **56**, 287 (1965).
44. T. Ishikawa and R. B. McLellan, Journal of Physics and Chemistry of Solids **46**, 445 (1985).
45. L. Katz, M. Guinan, and R. J. Borg, Physical Review B **4**, 330 (1971).
46. X. W. Zhou, F. El-Gabaly, V. Stavila, and M. D. Allendorf, J. Phys. Chem. C **120**, 7500 (2016).
47. J. A. Turnbull, C. A. Friskney, F. A. Johnson, A. J. Walter, and J. R. Findlay, J. Nucl. Mater. **67**, 301 (1977).
48. D. R. Olander and P. van Uffelen, J. Nucl. Mater. **288**, 137 (2001).
49. J. C. Fisher, J. Appl. Phys. **22**, 74 (1951).
50. For example, I. Kaur, Y. Mishin, and W. Gust, *Fundamentals of Grain and Interphase Boundary Diffusio*n (New York: Wiley, New York, 1995).
51. A. Suzuki and Y. Mishin, Interface Science **11**, 131 (2003).
52. K. Heinola and T. Ahlgren, J. Appl. Phys. **107**, 113531 (2010).
53. R. Frauenfelder, J. Vac. Sci. Tech. **6** 388 (1969).

4. Plans and Upcoming Events

(a) Plan to develop and run Molecular Dynamics simulations for electron transport between the cathode-anode region of a nanoemitter array structure. Newtonian mechanics will be used for electron motion, with the force on any electron being calculated as the collective sum of the external electric field, and the pairwise sum of Coulombic forces form the remaining N-1 neighbors. In addition, *image charges* will need to be placed within the electrodes to account for the presence of boundaries. Similar MD calculations have been reported by Torfason et al. [K. Torfason, A. Valfells, and A. Manolescu, Physics of Plasmas 23, 123119 (2016) ; K. Torfason, A. Valfells, and A. Manoles, Physics of Plasmas 22, 033109 (2015)]. It would be possible to probe the role of screening and dynamic effects.

(b) Include photoemission from nanoemitter arrays by taking account of photogeneration in the metal, with subsequent transport towards the surface in the presence of scattering. This would yield more accurate characterization of the velocities and energies for electrons incident at the surface.

(c) Another important aspect that is planned for the upcoming year would be to look at oxide coatings that may form on the metal copper electrodes. This could alter the Work Function, and perhaps change the wavefunctions as well. . So, the Density of States (DoS) and electronic wavefunctions which affect and influence the field-driven electron field-emission currents will be probed.

(d) Complete the simulations for inflows as well as out-gassing of hydrogen gas at different temperatures, energies and incident angle. The local increases in temperature due to inelastic energy exchanges between the incident electrons and the host lattice, which would enhance outgassing would be included. Similarly, the inclusion of inflow at the surface would ensure a balanced calculation with both inflows and outflows taken into account.

In addition, energy thresholds should also become available. Analytic expressions for the net outflow rate could then be set up, which would be very useful for PIC codes that could analyze the performance of such HPM structures with inclusion of outgassing.

(e) Calculations of material properties of nanoemitters, such as the thermal conductivity, taking account of the effects of reduced dimensionality. With micron-sized (or smaller) emitters, the current emission at the tip can be expected to lead to local heating. Unlike bulk material, in which the heat can flow in all six directions, the thermal dissipation in such situations is only possible in one direction. This can be expected to dramatically reduce the ability of the material to conduct heat, thereby lowering the thermal conductivity parameter. Such quantities and material characteristics will be obtained through Molecular Dynamics simulations.

5. Transitions and Impacts

None.

6. Collaborations

Dr. Rehan Kapadia, University of Southern California
Dr. John Luginsland, Confluent Sciences
Prof. John Verboncoeur, Michigan State University
Dr. Allen Garner, Purdue University

7. Personnel

Principal investigator	Ravindra P. Joshi
Co-investigator or Co-PI	Andreas Neuber, John Mankowski, James Dickens
Business Contact	Amy Cook, TTU Associate Vice-President for Research
Team Members	None
Subs	None

8. Students

Dong Guo – PhD student
S. Sami – PhD student
Lily Qiu – PhD student

9. Technology Transfer

None.

10. Products, Publications, Patents, License Agreements, etc.

Archival Publications #1

a. Article Title: Model Evaluations of Surface Modification by Energetic Incident Carbon Atoms on Graphene Coated Copper Electrodes
b. Journal: Physics of Plasmas
c. Authors: X. Qiu, J. Mankowski, J. C. Dickens, A. A. Neuber, and R. P. Joshi
d. Keywords: Incident Atoms, Surface Modification, Damage, Electrodes
e. Distribution Statement: Unrestricted distribution
f. Publication Status: Published
g. Publication Identifier Type: https://doi.org/10.1063/1.5056766
h. Publication Identifier: https://doi.org/10.1063/1.5056766
i. Publication Date: January 2019
j. Volume: 26
k. Issue: 1
l. First Page Number: 013501-1
m. Publication Location: New York, USA
n. Acknowledgement of Federal Support? (Yes/No): Yes
o. Peer Reviewed? (Yes/No): Yes

Archival Publications #2

a. Article Title: Simulation of a High Repetition Rate S-Band MILO
b. Journal: Plasma
c. Authors: M. Abide, J. Dickens, R. P. Joshi, A. Neuber, and J. Mankowski
d. Keywords: MILO, Simulations, S-Band
e. Distribution Statement: Unrestricted distribution
f. Publication Status: Published
g. Publication Identifier Type: https://doi:10.3390/plasma2020011
h. Publication Identifier: https://doi:10.3390/plasma2020011
i. Publication Date: May 2019
j. Volume: 2
k. Issue: 1
l. First Page Number: 138
m. Publication Location: Basel, Switzerland
n. Acknowledgement of Federal Support? (Yes/No): Yes
o. Peer Reviewed? (Yes/No): Yes

Archival Publications #3

a. Article Title: Electron emission from metal emitters subject to a high intensity laser in the presence of DC electric fields
b. Journal: AIP Advances
c. Authors: D. Guo, S. N. Sami, and R. P. Joshi
d. Keywords: Electron emission, Lasers, DC fields
e. Distribution Statement: Unrestricted distribution
f. Publication Status: Published
g. Publication Identifier Type: https://doi.org/10.1063/1.5122212
h. Publication Identifier: https://doi.org/10.1063/1.5122212
i. Publication Date: October 2019
j. Volume: 9
k. Issue:
l. First Page Number: 105302

m. Publication Location: New York, USA
n. Acknowledgement of Federal Support? (Yes/No): Yes
o. Peer Reviewed? (Yes/No): Yes

Archival Publications #4

a. Article Title: Probing Changes in Secondary Electron Yield from Copper Electrodes Due to Surface Defects and Changes in Crystal Orientation
b. Journal: Journal of Applied Physics
c. Authors: H. K. A. Nguyen , M. Sanati, and R. P. Joshi
d. Keywords: Secondary emission, Defects, Orientation, Electron yield
e. Distribution Statement: Unrestricted distribution
f. Publication Status: Published
g. Publication Identifier Type: https://doi.org/10.1063/1.5113642
h. Publication Identifier: https://doi.org/10.1063/1.5113642
i. Publication Date: September 2019
j. Volume: 126
k. Issue:
l. First Page Number: 123301
m. Publication Location: New York, USA
n. Acknowledgement of Federal Support? (Yes/No): Yes
o. Peer Reviewed? (Yes/No): Yes

Archival Publications #5

a. Article Title: Numerical Evaluation of Hydrogen Outgassing from Copper Electrodes With Mitigation Based on a Tungsten Capping Layer
b. Journal: Physics of Plasmas
c. Authors: J. Acharjee and R. P. Joshi
d. Keywords: Outgassing, Hydrogen, Copper electrodes, Mitigation
e. Distribution Statement: Unrestricted distribution
f. Publication Status: Published
g. Publication Identifier Type: https://doi.org/10.1063/1.5109682
h. Publication Identifier: https://doi.org/10.1063/1.5109682
i. Publication Date: September 2019
j. Volume: 26
k. Issue:
l. First Page Number: 093504
m. Publication Location: New York, USA
n. Acknowledgement of Federal Support? (Yes/No): Yes
o. Peer Reviewed? (Yes/No): Yes

There is currently one other journal article under review. Details are as: X. Qiu, B. Esser, I. Aponte, J. Mankowski, J. C. Dickens, A. A. Neuber, and R. P. Joshi, "Assessing the Role of Photon Processes in Facilitating Radio-Frequency Breakdown of Air at Atmospheric Pressure in Millimeter Gaps," submitted for publication, October 2019.

In addition, the following presentations were made at the Pulsed Power and Plasma Science (PPPS-2019) conference in Orlando. These talks at the conference were within the June 23-28, 2019 period. The specific details are:

1. H. Nguyen. Q. Xiu, M. Sanati, J. Mankowski, J. Dickens, A. Neuber, and R. P. Joshi, "Numerical Evaluations of Secondary Electron Emission and Outgassing from Copper Electrodes," IEEE Int'l Pulsed Power and Plasma Science (PPST) Conference, Orlando, June 22-28, 2019.

2. S. N. Sami, D. Guo, and R. P. Joshi, "Electron Emission from a Metal Electrode Subject to a High Intensity Laser in the Presence of DC Electric Fields," IEEE Int'l Pulsed Power and Plasma Science (PPST) Conference, Orlando, June 22-28, 2019.

3. M Abide, J. Dickens, A. Neuber, R. P. Joshi, J. Mankowski, "Low-Impedance S-Band MILO," IEEE Int'l Pulsed Power and Plasma Science (PPST) Conference, Orlando, June 22-28, 2019.

4. D. Guo, S. N. Sami, and R. P. Joshi, ″Electron emission from metal emitters subject to a high intensity laser in the presence of DC electric fields,″ Joint International Vacuum Nanoelectronics (IVNC) and International Vacuum Electron Sources (IVESC) Conference, Cincinnati, Ohio, July 22-26, 2019.

Honors and Awards

. President's Excellence Research Professorship (TTU, 2019)
. Fulbright Research Scholar Award (2019)
. TTU Barnie Rushing Jr. Faculty Distinguished Research Award (2019)

11. Point of Contact in the Navy

Ryan Hoffman, Program Officer, Office of Naval Research

12. Acknowledgement/Disclaimer

This work was sponsored by the Office of Naval Research (ONR), under grant number N00014-18-1-2382. The views and conclusions contained herein are those of the authors only and should not be interpreted as representing those of ONR, the U.S. Navy or the U.S. Government.

A High Repetition Rate, Long Lifetime Magnetically Insulated Line Oscillator (MILO)

Grant No. N00014-18-1-2384

Period of Performance: October 1, 2018 to September 30, 2019

Prepared by:
Dr. John Mankowski, Principal Investigator
Center for Pulsed Power and Power Electronics (P3E)
Texas Tech University
Department of Electrical and Computer Engineering
2500 Broadway, MS3102
Lubbock, TX 79409-3102
Tel: (806) 834-3168
Email: john.mankowski@ttu.edu

DEPARTMENT OF THE NAVY · UNITED STATES MARINE CORPS

This work was sponsored by the Office of Naval Research (ONR), under grant number N00014 - 17-1-2848. The views and conclusions contained herein are those of the authors only and should not be interpreted as representing those of ONR, the U.S. Navy or the U.S. Government.

Grant or Contract Number: N00014-18-1-2384
Date Prepared: 1/25/2020
Project Title: A High Repetition Rate, Long Lifetime Magnetically Insulated Line Oscillator (MILO)
Annual Summary Report: FY2019
Principle Investigator:

Texas Tech University (TTU)
Center for Pulsed Power and Power Electronics (P3E)
Dr. John Mankowski
john.mankowski@ttu.edu

Co- Principle Investigators:

Texas Tech University (TTU)

Dr. James Dickens
james.dickens@ttu.edu

Dr. Andreas Neuber
andreas.neuber@ttu.edu

Dr. Ravi Joshi
ravi.joshi@ttu.edu

Financial POC:

Texas Tech University (TTU)
Office of Research Service
Ms. Amy Cook
amy.cook@ttu.edu

Section I: Project Summary

1. Overview of Project

The overall goals of this project are to design, fabricate and test a 1 GW class magnetically insulated line oscillator (MILO) capable of high repetition rates. The MILO source will be a hardtube design with advanced materials for high rep-rate operation. To that end, we are using particle in cell (PIC) simulation code to model the MILO source structure and materials for a prediction of output RF power and efficiency. In conjunction with the MILO development, we are constructing a low impedance (~10 Ω) Marx generator to drive the MILO and test in single shot mode. Since the project is 9 months in to a 3-year program, the bulk of this report discusses the MILO PIC simulations and Marx generator development.

The fundamental objective of this applied research is to develop an enabling technology for future pre-detonation Counter Improvised Explosive Device (CIED) systems. HPRF system power requirements are primarily driven by range (stand-off), and the pulse repetition frequency correlates to the desired speed of the USMC tactical vehicle. Current conventional microwave tube technology used for such systems is limited by output power to single digit MW and total system weight can exceed 20,000 lbs. By comparison, relativistic High Power Microwave (HPM) sources such as Relativistic Magnetrons (RelMags) and Magnetically Insulated Line Oscillators (MILO) can be driven by short pulse Marx generator pulsed power devices and produced with total weights on the order of 2,000 lbs or less in compact form factors. This reduction in weight by an order of magnitude has potential to enable integration into a wide variety of Marine Corps tactical vehicles to include Mine Resistant Ambush Protected Vehicles (MRAPs) and High Mobility Multipurpose Wheeled Vehicles (HMMWVs). If the size and weight can be further reduced, there is even potential to employ this counter IED technology on small unmanned ground vehicles with on board power. Additionally, there is potential to utilize this emerging technology for countering emerging Unmanned Aerial System threats. RelMags and MILO tube designs offer potential for achieving substantial increases in peak output RF power compared to existing commercial-off-the-shelf (COTS) magnetron and klystron tubes, but at the expense of efficiency. The inherent shortcoming of these relativistic tubes is pulse shortening which is an important factor when operating in the relativistic regime. Additionally, the lifetime of these novel tube design geometries has not been characterized.

Abstract:

This report details the development of a hardtube Magnetically Insulated Line Oscillator (MILO) for testing in the high repetition rate regime. A brief background of the project is first discussed. The narrative portion of activities and accomplishments are divided into two segments. The first part details the completed MILO design, fabrication and assembly. The second part reports on the construction of a low inductance Marx generator which will drive the MILO, cathode development, and trigger pulse generator. Finally, findings and plans are presented for the upcoming year.

Objective: The objective of this research is to develop a 1 GW class, hardtube MILO that will be capable of high repetition rate operation.

List of Figures

Background:

The program objective is to design and construct a high-power microwave source capable of high RF power (> 1 GW) and high repetition rate. To this end we are proposing the development of a hard tube magnetically insulated line oscillator (MILO). This type of performance can be achieved by fabrication using advanced materials and sealed tube technology as well as design optimization through PIC code simulation. The high diode peak power will induce extreme temperatures within tube components. Advanced materials such as pyrolitic graphite can withstand these conditions which will result in shot lifetimes many orders of magnitude greater than traditionally used materials. These operating conditions will also create plasma within the AK gap which can result in pulse shortening. Sealed tube technology has been shown to reduce plasma generation as well as decrease plasma lifetime. Finally, PIC code simulation will be used to optimize MILO performance resulting in higher power efficiency and lower losses.

2. Activities and Accomplishments

MILO Source Development – Predicted Performance from PIC Simulation

Much of the first year focused on MILO source design using PIC code simulation in CST. The simulations included baseline design, material conductivity properties, lumped circuit element excitation and variable beam dump positioning. The baseline 3D model is shown in Figure 1. Predicted RF output from the baseline model is shown in Figure 2. Results verified an expected RF peak power of approximately 4.5 GW at 2.5 GHz operating in the TM_{01} mode when excited with an input signal that has a peak voltage of 600 kV while providing a peak current of 58 kA. The simulation confirms the design should perform within these constraints.

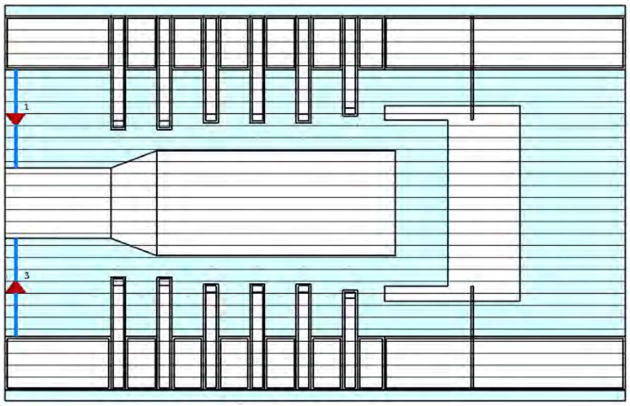

Figure 2. Baseline MILO model in CST PIC code.

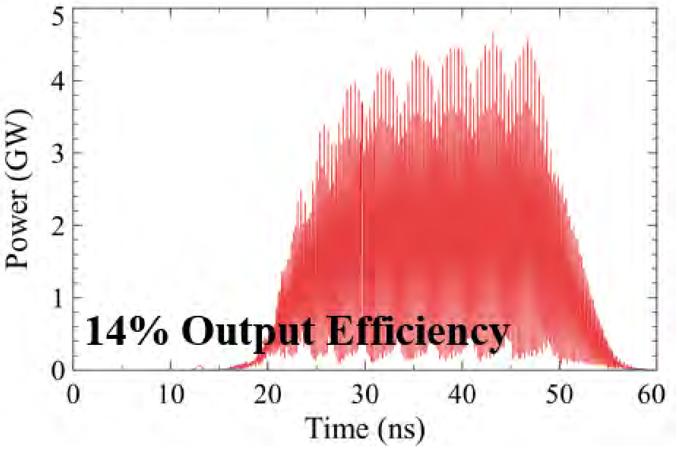

Figure 3. RF output of the baseline MILO model.

MILO Fabrication and Assembly

We started the year with most of the design and simulation work for the MILO completed. The PIC model was then mechanically designed in a 3D CAD program, as shown in Figure 3, with key components labelled. This CAD model through several rounds of alterations during the early months of the year. The changes focused around the design of the beam dump and the connecting slide of the MILO vane structure to the output port that allows adjustment of the location of the beam dump in reference to the cathode as per plans from the simulation.

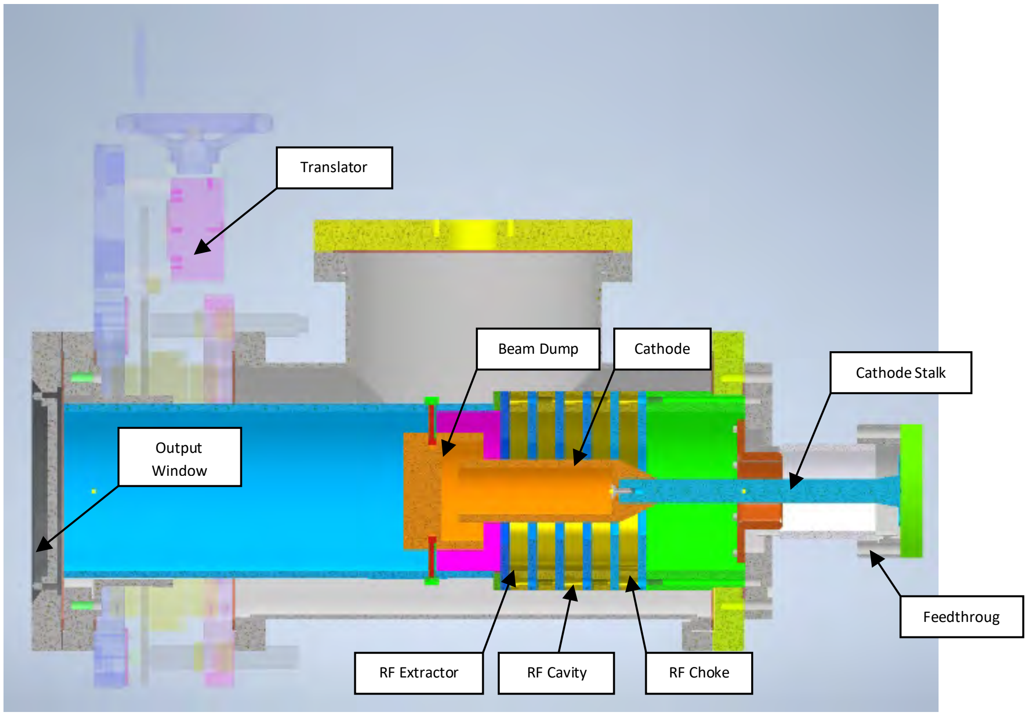

Figure 4. 3D Inventor model of the MILO source.

Simulations of the beam dump thermal characteristics were performed to determine check performance. There were some concerns about possible sublimation of the beam dump during repeated firing of the MILO due to thermal build up. Several types of beam dump and stub materials were modeled leading to the selection of a graphite beam dump with pyrolytic graphite connecting stubs, as shown in Figure 4, to the anode bulk material provided enough thermal conduction to keep the beam dump well below sublimation point. These simulation results showed a steady state temperature of 2400 K which is well below the 3800 K sublimation temperature for each material.

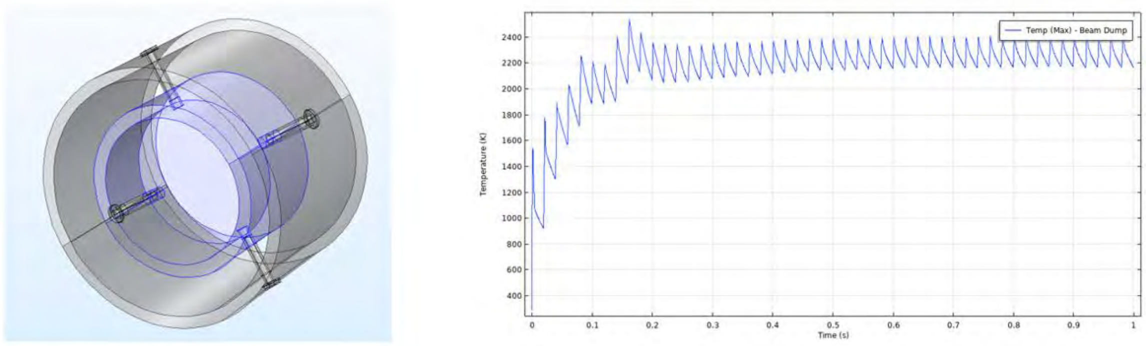

(a) (b)

Figure 5. Thermal modeling of the MILO beam dump (a) CST model and (b) thermal response of a graphite beam dump with pyrolytic graphite posts. Excitation is a reprate of 50 Hz for 1 second.

In the latter half of the year we began construction of the MILO. Components such as the translator and vacuum tee were ordered and received. Pyrolitic parts such as the cavity vanes and beam dump posts were machined out of house and have been received. Most of the custom machined components such as the feedthrough, cathode, and waveguide parts were fabricated in-house. Currently, the device is nearly completed with a few components needing to be machined for their final fitting and waiting on a few other components to arrive from vendors. Many of these parts and a partial assembly of the source are shown in Figure 5.

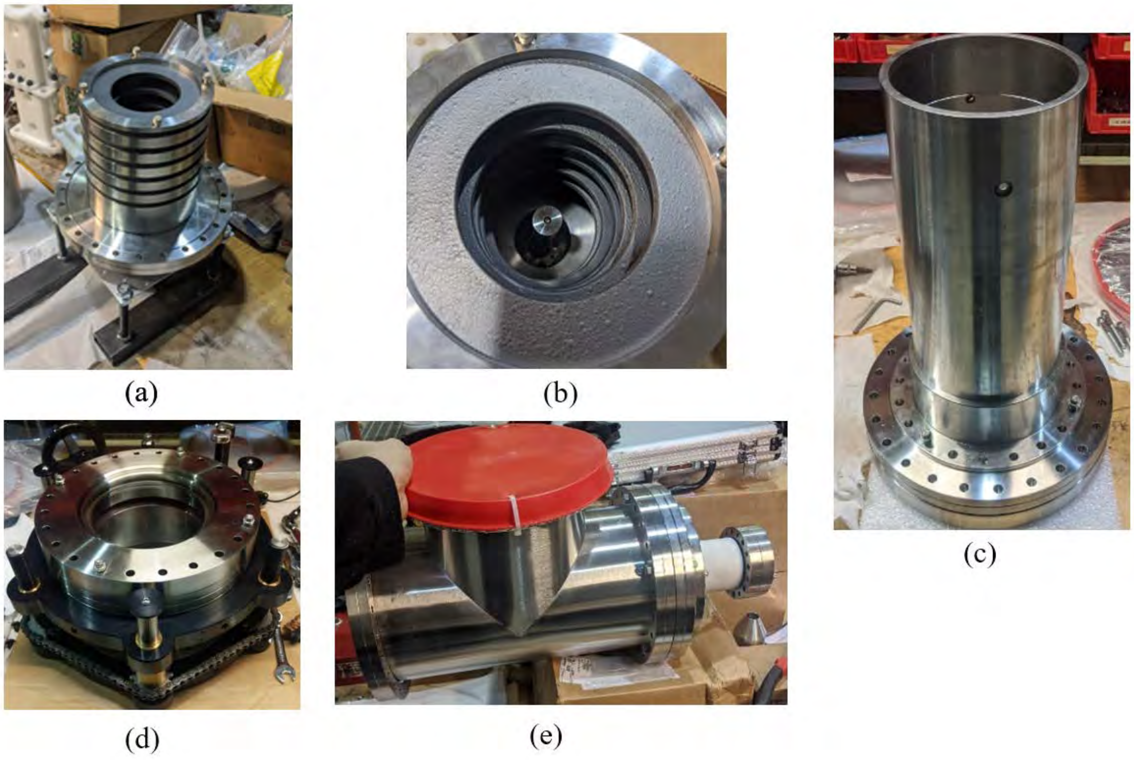

Figure 6. Parts and partial assembly of the MILO.

Marx Generator Fabrication and Testing

In order to effectively drive the low impedance of the MILO, a high current Marx generator needs to be designed and fabricate. The performance goals of the Marx are an output voltage of > 450 kV, output current > 40 kA, risetime < 150 nsec, and pulsewidth > 300 nsec. These performance goals were determined from PIC simulation of the MILO such that an RF efficiency (>10%) and RF peak power (> 1 GW) can be achieved.

Using the simulation data and the smaller 4-stage Marx generator described in the previous yearly update, a larger 6-stage Marx generator was built in order to verify the results. The 6-stage design, with output waveform shown in Figure 6, utilized the same capacitors as the 4-stage version, except each of the 6 stages contained two capacitors initially in parallel, resulting in a per-stage capacitance before the Marx is erected of 440 nF. Custom spark gap modules and charging inductors are used to complete the main circuit elements, with additional mounting and support materials used as well to ensure a robust and rigid design. From SPICE simulations, the 18-stage version gave an output current of 45 kA and an output voltage of 570 kV into a 12 Ω load that is used to simulate the MILO. The risetime and pulsewidth are also within acceptable limits, being 170 ns and 540 ns, respectively.

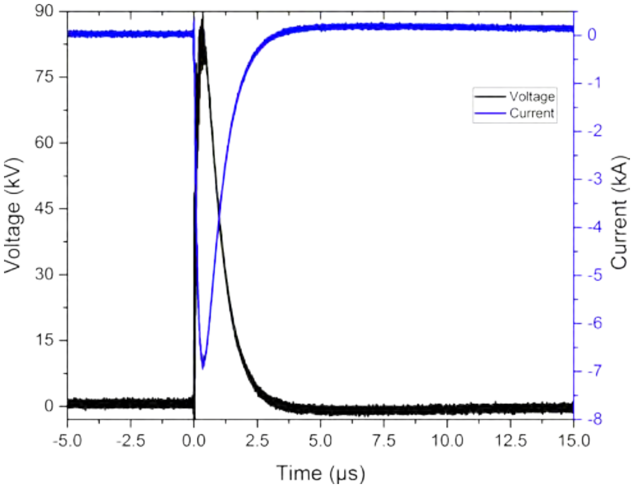

Figure 7. Marx generator output with 6-stages charged to 20 kV.

After this verification was completed, the capacitors were tested to see if they could be rep-rated, which was done using a single stage of the Marx and an output spark gap switched into a water load. From this test, a rep-rate of 22 Hz was demonstrated as is shown in Figure 7. Increased power from the charging supply would have allowed >50 Hz repetition rate.

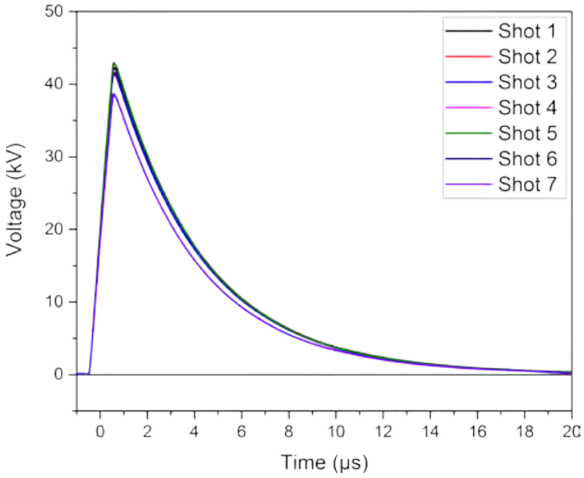

Figure 8. A 7-shot burst at 22 Hz from a single stage of the Marx generator demonstrating repratability of the capacitors.

Shortly after these tests, the shipment of the rest of the capacitors arrived, which allowed the full 18-stage Marx generator, shown in Figure 8, to be constructed and tested. A considerable amount of troubleshooting was conducted on the full setup, with early breakdown issues and diagnostic calibrations needing to be isolated and remedied in order to achieve a high fidelity of data.

Figure 9. Full 18-stage Marx generator.

Once the breakdown issue was rectified, focus was placed upon calibrating the non-intrusive probes for the current and voltage waveforms. Several 25 kV shots were taken, and a resulting waveform can be seen attached. The capacitive voltage probe (CVP) waveform is ran through a digital 1.2 MHz low-pass filter to remove the noise, and the Rogowski current probe waveform is integrated to acquire the appropriate current waveform. The filtering and integrating processes of the two probes results in a shortening and widening of the waveforms, respectively. A Pearson coil is used to verify the waveforms. At a 25 kV charge on the capacitors, the output current measured is approximately 17 kA and the output voltage is approximately 210 kV. After investigation it was realized that the CVP was damaged. Once the probes have been repaired and calibrated tests up to 50 kV charge will be performed.

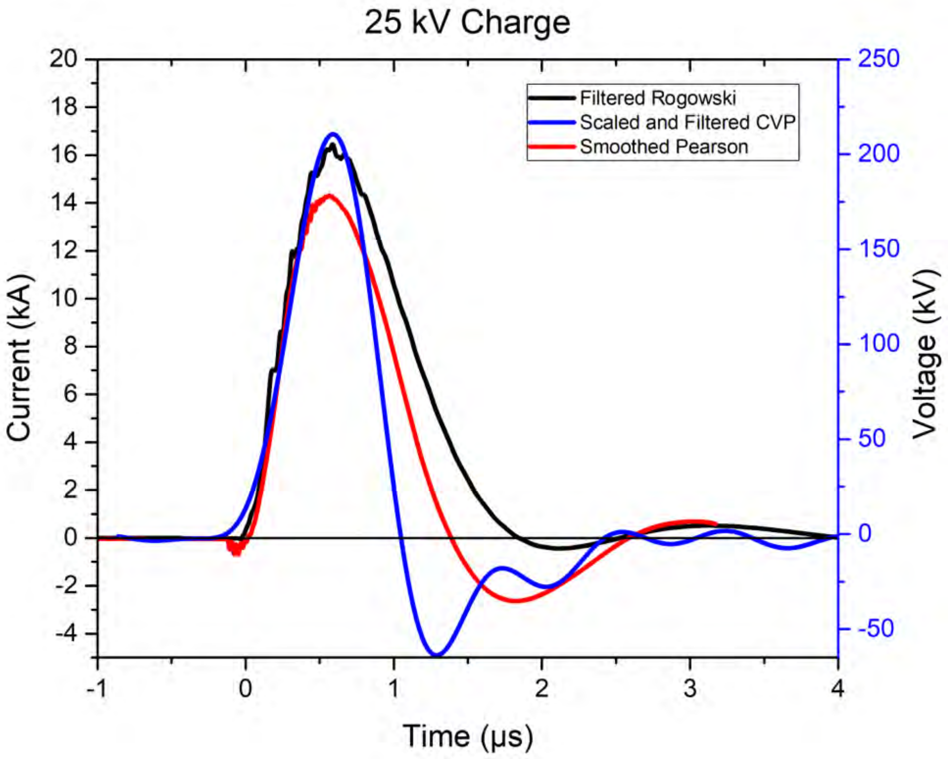

Figure 10. Output voltage and current from the 18-stage Marx at 25 kV charge.

<u>Cathode Development</u>

A 4-shaft floor loom was acquired in order to weave carbon fiber into various velvet structures to allow for rapid prototyping and testing of various cathode structures. Initial weaves have been created of both plain yarn and carbon fiber thread, as shown in Figure 10, with development of velvet structures to begin shortly. In addition to carbon fiber velvet we have purchased AF-1 carbon fabric from ceramaterials which is currently used by AFRL as a carbon fiber velvet substitute. For bonding we will initially try an ultra-high vacuum conductive epoxy. If this does not work, we will braze the carbon fabric to the stainless steel substrate.

Figure 11. Carbon fiber plain weave cloth

Trigger Pulse Generator

A high voltage pulse generator is required for reliable triggering of the Marx generator. This specific design is unique in its quick rise times and ability to re-trigger reliably at high repetition rates (~100Hz). This pulser is composed of two parts: control and high voltage. While both parts are crucial in the success of the end product, the high voltage board is what actually generates the high voltage pulse. The control board, however, interfaces with a remote PC to determine when and the high voltage board should be triggered, as well as important aspects of the output pulse such as repetition rate and amplitude. A high-level view of the specific components involved in each board to accomplish these tasks is shown in Figure 11.

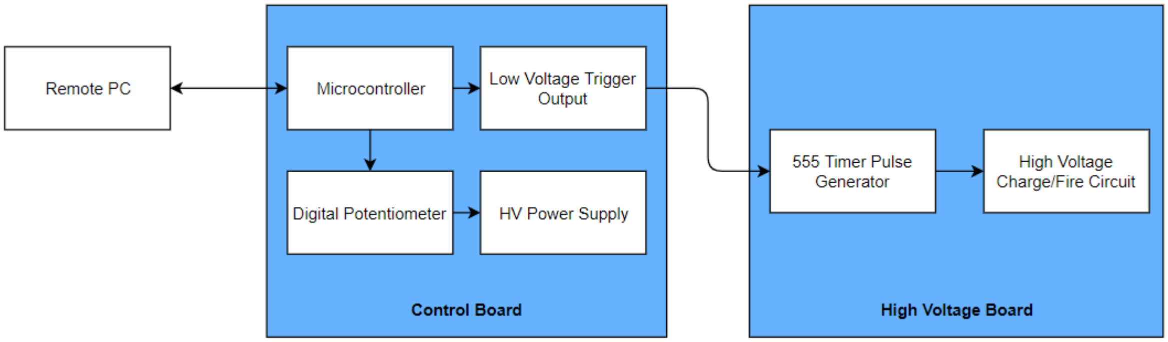

Figure 12: Simplified Block Diagram of Overall Trigger Generator Design

The motivation behind splitting the pulser into two boards is isolation. The microcontroller operates at 5V while the high voltage transformer operates at voltages approaching 4 kV. Putting both circuits on the same printed circuit board would leave the board prone to several failures, especially in the low voltage circuits. If the microcontroller fails, the pulser is still able to operate, however several features would no longer be available. It is for this reason that special care in isolating high voltage circuits is taken.

The control board is vital to the success of the overall project. The main purpose of the control board is to minimize the number of connections needed between a remote PC and the high voltage board. In doing so, the control board is able to receive information from the PC and send one single-pulse input to the high voltage board. This means the control board determines repetition rate, pulse amplitude, and any operational information the user should see on the PC.

The microcontroller communicates to and from a remote PC using the communication protocol UART. This reduces the number of connections to the remote PC to two fiber-optic lines, one for receiving and one for transmitting. In practice, using a microcontroller allows for the user to enable/disable the high voltage power supply, determine pulse amplitude, configure repetition rate, and view safety information (such as errors when firing or the presence of high voltage) all from a remote PC.

This specific microcontroller (model PIC16F18857) was chosen because it has more than enough GPIO pins for this application (up to 36), allows for communication via UART and SPI, and has an internal clock speed of up to 32 MHz. For this specific application, the GPIO pins are used to enable the high voltage power supply, control the digital potentiometer, trigger the high voltage board, and illuminate an LED to indicate if the high voltage supply is on. For reliability, Schottky diodes are placed on any GPIO pins that source current during operation (see Figure 12). Therefore, if the microcontroller fails in a state that permanently sinks current on any of the pins, the Schottky diodes will block the flow of current and the trace will not have to be scraped up for manual use of the board.

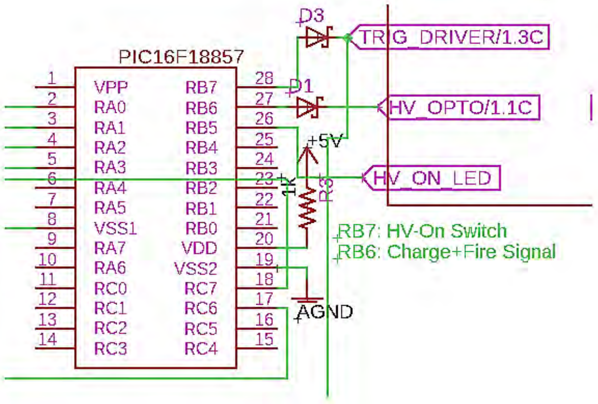

Figure 13: Schottky Diodes to Avoid Permanent Signal Sinking During Failure

Though the majority of the circuits on this board operate at low voltages, the control board also interfaces directly with the high voltage power supply used to power the output pulse. The power supply (model 4C24-P250) contains seven pins for controlling the high voltage output; all of these pins operate at low voltages (≤ 24 V) and are controlled by the microcontroller.

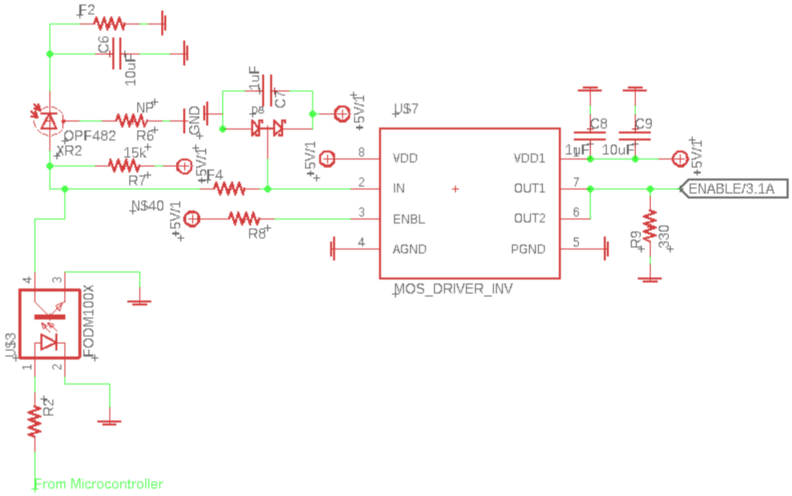

Figure 14: Opto-coupler With Inverted MOSFET Driver for Enabling/Disabling High Voltage Power Supply

An inverted driver chip is shown above in Figure 13 because the NPN optocoupler cannot source current for the chip’s input. Therefore, an inverted driver chip is used, and the opto-coupler is configured to pull down the input instead. A pull-up resistor is also included in place of a pull-down resistor so the output is disabled when the opto-coupler is not active. Similarly, pictured in Figure 13 is a fiber-optic input (labeled XR2). This is used in place of the microcontroller; it allows the user to enable/disable the power supply manually and behaves in a similar fashion to the opto-coupler, pulling down the input when active.

The high voltage board achieves a pulsed high voltage output by charging a buffer capacitance of 20nF and discharging it through a transformer. Several steps are taken to verify the safety and reliability of each component used with high voltage. This board is designed to take an input pulse of any duration and produce a 10 µs high voltage pulse. To do so, the board generates its own charge and fire signals using 555 timers, MOSFET drivers, and IGBTs. When firing, the only way to vary the pulse magnitude is by adjusting the charge voltage, which is determined separately by the control board.

For reliability, a MOSFET current driver (model 849-IXDN630YI) is used to provide up to 9A of current to drive a 1:1 isolation pulse transformer (model 580-1017C). The design also includes a fly-back diode and DC blocking capacitors (labeled C43 and C44 in Figure 14) to avoid damage to the MOSFET driver in the case of a long input pulse (longer than 10 µs for fire, 60 µs for charge). The experimental results of this part of the high voltage board are shown in Figure 15.

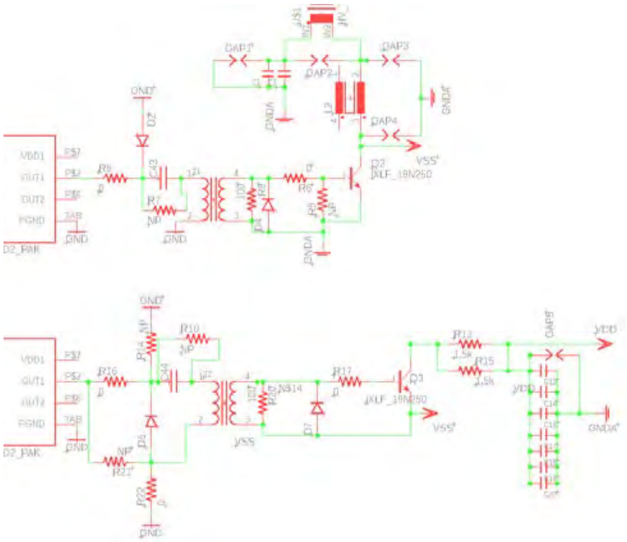

Figure 15: Fire (top) and Charge (bottom) Circuits for Pulsed High Voltage Output.

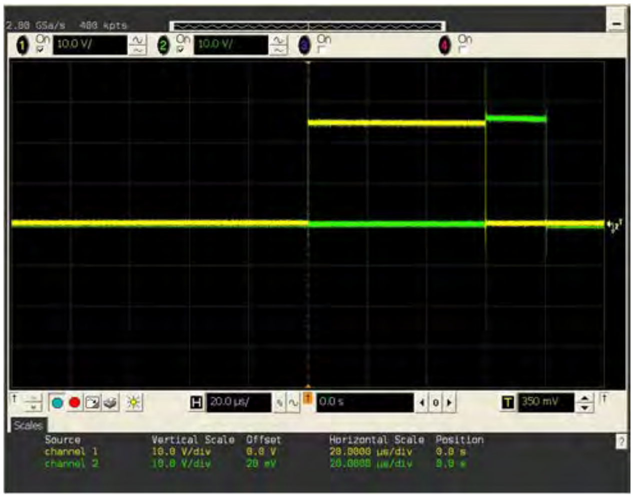

Source	Vertical Scale	Offset	Horizontal Scale	Position
channel 1	10.0 V/div	0.0 V	20.0000 µs/div	0.0 s
channel 2	10.0 V/div	20 mV	20.0000 µs/div	0.0 s

Figure 16: Oscilloscope Image of MOSFET Driver Chips With 555 Timer Inputs

Once the pulse is sent through the pulse transformer, an IGBT conducts (labeled Q3 in Figure 14) and allows the buffer capacitors (labeled C1 and C2 in Figure 6) to be charged by the high voltage power supply (labeled VDD in Figure 6); this occurs for 60 µs. Then, Q3 opens and another pulse is generated to conduct a separate IGBT (labeled Q2 in Figure 14). This gives the buffer capacitors a path to ground, leaving the full voltage drop to be realized across the transformer.

There are two places in the high voltage board where inductor core saturation must be paid attention to. These include the high voltage transformer, and the saturable inductor (labeled U$1 and L2 respectively in Figure 16). In the case of the high voltage transformer, inductor core saturation is something that must be avoided. According to equation 1, the saturation of an inductor depends on several variables, including the number of turns on the primary side. Therefore, based on the other known variables, it can be calculated that 33 turns on the primary side must be used, ideally, for no saturation to occur.

$$V = \frac{N * A_c * \Delta B}{100 * \Delta t} \tag{1}$$

Additionally, the core must be "reset." In other words, sending current through the core repeatedly in the same direction will eventually cause saturation. To mitigate this, the charging mechanism involves sending current through the transformer opposite the direction current flows during discharging. Therefore, the core is reset every time this circuit is fired.

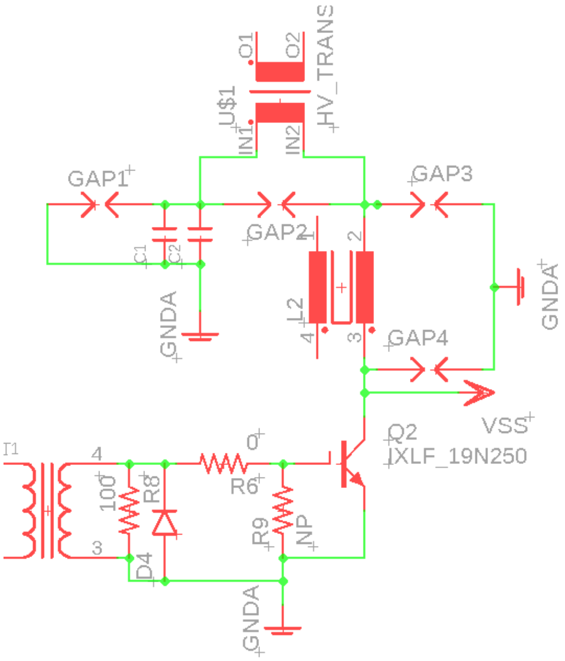

Figure 17: High Voltage Firing Circuit Involving Inductor Core Saturation

Conversely, the saturable inductor (labeled L2) is designed to saturate very quickly each time this circuit is fired. This works by using the IGBT to control the buffer capacitors' only DC path to ground. In doing so, current must flow through the saturable inductor. This allows the IGBT to fully close and reshapes the pulse to a faster rise time. Because the pulse is triggered purely by the IGBT, the repetition rate can be much higher. Similar to the high voltage transformer, the change in polarity between charge and discharge also allows for the core to be reset with each shot.

3. Findings and Conclusions

There are several findings and conclusions during FY 2019 of this program. First, the fabrication of the MILO source is nearly complete. Second, fabrication of the Marx generator was completed and testing ensued. Initial test results confirm the predicted output performance of the Marx based upon the small stage tests and modeling. Fabrication of carbon fiber velvet was initiated as well as the procurement of other carbon fiber fabrics and bonding agents. Finally, the solid-state trigger generator hardware fabrication was completed.

4. Plans and Upcoming Events

Immediate plans are to begin single shot testing of the MILO source as soon as possible. Assembly and bakeout of the MILO source should be completed by March 2020. Testing of the Marx generator should be completed by February 2020. Fabrication of the in-house carbon fiber velvet should be completed by April 2020 with comparative testing with the other cathodes to be done by June 2020.

5. Transitions and Impacts

None

6. Collaborations

We have had discussions with Sterling Beeson at AFRL regarding their development of a low-cost technique of bonding commercially available carbon fiber fabric, such as that used in hydrogen fuel cell manufacturing, to graphite. This would be a method we would like to employ in the fabrication of the MILO cathode.

7. Personnel

Principal investigator: John Mankowski, 1 month effort

Team Members: Senior Research Associate, David Barnett, 6 month effort
Machinist, Lee Waldrep, 3 month effort
Technician, Joel Perez, 2 month effort

8. Students

2 PhD students, 1 Master’s student, 2 undergraduate assistants

9. Technology Transfer

None at this time.

10. Products, Publications, Patents, License Agreements, etc.

Publications resulting from this project:

Abide, M., Dickens, J., R. Joshi, Neuber, A., and Mankowski, J., "Simulation of an S-band MILO with Adjustable Beam Dump," *Plasma*, 2 (2), 2019.

Buntin, T., Collier, L., James, C., Dickens, J., Mankowski, J., and Neuber, A., "Magnetic Shielding Effectiveness of Layered Medium-Walled Structures," *2019 IEEE Pulsed Power and Plasma Science Conference*, 2019.

Abide, M., Buntin, T., Dickens, J., Neuber, A., Joshi, R., and Mankowski, J., "Low-Impedance S-Band MILO," *2019 IEEE Pulsed Power and Plasma Science Conference*, 2019.

11. Point of Contact in Navy

Contact: Matt Mcquage, NSWCDD, E05

Contact information: matthew.mcquage@navy.mil

Date of last contact: Kickoff meeting on 7/31/2018

12. Acknowledgement/Disclaimer

This work was sponsored by the Office of Naval Research (ONR), under grant number N00014-18-1-2384. The views and conclusions contained herein are those of the authors only and should not be interpreted as representing those of ONR, the U.S. Navy or the U.S. Government.

Novel High Power Microwave System Designs Using Nonlinear Transmission Lines

Grant No. N000014-18-1-2341

Period of Performance: October 1, 2018 to September 30, 2019

Prepared by:
Dr. Allen L. Garner, Principal Investigator
Associate Professor and Undergraduate Program Chair, School of Nuclear Engineering
Purdue University
516 Northwestern Ave.
West Lafayette, IN 47906
Tel: (765) 494-0618
Email: algarner@purdue.edu

This work was sponsored by the Office of Naval Research (ONR), under grant number N000014-18-1-2341. The views and conclusions contained herein are those of the authors only and should not be interpreted as representing those of ONR, the U.S. Navy or the U.S. Government.

Grant or Contract Number: N00014-18-1-2341
Date Prepared: 22JAN2020
Project Title: Novel High Power Microwave System Designs Using Nonlinear Transmission Lines
Annual Summary Report: [FY2019]
Principal Investigator: Allen L. Garner, (office): 765-494-0618, algarner@purdue.edu, Purdue University

Section I: Project Summary

1. Overview of Project

Abstract: Nonlinear transmission lines (NLTLs) are of great interest to the Navy for solid state high repetition rate directed energy systems. This project investigates the suitability of novel composite materials for NLTLs in a high power microwave (HPM) source. Since understanding the current state of NLTL research will guide potential areas of improvement, we have performed an extensive review of current NLTL technology and topologies. This report provides an executive summary of the review paper that will be edited and submitted for. We have constructed composites with various volume loadings of barium strontium titanate (BST) and/or nickel zinc ferrite (NZF), which exhibit nonlinear permittivity and permeability, respectively. We report the linear permittivity of BST, NZF, and BST/NZF composites as a function of volume loading and the linear permeability as a function of frequency and volume loading. We observe notable increases in permeability as we exceed 15% NZF for the NZF composites and 10% NZF for the NZF/BST composites. We observe reasonable agreement between effective medium theories (EMTs), finite element simulation using CST Microwave Studios, and experiment from 1 to 4 GHz for the various composites. The main outstanding challenge is measuring bulk BST permittivity for entering in the model. Ongoing work for measuring nonlinear permittivity and permeability and assessing the dielectric breakdown strength of the materials is discussed.

Objective: The goal of this project is to evaluate the feasibility of creating novel nonlinear dielectric materials by mixing nonlinear inclusions into a polymer base dielectric. The resulting composite dielectric properties will be measured using a vector network analyzer (VNA) to determine the complex permittivity and permeability of the composite. This will provide a baseline for determining the relationship between the volume loading of the nonlinear electric and nonlinear magnetic inclusions in a material to the dielectric properties of the composite. These measurements will be used to develop a model based on common effective medium theories, such as the Maxwell Garnett model, to guide material design. This model can be coupled with electromagnetic simulations to optimize an NLTL system as a radio frequency (RF) source.

Introduction: Increased global volatility motivates the development of devices for nonlethal deterrence. Directed energy devices can provide forceful persuasion at a distance for both civilian and military peacekeepers. Additionally, increasing occurrences of vehicular terrorism further drive the development of technology to stop vehicles from a distance before they can injure civilians or destroy property. Militarily, disabling motorized attacks before contact with troops is critical for reducing casualties while keeping the attackers alive for future interrogation. Directed energy technology can provide these capabilities, although system size often limits application in the field.

Thus, developing compact HPM devices could facilitate fielding devices for nonlethal defense with increased standoff range or for radar or weapons systems for aircraft or ships. This effort assesses the design of novel NLTLs by examining the impact of composites comprised of various combinations of dielectric and magnetic inclusions and leveraging various geometries, such as tapering, used in conventional transmission lines for matching. This may increase efficiency and energy in the RF output as it relates to pulse width while also providing additional flexibility in design.

Background:

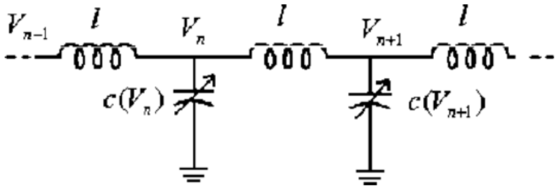

Fig. 1 Representative circuit model for a NLTL with nonlinear capacitors.

Materials are a challenge for NLTL design. Figure 1 shows a simple example of a NLTL. One may represent a conventional transmission line with lumped elements as an inductor in series with a resistor on the top line and a capacitor in parallel with a shunt conductor in the vertical lines with the resistor and conductor representing losses. An NLTL has a similar setup, as shown in Figure 1, except that either the inductor or capacitor (or both) vary with current or voltage, respectively. This modulates the delivered pulse to generate an RF signal with tunability of the NLTL important for controlling the frequency of the resulting RF.

While NLTLs are growing in importance for generating RF, challenges remain in constructing them with high voltage and power capabilities, as required in many HPM applications, and in tunability for wideband applications or capability to be used at multiple frequencies. Based on the definitions above and the circuit diagram in Figure 1, one method to generate an NLTL involves using a varactor, whose capacitance varies with applied voltage, generally sigmoidally (rapidly increasing over a narrow voltage range). Understanding the importance of this dependence is critical for understanding the potential flexibility in design. Early NLTLs often used nonlinear capacitance to induce this phenomena, resulting in soliton formation.

Varactors are generally low voltage devices, which presents a challenge for high power applications. Additionally, the frequency cannot be tuned for a given varactor. A recent alternative growing in popularity involves using ferrites to provide nonlinear inductance in meandering NLTLs. Texas Tech University (TTU), the Air Force Research Laboratory (AFRL), and others have also developed and applied such approaches for gyromagnetic NLTLs for HPM and high power radiofrequency applications. The initial TTU NLTLs provided peak voltages of approximately 50 kV with 15% power efficiency and frequencies of a few GHz. TTU next considered the impact of material, such as nickel-zinc, yttrium iron garnet, magnesium-zinc, and lithium ferrites, on performance. They demonstrated that varying the material’s bias magnetic field provided active delay control and that the material’s ferromagnetic resonance line width played a significant role in microwave generation. TTU next showed that one could effectively tune the output by controlling the bias voltage, which subsequently impacted the electrical properties of the NLTL due to its nonlinear nature, enabling the construction of a single, frequency-agile device capable of operating from 1.8 to 2.6 GHz with powers from 1 MW to 3 MW; however, higher voltages (on the order of 40 kV) resulted in corona discharge, limiting application at higher voltages. Thus, attaining higher powers required combining multiple NLTLs, which they demonstrated for arrays of either two or four NLTLs. The NLTL could then be incorporated into a solid-state HPM source to generate microwave pulses with a microwave frequency of 2.1 GHz with a pulse repetition frequency of 65 MHz. AFRL designed a spatially dispersive ferrite NLTL with axial bias that was frequency tunable from 0.95 to 1.45 GHz with instantaneous power levels of tens of MW and durations from 4 to 17 ns.

A Russian group from the Institute of High Current Electronics has also studied gyromagnetic RF sources using NLTLs. Their early work used saturated NiZn ferrites as an active nonlinear medium and found an optimum length of approximately 1 m for producing a 1000 pulse burst at 200 Hz repetition rate for a peak RF power of 260 MW with a central frequency of 1.2 GHz and of 0.25 GHz at -3 dB level and 0.4 GHz at -10 dB level. They have also demonstrated electronically controlled beam steering by connecting two NLTLs to one high voltage driver with each NLTL capable of producing RF pulses from 50-700 MW at frequencies from 0.5 to 1.7 GHz with 100 Hz repetition rate. Gyromagnetic NLTLs have also generated high power ns RF pulses with field strengths up to 40 kV/cm, durations from 4 to 25 ns, and frequency from 0.6 to 1.0 GHz to provide flexible output at laboratory scale for biological experiments. They have also subsequently extended their frequency output to 4 GHz with a peak voltage of 175 kV for 100 Hz repetition rates during one second. Their ferrite line in the NLTLs implements a continuous unit of NiZn rings of M200VNP type of a total length of 700 mm. At lower frequencies (~300 MHz), they have also used a gyromagnetic NLTL as a peak power amplifier of an input pulse. They applied a 500 kV pulse with a full-width-half-max duration of 7 ns to the NLTL to increase the pulse amplitude to 740 kV while reducing the pulse duration to ~2 ns. This increased the power from ~ 6 GW on the input to ~13 GW on the output at a 1 kHz pulse repetition rate in burst mode.

Alternatively, the University of New Mexico developed a hybrid line consisting of both nonlinear capacitors and inductors. While this is a promising approach that could provide some ability for tunability, one must attain appropriate inductance and capacitance behavior to achieve a constant transmission line impedance.

2. Activities and Accomplishments

Table 1. Permittivity of NZF, BST, and a mixture of both at ~2 GHz

NZF	ε_r	BST	ε_r	(BST/NZF)		ε_r
5	3.41±0.23	5	3.47 ±0.15	5	5	4.01 ±0.20
10	3.69±0.19	10	4.20 ±0.10	5	10	4.89 ±0.20
15	4.02±0.26	15	5.14 ±0.04	10	5	5.15 ±0.10
20	4.73±0.22	20	6.29 ±0.20	10	10	6.08 ±0.12
25	5.77±0.33	25	7.44 ±0.29	10	15	6.65 ±0.21
/	/	/	/	15	10	7.11 ±0.15

We manufactured single inclusion composites comprised of various volume loadings of 5%, 10%, 15%, 20%, and 25% of BST or NZF. Multi-inclusion composites containing 5% of NZF with 5 or 10% of BST, 10% of NZF with 5, 10, or 15% of BST, 15% of NZF with 10% of BST, and 10% of both NZF and BST were also produced. The composites were enclosed in a silicone-based host. Four duplicates of each condition were manufactured to quantify statistical variation in parameters.

To characterize variation of the permittivity and permeability as a function of volume loading, we equipped the composites with an outer and inner conductor to form a coaxial transmission line that we connected to a network analyzer. We used the network analyzer to obtain the S-parameters from 1-4 GHz and then calculated the dielectric and magnetic properties using Keysight Material Measurement Suite Software. Table 1 summarizes the linear regime permittivity for BST, NZF, and the combined sample while Table 2 summarizes the linear regime permeability. For composites consisting of only BST inclusions, the relative permittivity increased with volume fraction while the permeability remained relatively constant. For composites consisting of only NZF inclusions, both permittivity and permeability increased with volume fraction. Interestingly, the permeability depends on frequency, especially at higher volume loadings, in the linear regime. The permittivity of composites containing both BST and NZF inclusions increased with BST volume fraction while increasing NZF volume fraction increased permeability. The permeability behaved similarly with a much lower magnitude of change.

Table 2. Permeability of BST, NZF, and a mixture as a function of frequency.

BST	**1 GHz**	**2 GHz**	**3 GHz**	**4 GHz**
5%	1.00±0.01	1.01±0.01	1.02±0.01	1.03±0.01
10%	1.07±0.01	1.04±0.01	1.02±0.01	1.04±0.01
15%	1.02±0.01	1.04±0.01	1.04±0.02	1.03±0.01
20%	1.01±0.01	1.01±0.02	1.03±0.01	1.05±0.01
25%	1.01±0.01	1.01±0.01	1.01±0.01	1.00±0.02
NZF				
5%	1.08±0.03	1.07±0.03	1.06±0.02	1.06±0.02
10%	1.09±0.02	1.09±0.05	1.08±0.02	1.08±0.02
15%	1.24±0.05	1.19±0.04	1.16±0.04	1.16±0.04
20%	1.30±0.08	1.26±0.06	1.21±0.06	1.21±0.06
25%	1.49±0.04	1.32±0.02	1.23±0.01	1.22±0.01
NZF/BST				
5%/5%	1.06±0.02	1.05±0.01	1.05±0.01	1.04±0.01
5%/10%	1.05±0.01	1.06±0.01	1.05±0.02	1.03±0.03
10%/ 5%	1.15±0.03	1.13±0.04	1.11±0.03	1.08±0.04
10%/10%	1.13±0.02	1.12±0.05	1.10±0.05	1.09±0.04
10%/15%	1.11±0.01	1.10±0.02	1.08±0.02	1.06±0.03
15%/10%	1.19±0.02	1.17±0.04	1.13±0.03	1.11±0.05

We also performed X-Ray Tomography scans and image analysis for a sample containing both BST and NZF, as shown in Fig. 1. The analysis could discern between the NZF and the PDMS/BST; however, the resolution was not fine enough to discern between the BST and PDMS. Additional scans can be performed to separate the two may ultimately conducted but were omitted due to the additional expense introduced due to the required scan time and image processing and the minimal information that would be added. The resolution of the current scans is ~5 µm and the scan would require a resolution of at least 800 nm, or finer, to see the 800 nm diameter BST particles.

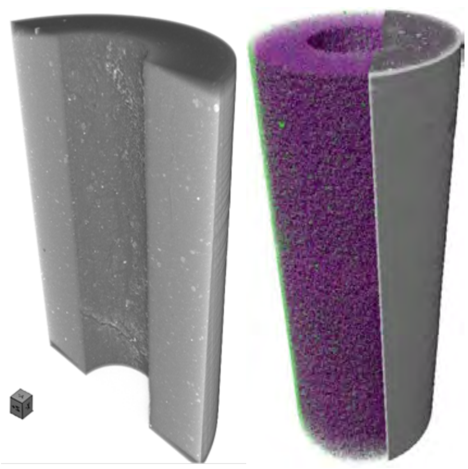

Fig. 1: The X-Ray Tomography scan of the samples with the (left) compiled image of the sample with 10 % NZF and 15 % BST and (right) the scan with the different particles separate by density for NZF (green) and BST/PDMS (purple).

We have purchased the components and power supply to measure the nonlinearity of the

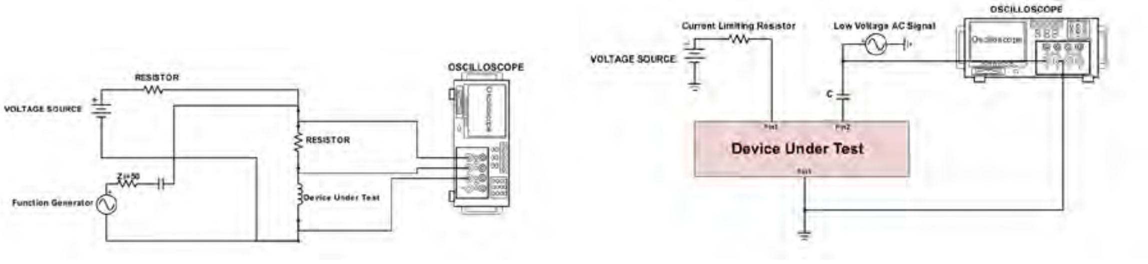

Fig. 2. Experimental setups to measure nonlinear (left) permeability and (right) permittivity.

permeability of the composites with NZF inclusions. We are constructing a solenoid to produce a magnetic field ~0.3 T that will vary with the input current from the power supply. We will measure the permeability as a function of applied magnetic field to determine the nonlinear behavior of permeability to design a complete NLTL. We have communicated with Metamagnetics while designing the solenoid and they have confirmed that our approach is appropriate to measure the nonlinear permeability. We are also insulating a bias tee to measure the nonlinear permittivity of BST and BST composites. We are working to mitigate electrical breakdown in the circuit to eliminate potential transients on our network analyzer. We have been in contact with Kevin O'Connor with NanoEM to evaluate the feasibility of pushing the BST composites into a nonlinear regime. Figure 2 shows circuit schematics of these devices.

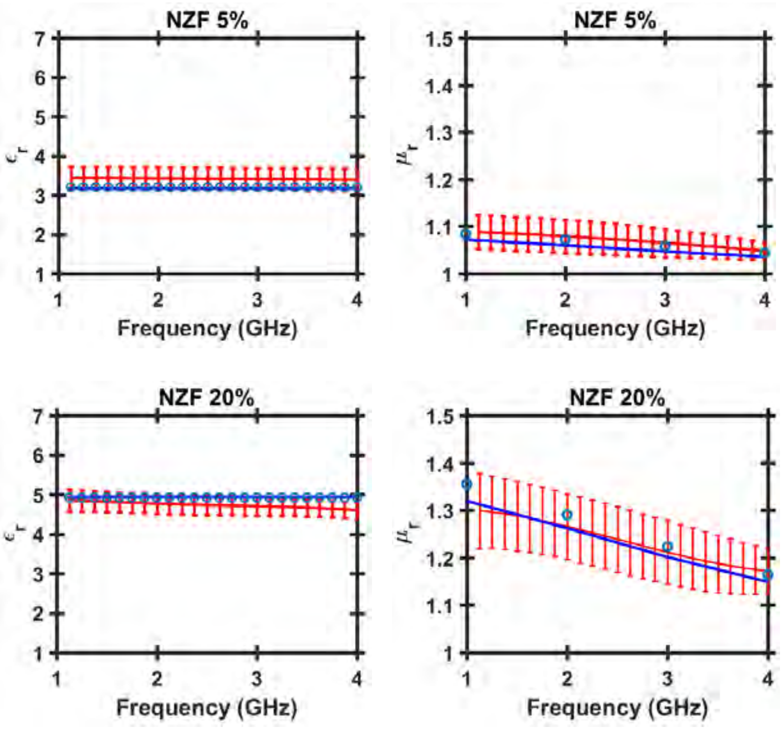

Fig. 3. Experimental (red line with error bars), CST simulation (blue circles), and LI (Lichtenecker) mixing rule calculations for effective permittivity ε_r and permeability μ_r for composites containing nickel zinc ferrites 5% and 20% volume loadings of nickel zinc ferrite.

We have also progressed on applying effective medium theories (EMTs) and CST Microwave Studios (CST MWS) to predict composite properties. The real permeability of NZF depends more strongly on frequency for higher volume loading. Using this frequency-dependent data from 1 ~ 4 GHz for NZF yields excellent agreement in composite effective real permeability between CST MWS, the Lichtenecker (LI) EMT, and experiment except for 10% NZF composites.

Figure 3 shows sample comparison between measurement (red with error bars), LI (blue line) and CST MWS (blue circles) for 5% and 20% NZF volume loadings as a function of frequency. The results generally agree, even for higher volume loadings. Figure 4 examines real permittivity and real permittivity as a function of volume loading at 1 GHz.

The 10% NZF composites is unexpectedly low compared to the 5% and 15% loadings (and almost the same as the 5% loading). Future studies should reconsider this volume loading to assess potential measurement, analysis, or material issues.

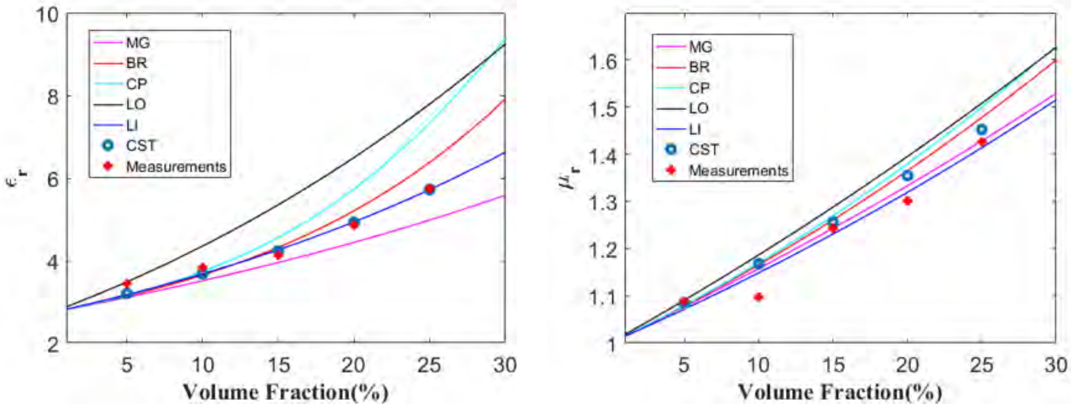

Fig. 4. Comparison of the effective real permittivity (left) and permeability (right) of NZF composites as a function of inclusion volume fraction at 1 GHz with effective medium theories: MG: Maxwell- Garnett, BR: Bruggeman, CP: coherent potential, LO: Looyenga, LI: Lichtenecker.

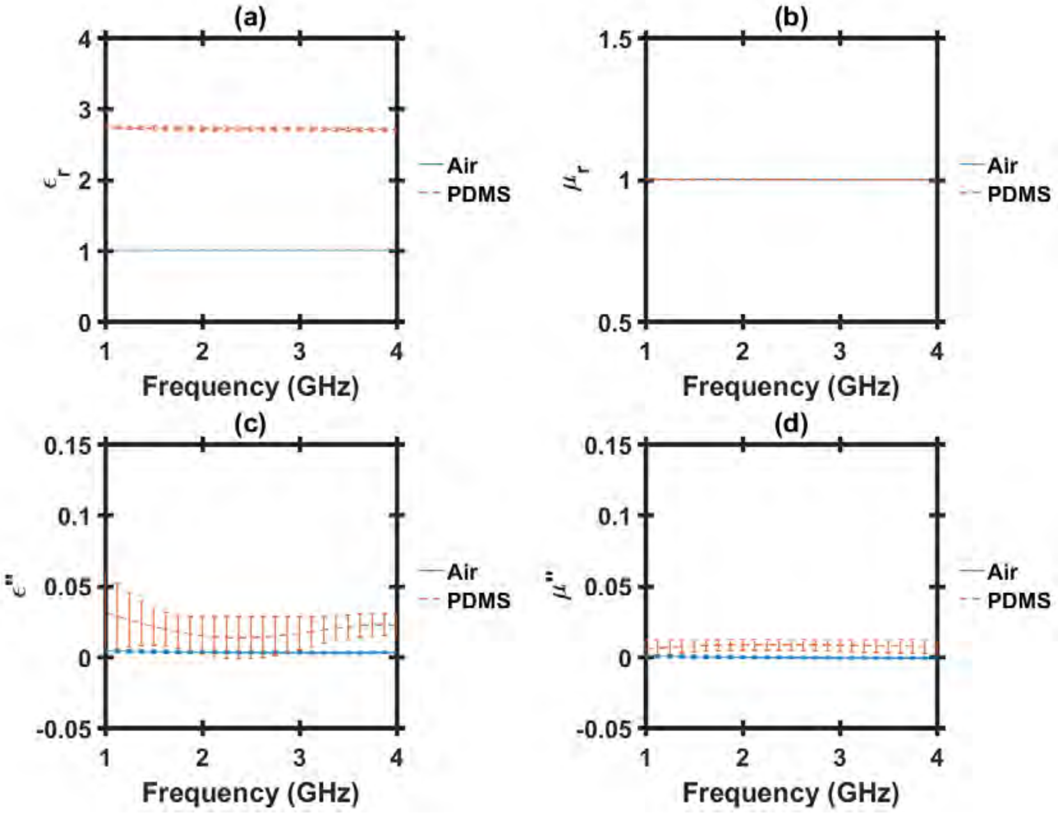

Fig. 5. Measurements of the dielectric properties of PDMS and air.

Our present assessment of BST composites assumes real permittivity ε'_{BST} = 960 at 1 GHz, loss tangent of BST of $\tan\delta$ = 0.021 at 500 MHz, and PDMS measurements from Fig. 5. The real permittivity of PDMS is constant, while the imaginary component exhibits a slight frequency dependence.

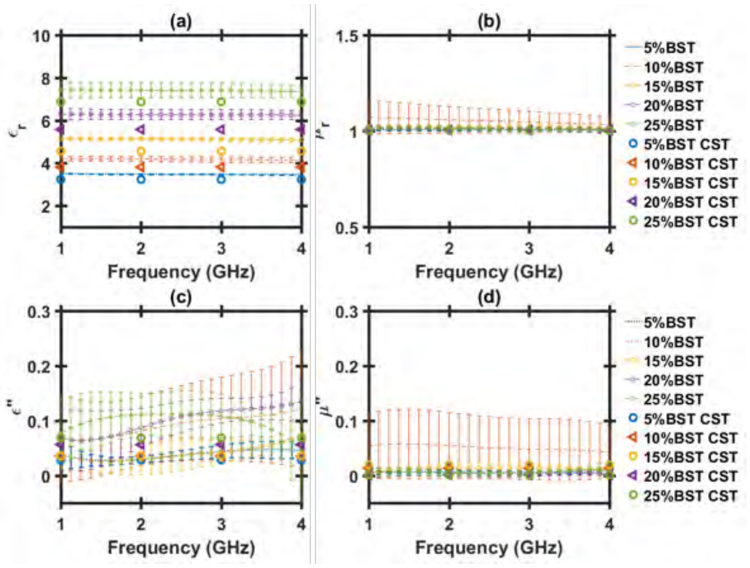

Fig. 6. Comparisons of BST composite (a) effective real permittivity, (b) effective real permeability, (c) effective imaginary permittivity, and (d) effective imaginary permeability. The lines with error bars are from measurements. The inputs in CST MWS for BST: ε'_{BST} = 960, tan δ = 0.021 (at 500 MHz), μ'_{BST} = 1, tan δ_m= 0.

Figure 6 shows that the imaginary permittivity from simulation agrees within an order of magnitude of measurements and underpredicts the real permittivity at 1 GHz. This suggests that some common factor (perhaps the inclusion permittivity is lower than predicted) requires adjustment; however, more data is required concerning the dispersions of the effective ε''_{BST} to further benchmark to theory.

Comparing $\sigma_s/(\varepsilon_0\omega)$ with ε''_{BST} = 20.16 suggests that the loss contribution from the conductivity is negligible (assuming a static conductivity for BST of σ_s = 10^{-10} S/m). The large contrast between the imaginary permittivity ε''_{PDMS} < 0.05 and ε''_{BST} = 20.16 also explains why the classical EMTs failed to yield estimates.

The application of EMTs to composites with a large contrast between dielectric properties is challenging. One alternative used previously for electromagnetic shielding composites containing stainless steel inclusions (σ = 1.4×10^6 S/m) in a plastic host material (ε = 3) applies the generalized effective medium theory (GEMT). In this case, the GEMT was treated as a first principles inspired semi-empirical model with the parameters fit such that as many parameters as possible were either fixed or exhibited clear trends with respect to frequency, material, and/or volume loading. Trends in these fitting parameters were noted with different inclusion shape (for instance, spheres, cylinders, and flakes). Such an approach may be applied here to account for this dielectric contrast.

3. Findings and Conclusions

The results to date have demonstrated the feasibility of tuning the dielectric and magnetic properties of composites comprised of BST and/or NZF in a ceramic material. Additionally, both simulation and effective medium theories (EMTs) can predict these values for potential use in future high power microwave device modeling.

4. Plans and Upcoming Events

Key tasks and accomplishments for FY2020 follow:

1) We have completed a draft of the NLTL review article and are working to revise it for submission for publication.
2) We will develop sample NLTLs to take to the University of Michigan and Eagle Harbor Testing to test at voltage using a linear transformer driver (LTD) and an inductive adder, respectively.
3) The main material challenges for the coming year involve better characterizing the properties of bulk BST for incorporation into theory and simulation and characterizing the nonlinear properties of BST and NZF composites with respective to voltage and current, respectively, to develop nonlinear EMTs.
4) Another major aspect before implementation for high power devices is the ability of the composites to withstand high voltages, so future tests with high potential testing devices will determine the dielectric breakdown conditions for these composites.
5) We will also begin developing a model of a full high power microwave system model that may be used in future system design and development.

5. Transitions and Impacts

Not applicable.

6. Collaborations

Brad Hoff, Air Force Research Laboratory
Jack Chen, Naval Surface Warfare Center Dahlgren Division
Eagle Harbor Technologies
Ryan McBride, University of Michigan
Walter Sessions, GTRI

7. Personnel

Principal Investigator: Allen L. Garner, 0.54 person-month, National Academy Member (N).
Co-PI: Wenzhuo Wu, <0.5 person-month, National Academy Member (N).
Teams Members:
Travis Crawford, graduate student, 1.12 person-months, National Academy Member (N).
Andrew J. Fairbanks, graduate student, 3.75 person-months, National Academy Member (N).
Xiaojun Zhu, graduate student, 6 person-months, National Academy Member (N).
Amanda Loveless, graduate student, 0.6 person-months, National Academy Member (N).
Business Contact: Carrie Solomon
Subs: GTRI: <1 person-month.

8. Students

5 graduate students/3 undergraduates (research for credit).

9. Technology Transfer

We are continuing to work with Jack Chen from NSWCDD concerning the incorporation of NLTLs into high power microwave systems and Brad Hoff from AFRL concerning NLTL physics and characterization of the electromagnetic properties. We will continue to work with them as we finalize the review and begin measuring nonlinear electromagnetic properties.

10. Products, Publications, Patents, License Agreements, etc.

Publications resulting from this project:

1. A. J. Fairbanks, A. M. Darr, and A. L. Garner, “Review of Nonlinear Transmission Line Designs,” under preparation for *IEEE Access*.

Conference Oral Presentation Abstracts

1. A. Fairbanks, X. Zhu, J. Hernandez, S. Gao, W. Wu, T. Tallman, and A. Garner, “Development and Diagnostics on Composites for Nonlinear Transmission Lines,” IEEE Pulsed Power and Plasma Science Conference, 2C3, 24 June 2019.

2. X. Zhu, A. J. Fairbanks, and A. L. Garner, “Assessing Effective Medium Theories for Designing Composites for Nonlinear Transmission Lines,” IEEE Pulsed Power and Plasma Science Conference, 2C2, 24 June 2019.

Conference Poster Presentation Abstracts

1. A. J. Fairbanks, X. Zhu, J. A. Hernandez, T. N. Tallman, A. L. Garner, “Composite Material Development for Nonlinear Transmission Lines,” 21st Annual Directed Energy Science & Technology Symposium, Open and Limited Poster Session, 09 April 2019, Destin, FL, USA.

11. Point of Contact in Navy

Jack Chen, NSWCDD, 28JUN2019
Brad Hoff, AFRL, 11JUL2019.

12. Acknowledgement/Disclaimer

This work was sponsored by the Office of Naval Research (ONR), under grant (or contract) number N00014-18-1-2341. The views and conclusions contained herein are those of the authors only and should not be interpreted as representing those of ONR, the U.S. Navy or the U.S. Government.

Nanoscale Effects on Gas Breakdown and Electron Emission

Grant No. N000014-17-1-2702

Period of Performance: October 1, 2018 to September 30, 2019

Prepared by:
Dr. Allen L. Garner, Principal Investigator
Associate Professor and Undergraduate Program Chair, School of Nuclear Engineering
Purdue University
516 Northwestern Ave.
West Lafayette, IN 47906
Tel: (765) 494-0618
Email: algarner@purdue.edu

This work was sponsored by the Office of Naval Research (ONR), under grant number N00014 - 17-1-2848. The views and conclusions contained herein are those of the authors only and should not be interpreted as representing those of ONR, the U.S. Navy or the U.S. Government.

Grant or Contract Number: N000014-17-1-2702
Date Prepared: 10JAN2020
Project Title: Nanoscale Effects on Gas Breakdown and Electron Emission
Annual Summary Report: FY2019
Principal Investigator: Allen L. Garner, 765-494-0618, algarner@purdue.edu, Purdue University

Section I: Project Summary

1. Overview of Project

Abstract: Accurately predicting gas breakdown voltage is becoming increasingly important as the trend toward electronics miniaturization increases. Microelectromechanical systems (MEMS), such as microactuators, pressure sensors, and high-frequency circuits, require microscale gaps and high operating voltages. Accurate breakdown voltage predictions for these systems will prevent discharges that could damage or destroy the device. Conversely, microplasmas use microdischarges for various applications, such as electric micropropulsion and environmental mitigation. Present research trends focus on developing micro- and nano-vacuum electronics for providing increased power densities and frequency for directed energy applications, including radar platforms for shipboard and aircraft systems. In particular, the Air Force and Navy have ongoing efforts exploring the field emission (FE) characteristics of arrays of carbon nanotubes, particularly exploring the implications of distance between emitters and variation of work function on electric field characteristics.

Objective: This effort will elucidate the impact of nanoscale effects on gas breakdown for microscale and smaller gaps by combining experiment, numerical analysis, and theoretical analysis. Specifically, it will assess the impact of surface irregularities, which alter the work function and field enhancement factors that drive field emission. This research fills a gap in understanding the influence on surface structure for electron emission and breakdown, which have significant implications for efficiency and equipment durability.

Introduction: Accurately predicting gas breakdown voltage is becoming increasingly important as the trend toward electronics miniaturization increases. From a directed energy perspective, which is critical for Navy and Air Force applications, present research trends focus on developing micro- and nano-vacuum electronics for providing increased power densities and frequency for shipboard and aircraft radar platforms. In particular, the Air Force and Navy have ongoing efforts exploring the field emission characteristics of arrays of carbon nanotubes, particularly exploring the implications of distance between emitters and variation of work function on electric field characteristics. Directed energy systems using laser or intense electromagnetic systems, including pulsed power and high power microwave technologies, are constantly striving to achieve very high power densities using high frequency and more compact systems. As one goes to these smaller systems, higher electric fields arise and issues concerning breakdown, field emission, and space-charge limited flows increase significantly.

Background: Elucidating the impact of nanoscale effects on gas breakdown for microscale and smaller gaps requires combining experiment, numerical analysis, and theoretical analysis. Initial efforts involve the following:

- Assessing and applying analytic models relating field emission and space-charge limited flow, both at vacuum and general pressure, will elucidate the potential impact of space charge on field enhancement to determine the point at which pressure no longer contributes.

- Performing experiments and developing analytic models will determine the impact of surface roughness and various flaws on surface on the work function and field enhancement, which measures the energy necessary to remove an electron from the cathode and plays a crucial role in the determining the field emission current.
- Performing molecular dynamics simulations to determine the implications of surface roughness on both electron emission and space charge effects to provide data to put into continuum models of gas breakdown.

These results will then be applied to understand experimental and theoretical analyses of gas breakdown for microscale gaps and smaller. Specific next steps will include:
- Further coupling the existing electron emission and breakdown models to the one-dimensional Schrödinger equation to develop a universal breakdown model from the classical Paschen law to quantum scale for multiple gases.
- Analytic and numerical models developed by the Principal Investigator's group will be modified to incorporate the effects of surface roughness and space charge on field enhancement and work function and compared to the parametric experiments.
- Experimental measurements will be performed for gaps from microscale to approximately 100 nm at vacuum and atmospheric pressure to provide a basic parametric study of the mechanisms responsible for breakdown across a wide range of parameters.

This effort will ultimately pave the way for future work unifying all relevant modes of breakdown and electron emission across gap pressure and distance for numerous applications relevant to the Department of Defense, including directed energy, field emission, and micropropulsion.

2. Activities and Accomplishments

FY 2019 focused on extending our previous theories to pressures between vacuum and atmospheric and length scales from micro- to nanoscale, and performing experiments on breakdown and electron emission down to nanoscale at atmospheric pressure.

UNIFIED EMISSION AND BREAKDOWN THEORY FROM QUANTUM SCALE TO PASCHEN'S LAW

One major achievement in FY-20 was completing the unification of emission and breakdown theories from quantum scales to the classical Paschen's law (PL) using a single normalization framework rather than the previous piecemeal approach. We start by defining the governing equations. For Townsend avalanche (TA), the standard PL is given by

$$V = \frac{Bpd}{\ln(Apd) - \ln[\ln(1+\gamma_{SE}^{-1})]}, \qquad (1)$$

where V is the breakdown voltage, p is the gas pressure, d is the gap distance, γ_{SE} is the secondary electron emission coefficient, and A and B are gas dependent parameters.

For the coupled TA/FE regime (what we consider the "microscale" regime, in general), we considered the coupled breakdown criterion given by

TABLE I. SCALING PARAMETERS FOR NONDIMENSIONALIZING (1)-(6)

Scaling Parameter	**Equation**
Pressure	$p_* = E_*/B_p$ [Torr]
Electric Field	$E_* = D'_{FN} = 0.95B_{FN}\phi_*^{3/2}$ [V/m]
Current Density	$j_0 = C'_{FN}E_*^2 = \frac{A_{FN}}{\phi_* t^2(y)}E_*^2$ [A/m^2]
Temperature	$T_* = \frac{\pi m_g \sigma_{CE}}{2ekB_p}\left[\frac{C'_{FN}D'_{FN}L^2A_p p_*}{2\varepsilon_0}\right]^2$ [K]
Length	$L = \left[\frac{\hbar}{2m_e eE_*}\right]^{1/3}$ [m]
Time	$\tau_*^2 = \frac{m_e L}{eE_*}$ [s^2]
Mobility	$\mu_* = \frac{e\tau_*}{m_e}$ [m^2/Vs]
Work Function	$\phi_*^{1/2} = \left[\frac{2A_{FN}^3 m_e \hbar(0.95B_{FN})}{\left(\varepsilon_0 t^2(y)\right)^3 e^2}\right]^{1/3}$ $\left[\mathrm{eV}^{1/2}\right]$
Wave Function	$\psi_*^2 = \varepsilon_0 E_*/eL$ [m^{-3}]
Electron Energy	$U_* = eV_*$[eV]

$$\frac{2E^2 v_d \varepsilon_0}{D_{FN} dJ_{FN}} \frac{\{1-\gamma_{SE}[\exp(\alpha d)-1]\}}{[\exp(\alpha d)-1]} = \frac{\exp(x_0)\,(1+2\bar{E}x_0)}{x_0}, \qquad (2)$$

where E is the breakdown electric field, α is the ionization coefficient, v_d is the drift velocity, J_{FN} is the Fowler-Nordheim current, D_{FN} is a field emission parameter, and x_0 is a function of E. While this formulation assumes a uniform E, recent efforts have been made to generalize this assumption.

Next, for the transitions between FN and CSCL with Child-Langmuir at vacuum and Mott-Gurney (MG) with collisions we consider Poisson's equation, given by

$$\frac{d^2V}{dx^2} = \frac{J}{\varepsilon_0 v}, \qquad (3)$$

where x is the position, J is the current density, and v is the electron velocity, and a force balance that incorporates electron mobility μ as

$$m\frac{dv}{dt} = e\frac{dV}{dx} - \frac{ev}{\mu}, \qquad (4)$$

where m is the electron mass and e is the electron charge.

For the CSCL to QSCL transition we consider (3), Schrödinger's 1D wave equation (SWE), given by

$$\frac{\hbar^2}{2m}\frac{d^2\psi}{dx^2} - eV\psi = U\psi, \tag{5}$$

where ψ is the wave function and U is the electron injection energy, and

$$J = e\left(\frac{i\hbar}{2m}\right)\left[\psi\psi^{*\prime} - \psi^{*}\psi'\right], \tag{6}$$

where $'$ represents a derivative with respect to position and * represents the complex conjugate.

Defining a common set of nondimensional parameters as summarized in Table 1, we solve the equation of motion, and taking various limits gives a set of dimensionless equations characterizing electron emission and gas breakdown from QSCL to PL gives

$$\begin{gathered}\frac{1}{\bar{U}}\frac{d^2q(\bar{x})}{d\bar{x}^2} + \left[\left(\frac{\bar{V}}{\bar{U}}+1\right) - \frac{\left(\lambda_q/4\right)^2}{[q(\bar{x})]^4}\right]q(\bar{x}) = 0;\\ \frac{d^2\bar{V}}{d\bar{x}^2} = [q(\bar{x})]^2;\; \bar{J} = 2\theta'(\bar{x})q^2(\bar{x});\; \lambda_q = \frac{2\bar{J}}{\bar{U}^{1/2}},\end{gathered} \tag{9}$$

for QSCL,

$$\bar{J}_{CSCL} = \frac{8}{9}\frac{\bar{V}^{3/2}}{\bar{d}^2}, \tag{10}$$

$$\bar{J}_{MG} = \frac{9\sqrt{2}}{8}\frac{\bar{\mu}\bar{V}^2}{\bar{d}^3}, \tag{11}$$

$$\bar{J}_{FN} = \frac{\bar{V}^2}{\bar{d}^2}\frac{\beta^2}{\bar{\phi}}\exp\left(-\frac{\bar{\phi}^{3/2}\bar{d}}{\beta\bar{V}}\right)\exp\left(\frac{\Gamma}{\bar{\phi}^{1/2}}\right), \tag{12}$$

for CSCL, MG, and FN,

$$\begin{gathered}\frac{2\varepsilon_0\exp\left(\frac{\bar{\phi}^{3/2}}{\beta\bar{E}}\right)t^2(y)}{0.95B_{FN}\phi_*^{1/2}\bar{\phi}^{1/2}LA_{FN}\beta\exp(\Gamma/\bar{\phi}^{1/2})}\sqrt{\frac{2ekT_*B_p}{\pi m_g\sigma_{ce}}}\sqrt{\frac{\bar{T}\bar{E}}{\bar{p}\bar{d}^2}}\frac{\left\{1-\gamma_{SE}\left[\exp\left(\bar{\alpha}\bar{d}\right)-1\right]\right\}}{\left[\exp\left(\bar{\alpha}\bar{d}\right)-1\right]}\\ = \frac{\exp(x_0)\,(1+2\bar{E}x_0)}{x_0},\end{gathered} \tag{13}$$

where $x_0 = (\sqrt{1+8\bar{E}}-1)/(4\bar{E})$ for microscale, and

$$\bar{V} = \frac{\bar{p}\bar{d}}{\ln\left(\Omega\bar{p}\bar{d}\right) - \ln[\ln(1+\gamma_{SE}^{-1})]} \tag{14}$$

for PL, where $\Omega = A_pE_*L/B_p$is a gas-dependent term.

We determined the transitions between the various emission mechanisms by equating their various asymptotic solutions. For a given gap distance and injection energy, we may numerically solve for the voltage that yields a QSCL current density equal to that from (10), representing the transition point between QSCL and CSCL. Similarly, equating (10) and (11) and solving for $\bar{V}$ as a function of either $\bar{d}$ or $\bar{\mu}$ gives the transition between CSCL and MG as $\bar{V} = \left(64\sqrt{2}\bar{d}/(162\bar{\mu})\right)^2$. An analogous procedure equating (10) to (12) and (11) to (12) yields $\bar{V}^{-1/2}\exp\left(\bar{\phi}^{3/2}\bar{d}\beta^{-1}\bar{V}^{-1}\right) = 9\beta^2\exp\left(\Gamma/\bar{\phi}^{1/2}\right)/(8\bar{\phi})$ for the transition from CSCL to FN and $\bar{V} = \bar{\phi}^{3/2}\bar{d}\beta^{-1}\left[\Gamma\bar{\phi}^{-1/2} - \ln\left(9\sqrt{2}\bar{\mu}\bar{\phi}\beta^{-2}\bar{d}^{-1}/8\right)\right]^{-1}$ for the transition from MG to FN. The intersection of the transitions from CSCL to FN and MG to FN defines a third order nexus between CSCL, MG, and FN.

Figure 1 demonstrates the transition from PL to FE-driven breakdown for microscale gaps. The exact microscale solution from (13) picks up this transition, while the analytic and limiting solutions do not since they represent the asymptotic behavior of the FE-driven breakdown and would be strictly valid only when $\bar{d}$ is much less than the transition value. The asymptotic solution also shows that $\bar{V} \propto \bar{d}$ in the FE-driven breakdown regime, as noted in previous applications of this theory to experimental behavior. Additionally, Fig. 1 shows that the transition from FE-driven breakdown to PL may occur on either the left or right of Paschen's minimum (PM) depending on $\bar{p}$. Electrode properties, particularly $\bar{\phi}$ and β, may also influence the intersection of these regimes with respect to the PM.

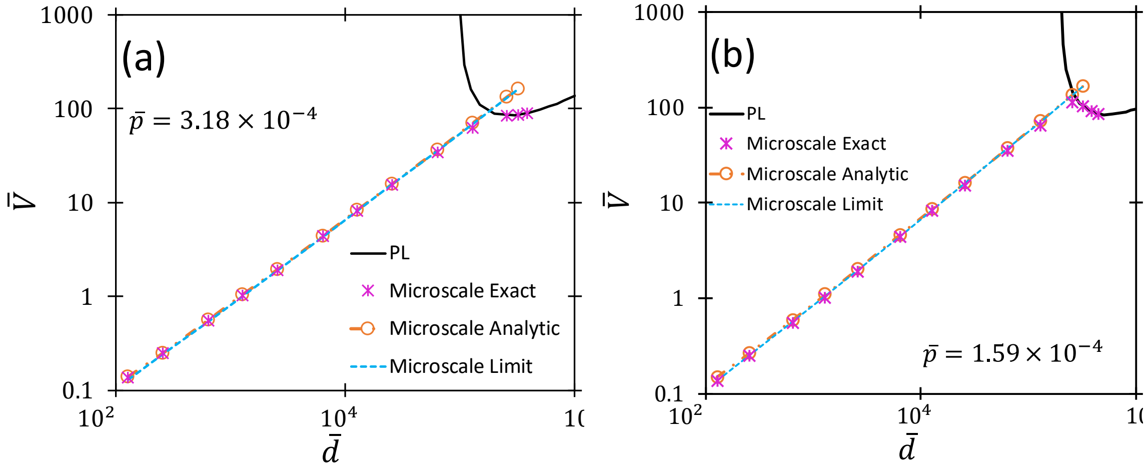

FIG. 1. Dimensionless breakdown voltage, $\bar{V}$, as a function of dimensionless gap distance, $\bar{d}$, for dimensionless pressures of (a) $\bar{p} = 3.18 \times 10^{-4}$ and (b) $\bar{p} = 1.59 \times 10^{-4}$, using the exact (13), analytic (A54), and limiting equation (A55) for microscale and PL (14) with nitrogen considering $\gamma_{SE} = 10^{-3}$. The transition from microscale breakdown to the traditional PL can occur to either the left or the right of the Paschen minimum depending on the pressure.

Further decreasing gap distance beyond the FE-driven breakdown regime leads to a purely electron emission regime characterized by FN, MG, and CSCL. Figure 2 shows the transition between these regimes at $\bar{d} = 129$ ($d = 10$ nm) for low and high $\bar{\mu}$, demonstrating the transition of the exact solution for FN at low $\bar{V}$ to the MG regime at mid-$\bar{V}$, and, finally, to CSCL at high $\bar{V}$ for a given $\bar{\mu}$ [9]. A lower $\bar{\mu}$ yields a lower $\bar{J}$ since the electrons undergo more collisions. Since $\mu \propto$

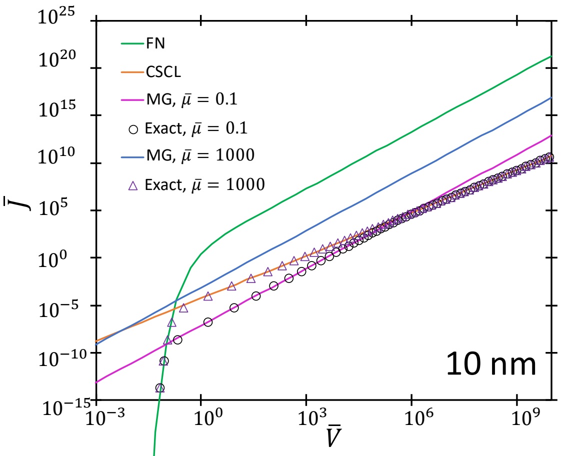

FIG. 2. Dimensionless current density $\bar{J}$ as a function of dimensionless breakdown voltage $\bar{V}$ demonstrating the transition of the exact solution between CSCL, FN, and MG, and the implications of increasing.

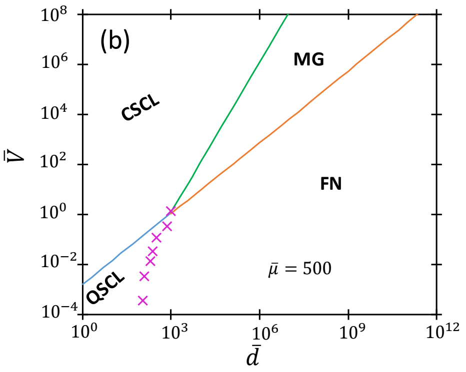

FIG. 3. Dimensionless breakdown voltage, $\bar{V}$, as a function of dimensionless gap distance, $\bar{d}$, demonstrating the regions where each emission mechanism should dominate for dimensionless mobility $\bar{\mu} = 500$.

$1/P$ (or, alternatively, mobility is inversely proportional to collisionality), this intuitively means that J will be lower for a given V at high p, yielding an MG-driven regime. Figure 5 shows that the exact solution for $\bar{\mu} = 1000$ never follows the MG equation for $\bar{\mu} = 1000$. Rather, there is a direct transition from FN to CL under these conditions. Thus, electron emission may transition to MG depending on the system pressure, or collisionality.

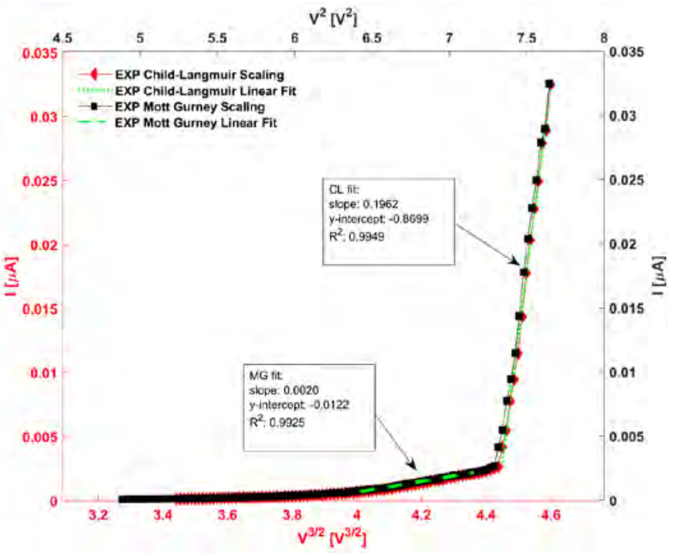

FIG. 4. Experimental measurements called to either Mott-Gurney (black square) of Child- Langmuir (red diamond) for 230 nm gap size at atmospheric pressure.

Figure 3 shows a state diagram demonstrating the transitions between the asymptotic solutions of the various emission mechanisms at $\bar{\mu}$ =500 and $\bar{d} = 129$ (d = 10 nm), where all four asymptotic solutions intersect for a fourth order nexus. The curves representing the transitions for QSCL to FN and CSCL to FN do not shift with changing $\bar{\mu}$ because they are independent of $\bar{\mu}$. At the highest $\bar{\mu}$, corresponding to the lowest pressure (closest to vacuum), the transition from QSCL to FN occurs to the left of the nexus between CSCL, MG, and FN; reducing $\bar{\mu}$ below 500 further shifts the transition from CSCL to MG to the left.

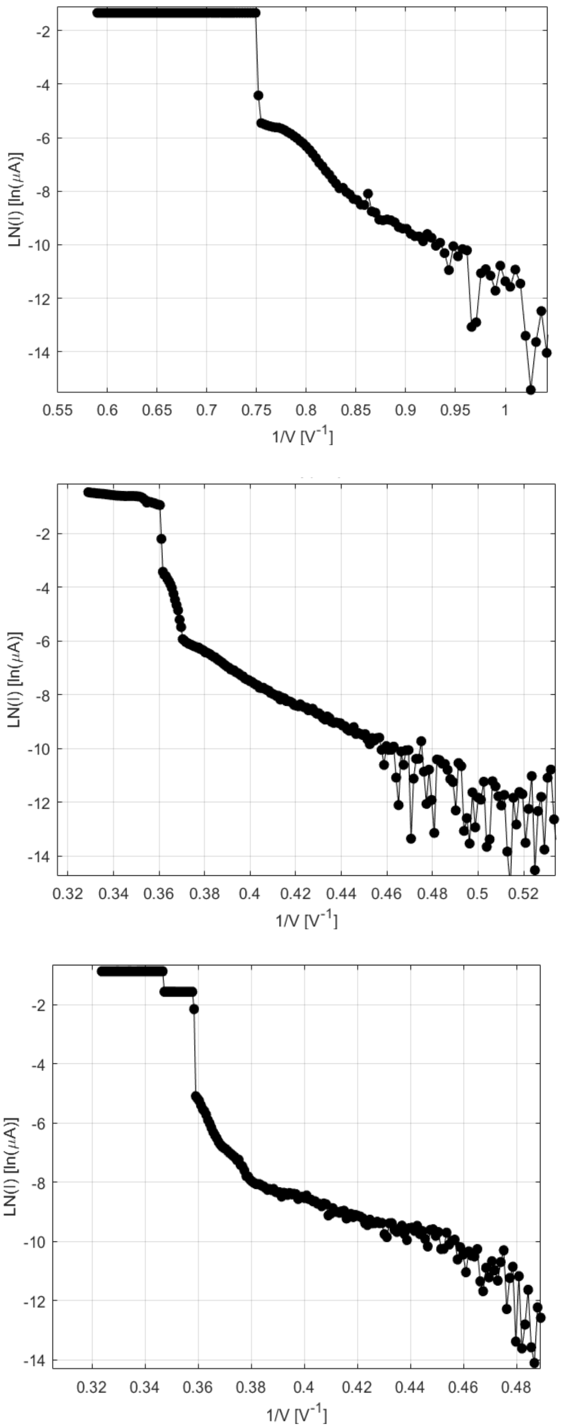

FIG. 5. Fowler-Nordheeim curves at atmospheric pressure for gaps of (top) 28 nm, (middle) 230 nm, and (bottom) 750 nm.

EXPERIMENTAL UDPATE

We have examined emission characteristics for nanoscale devices with gap sizes of 28 nm, 230 nm, and 750 nm and various aspect ratios at atmospheric pressure to examine scaling with FN, CL, and MG. Figure 4 shows the MG and CL scaling for the 230 nm case, which is the estimated gap distance for a third order nexus between MG, CL, and FN at atmospheric pressure. The sharp knee could correspond to a sudden change emission area or mechanism, although distinguishing between MG and CL scaling over this relatively small range of voltage is difficult. The region at the "knee" in Fig. 4 appears to fit with FN, further suggesting that we are near the "triple point" regime where one can easily transition between mechanisms and may lend further credence to the idea that we are dramatically changing the emission area in this regime.

Also interesting is the behavior with gap distance. As discussed in the Theory section, gas breakdown is driven by TA at classical length scales and FN at microscale. Reducing the gap distance further causes electron emission to be driven by either CL or MG, meaning that breakdown should shift. Our experimental results for FN curves in Fig. 5 demonstrate this. At 28 nm (below the electron mean free path), we note linear behavior on the FN curve, indicating FE; at higher voltages, the curve becomes nonlinear, indicating a transition to CL. This behavior is consistent with theory and experiment for vacuum. At higher voltages, the current spikes, consistent with breakdown driven by space-charge limited emission (SCLE) rather than FE. At 230 nm, near the MG/CL/FN nexus, and at 750 nm, we note a more prolonged linear regime indicative of field emission, followed by a rapid rise with increasing voltage, indicating breakdown in the FE regime. This suggests that space-charge limited emission may drive breakdown for gaps on the order of 100 nm.

3. Findings and Conclusions

These efforts have elucidated gas breakdown and electron emission at nanoscale. Our published work in 2019 showed the impact of surface roughness at atmospheric pressure and electrode properties on sub-atmospheric pressure breakdown. Since many directed energy devices are exploring nanoscale devices and vacuum may not be perfect, our results provide insight into how electron emission, including space-charge limited emission, may drive breakdown at nanoscale. Molecular dynamics simulations and experiments at intermediate pressures in 2020 will begin characterizing this regime and elucidate device design limitations.

4. Plans and Upcoming Events

Upcoming significant events:

1) Complete theory connecting quantum breakdown to Paschen's law.
2) Assess electron emission at nanoscale experimentally and using simulations.
3) Complete theoretical assessment of surface roughness on work function.

Future transitions:

1) Continue discussions with AFRL – particularly concerning sub-microscale breakdown experiments as this expands to sub-atmospheric pressure.
2) Work with NRL to transition breakdown theory (Kevin Jensen) and surface roughness effects (Ray Allen) for larger devices.
3) Continue discussions with NSWCDD (Matt McQuage and Jack Chen) concerning relevant 6.2 applications of the studied phenomena.
4) Discussions with Sandia National Laboratories about electron emission and breakdown.

5. Transitions and Impacts

None at present, although future goals for Year 3 are outlined in Section 4.

6. Collaborations

Guodong Meng, international collaborator, N/A, National Academy Member (N), China
Ágúst Valfells, international collaborator N/A, National Academy Member (N), Iceland,

7. Personnel

Principal Investigator: Allen L. Garner, 2.41 person-months, National Academy Member (N).
Teams Members:
Amanda M. Loveless, graduate student, 5.4 person-months, National Academy Member (N).
Russell S. Brayfield, graduate student, 4.5 person-months, National Academy Member (N).
Andrew J. Fairbanks, graduate student, 0.75 person-months, National Academy Member (N).
Weihang Li, undergraduate student, 0.25 person-months, National Academy Member (N).
Business Contact: Carrie Soloman
Subs: None

8. Students

Three graduate students/4 undergraduate students assisting (research for credit and pay for 4 students) during reporting period

9. Technology Transfer

None.

10. Products, Publications, Patents, License Agreements, etc.

Publications resulting from this project:

Archival Publications

1. A. M. Darr, A. M. Loveless, and A. L. Garner, "Unification of field emission and space charge limited emission with collisions," *Applied Physics Letters* **114**, 014103 (2019). Peer-reviewed, Distribution A, Federal Funding Acknowledged. https://doi.org/10.1063/1.5066236

2. G. Meng, Q. Ying, A. M. Loveless, F. Wu, K. Wang, Y. Fu, A. L. Garner, and Y. Cheng "Spatio-temporal Dynamics of Pulsed Gas Breakdown in Microgaps," *Physics of Plasmas* **26**, 014506 (2019). Peer-reviewed, Distribution A, Federal Funding Acknowledged. https://doi.org/10.1063/1.5081009

3. A. M. Loveless, G. Meng, Q. Ying, F. Wu, K. Wang, Y. Cheng, and A. L. Garner, "The Transition to Paschen's Law for Microscale Gas Breakdown at Subatmospheric Pressure," *Scientific Reports* **9**, 5669 (2019). Peer-reviewed, Distribution A, Federal Funding Acknowledged. https://doi.org/10.1038/s41598-019-42111-2

4. R. S. Brayfield, II, A. J. Fairbanks, A. M. Loveless, S. Gao, A. Dhanabal, W. Li, C. Darr, W. Wu, and A. L. Garner, "The Impact of Cathode Surface Roughness and Multiple Breakdown Events on Microscale Gas Breakdown at Atmospheric Pressure," *Journal of Applied Physics* **125**, 203302 (2019). Peer-reviewed, Distribution A, Federal Funding Acknowledged. https://doi.org/10.1063/1.5085217

5. **[Tutorial]** A. L. Garner, A. M. Loveless, J. N. Dahal, and A. Venkattraman, "A Tutorial on Theoretical and Computational Techniques for Gas Breakdown in Microscale Gaps," *IEEE Transactions on Plasma Science*, Under Preparation.

6. A. M. Loveless, A. M. Darr, and A. L. Garner, "Unification of Electron Emission and Breakdown Mechanism Theories from Quantum Scales to Paschen's Law," *Physical Review Research*, Under Preparation.

7. J. R. Malayter and A. L. Garner, "Theoretical Assessment of Surface Waviness on Work Function," *Journal of Chemical Physics*, Under Preparation.

Mini-courses and Special Presentations:

1. A. L. Garner, "Microscale to Nanoscale Gas Breakdown: From Paschen's Law to Schrödinger's Equation," Mini-course on Theoretical and Computational Methods in Plasma Physics, 2019 Pulsed Power and Plasma Science Conference, Orlando, FL, 23 June 2019.

Conference Papers

1. A. L. Garner, A. M. Loveless, R. S. Brayfield II, A. M. Darr, J. R. Malayter, and G. Meng, "Gas Breakdown and Electron Emission for Microscale Gaps: Unified Theory and Nanofeature Effects," Joint Meeting of the 32nd International Vacuum Nanoelectronics Conference (IVNC) and 12th International Vacuum Electron Sources Conference (IVESC), Cincinnati, OH, 13.1, 25 July 2019.

2. A. M. Loveless, A. M. Darr, R. S. Brayfield II, J. R. Malayter, S. A. Lang, and A. L. Garner, "The Implications of Nanoscale Features for Microscale and Smaller Gaps on Electron Emission," Joint Meeting of the 32nd International Vacuum Nanoelectronics Conference (IVNC) and 12th International Vacuum Electron Sources Conference (IVESC), Cincinnati, OH, 18.1, 24 July 2019.

3. A. M. Loveless, A. M. Darr, R. S. Brayfield II, J. R. Malayter, S. A. Lang, and A. L. Garner, "Nanoscale Feature Implications on Electron Emission and Gas Breakdown," Trans. Am. Nucl. Soc., submitted.

Invited Oral Presentations

1. A. L. Garner, A. M. Loveless, R. S. Brayfield II, A. M. Darr, J. R. Malayter, and G. Meng, "Gas Breakdown and Electron Emission for Microscale Gaps: Unified Theory and Nanofeature Effects," Joint Meeting of the 32nd International Vacuum Nanoelectronics Conference (IVNC) and 12th International Vacuum Electron Sources Conference (IVESC), Cincinnati, OH, 13.1, 25 July 2019.

Conference Oral Presentations

1. A. Darr and A. Garner, "A Coordinate Invariant Theory for Space Charge Limited Emission using Variational Calculus," IEEE Pulsed Power and Plasma Science Conference, 10A5, 28 June 2019.

2. G. Meng, Q. Ying, A. Loveless, F. Wu, K. Wang, Y. Fu, A. Garner, and Y. Cheng, "Spatio-temporal Dynamics of Pulsed Gas Breakdown in Microgaps," IEEE Pulsed Power and Plasma Science Conference, 10C2, 28 June 2019.

3. A. Darr, A. Loveless, and A. Garner, "Incorporating Resistance into the Unification of Field Emission and Space Charge-Limited Emission with Collisions," IEEE Pulsed Power and Plasma Science Conference, 7A3, 27 June 2019.

4. R. Brayfield, A. Fairbanks, A. Loveless, S. Gao, C. Darr, J. Malayter, W. Wu, and A. Garner, "Microscale Gas Breakdown Voltage Dependence on Electrode Surface," IEEE Pulsed Power and Plasma Science Conference, 3F3, 25 June 2019.

5. A. Loveless, A. Darr, and A. Garner, "Electron Emission and Gas Breakdown: Unification of Theory from Schrodinger's Equation to Paschen's Law," IEEE Pulsed Power and Plasma Science Conference, 3F2, 25 June 2019.

6. R. S. Brayfield, II, A. J. Fairbanks, A. M. Loveless, S. Gao, W. Li, C. Darr, J. R. Malayter, W. Wu, and A. L. Garner, "Experimental assessment of electrode effects on gas breakdown for microscale gaps," 21st Annual Directed Energy Science & Technology Symposium, Student Workshop II, 10 April 2019, Destin, FL, USA.

7. A. M. Loveless, A. M. Darr, S. Dynako, and A. L. Garner, “Transition of Electron Emission and Gas Breakdown Mechanisms from Microscale to Nanoscale,” 21st Annual Directed Energy Science & Technology Symposium, Student Workshop I, 09 April 2019, Destin, FL, USA.

8. A. Loveless, A. Darr, S. Dynako, and A. Garner, “Unification of Gas Breakdown and Electron Emission,” American Physical Society March Meeting 2019, Bull. Am. Phys. Soc., Vol. 64, R18.00004 (2019).

9. A. Loveless and A. Garner, “Electron Emission and Gas Breakdown from Schrödinger’s Equation to Paschen’s Law,” American Physical Society Division of Plasma Physics, Vol. 63, NO8.00002 (2018).

Conference Poster Presentations

1. A. M. Loveless, A. M. Darr, R. S. Brayfield II, J. R. Malayter, S. A. Lang, and A. L. Garner, “The Implications of Nanoscale Features for Microscale and Smaller Gaps on Electron Emission,” Joint Meeting of the 32nd International Vacuum Nanoelectronics Conference (IVNC) and 12th International Vacuum Electron Sources Conference (IVESC), Cincinnati, OH, 18.1, 24 July 2019.

2. R. Brayfield, A. Fairbanks, A. Loveless, W. Li, C. Darr, and A. Garner, “Submicroscale Gas Breakdown as a Function of Cathode Protrusion,” IEEE Pulsed Power and Plasma Science Conference, 1P21, 24 June 2019, Orlando, FL USA.

3. A. Loveless, K. Torfason, A. Valfells, and A. Garner, “Investigation of Electron Emission using Molecular Dynamics Simulations,” IEEE Pulsed Power and Plasma Science Conference, 1P05, 24 June 2019, Orlando, FL, USA.

4. J. Malayter, R. Brayfield, A. Loveless, and A. Garner, “Implications of surface roughness on microscale gas breakdown theory,” IEEE Pulsed Power and Plasma Science Conference, 1P02, 24 June 2019, Orlando, FL, USA.

Invited Colloquia and Seminars

1. A. L. Garner, “Unified Electron Emission Theory and Experimental Validation,” Department of Electrical and Computer Engineering, University of New Mexico, Albuquerque, NM, 06 December 2019.

2. A. L. Garner, “Theoretical and Experimental Unification of Electron Emission Mechanisms,” Department of Electrical and Computer Engineering, Boise State University, Boise, ID, 04 December 2019.

3. A. L. Garner, “Electron Emission and Gas Breakdown from Quantum to Classical Lengths,” Plasma Seminar Series, University of Washington, Seattle, WA, 02 December 2019.

4. A. L. Garner, “Progress Toward a Universal, Unified Electron Emission Theory,” Air Force Research Laboratory, Air Force Research Laboratory, Albuquerque, NM, 11 July 2019.

5. A. L. Garner, “Unification of Electron Emission and Gas Breakdown Mechanisms: Experiment and Theory,” Sandia National Laboratories, Albuquerque, NM, 10 July 2019.

11. Point of Contact in Navy

Kevin Jensen, NRL, 01AUG2019; Joe Schumer, NRL, 28JUN2019; Tom Mehlhorn, NRL, 28JUN2019; Jack Chen, NSWCDD, 28JUN2019; Wilkin Tang, AFRL, 11JUL2019; Don Schiffler, AFRL, 11JUL2019; Alex Sheets, AFRL, 26SEP2019; John Harris, AFRL, 28JUL19.

12. Acknowledgement/Disclaimer

This work was sponsored by the Office of Naval Research (ONR), under grant number [N000014-17-1-2702]. The views and conclusions contained herein are those of the authors only and should not be interpreted as representing those of ONR, the U.S. Navy or the U.S. Government.

Compact High-Power Microwave Oscillators

Grant No. N62909-18-1-2122– GRANT12538355, N00014-18-S-B001

Period of Performance: Oct 1, 2018 to September 30, 2019

Prepared by:

Dr. Alan Phelps, Principal Investigator
Physics Department
University of Strathclyde
John Anderson Building
107 Rottenrow East
Glasgow, Scotland, UK G4 0NG
Tel: +44 141 548 3166
Email: a.d.r.phelps@strath.ac.uk

This work was sponsored by the Office of Naval Research (ONR), under grant number N00014 -17-1-2848. The views and conclusions contained herein are those of the authors only and should not be interpreted as representing those of ONR, the U.S. Navy or the U.S. Government.

Grant or Contract Number: N62909-18-1-2122– GRANT12538355, N00014-18-S-B001
Date Prepared: 30th December 2019
Project Title: Compact high-power microwave oscillators
Annual Summary Report: ONR HPM 2019 Program – End of Year report
Principal Investigator: Alan Phelps, +44141 548 3166, a.d.r.phelps@strath.ac.uk
University of Strathclyde, Scotland, UK

Section I: Project Summary

1. Overview of Project

1.1 Abstract:

Researchers in the ABP Group, at The University of Strathclyde, Scotland, UK, have been tasked with development of a proof-of-concept high-power microwave source, operating in the X-band ($8-12GHz$), that does not require an externally applied magnetic field. This mitigates the energy overhead associated with operation of a (typically high-field) solenoid, resulting in a source where the electronic energy extraction efficiency and the overall device efficiency are similar.

Nominally a variant of the relativistic Backward-Wave Oscillator, the source performance is in the high-power microwave tube regime, with predicted output powers of $\sim 300MW$ from a $500kV, 2kA$ electron beam, corresponding to a conversion efficiency of $\sim 30\%$. The resonant frequency is insensitive to variation in the beam energy, remaining at $\sim 9.4GHz$ over an extended range of the examined beam parameter space.

1.2 Objective:

Develop an experimental prototype of a high-power ($\gtrsim$ 100MW), frequency stable, Self-Insulating Backward-Wave Oscillator, (SIBWO), focused on simulations and numerical design in Project Year 1 and progressing to manufacture and an initial experimental test by the end of Project Year 2. In Project Year 3 the main objective is the experimental characterization of the new source and comparison of the experimental results with the numerical simulations (each Project Year runs from 15 June to 14 June).

1.3 Introduction:

Since 15 June 2018 The University of Strathclyde (UoS) has been engaged in the development of a novel microwave source nominally a self-insulating variant of the Backward-Wave Oscillator [1-2]. Termed the SIBWO, the source aims to improve the practicality of the relativistic BWO by removing the requirement for a guiding solenoidal magnetic field; thereby significantly reducing the footprint, including the volume, weight, energy and systems complexity requirements of the device as a whole. The work presented here reports the highlights of research over the reporting year, October 2018 to September 2019, which includes portions of both Project Year 1 and Project Year 2.

1.4 List of abbreviations / terms:

2.5D modeling	2-dimensional numerical representation of the electromagnetic field profile, with particle trajectories / momentum vectors calculated in 3-dimensions.
3D modeling	Numerical representation of both EM-fields and particles in 3-dimensions
AK-gap	Anode-cathode gap
BWO	Backward-Wave Oscillator
Cold / hot measurement	Experimental measurement of performance with (hot) and without (cold) the presence of an electron beam.
CST Studio Suite	A suite of numerical codes used to model EM fields in isolation (CST: Microwave Studio, CST: MWS) or in concert with energetic particles (CST: Particle Studio, CST:PS).
EM	Electromagnetic field / wave /spectrum
HE_{11}	Eigenmode resulting from coupling of the TE_{11} and TM_{11} modes within the vicinity of the SWS. The, now present, E_z field component allows for effective modulation-of / coupling-with the electron beam.
Hot-test	Testing of a microwave device, as a whole, using an electron beam as the energy source for generating / amplifying the EM wave.
KARAT	PiC code used to predict the time-dependent evolution of the interaction between charged particles and EM fields.
PiC	Particle in Cell: a numerical code that considers both the electromagnetic fields and discrete particles within the "cells" used to define the simulation volume.
PPS	Pulsed Power Supply: 1.5MV capable, 25kA, 200 – 250ns single-shot pulsed power supply based in the ABP laboratory at the UoS.
SIBWO	Self-Insulating Backward Wave Oscillator
SWS	Slow-Wave Structure: refers to the corrugation of the SIBWO interaction region.
TE_{mn}	Transverse-Electric mode: a supported EM field pattern that has no longitudinal E-field component. The designations "m" and "n" refer to the number of full wave variations seen azimuthally and half wave variations seen radially (respectively) in the pattern.
TM_{mn}	Transverse-Magnetic mode: a supported EM field pattern that has no longitudinal H-field component. The "m" and "n" designations share definitions with those of the TE modes.
UoS	University of Strathclyde.
VNA	Vector network Analyser
X-band	A region of the electromagnetic spectrum between 8 – 12GHz.

1.5 Figure list:

1.6 Background:

Since previous reporting [1-2] the UoS has continued its numerical and experimental work program into the development of the X-band $(8-12GHz)$ SIBWO.

1.6.1 Numerical work

The numerical study presented in [1] was undertaken using the 2.5D Particle-in-Cell (PiC) code KARAT [3]. For more complete modeling of the beam-wave interaction, the UoS progressed to full 3D PiC calculation, using CST: Studio Suite [4] The work presented here reports on the current progress of the 3D model, specifically relating to the tolerance of the source to variation in the input electron beam parameters, both in terms of output power and overall efficiency.

1.6.2 Experimental work

The experimental program focused on preparation of the laboratory space for initial hot testing of the SIBWO by the end of Project Year 2. This involved commissioning of the pulsed power supply (PPS), design and test-construction of the required X-ray shielding arrangement and some cold-testing (microwave signal only) of an initial interaction region test-piece.

2. Activities and Accomplishments

2.1 Numerical investigation of the SIBWO

As reported in [2] operation of the SIBWO, in the TM_{01} mode was recovered via adjustment of both the interaction region geometry and the electron beam parameters, resulting in a saturated output power of $\sim 200MW$ at $\sim 9.6GHz$, when driven by a $500keV(\pm 10\%), 2kA$ electron beam. The corresponding conversion efficiency was therefore $\sim 20\%$.

This was improved through the introduction of an additional resonant structure within the SWS, as shown in Figure 2-1. Analysis of the impact of this resonator (hereafter called the modulator), on SIBWO operation, shows that it has two important effects:

- It provides a degree of additional feedback in the SWS section preceding the “modulator”, enhancing the initial modulation of the electrons and setting the resonant frequency
- It allows for potential phase-adjustment of the electron beam, relative to the EM wave, enhancing the energy extraction in the SWS following the modulator.

The extent of the influence of the latter point, on the operation of the SIBWO, decreases as the modulator is moved towards the end of the SWS – as one would expect – while the exact resonant frequency enhanced in the former point was found to be a function of position as well as radius and axial width; the resonance was found to be higher when placed at minima, lower at the maxima, with a general trend for the frequency to decrease as the modulator position moved towards the exit of the SWS. Optimizing for a given resonant frequency therefore involves adjustment of not just the initial cavity resonator length and SWS parameters, but also the location and geometry of the modulator, greatly increasing the operational parameter space.

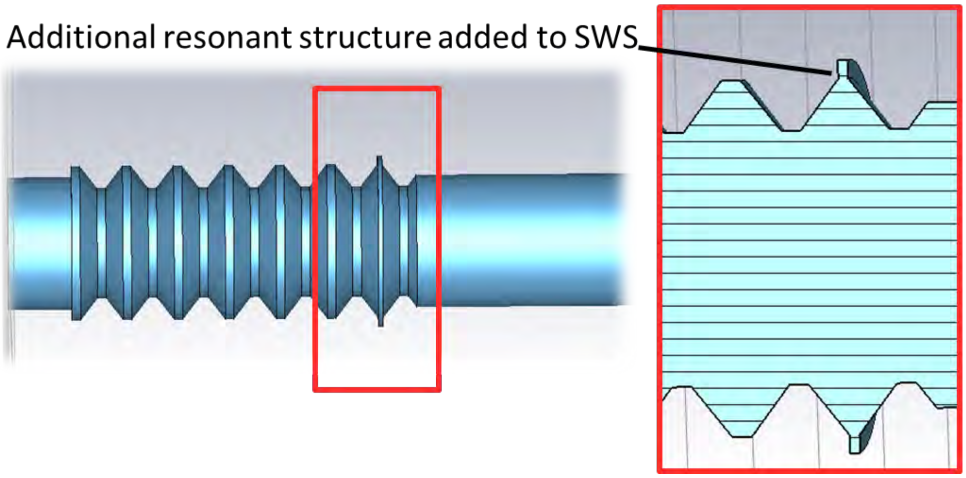

Figure 2-18. Shows the geometry of the Enhanced SIBWO indicating the location of the additional resonator in the SWS.

As reported in [2] the predicted output power was $\sim 300MW$ ($\sim 30\%$ efficiency) at a resonant frequency of $\sim 9.4GHz$, again using a $500keV(\pm 10\%), 2kA$ electron beam. The geometric parameters used were:

r_0/mm	d_z/mm	r_1/mm	z_{cav}/mm	No. periods	r_{cav} $/mm$	z_{cav} $/mm$	Cavity location (1/2 period)
18	14	3	17.5	7	23.2	1.2	12

Where r_{cav} is the radius of the additional resonator, z_{cav} is its axial length and the cavity location relates to the number of $1/2$ periods along the SWS before reaching the modulator ('even' being peaks and 'odd' being troughs).

A study of the tolerance of the interaction to variation in the beam parameters indicated, over the range of values expected in the experiment, the output power did not drop below 250MW (25% efficient), with the resonant frequency remaining unchanged. The output power envelopes from this study can be seen in Figure 2-2, while the associated spectral contents are shown in Figure 2-3.

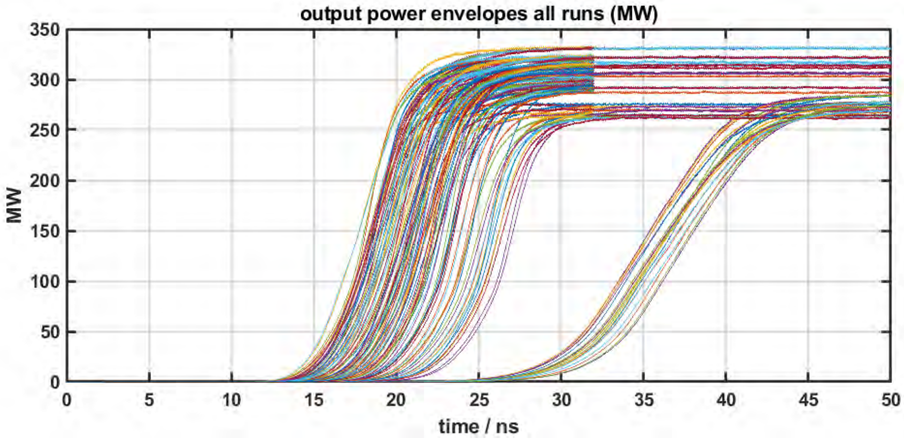

Figure 2-19. Shows the output power envelopes for each run in the beam tolerance study. The beam parameters were varied over 500keV(+/- 5%, 10%), 1.8-2.2kA, angular spread 1-2%, beam "fill-factor" 80-100% of drift-tube radius.

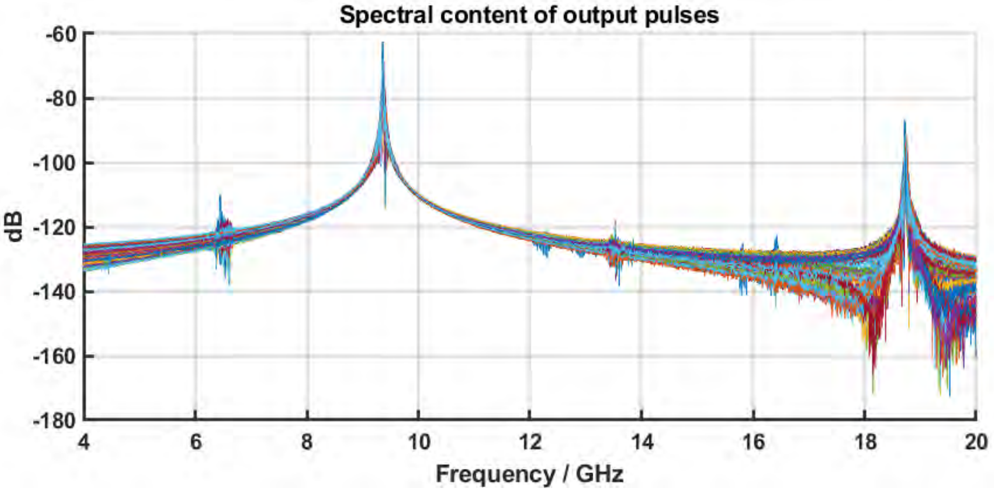

Figure 2-20. Shows the spectral content associated with the power envelopes shown in Figure 2-2.

This shows that the enhanced SIBWO is relatively insensitive to variation in the beam parameters, indicating it should function well in experiment, provided the experimental beam lies within the bounds of the parameter space indicated in Figure 2-2.

The design of the required electron accelerator is on-going, however, through the collaborative efforts of the UoS and NRL it appears feasible that a practical gun can be manufactured, of similar design to that presented in [2], that would provide a sufficiently good quality beam for an initial prototype experimental study to commence before the end of Project Year 2.

2.2 Experimental investigation

Since reporting in [2] the UoS has manufactured a test-piece of the SIBWO interaction region and completed cold-measurement of its performance for comparison with numerical prediction. Measurements were taken using a Vector Network Analyzer (VNA) (see Figure 2-4), calibrated over the range $8-12GHz$ and launching / receiving in the TE_{10} rectangular waveguide mode. It was therefore necessary to convert this to the TM_{01} cylindrical waveguide mode prior to propagation through the interaction region, then convert back to the TE_{10} rectangular waveguide mode for measurement. This required the use of serpentine mode converters [5], which have an operational bandwidth of $9-10GHz$, constraining the meaningful measurement to this range, as indicated in Figure 2-5. This was not deemed an issue as the expected operating frequency for the manufactured SIBWO interaction region is $\sim 9.4GHz$.

Accepting the constraint placed on the measurement by the bandwidth of the serpentine converters, excellent agreement was obtained between the CST MWS prediction of performance and that measured by the VNA. This gives confidence both in the numerical predictions from CST Studio, for the modeling, and in the techniques used to manufacture the interaction region for hot testing. A “hot-test” version of the interaction region was being manufactured at the time of writing.

Construction of components for the electron accelerator is expected in the near future, with characterization of the performance occurring soon after. We intend to progress to full hot testing in-line with the project schedule for the end of Project Year 2 in June 2020.

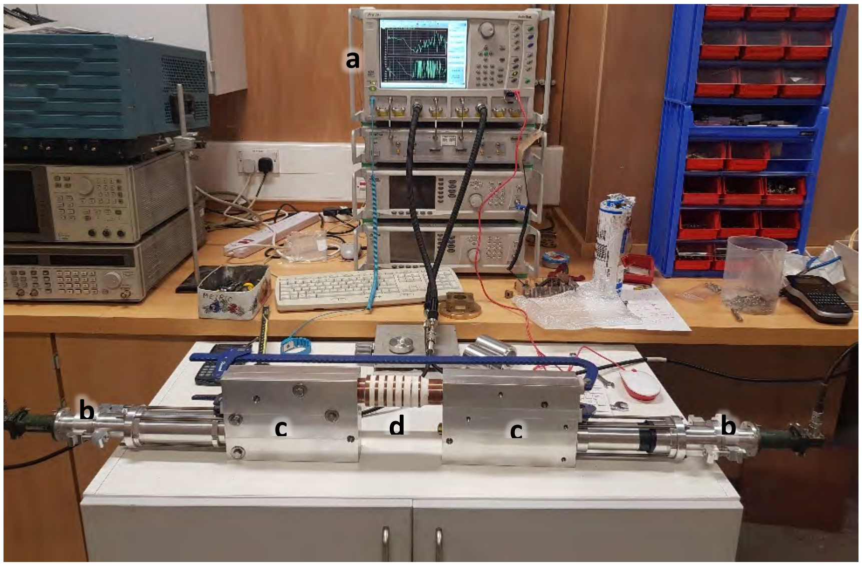

Figure 2-21. Shows the experimental setup for measurement of the cold-performance of the SIBWO interaction region. Components are: (a) Vector Network Analyzer, (b)TE_{01}-TE_{11} mode converter, (c) TE_{11}-TM_{01} Serpentine mode converter, (d) SIBWO.

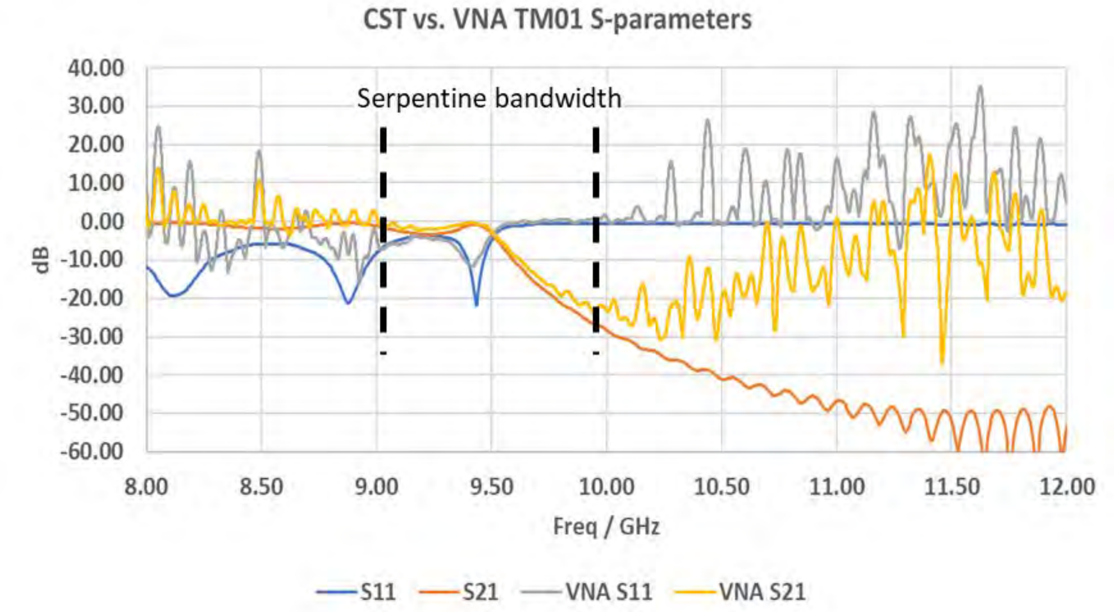

Figure 2-22. Shows a comparison of the predicted and measured S-parameters for the SIBWO interaction region, noting the meaningful result is contained within the bandwidth of the Serpentine mode converters.

2.3 References

1. Phelps A.D.R, Compact High-Power Microwave Oscillators, *ONR HPM 2018 Program, End of Year Report*, November 2018.
2. Phelps A.D.R., Compact High-Power Microwave Oscillators, *ONR HPM 2018 Program, End of 1st Project Year Report*, July 2019.
3. Tarakanov V.P., *User's Manual for Code KARAT,* Distributed by Berkeley Research Associates Inc., Springfield, VA.
4. Dassault Systemes, CST Studio Suite User Manual.
5. Lee B.M., et al., 2004, *Electronics Letters,* 40 (18), pp.1126 – 1127.

3. Findings and Conclusions

The numerical study has produced an enhanced geometry for the SIBWO that shows $\sim 300MW$ of output power at $\sim 9.4GHz$, corresponding to a conversion efficiency of $\sim 30\%$, when driven by a $500keV, 2kA$ electron beam. The enhanced SIBWO is relatively intolerant to variation in the beam quality, showing a worst-case output power of $\sim 250MW$ ($\sim 25\%$ efficient), with no shift in resonant frequency, or increased risk of exciting competing modes.

Experimental work is underway, with initial cold-measurement of an interaction region test-piece showing excellent agreement with numerical predicted performance. Preparation of the laboratory space is underway to facilitate initial hot testing of the prototype source.

4. Plans and Upcoming Events

The "hot-test" version of the SIBWO SWS is expected to be ready for cold testing by the beginning of 2020, and is "on course" for hot testing later in the year. The electron accelerator design is expected to be completed by the beginning of 2020, with manufacture to be completed in the first quarter of 2020. Similarly, all required ancillary components are expected to be manufactured and assembled on schedule for commencement of initial hot testing by mid-June 2020 i.e. by the end of Project Year 2.

5. Transitions and Impacts

Not yet applicable at this stage

6. Collaborations

Collaboration with Dr. Simon Cooke and Dr. Igor Chernyavskiy at NRL in modeling and design of the electron accelerator.

7. Personnel

Principal investigator: Prof. Alan D. R. Phelps
Person months worked: 4
National Academy Member: Yes
Nationality: UK

Co-investigator and Co-PI: Dr. Kevin Ronald
Person months worked: 4
National Academy Member: Yes
Nationality: UK

Co-investigator: Dr. Philip MacInnes
Person months worked: 12
National Academy Member: No
Nationality: UK

Business Contact: Mrs. Alison McFarlane, RKES, University of Strathclyde, Glasgow, UK

8. Students

No students engaged with this project at this stage

9. Technology Transfer

We have undertaken collaborative discussions with Dr. Simon Cooke and Dr. Igor Chernyavskiy, NRL, regarding the design of the required electron accelerator.

10. Products, Publications, Patents, License Agreements, etc.

Publications resulting from this project: 1

Conference Paper:

a. Enhanced operation from a self-insulating X-band Backward-Wave Oscillator
b. P. MacInnes, S.J. Cooke, I.A. Chernyavskiy, K. Ronald, A.D.R. Phelps
c. UK/US Directed Energy Workshop (DEPS) 2019
d. 22 – 26 July 2019
e. Swindon, England, UK

11. Point of Contact in Navy

Ryan Hoffman ONR

Tim Andreadis NRL

Dave Abe NRL

Jesus GilGil NRL

Simon Cooke NRL

Igor Chernyavskiy NRL

Matthew McQuage NSWC

Isaac Bankman ONRG (up to Sept 2018)

Predrag Milojkovic ONRG (from Oct 2018)

12. Acknowledgement/Disclaimer

This work was sponsored by the Office of Naval Research (ONR), under grant number N62909-18-1-2122. The views and conclusions contained herein are those of the authors only and should not be interpreted as representing those of ONR, the U.S. Navy or the U.S. Government.

High-Power Microwave Generation by Compact Linear Transformer Driver Technology

Grant No. N00014-18-1-2499

Annual Report for Fiscal Year 2019

Period of Performance: October, 1, 2018 to September 30, 2019

Prepared by:

Professor Ryan McBride, Principal Investigator
University of Michigan
Department of Nuclear Engineering and Radiological Sciences
2355 Bonisteel Blvd
1906 Cooley Building
Ann Arbor, MI 48109-2104
Tel: (734) 763-7504
Email: mcbride@umich.edu

DEPARTMENT OF THE NAVY · UNITED STATES MARINE CORPS

This work was sponsored by the Office of Naval Research (ONR), under grant number N00014 - 17-1-2848. The views and conclusions contained herein are those of the authors only and should not be interpreted as representing those of ONR, the U.S. Navy or the U.S. Government.

Grant or Contract Number: N00014-18-1-2499
Date Prepared: January 31, 2020
Project Title: High-Power Microwave Generation by Compact Linear Transformer Driver Technology
Annual Summary Report: CY2019
Principle Investigator: Ryan McBride, 734-763-7504, mcbrider@umich.edu
University of Michigan, Department of Nuclear Engineering and Radiological Sciences

Section I: Project Summary

1. Overview of Project

Abstract: The efficient generation of high-power microwaves (HPM) from compact generating equipment is of critical importance to the United States Navy and Department of Defense (DoD). Applications include: radar, signal jamming, electronic warfare, counter IED (improvised explosive device), and vehicle stoppers. Example systems where HPM is critical include the Patriot Missile and the Aegis Combat/Weapon System. This project is exploring the use of compact linear transformer driver (LTD) technology to drive various gigawatt-class, narrow-band (~1 GHz), high-power microwave (HPM) sources, such as the magnetically insulated line oscillator (MILO). LTDs are low-voltage, low-impedance drivers. An LTD-driven HPM source could become one of the most compact, low-voltage, GW-class HPM sources available for ONR/DoD directed energy programs. To obtain this performance, a rich assortment of physics issues will be studied. For example, as we increase the driver power, electrode plasmas (particularly from contaminants adsorbed onto electrode surfaces) can become problematic. If plasmas form in the anode-cathode gap with densities >1e10 electrons/cc, then L-band microwaves (1 GHz) can become attenuated significantly. We will study these low-density plasmas by combining particle-in-cell simulations with experimental measurements from a vast array of diagnostics, including energetic particle detectors, Zeeman and Stark spectroscopy, self-emission imaging, and laser-based probing and imaging techniques. The use of LTD technology to drive an HPM source is advantageous for several reasons: First, the driver impedance and driver voltage is tunable, because LTD systems are modular. The PI's team is assembling a 4-cavity LTD facility called BLUE (Bestowed LTD from the Ursa-minor Experiment) at the University of Michigan (UM). The driver impedance of BLUE can be varied from 1 to 30 ohms. Second, the pulsed-power components in LTDs are completely encased in metal, thus minimizing stray high-voltage fields and electrical interference. Third, LTDs can be rep-rated up to (and possibly beyond) 0.1 Hz, thus increasing the average power. Additionally, rep-rating has the potential benefits of electrode conditioning and decontamination, therefore allowing us to emulate standard industry practices in the fabrication of commercial microwave tubes. The effects of various rep-rates will be tested directly. This document describes the progress to date on this project, which includes the status of the BLUE facility, the status of a MILO recently acquired for this project, and simulations of this MILO driven by an input power pulse similar to what BLUE will provide. This document also describes the research products produced by this effort, including publications and presentations.

Objective: To explore the use of linear transformer driver (LTD) technology for driving high-power microwave (HPM) sources, including GW-class magnetically insulated line oscillators (MILOs) and potentially other crossed-field devices.

Introduction: This project will study GW-class, narrow-band HPM devices, operating at a frequency ~1 GHz. Such devices are driven by pulsed power technology. Pulsed power involves the use of high-voltage capacitors and fast switching techniques to store electrical energy over long time scales and discharge the energy over fast time scales; because power is the rate at which energy is delivered, the fast discharge time leads to power amplification. Often the peak powers obtainable in HPM can be quite large (~GW), but this usually comes at the expense of high average powers. This project will explore the use of LTD technology (an exciting new compact and efficient pulsed power technology) to drive various HPM sources. An important attribute of LTD technology is that it has the potential to be rep-rated up to (and possibly beyond) 0.1~Hz.

In narrow-band HPM, the pulsed-power driver is used to apply a large, fast-rising voltage pulse across a vacuum-filled anode-cathode gap (A-K gap). This A-K gap then serves as the load for the pulsed-power driver, sometimes being referred to as a "diode" load. The large applied voltage (and its associated electric field) can cause electrons to be emitted from the cathode surface; this is especially true if the cathode is treated in a way that favors emission of electrons (e.g., velvet covered cathodes). If the voltage applied across the A-K gap is an appreciable fraction of the electron's rest mass energy (511 keV), then the predominantly vacuum-filled region within the A-K gap can become populated with relativistic electrons. Longer timescale electromagnetic fields [~DC fields relative to the faster radio frequency (RF) timescales of interest] can then be applied to direct these electrons into a well-formed electron beam. The electron beam can then be modulated to amplify and/or excite RF electromagnetic waves.

In crossed-field devices (CFDs) – such as relativistic magnetrons and crossed-field amplifiers – an approximately DC electric field **E** and an approximately DC magnetic field **B** are applied at right angles to one another, so that the well-known $\mathbf{E}\times\mathbf{B}$ drift velocity ($\mathbf{v} = \mathbf{E}\times\mathbf{B}/B^2$, where B is the scalar magnitude of the magnetic field) can be used to drive and steer the electron beam. To get the beam to interact with an RF field, the beam is driven in close proximity to a slow-wave structure (i.e., an anode structure with periodically spaced metal vanes). A synchronized, modulating interaction between the beam and the RF wave can then be obtained if the magnitude of the drift velocity $v=E/B$ is well matched to the phase velocity of the RF wave propagating in the slow-wave structure. A bunching instability, called the phase-focusing mechanism, causes the beam to become modulated, enhancing the RF output.

To drive the electron beams, this project will use a pulsed-power technology called linear transformer drivers (LTDs). The LTD concept was pioneered in 1995-1997 at the High Current Electronics Institute (HCEI), in Tomsk, Russia, by Kovalchuk, Vizir, Kim, and colleagues. Since then, the LTD concept has been advanced further by HCEI as well as researchers at Sandia National Laboratories and many others worldwide. LTDs have been called the greatest advance in prime-power generation since the invention of the Marx generator in 1924.

In the late 2000's, a collaboration was developed between HCEI, Sandia National Laboratories, and the University of Michigan (UM) to bring LTD technology to the United States. In 2006--2007, five 3-m-diameter, 1-MA, 100-ns LTD cavities were tested at HCEI with resistive and electron-beam diode loads. In July of 2007, one of these HCEI cavities was shipped to UM, becoming the MAIZE facility and the first 1-MA, 100-ns LTD in the United States. In 2008, ten more 1-MA, 100-ns LTDs cavities were shipped to Sandia, becoming part of the Mykonos facility. Additionally, smaller (1.25 m in diameter), lower-current cavities were shipped to Sandia, becoming the Ursa

Minor facility. The Ursa Minor facility stacked 21 of these 1.25-m-diameter cavities together to obtain a high-impedance driver for high-energy x-ray source development. https://www.sandia.gov/Pulsed-Power/research_facilities/Ursa_Minor.html

Four of the Ursa Minor cavities were recently shipped to UM, where we are now assembling them into the BLUE facility (Bestowed LTD from the Ursa-minor Experiment) to drive HPM sources for this project (see Figure 1).

Figure 23. The BLUE pulsed power facility being received at the University of Michigan. These four LTD cavities were previously part of the 21-cavity Ursa Minor facility at Sandia National Laboratories. This technology transfer is part of Sandia's Stevenson-Wydler Gift Program. [Pictured from left to right: Prof. Ryan McBride (PI), Dr. Nick Jordan (lab manager, research scientist, and Co-I), Steven Exelby (HPM PhD graduate of Prof. Gilgenbach), and Mark Perreault (senior lab technician and safety coordinator).

Background: Over the past three decades, the University of Michigan (UM) has developed an expertise in both experimental and theoretical investigations of HPM devices under the supervision of Professors Ron Gilgenbach and Y. Y. Lau. Most of the experiments have been carried out on the Michigan Electron Long-Beam Accelerator (MELBA), which is a Marx-generator-based pulsed-power machine at UM. Some of the experimental CFDs studied recently with MELBA include the recirculating planar magnetron (RPM), the multi-frequency recirculating planar magnetron (MFRPM), and the recirculating planar crossed-field amplifier (RPCFA), all of which have been met with success.

This new project, using LTDs to drive HPM sources, is both basic and applied research, involving HPM design and optimization with particle-in-cell (PIC) simulations and experimental optimization of driver impedance using the 4-cavity BLUE LTD facility. BLUE will provide a variable drive voltage of 50–800 kV and a variable drive impedance of 1–30 Ω. Our approach will also involve the study of electrode plasmas (particularly from contaminants adsorbed onto electrode surfaces), which can become problematic. If plasmas form in the anode-cathode gap with densities $>10^{10}$ electrons/cc, then L-band microwaves (1 GHz) can become attenuated significantly. We will study these low-density power flow plasmas by combining particle-in-cell simulations with experimental measurements from a vast array of diagnostics, including energetic particle detectors, Zeeman and Stark spectroscopy, self-emission imaging, and laser-based probing and imaging techniques.

2. Activities and Accomplishments

The first BLUE cavity is now operational (see Figures 2 and 3). We were fortunate to recruit a talented PhD student to work on this project, Brendan Sporer. In a very short period of time, Brendan (working with guidance from Co-I Nick Jordan and PI Ryan McBride) has taken BLUE from assorted parts in crates and boxes to a working pulsed power facility, complete with:

- A newly designed and fabricated Arduino-based control system and panel (see Fig. 3)
- Two newly procured high-voltage power supplies (+/-) capable of supporting rep-rated operation at 1.5 Hz on BLUE (see Fig. 3)
- Two newly procured vacuum chambers (one with multiple diagnostic ports)
- A newly procured scroll pump for rough vacuum and a turbo pump for high vacuum.
- A newly constructed trigger generator (see Fig. 4)
- A newly constructed high-power relay circuit (see Fig. 4)
- A newly constructed 3-brick testing system
- Newly fabricated charging resistors and trigger inductors
- A newly procured 3D printer
- Novel 3D-printed electrical feedthroughs
- A newly fabricated resistive load for testing
- A newly procured and mounted current viewing resistor (CVR) for current monitoring and calibration testing
- A fiber-optic-based switch monitoring diagnostic based on our recent journal publication in *Review of Scientific Instruments*: https://doi.org/10.1063/1.5113866
- A newly developed LTspice circuit model

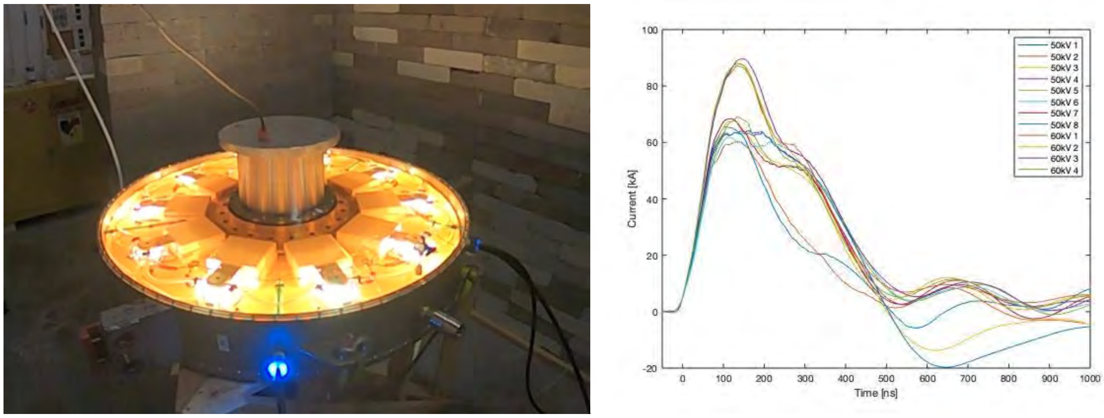

Figure 24. (Left) First shot on BLUE, which was into a resistive load for testing. The clear plastic lid allows the interior of the cavity to be observed during operation and for operation without ferromagnetic cores. (Right) Subsequent pulsed-power testing on BLUE. These are the first 12 shots taken with the newly acquired CVR for current calibration. These shots were taken with charging voltages of +/- 50 kV or +/- 60 kV.

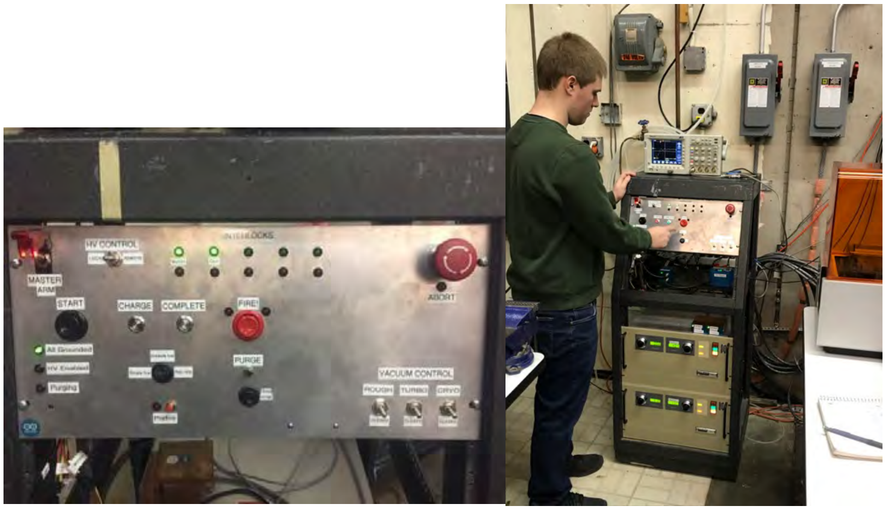

Figure 25. Photos of BLUE's control panel being operated by PhD student Brendan Sporer.

Trigger generator consists of 10-gal oil drum containing single brick with new generation L3 switch. PT55 used to break down L3 switch. Output split to four positive (or four negative) cables. Unused polarity is grounded.

All three relays can fit in 20-gal oil drum. Feedthroughs will be similar to those on trigger generator.

Figure 26. Trigger generator (left 2 images) and relay circuit (right image) fabricated in-house for BLUE.

Work has also been completed on adapting a newly acquired brazed MILO to BLUE. The MILO is shown in Fig. 5. The flange designed to mate this MILO to BLUE is shown in Fig. 6. This flange was designed and procured by PhD student Alexander Mazarakis, who was recruited to implement the experimental testing of this MILO on BLUE. Alexander began working on this project upon his arrival at UM in September 2019.

Figure 27. (Left two images) The two brazed MILOs acquired for testing on BLUE. (Right image) The assembled MILO ready to be mounted on BLUE.

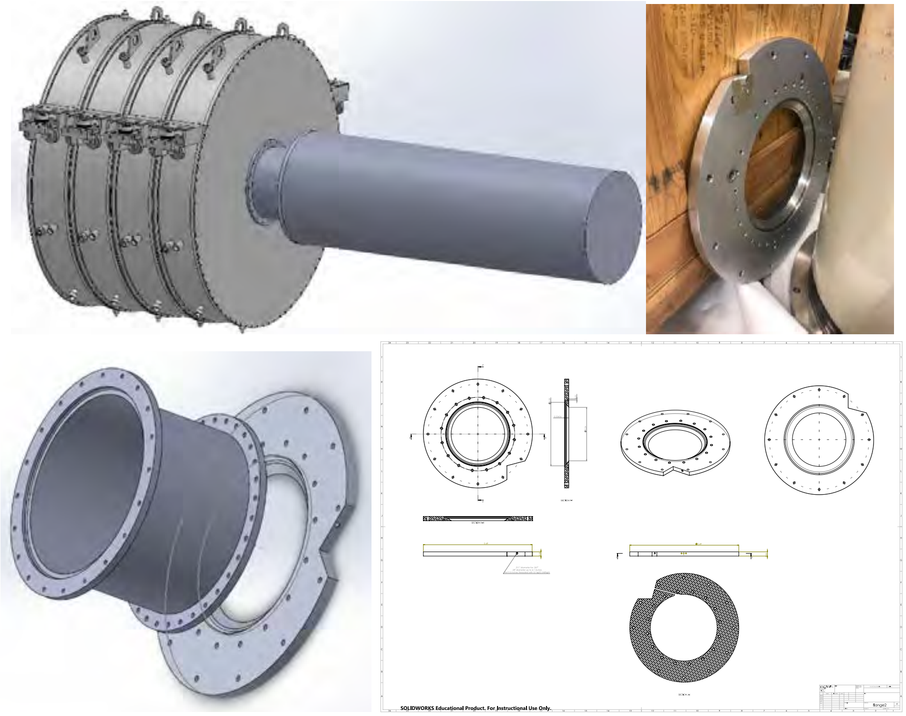

Figure 28. (upper left) SolidWorks model of the brazed MILO mounted to the 4-cavity BLUE facility. (upper right) The flange fabricated for mounting the MILO to BLUE. (lower images) SolidWorks model (left) and engineering drawing (right) of the mounting flange. The slot cut in the flange allows a Rogowski coil to be fielded for measuring the total current delivered to the MILO. The flange was designed and procured by PhD student Alexander Mazarakis.

To simulate the performance of this MILO on BLUE, PhD student Drew Packard (advised by Prof. Ronald Gilgenbach) mentored an undergraduate student researcher, Anna Cooleybeck (advised by PI Ryan McBride), to run several new simulations using HFSS and CST particle-in-cell (PIC) simulations. This work was summarized in an article submitted recently to *IEEE Transactions on Plasma Science* for the journal's special issue on HPM devices:

- Drew A. Packard, Anna Cooleybeck, Nicholas M. Jordan, Brendan J. Sporer, Alexander E. Mazarakis, Y. Y. Lau, Ronald M. Gilgenbach, and Ryan D. McBride, "HFSS and CST Simulations of a GW-Class MILO", submitted to IEEE Trans. Plasma Sci. (2019).

This modeling and simulation effort included the use of both HFSS (EM simulation) and CST-Particle Studio (PIC simulation) – see Fig. 7.

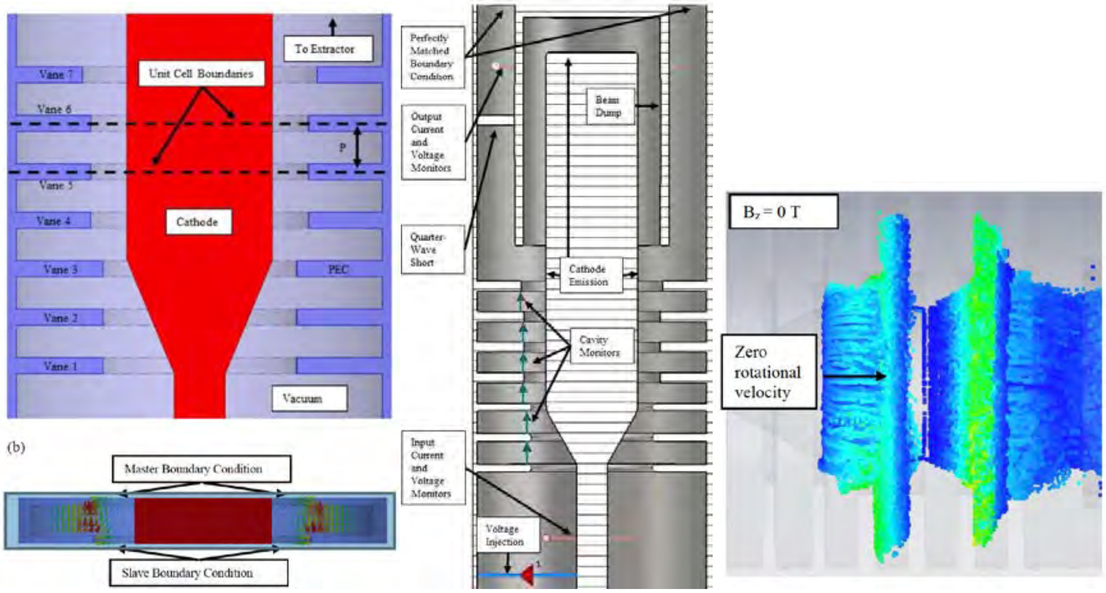

Figure 29. (left images) EM simulation setup and field intensities in HFSS. (middle image) PIC simulation setup in CST-Particle Studio. (right image) PIC simulation results in CST-Particle Studio demonstrating successful electron spoke formation in pi-mode.

3. Findings and Conclusions

In our MILO simulation studies, the expected ~1-GW operation was confirmed, in agreement with past simulations and experiments [S. E. Calico et al. SPIE's 1995 Int. Symp. on Opt. Sci., Eng., and Instrm. (1995)], where the voltage and current delivered to the MILO were ~500 kV and 50 kA, respectively (see Fig. 8, left side). These are conditions very similar to what the full 4-cavity BLUE facility will deliver. For example, compare the simulated current pulse plotted on the left side of Fig. 8 with the experimental current pulses plotted on the right side of Fig. 2, which were obtained recently on BLUE. The charge voltages for the shots on BLUE were +/- 50 kV or +/- 60 kV. Thus, because of the bipolar charging and operation of BLUE, the open-circuit output voltage for this single cavity would be twice the charging voltage; i.e., 100 kV or 120 kV. With 4 cavities, a +/- 60-kV charge voltage would generate an open-circuit output voltage of approximately 480 kV, while leaving the current pulse largely unchanged.

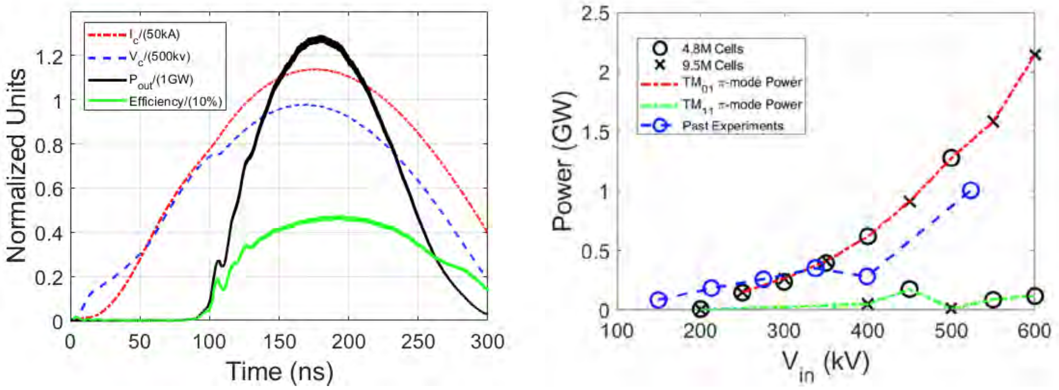

Figure 30. (Left) Output power, efficiency, injected current, and cathode voltage for a CST-PS simulation over time. (Right) A comparison of experimental [S. E. Calico et al. SPIE's 1995 Int. Symp. on Opt. Sci., Eng., and Instrm. (1995)] and simulated (this work) peak output power of the TM_{01} and TM_{11} π-mode as a function of injected voltage.

Our simulations also considered the effects of varying the drive voltage, just as the drive voltage will be varied on BLUE, when testing 1, 2, 3, or 4 cavities stacked in series. The results of this scan are presented on the right side of Fig. 8. From this scan, and from previous experimental results, we may expect our first cavity on BLUE to generate ~100 MW of HPM from our brazed MILO.

Another one of the major success stories of this past year (in addition to BLUE becoming operational, the acquisition and preparation of the brazed MILO, and the recent simulation results and journal article submission) was figuring out how to get our triggered L3 spark-gap switches to work properly in our other LTD facility (MAIZE). This was important to figure out because BLUE uses the same switches. The faulty operation was found to be due to debris being generated in the switches. This debris can cause tracking on the switch bodies (see Fig. 8). To mitigate these issues, several protocols were put in place, including high-pressure gas purges, high-pressure charge-and-holds to corona-discharge-clean the electrodes, the use of ultra-zero-grade dry air from Matheson Tri-Gas, Inc., etc. These findings have helped enable the successful operation of BLUE.

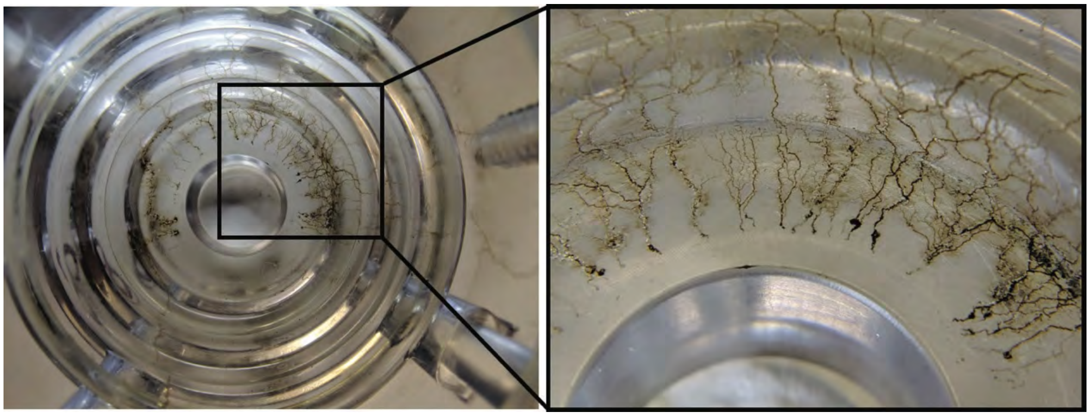

Figure 31. Tracking observed along the switch bodies of L3 spark-gap switches (model 40264-200) after initial (unsuccessful) testing in MAIZE. These switches are now being used successfully in BLUE.

4. Plans and Upcoming Events

Our plans for the near-term future begin with mounting and testing the MILO on BLUE. In these preliminary tests, we will use just a single BLUE cavity and measure the RF output power via several magnetic B-dot loops included in the MILO structure. Simultaneously, we will be working to incorporate the remaining BLUE cavities into a staked LTD module, with either 1, 2, 3, or 4 cavities employed. Since increasing the number of cavities stacked together in series increases both the driver voltage and driver impedance while leaving the nominal current unchanged, we will be able to directly test the effects of driver impedance on MILO performance. These tests will be accompanied by PIC simulation efforts to better understand the experimental results.

5. Transitions and Impacts

This research project (and Prof. McBride's HPM program) just began in June of 2018, thus all of the transitions and impacts have been in the direction from Sandia and AFRL to the University of Michigan. Upon testing the donated equipment, we will begin to transition research outputs, technology products, and trained students/PhDs back to these labs.

6. Collaborations

As part of this program/project, we are collaborating with Dr. Brad Hoff of the AFRL, who is providing guidance on what is important to directed energy programs in the Navy and Air Force and who has also sent us a mini-LTD pulser for HPM device testing. Similarly, we are collaborating with Dr. Kyle Hendricks of the AFRL, who has sent us a working crossed-field HPM device (along with its CAD models) for testing on BLUE.

We have also been collaborating with Dr. Jon Douglass, Mr. Tommy Mulville, Mr. Matt Sceiford, Dr. Josh Leckbee, and (previously) Dr. Matt Wisher, all of Sandia National Laboratories, who have been working to help us with the transition of the four Ursa Minor cavities to the University of Michigan, where they are part of the BLUE LTD facility. It is of strategic importance to Sandia's pulsed-power development labs that students are being trained in new LTD technology.

Additionally, we have been working with Dr. Patrick Corcoran and Dr. David Phipps (both of L3Harris) to work through the issues with our L3 switches on both MAIZE and BLUE.

This program is also allowing us to collaborate with Prof. Allen Garner of Purdue University, who has his own ONR HPM funding to test out a non-linear transmission line (NLTL) HPM source on an LTD. We will be providing the LTD and Prof. Garner's group will be providing the NLTL source.

7. Personnel

Principal investigator
Prof. Ryan McBride
~1.5 person months worked
National Academy Member: No

Co-investigator or Co-PI
Dr. Nicholas Jordan
~4 person months worked
National Academy Member: No

Business Contact
Ms. Tawny Dekar
No time charged to this project (she is covered by IDCs)
National Academy Member: No

Team Members
Mr. Brendan Sporer
~12 person months worked
National Academy Member: No

Team Members
Mr. Alexander Mazarakis
~4 person months worked
National Academy Member: No

Team Members
Mr. Drew Packard
No time charged to this project, but he has contributed significantly via simulation support
National Academy Member: No

Team Members
Ms. Anna Cooleybeck
~1 person month worked as undergraduate student researcher throughout the year
National Academy Member: No

8. Students

3 graduate students, 1 undergraduate student:

Mr. Brendan Sporer: PhD student
Fully supported by this ONR YIP MILO project (construction of BLUE)

Mr. Alexander Mazarakis: PhD student
Fully supported by this ONR YIP MILO project (experimental testing of MILO on BLUE)

Mr. Drew Packard: PhD student
MILO simulation for this ONR YIP MILO project (supported by other ONR HPM projects: Multi-Frequency RPM and/or applied-B/planar MILO projects)

Ms. Anna Cooleybeck: Undergraduate student
MILO simulation for this ONR YIP MILO project

9. Technology Transfer

We are presently perusing a patent for a MILO design that we would like to test on the BLUE LTD. This effort is being led by Prof. Y. Y. Lau, as the MILO design is his. The UM Office of Technology Transfer has conducted a “prior art search”. We will know more about our chances of obtaining a patent after initial MILO testing on BLUE.

Regarding LTD work in general, we have been in communication with folks at the Naval Research Lab (Joe Schumer, Jacob Zier, and Tom Mehlhorn), Sandia National Labs (see above), and the AFRL (see above). In 2018, we published an invited tutorial on LTDs with Joe Schumer and Jacob Zier of the NRL and Jon Douglass and Josh Leckbee of Sandia National Laboratories (see Section 10 below). In 2019, we published a new fiber-optic-based technique for monitoring many spark-gap switches in an LTD cavity with a limited number of oscilloscope channels with Sonal Patel of Sandia.

10. Products, Publications, Patents, License Agreements, etc.

Publications resulting from this project:

Archival Publications (publication reference information (article title, authors, journal, date, volume, issue) can be automatically entered using a DOI)

a. A Primer on Pulsed Power and Linear Transformer Drivers for High Energy Density Physics Applications
b. IEEE Transactions on Plasma Science
c. R. D. McBride, W. A. Stygar, M. E. Cuneo, D. B. Sinars, M. G. Mazarakis, J. J. Leckbee, M. E. Savage, B. T. Hutsel, J. D. Douglass, M. L. Kiefer, B. V. Oliver, G. R. Laity, M. R. Gomez, D. A. Yager-Elorriaga, B. M. Kovalchuk, A. A. Kim, P.-A. Gourdain , S. N. Bland, S. Portillo, S. C. Bott-Suzuki, F. N. Beg, Y. Maron, R. B. Spielman, D. V. Rose, D. R. Welch, J. C. Zier, J. W. Schumer, J. B. Greenly, A. M. Covington, A. M. Steiner, P. C. Campbell, S. M. Miller, J. M. Woolstrum, N. B. Ramey, A. P. Shah, B. J. Sporer, N. M. Jordan, Y. Y. Lau, and R. M. Gilgenbach
d. Equation of state, high-energy-density physics (HEDP), inertial confinement fusion (ICF), laboratory astrophysics, linear transformer driver (LTD), magnetized liner inertial fusion (MagLIF), material properties, pulsed power, radiation effects, radiation science, radiation sources.
e. Unrestricted distribution (open access)
f. Published
g. DOI
h. 10.1109/TPS.2018.2870099
i. November 8, 2018
j. Volume 46
k. Issue 11
l. Page 3928
m. Piscataway, New Jersey
n. Acknowledgement of Federal Support: Yes
o. Peer Reviewed: Yes

a. Optimization of switch diagnostics on the MAIZE linear transformer driver
b. Review of Scientific Instruments
c. A. P. Shah, P. C. Campbell, S. M. Miller, J. M. Woolstrum, B. J. Sporer, S. G. Patel, N. M. Jordan, R. M. Gilgenbach, and R. D. McBride
d. None/NA
e. Unrestricted distribution (open access)
f. Published
g. DOI
h. 10.1063/1.5113866
i. December 20, 2019
j. Volume 90
k. N/A
l. Page 124707
m. Melville, NY
n. Acknowledgement of Federal Support: Yes
o. Peer Reviewed: Yes

Conference Papers

a. Construction of the BLUE Linear Transformer Driver System at the University of Michigan
b. Brendan Sporer, Nick Jordan, and Ryan McBride
c. 60th Annual Meeting of the APS Division of Plasma Physics
d. November 5-9, 2018
e. Portland, OR, USA
f. Abstract published, poster presented
g. Friday, November 9, 2018
h. None
i. None
j. Acknowledgement of Federal Support: Yes

a. Construction of the BLUE Linear Transformer Driver System at the University of Michigan
b. Brendan Sporer, Nick Jordan, and Ryan McBride
c. 9th Annual Graduate Student Symposium
d. November 14, 2018
e. Ann Arbor, MI, USA
f. Abstract published, poster presented
g. November 14, 2018
h. None
i. None
j. Acknowledgement of Federal Support: Yes

a. Status Update on the BLUE Linear Transformer Driver (LTD) System at the University of Michigan
b. Brendan Sporer, Nick Jordan, and Ryan McBride
c. IEEE Pulsed Power and Plasma Science Conference
d. June 23-28, 2019
e. Orlando, FL, USA
f. Abstract published, poster presented
g. June 27, 2019
h. None
i. None
j. Acknowledgement of Federal Support: Yes

a. Status Update on the BLUE Linear Transformer Driver (LTD) System at the University of Michigan
b. Brendan Sporer, Nick Jordan, and Ryan McBride
c. 61st Annual Meeting of the APS Division of Plasma Physics
d. October 21-25, 2019
e. Fort Lauderdale, FL, USA
f. Abstract published, poster presented
g. October 22, 2019
h. None
i. None
j. Acknowledgement of Federal Support: Yes

Books: None

Book Chapter: None

Theses: None

Websites: None

Patents: None

Other Products: Identify any other significant products that were developed under this project. Describe the product and how it is being shared.

a. Description: Developed models and simulations of crossed-field devices for use on the BLUE LTD facility. Also developed a SolidWorks CAD model of the BLUE LTD facility.
b. Product Type: models

11. Point of Contact in Navy

Dr. Joseph Schumer
Plasma Physics Division
Naval Research Laboratory

Date we last discussed HPM research: June 25, 2019

12. Acknowledgement/Disclaimer

This work was sponsored by the Office of Naval Research (ONR), under grant (or contract) number N00014-18-1-2499. The views and conclusions contained herein are those of the authors only and should not be interpreted as representing those of ONR, the U.S. Navy or the U.S. Government.

Improved Computational Tools for Navy High Power Microwave Applications

Grant No. N68335-18-C-0060

Period of Performance: October, 1, 2018 to November 13, 2019

Prepared by:
Dr. Peter Stoltz, Principal Investigator
Tech-X Corporation
5621 Arapahoe Ave
Boulder, CO, 80303
Tel: (720) 563-0336
Email: pstoltz@txcorp.com

TECH-X
SIMULATIONS EMPOWERING YOUR INNOVATIONS

DEPARTMENT OF THE NAVY · UNITED STATES MARINE CORPS ·

This work was sponsored by the Office of Naval Research (ONR), under grant number N00014 - 17-1-2848. The views and conclusions contained herein are those of the authors only and should not be interpreted as representing those of ONR, the U.S. Navy or the U.S. Government.

Grant or Contract Number: N68335-18-C-0060
Date Prepared: Jan 28 2020
Project Title: Improved Computational Tools for Navy High Power Microwave Applications
Annual Summary Report: 2019
Principal Investigator: Dr. Peter Stoltz, (720) 563-0336, pstoltz@txcorp.com
Tech-X Corporation, 5621 Arapahoe Ave, Boulder, CO, 80303 303-448-0727

Section I: Project Summary

1. Overview of Project

Abstract: In this document, we show recent progress on applying modern plasma simulation tools to projects of interest to the Navy. We show results of a kinetic code (VSim) and a fluid code (USim) to four problems: high power microwave transmission line gap closure, a dense plasma focus neutron source, a relativistic planar magnetron microwave source, and a klystron microwave source.

Objective: The objective of this work is to undertake a comprehensive study of where in the Navy modeling space, given recent advances in plasma modeling, one can apply fluid approaches with sufficient accuracy and where kinetic models are required. We will compare the trade-off of accuracy of results with computational speed, attempting to use automated optimization tools to tailor both approaches.

Introduction: Modeling and simulation play a critical role in the design and evaluation of high power microwave (HPM) devices. However, many of the most recent simulation methods have yet to be adopted by Navy scientists in their design process, in part because these methods need additional improvements and need to be shown to work on problems of interest to the Navy. Magnetohydrodynamics (MHD) and Particle-in-Cell (PIC) are two standard techniques that Navy researchers have relied on for many decades. More recently, however, AFOSR has sponsored the development of two-fluid electromagnetic models that bridge the gap between these two regimes, in a fashion that enables DoD researchers to solve problems of interest in the hypersonics and high energy density plasma community. However these new two-fluid electromagnetic models require further improvement to solve the range of problems involved in HPM design. With regard to kinetic PIC modeling, embedded boundaries are a new advance with promise for significantly improving modeling of HPM sources.

Background: Our approach is to modify two existing simulation tools, a multifluid modeling tool USim and a kinetic modeling tool VSim, to meet the needs of Navy high power microwave research. In collaboration with Naval Research Lab scientists, we will identify representative problems on which we can apply these tools to demonstrate the improved capabilities.

2. Activities and Accomplishments

Our activities and accomplishments include creating a synthetic x-ray pinhole diagnostic for high energy density plasma. A main diagnostic for HED plasma and therefore for emerging HPM systems is x-ray pinhole imaging. Consequently, we developed a synthetic x-ray pinhole image diagnostic and benchmarked against the NRL Hawk dense plasma system. Although we use Hawk as a benchmark case, x-ray pinhole imaging is used (for example) in diagnosing multipactor in the output cavity of high power klystrons [A. S. Gilmour, Jr. *Klystrons, Traveling Wave Tubes, Magnetrons, Cross-Field Amplifiers, and Gyrotrons*, Artech House, Boston-London, 2011]. In Figure 1, we show the results of our benchmark, with the experimental image on the left and the synthetic diagnostic on the right. In this particular case, the diagnostic was used with a fluid simulation (USim), but the same technique would apply with a kinetic simulation. We believe adding these synthetic diagnostics to simulation will allow researchers to more accurately compare simulation results to experiment for HPM systems.

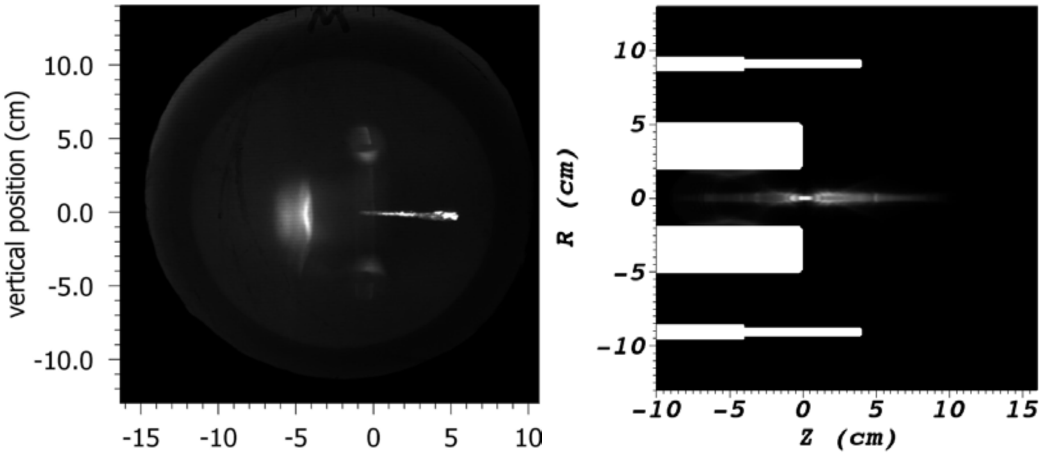

Figure 1: *Experimental x-ray image (left) and simulated Bremsstrahlung radiation energy (right). We believe adding these synthetic diagnostics to simulation will allow researchers to more accurately compare simulation results to experiment for HPM systems.*

Another highlight is a new high current emission capability. In Figure 2, we show a geometry for a high power microwave source called a magnetically insulated line oscillator (MILO). One particular challenge to modeling these kinds of high power microwave devices is that the emitted current is so high, it can change the fields significantly. Getting these high current emissions correct in simulation is challenging. In Figure 3, we show an FFT of the emitted and absorbed current. Both the emitted and absorbed current show frequency peaks at the tube operating frequency of 13 GHz and at harmonics. These frequency peaks in the current demonstrate that the emission algorithm we have developed is working properly. This new emission model allowed us to study this MILO far into the nonlinear operating regime, particularly including ion effects. In Figure 4, we show how the electrons take on a spiral shape in the presence of ions.

An important part of this project is comparing fluid and particle models. In Figure 5, we show both a fluid model (top) and a kinetic model (bottom) of the 13 GHz model. This demonstrates how both approaches can accurately reproduce the physics of HPM devices.

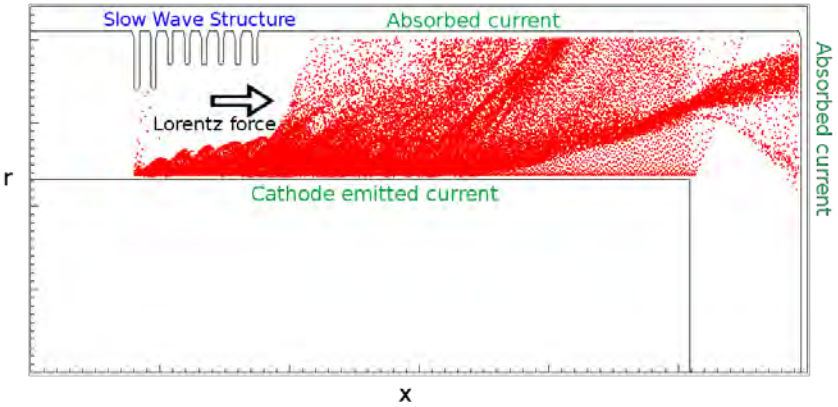

Figure 2*: We applied our new space charge limited emission algorithm to high power microwave systems, including the 13 GHz MILO shown here.*

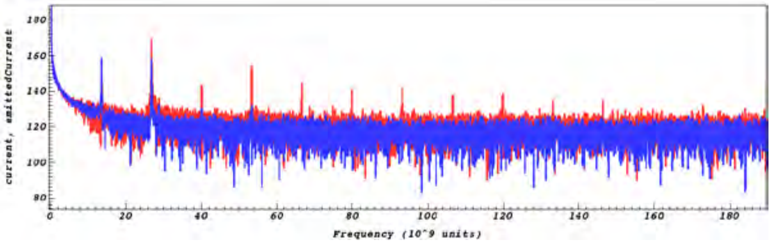

Figure 3: *The emitted current (blue) and the absorbed anode current (red). The frequency peaks in the current at the operating frequency and harmonics demonstrate that the emission algorithm we have developed is working properly.*

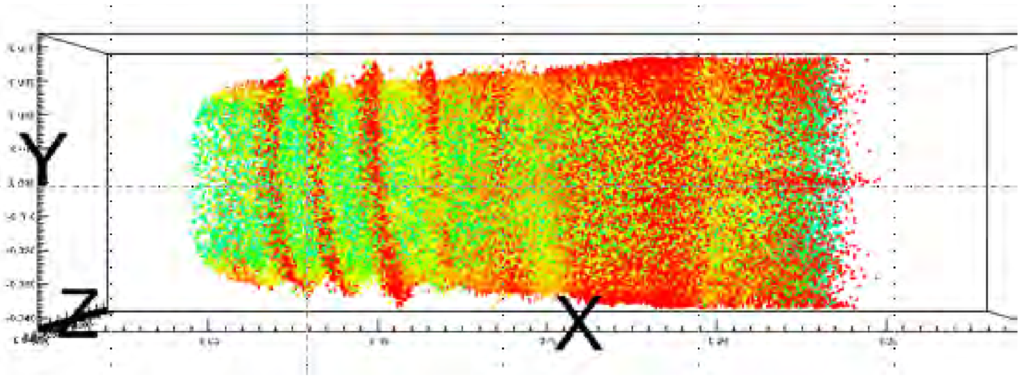

Figure 4: *Electron spokes color coded by axial velocity in the presence of high density ions.*

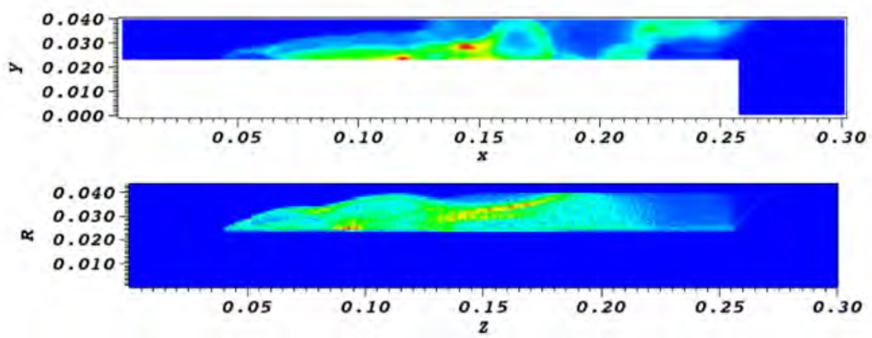

Figure 5*: Comparison of fluid (top) and kinetic calculations (bottom) for the 13 GHz MILO. The color map shows electron density on the same scale.*

We report one final accomplishment: the application of machine learning to improve HPM device design [*Machine Learning Investigation of the Rising Sun Magnetron Design and Operation,* A. Spirkin, P. Stoltz, J. Luginsland, IEEE Trans. on Plasma Science, v48, 1, p. 133 (2020)]. For this work, we used a 2 GHz magnetron design. Magnetron operation is characterized by electron spoke formation. We used machine learning and image classification to determine automatically when simulations exhibited spoke formation. In Figure 6, we show the various simulation results (left) from VSim, the different classification algorithms (center), and the resulting categorizations (some spoke formation, right top, clear five spoke formation, right center, and no spoke formation, right bottom). This automatic classification allows us to perform hundreds of simulations with no human intervention required. In turn, this allowed us to determine how much power one can efficiently extract from a magnetron before the electron spokes are lost. In Figure 7, we show the total power on the vertical axis versus the power extracted on the horizontal axis, including plots of the electron spoke structure. The machine learning capability we developed allowed us to determine if the magnetron was still operating cleanly (with spokes) for each operating point we simulated on this curve, in turn determining the overall efficiency of this device.

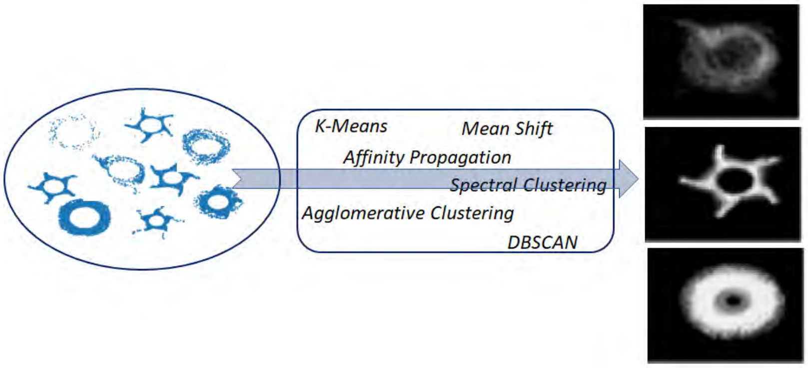

Figure 6*: Unsupervised image classification allows us to automatically determine the operating condition in a simulated magnetron.*

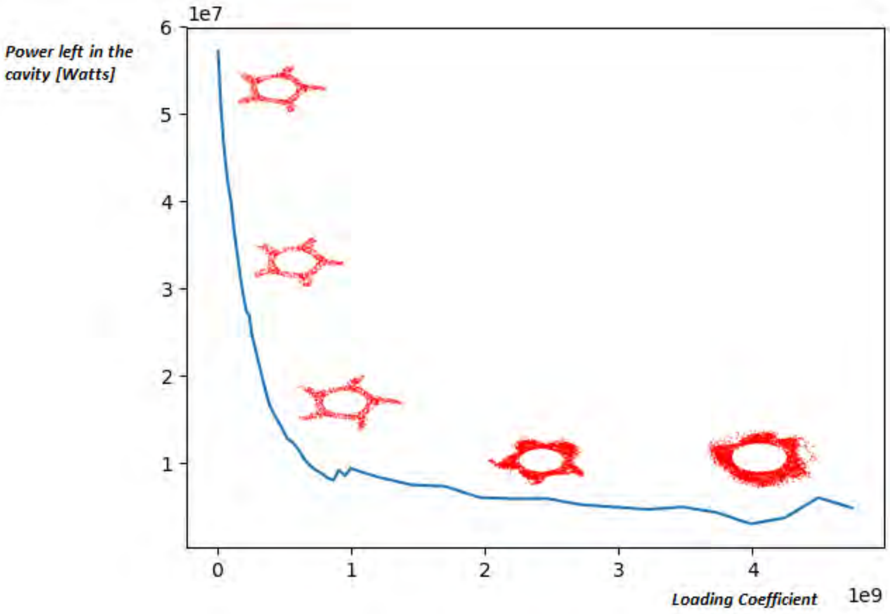

Figure 7*: Power remaining in the extraction cavity as a function of loading coefficient and corresponding electron phase-space formations. The machine learning capability we developed allowed us to determine if the magnetron was still operating cleanly (with spokes) for each operating point we simulated on this curve, in turn determining the overall efficiency of this device.*

3. Findings and Conclusions

Our conclusions are that USim and VSim are capable of modeling devices relevant to the Navy mission, specifically high power microwave devices and dense plasma focus neutron sources. We have transitioned these capabilities to scientists at the NRL.

4. Plans and Upcoming Events

We plan to apply the codes to further study of HPM devices through teaming with scientists at NRL, AFRL, and others. We are also expanding to other fields where dense plasma science is important, including magnetized target fusion. We have a pending proposal with Notre Dame and Boise State researchers, and we have an upcoming trip to Verus Research to discuss future collaboration.

5. Transitions and Impacts

We have transitioned our work to NRL scientists for future application. We believe our main impact was showing application of PIC and fluid codes to several stages of HPM design: power flow, sources, and diagnostics.

We also believe our work on machine learning for optimization of HPM devices could have an impact on future modeling efforts. We focused on publishing this work for this reason.

6. Collaborations

We have ongoing collaborations on high power microwave research with Naval Research Laboratories, Verus Research, Notre Dame, and Boise State.

7. Personnel

Principal investigator: Peter Stoltz, Tech-X Corp., 5.8 person months worked, not a National Academy Member, US citizen

Co-PI: John Luginsland, Confluent Sciences LLC, 5.7 person months worked, not a National Academy Member, US citizen

Business Contact: Laurence Nelson, Tech-X Corp., 0 person months worked, not a National Academy Member, US citizen

Team Members: Anton Spirkin, Tech-X Corp., 7.8 person months worked, not a National Academy Member, US citizen; Christine Roark, Tech-X Corp., 4.25 person months worked, not a National

Academy Member, US citizen; Andrew Chap, Tech-X Corp., 2.2 person months worked, not a National Academy Member; George Bell, Tech-X Corp., 0.9 person months worked, not a National Academy Member; Michel de Messiers, Tech-X Corp., 0.7 person months worked, not a National Academy Member;

Subs: see Co-PI

8. Students

N/A

9. Technology Transfer

We have an ongoing collaboration with Naval Research Laboratories that includes Joe Schumer, Stuart Jackson, Ian Rittersdorf, and Steve Richardson. We compare simulation results with NRL experimental results, specifically to the Hawk Dense Plasma Focus. We also compare with other NRL simulation results, specifically to ICEPIC and Neptune simulation results of a planar magnetron.

Regarding commercialization efforts, we have successfully obtained a commercial contract of $400,000 with a major customer who has asked not to be named for proprietary reasons. This work is directly related to the work done under our ONR contract.

We are also working with Verus Research scientists on models of plasma switches. We believe this effort may lead to future software sales and contract work.

10. Products, Publications, Patents, License Agreements, etc.

Publications resulting from this project:

<u>Archival Publications</u>

Machine Learning Investigation of the Rising Sun Magnetron Design and Operation; IEEE Transactions on Plasma Science, Anton Spirkin, Peter Stoltz, John Luginsland

keywords: computer simulation, high-power microwave generation, machine learning, optimization
Distribution A. Approved for public release: distribution unlimited
Publication Status: published
DOI: 10.1109/TPS.2019.2958289
Date of Publication: 20 December 2019
Volume 48; Issue: 1; Page 133
Publication Location: Piscataway, NJ, USA
Acknowledgement of Federal Support: Yes
Peer Reviewed: Yes

Conference Papers

Hybrid fluid/kinetic modeling of dense plasma focus devices using USim and VSim, Christine Roark, Peter Stoltz, Anton Spirkin, John Luginsland, Stuart Jackson, Andrey Beresnyak, Pulsed Power and Plasma Science, June 23-28, 2019, Orlando, FL, USA, other, N/A, abstract number, 4P38, Yes

Advanced optimization and machine learning for magnetron design, Anton Spirkin, Peter Stoltz, John Luginsland, Pulsed Power and Plasma Science, June 23-28, 2019, Orlando, FL, USA, other, N/A, abstract number, 1P33, Yes

Hybrid Kinetic-Fluid Simulations of a Ku-band MILO, Peter Stoltz, Anton Spirkin, John Luginsland, Christine Roark, Andrew Chap, Pulsed Power and Plasma Science, June 23-28, 2019, Orlando, FL, USA, other, N/A, abstract number, 2P13, Yes

11. Point of Contact in Navy

Joseph Schumer, PhD
Plasma Physics Division
Naval Research Laboratory

We last discussed our research in person with Dr. Schumer’s team in Sept. 2019.

12. Acknowledgement/Disclaimer

This work was sponsored by the Office of Naval Research (ONR), under grant (or contract) number N68335-18-C-0060. The views and conclusions contained herein are those of the authors only and should not be interpreted as representing those of ONR, the U.S. Navy or the U.S. Government.

Ultra-High-Efficiency Relativistic Magnetron and Improved MILO Capabilities

Grant No. N00014 -19-1-2155

Annual Report for Fiscal year 2019

Period of Performance: May, 1, 2019 to September 30, 2019

Prepared by:
Professor Edl Schamiloglu, Principal Investigator
University of New Mexico
Department of Electrical and Computer Engineering
Albuquerque NM 87131-0001
Tel: (505) 277-6095
Email: edls@unm.edu

DEPARTMENT OF THE NAVY • UNITED STATES MARINE CORPS

This work was sponsored by the Office of Naval Research (ONR), under grant number N00014 -17-1-2848. The views and conclusions contained herein are those of the authors only and should not be interpreted as representing those of ONR, the U.S. Navy or the U.S. Government.

Grant or Contract Number: N00014-19-1-2155
Date Prepared: January 18, 2020
Project Title: Ultra-High-Efficiency Relativistic Magnetron and Improved MILO Capabilities[1]
Annual Summary Report: FY2019

Principle Investigator: Edl Schamiloglu, 505-277-6095, edls@unm.edu, University of New Mexico, Department of Electrical and Computer Engineering; Salvador Portillo, 505-277-2436, sportil@unm.edu, University of New Mexico, Department of Electrical and Computer Engineering

Section I: Project Summary

1. Overview of Project

The relativistic magnetron is the most compact and efficient high power microwave source. The University of New Mexico (UNM) has been studying relativistic magnetrons for over 15 years. Our initial contribution was the invention of the "transparent cathode" (TC) that increased magnetron beam-to-microwave conversion efficiency and decreased the time-for-start of oscillations. Next, we showed that a TC in a magnetron with diffraction output (MDO) can achieve 70% beam-to-microwave efficiency, provided that axial loss current can be suppressed. We demonstrated how the use of endcaps on a TC can greatly diminish axial loss current. We then proposed a permanent magnet solution to a compact MDO where, for the price of decreased efficiency, a very compact high power RF (HPRF) source without the bulky extraction section can be realized. We next proposed a relativistic MDO without a physical cathode where a virtual cathode (VC) forms in the interaction region to power the MDO with efficiency comparable to that of an MDO with a TC. Most recently we proposed a magnetic mirror field for an MDO that can completely eliminate axial loss current. This half-cusp-like magnetic field configuration replaces the downstream VC that was described in our earlier work and demonstrates >90% efficiency in simulations. We believe that this MDO with VC and magnetic mirror will not suffer from pulse shortening since there is no physical cathode electrode in the interaction space for impedance collapse to take place. Hence, we believe this configuration can operate at exceptionally long pulse lengths. This unique device will also be studied for multi-tone and continuous tuning capabilities.

UNM has also been developing a magnetically insulated line oscillator (MILO) over the past few years to study plasma formation and evolution in the device and mitigating such plasmas to achieve higher efficiency operation. We plan to study simulation and experimental strategies for achieving higher efficiency MILO operation and multi-tone capabilities. UNM will also be advancing pulsed power drivers for MDOs and MILOs using a fast, high energy Marx generator and a linear transformer driver (LTD).

In terms of the Navy relevance of the project, this project will extend the UNM/University of Michigan (UM) successful HPRF partnership to MILOs, that were largely developed in the USA (1980's-2000), but recently have seen intensive research and development by potential competitor countries. Our goal is to address, via focused and transitional HPRF research, some of the critical problems facing Navy operations due to asymmetric electronic threats, such as those faced by Marine warfighters in forward operating bases to those in littoral waters, and protection of high

---

[1] This work was sponsored by the Office of Naval Research (ONR), under grant number N00014-19-1-2155. The views and conclusions contained herein are those of the authors only and should not be interpreted as representing those of ONR, the U.S. Navy or the U.S. Government.

value targets, such as U.S. embassies in potential hot spots around the globe. These asymmetric electronic threats can come in the form of small airborne electronic drones, perhaps even COTS-type devices employed in boat or automobile-sized machines.

Abstract: This annual report summarizes activity on the recently awarded ONR grant "Ultra-High-Efficiency Relativistic Magnetron and Improved MILO Capabilities" covering the period May 01, 2019 – September 30, 2019.

Objective: The objectives of this research are to i) increase the HPRF power/electron beam power efficiency of relativistic magnetrons and explore the MILO to further improve its performance. The MILO portion of this research is in collaboration with UM.

Introduction: The University of New Mexico (UNM) group excels in designing novel HPRF source concepts of relevance to the Navy, and then validating the source designs in experiment. UNM is proposing an ultra-high-efficiency relativistic magnetron that has demonstrated an outstanding 92% efficiency (beam-to-RF) in particle-in-cell (PIC) simulations. This is a record for any HPRF source! In addition, UNM is seeking to further the magnetically insulated line oscillator (MILO) through basic studies of surfaces plasmas within the device. This project seeks to continue this basic research program that has been in collaboration with our colleagues at the University of Michigan. Investigating frequency agile MDOs and MILOs will be an important consideration of our work.

Ultra-High-Efficiency Relativistic Magnetron

This part of the project builds on our previous ONR-sponsored work that was published in the archival literature. The basic idea here is that we use our magnetron with diffraction output (MDO) into which an electron beam is externally injected and forms a VC in the interaction space. This concept will be tested in a collaboration with NSWC at Dahlgren. The new idea we would like to test at UNM is to incorporate a magnetic mirror field at the output of the MDO. The advantage of this is that the magnetic mirror field absolutely suppresses axial leakage current and in PIC simulations we have achieved an astounding 92% efficiency, a world record. Figure 1 compares MDO performance without (top) and with (bottom) a magnetic mirror field to suppress axial leakage current.

In our experiments we propose to experimentally investigate the MDO with a transparent cathode and then later with a VC, both with a magnetic mirror by implementing the mirror field using a bucking coil and examining the use of a half-cusp magnetic field. We believe that the MDO with VC and magnetic mirror will not suffer from pulse shortening since there is no physical cathode electrode in the interaction space for impedance collapse to take place. Hence, we believe this configuration can operate at exceptionally long pulse lengths.

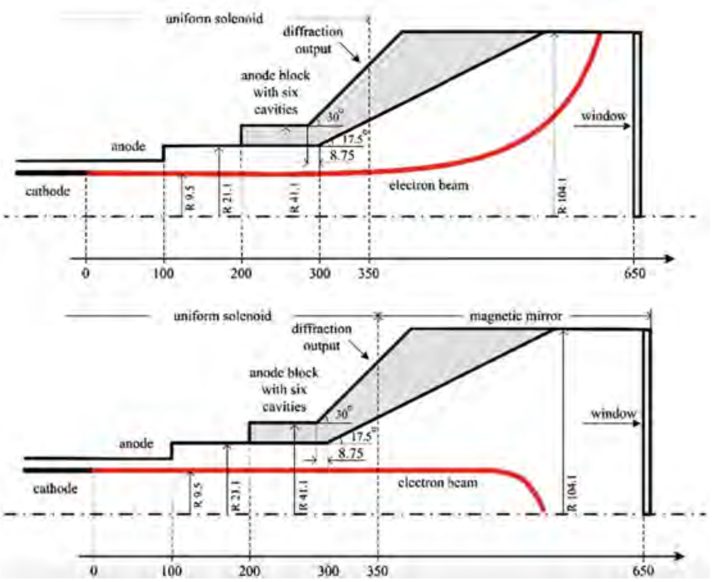

Figure 1. Top: MDO dimensions (mm) with two VCs and the low energy state between them. The leakage current after the second VC deposits onto the anode. Bottom: The same MDO with a magnetic mirror instead of a second VC. The electron beam in red is shown in both cases.

The Magnetically Insulated Line Oscillator (MILO)

The MILO is a crossed field HPM generator comprised of two structures, an inner conductor that serves as an electron field emitter and an outer conductor that contains the slow wave structure and ultimately where the electromagnetic energy is generated. Figure 2 shows a schematic of the AFRL hard tube (HT) MILO. There is continued interest in the MILO since it requires no external magnetic field and, therefore, from a system perspective, it is highly attractive. The onset of electron emission occurs when the work function of the material is overcome by the applied field. The emitted electrons traverse the interaction space, initially shorting the device; however, once the voltage pulse generates sufficient current the azimuthal magnetic field becomes high enough to insulate the electron flow. This parapotential current or critical current is called the Hull cut-off condition and, when achieved, the MILO operates nominally generating HPRF from the nonlinear beam/wave interaction.

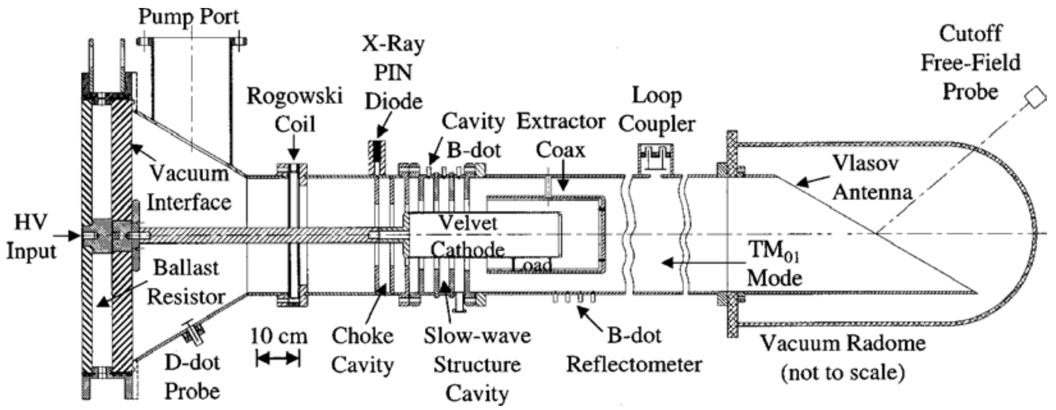

Figure 2. Schematic of the AFRL HT MILO

List of Abbreviations

A-K – anode-cathode gap
CsI – cesium iodide
ECE – Electrical and Computer Engineering
HPRF – high power RF
HT MILO – hard tube MILO
LTD – linear transformer driver
MDO – magnetron with diffraction output
MILO – magnetically insulated line oscillator
NSWCDD – Naval Surface Warfare Center Dahlgren Division
PIC – particle-in-cell
TC – transparent cathode
TFA – time-frequency analysis
TLD – thermoluminescent dosimeter
UM – University of Michigan
UNM – University of New Mexico
VC – virtual cathode

Administrative Point of Contact

Melissa Dee Sanchez – Sponsored Projects Specialist
(505) 277-7647, osp@unm.edu

Background: The approach that is being followed in the research under this grant is to i) utilize comprehensive PIC simulations using UNM's various virtual prototyping tools (ICEPIC, MAGIC, CST Particle Studio, LSP – which can handle surface plasmas in the MILO) and then validate the simulations using experiments. A modified PI-110 accelerator is used for the MDO experiments and a newly built Marx/PFL is used to drive the MILO. The MILO will be fitted with spectroscopic diagnostics to compare experimental results with LSP simulations.

2. Activities and Accomplishments

The current reporting period is May 01, 2019 – September 30, 2019 (5 months of effort).

UNM first tested the MDO using a TC with and without an endcap (Fig. 3). Although higher efficiency was observed with the endcap, the endcap electrically broke down after a few shots. This is being investigated further.

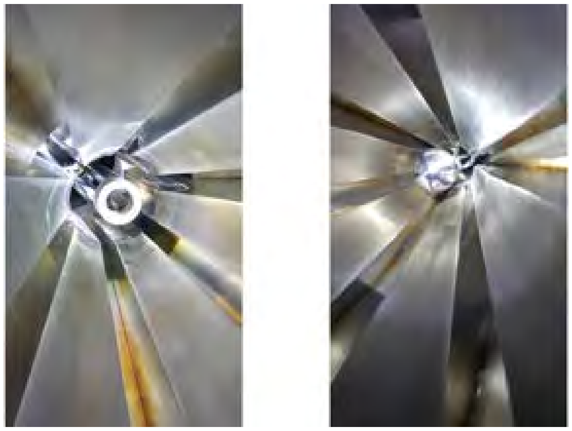

Figure 3. MDO with TC both without (left) and with (right) a cathode endcap.

We then performed a series of experiments where we operated the MDO with an endcap and fired once a minute for 20 or so minutes to assess any temperature rise. This was in conjunction with Verus Research, who was interested in this data as part of a Joint Nonlethal Weapon Directorate project. The temperature rise was not significant.

UNM tested its first configuration of the MDO with VC. In the first test, only a VC in the MDO was incorporated. Several shots were taken and HPRF was generated. To better understand the results, UNM blocked off the MDO cavities and observed the result Figs. 4, 5). A broadband RF signal was observed, presumably attributed to the VC in the MDO behaving like a vircator. Then the shim stock was removed, and coherent radiation was observed (Fig. 6). These are being investigated further.

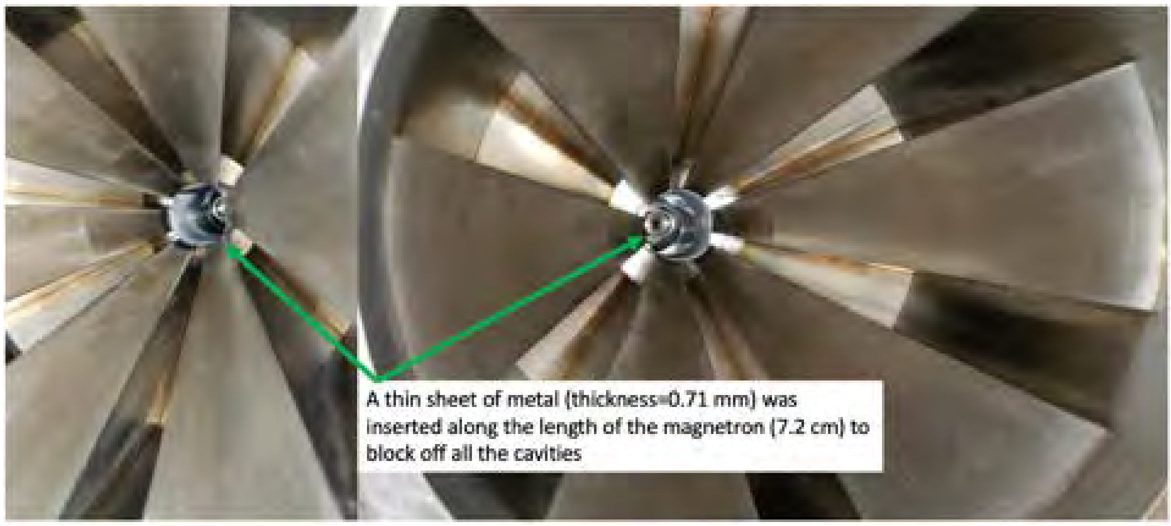
A thin sheet of metal (thickness=0.71 mm) was inserted along the length of the magnetron (7.2 cm) to block off all the cavities

Figure 4. Shim stock was installed to short-out the MDO cavities to observe whether HPRF was being generated by the VC in a vircator-like manner.

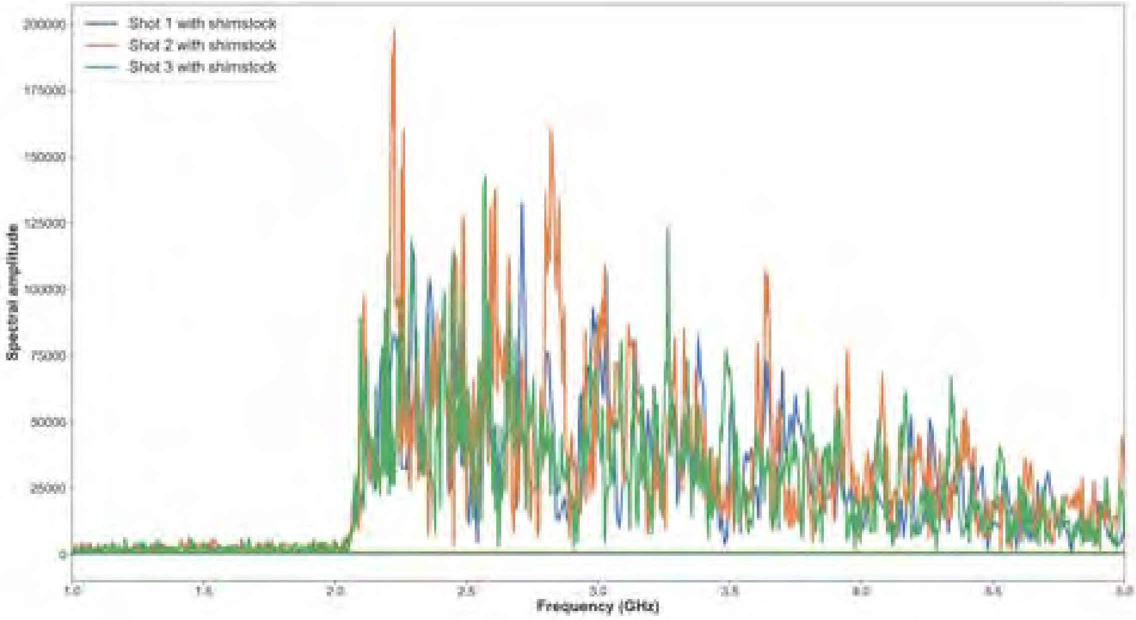

Figure 5. When the cavities are blocked off, we did not observe peaks in frequency, but rather a very long wide frequency signal.

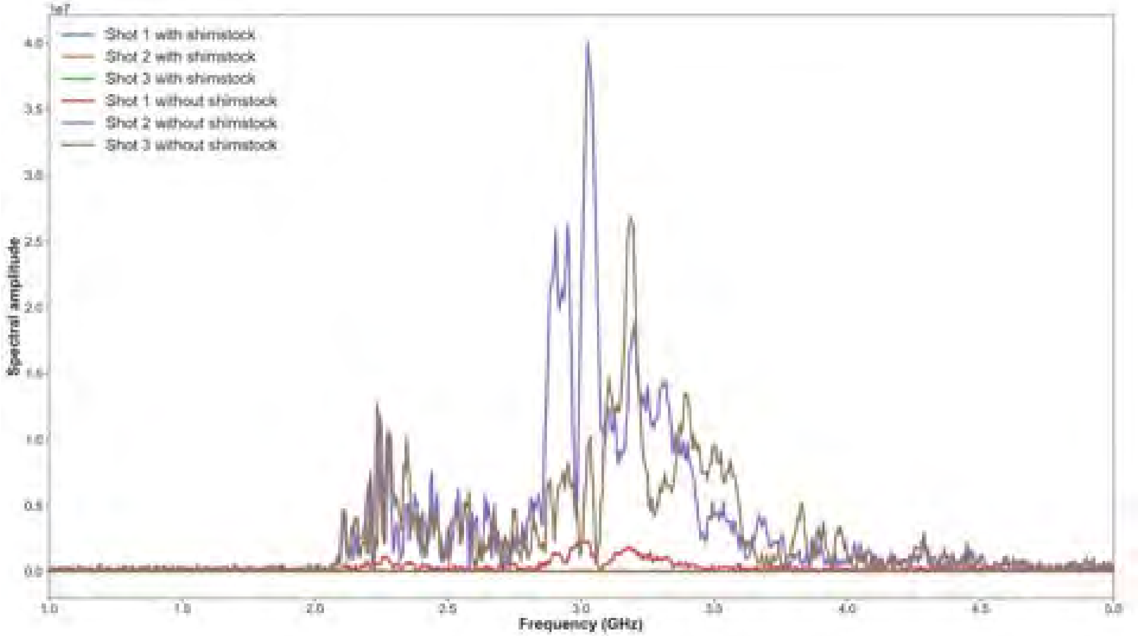

Figure 6. This graph shows plots of the FFTs of 6 shots. Three shots were performed with the cavities closed (with shim stock) and three shots were performed with open cavities (without shim stock). We can observe the amplitudes of the signals without shim stock is much greater and has peaks within the expected frequency range in PIC simulations. FFT of signals with cavities closed are barely noticeable on the graph.

Before firing the MDO with cavities blocked a new window was machined and installed at an output of the MDO. After three shots we observed breakdown signs on the surface of the window (Fig. 7). We suspect that this is the damage from electrons that had high velocity in axial direction. We do not believe this occurred because of high electric fields.

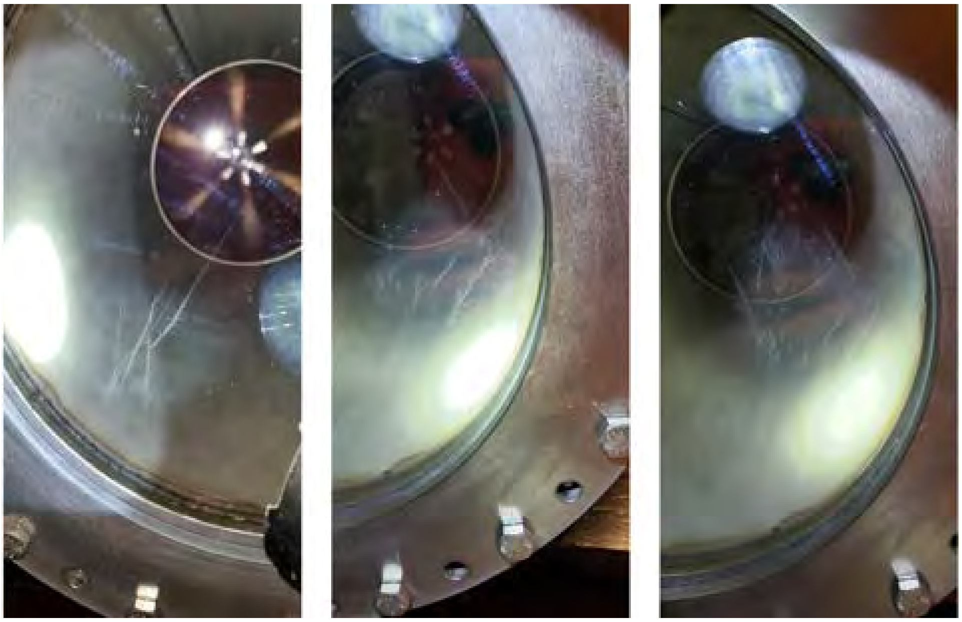

Figure 7. Streamers were observed on the surface of the dielectric window.

Figure 8 presents a time-frequency analysis (TFA) of the MDO and VC with the cavities closed. A broad spectrum is evident. Figure 9 presents a TFA of the MDO and VC with cavities opened.

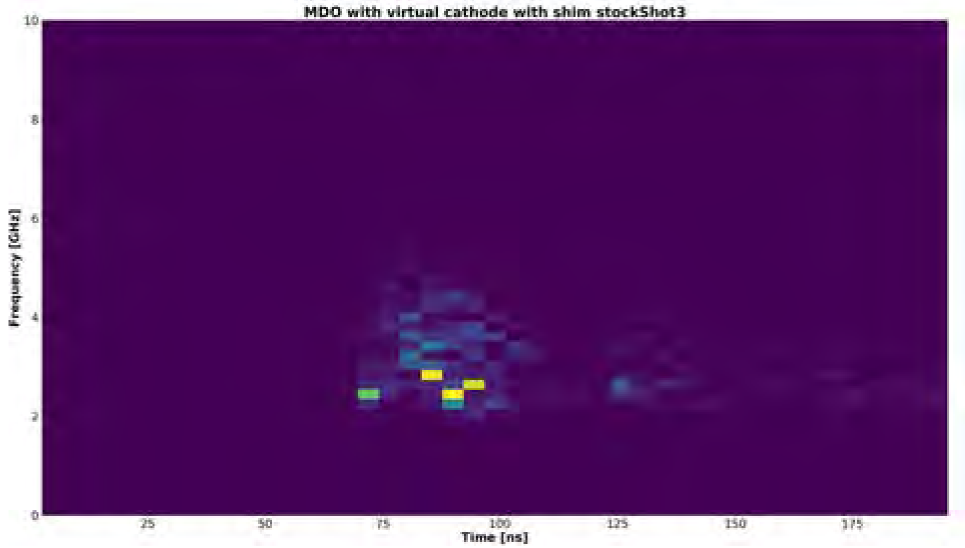

Figure 8. TFA of the output of the MDO with VC and cavities closed.

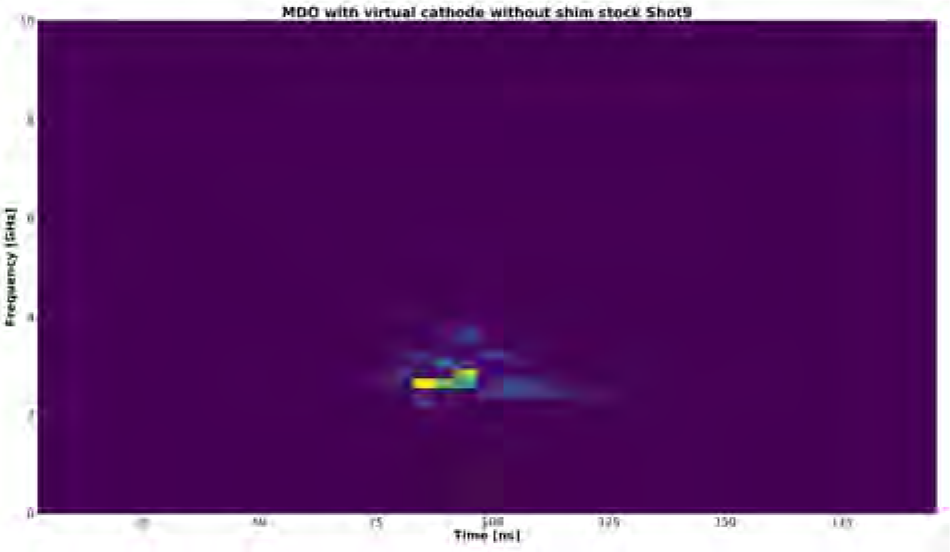

Figure 9. TFA of the output of the MDO with VC and cavities open.

UNM then proceeded to test the MDO with two VCs, one in the MDO and one at the output, and the diode shorted. The dead short shots that we experienced in attempting to operate the MDO with two virtual cathodes resulted in higher-than-average radiation readings in front of the MDO, as measured using thermoluminescent dosimeters (TLDs). UNM Radiation Safety provided a set of quick read dosimeters and we took a series of shots to mitigate this problem. We are also performing PIC simulations to redesign electron beam injection into the MDO with virtual cathode to mitigate the impedance collapse we observed in experiments.

The MILO laboratory has spent the initial 5 months first by building the cathode test bed and then by running experiments in collaboration with Dr. Steve Fairchild of Air Force Research Laboratory RX division. Dr. Fairchild spent 3 weeks at UNM and supplied several cathodes: CsI-coated carbon fiber and wound/sewn carbon nanotubes – the latter which were fired after this period of performance. Data has been collected at various voltages on the CsI cathode at various anode-cathode (A-K) gaps and with various voltages. This was preceded by the completion of the linear transformer driver (LTD) target housing and vacuum system, although the vacuum system had experienced some issues due to the nature of the LTD. During the next few months we continued firing the various cathodes, collecting electrical, imaging, and some interferometry data. The latter is somewhat in question as during the present experiments some of the cathodes have shown asymmetric emission and plasma generation or have not turned on at all. This data is consistent with Dr. Fairchild's previous experiments and, hence, the plan going forward is to increase the field strength by changing the A-K gap as well as increasing the accelerating voltage. There are some additional accelerator issues that we need to resolve but those are relatively easy (add another pump!) to solve.

Figure 9 shows a cut-away drawing of the test bed; of interest is 360º access provided by the various ports looking directly onto the target. The test bed is a dynamic structure with a variable A-K gap to suit the experiment. In this image there are two B-dots which were replaced by a Rogowski in the cathode section and one in the anode structure. This is what allows us to field our optical diagnostics. Figure 10 is an open shutter photograph of the LTD and the new target test bed prepared for a cathode shot. On this particular shot not all LTD bricks fired, as expected, as these are dependent on the charge voltage. Notice the light from the plasma emission on the 2.75 conflat window facing the camera.

Figure 11 shows the cathode on prior to mount on the cathode holder (the off-axis placement is not representative of operational use). Figure 12 shows two images, the first is with all three channels of the open shutter camera and the second is using only the 2nd channel. The black posts are for the return current.

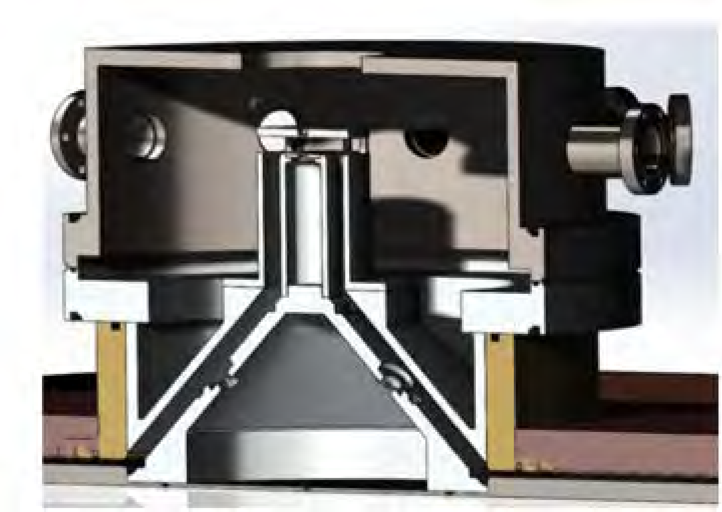

Figure 9. Cut-away parametric drawing of the experimental cathode test bed built for our LTD.

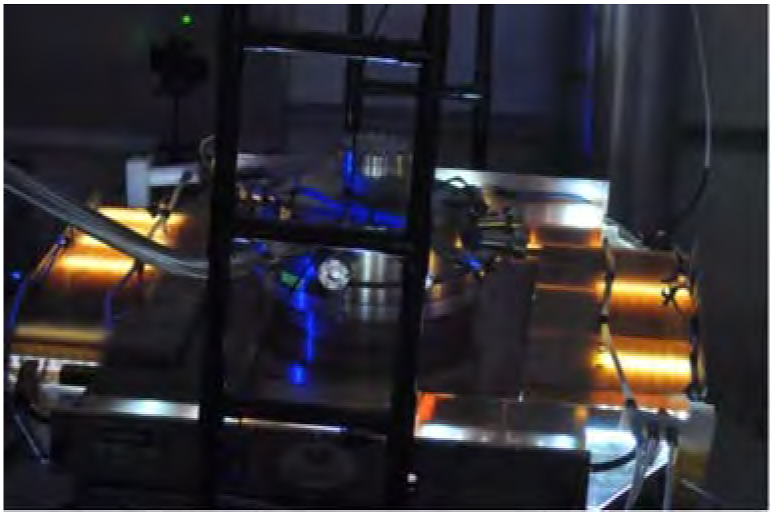

Figure 10. Photograph of the LTD firing with a cathode load.

Figure 11. Photograph of cathode prior to mounting on the test bed holder.

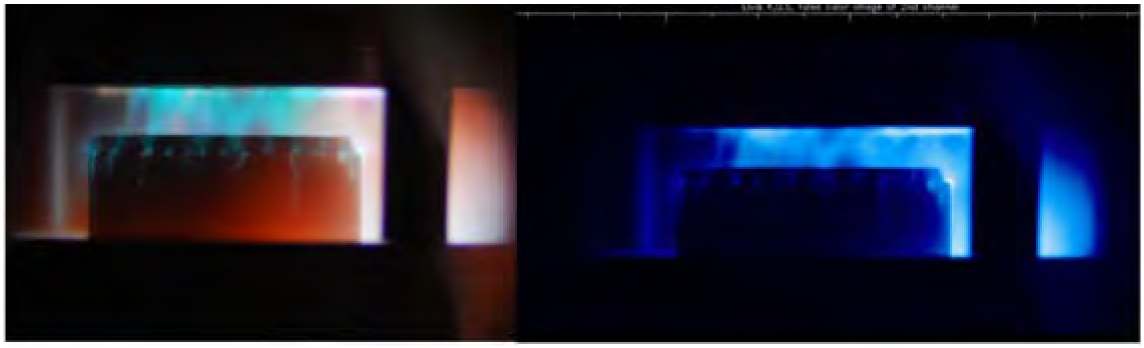

Figure 12. Open shutter images of the cathode being fired on the LTD test stand. The 2nd frame is post processed to look for hot spots and other evidence of emission areas.

The RF issue still needs to be addressed. It is unfortunate that high voltage switches are essentially dipole radiators of electromagnetic energy as a function of voltage and geometry and this work is ongoing. We are mapping this effect, but as it is dependent on voltage, it takes time to complete the survey. We will have to come up with some clever solution as we are mitigating the effects on a case by case basis (we are losing open shutter cameras and network control systems which control our accelerator and digitizers) from time to time.

Regarding the pulsed power LTD, the majority of our time these months was taken up by the LTD cathode experiments; however, we continue to make headway on our PIC simulations of the magnetron (and eventually MILO) frequency agile source. There is the issue that our principal code, LSP, is not generating the right geometry and this needs to be addressed. In the same vein, our work on the transmission line has shifted from using CST as our time-domain electromagnetics code to a field precision product called Aether, as the former is not capable of handling a time dependent switch conductivity which in turn keeps us from knowing the effect the peaker switch has on the rise time of the device.

During this period of performance, we carried out a series of numerical simulations on a modern MILO design to investigate voltage scaling, rise time effects as well as to optimize and validate our code. Figure 13 shows the geometry of these simulations.

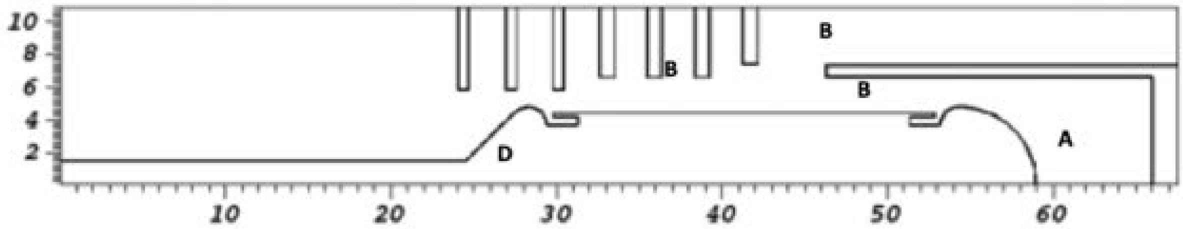

Figure 13. MILO geometry being investigated in our PIC codes. Of great interest are regions labeled by B as ion production regions, region A as a possible control for device operation, and region B for electron launch.

Figure 14 shows the results of the simulations, described in the caption.

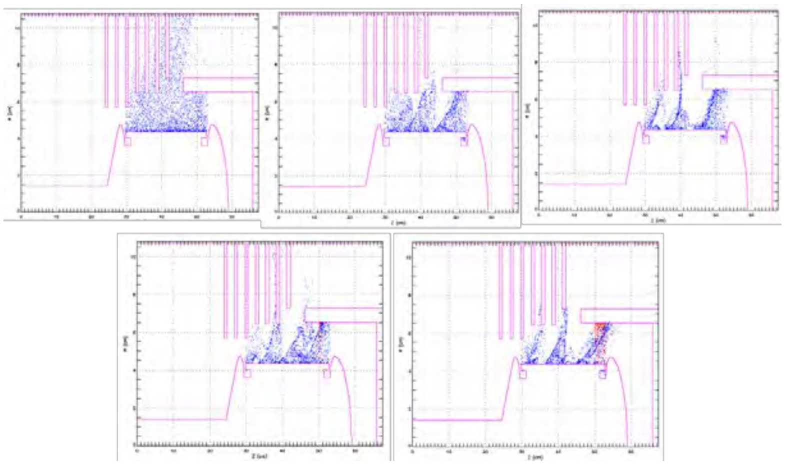

Figure 14. Discrete time steps in a MILO PIC simulation. Left to right shows at 5 ns large electron flow prior to critical current insulating the flow. At 20 ns, frame B, we start to see some organization and at 40 ns we see synchronicity. At the fourth frame, approximately 60 ns into the run we see the onset of neutral desorption from the beam dump region leading to ion production. This is a consistent region for electron energy deposition reaching temperatures where the threshold for desorption is exceeded. The last frame shows constant production of ions, difficult to see at 90 ns but still present are the ions produced from the vanes and cavities.

Figure 15 shows the results of a voltage scan on this geometry. The first frame is the voltage measured prior to the slow wave structures, the 2nd frame is the current and finally the 3rd frame is the impedance.

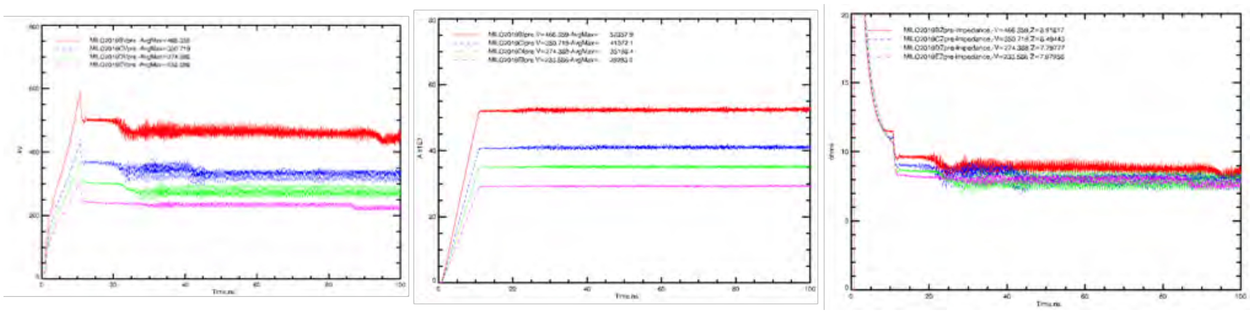

Figure 15. The results of voltage scan on the MILO in PIC simulations.

Figure 16 shows the spectral content (a) of these shots. For clarity of presentation 16(b) only shows the output of one shot of RF generation. Figure 16(c) shows the wavelet, time-frequency analysis showing one principal frequency.

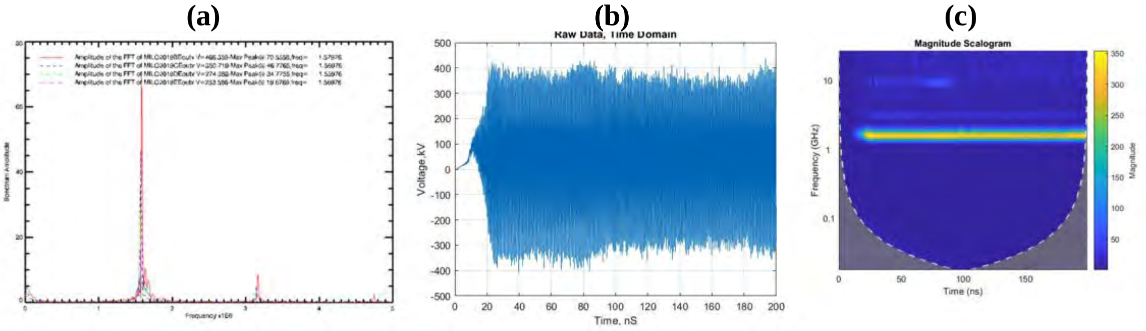

Figure 16. (a) Fourier transform of the out showing the spectral content; (b) the output of one shot of high power RF generation; (c) the wavelet, time-frequency analysis showing one principal frequency for the entire duration of the pulse.

3. Findings and Conclusions

The significance of the results achieved to-date is as follows. For the ultra-high-efficiency relativistic magnetron work, the most significant result achieved to-date is that the MDO with one VC did generate HPRF in the frequency range predicted by PIC simulations. Furthermore, when the MDO cavities were shorted, a low-level broadband spectrum of radiation was generated, presumably attributed to the vircator effect by the VC. This result is very promising in that it supports UNM’s hypothesis that the MDO with VC can operate with very long pulse length and not experience pulse shortening, a significant result for the Navy.

Another significant, although negative, result is that the MDO with VC completed led to a short. This requires a redesign of the inlet to the MDO.

Regarding the MILO, the significance of the results achieved to-date is that the behavior of our MILO in numerical space is understandable and allows for a much broader parameter scan. More specifically, how is the behavior of the device affected by switching from line to load impedance and does this improve the efficiency? Additionally, what changes in the structure, either material or geometric, must be made to reduce the amount of desorbed neutrals? Also, of key importance is whether we will be able to predict the load on the vacuum system which is a key factor driving the pulse repetition of these crossed field devices.

4. Plans and Upcoming Events

For the ultra-high-efficiency relativistic magnetron work, the plans in the upcoming year are to design a magnetic mirror field to implement with the MDO. The PI is supervising a UNM Electrical and Computer Engineering (ECE) senior design team who is working on this. Also, additional work redesigning the inlet to the MDO with VC is underway.

Major milestones would be successful testing of the MDO with VC and successful testing of the MDO with TC and magnetic mirror field.

For the MILO, as per our original proposal, we are beginning to plan for the development and build of a functional MILO for use as a test source by NSWC. This device will incorporate the best of our design choices at a relevant frequency and with relevant parameters for effects testing.

5. Transitions and Impacts

As part of its collaboration with NSWCDD, UNM is transitioning its MDO with TC, it will transition its MDO with VC, and it will transition its MDO with TC/VC and magnetic mirror field. A joint conference presentation was given at PPPS-2019 in Orlando in June:

> D. Andreev, A. Kuskov, D. Reass, A. Sandoval, E. Schamiloglu, Y.-J. Chen, J. Kreger, and J. Chaparro, "Rep-Rated Testing of a Compact Magnetron with Diffraction Output (MDO) and Plans for Testing the full MDO," IEEE PPPS-2019 (Orlando, FL, June 23-28, 2019).

Ongoing collaboration with Steven Fairchild from AFRL/RX will lead to joint publications.

Ongoing collaboration with AFRL/RD – Brad Hoff will lead to joint publications.

6. Collaborations

NSWCDD – John Kreger and Jack Chen - HRF collaboration – We discussed proceeding with MDO and transparent cathode testing at NSWC

AFRL/RX – Steven Fairchild – HPRF cathode collaboration – We are discussing collaborative research on HPM cathodes; Dr. Fairchild has made several visits to UNM for several weeks at a time

AFRL/RD – Brad Hoff – HPRF cathode and switch collaboration – We are discussing collaborative research on HPM cathodes and pulsed power switches

7. Personnel

Principal investigator – Edl Schamiloglu (0.5 person month)
Co-investigator or Co-PI – Salvador Portillo (2.5 person months)
Business Contact – Melissa Dee Sanchez
Team Members – none
Subs – none

8. Students

Artem Kuskov (Ph.D. student – 5 person months), Braulio Martinez-Hernandez (M.S. student – 5 person months) Stacie Hernandez (B.S. student, 2.5 person months)

9. Technology Transfer

N/A – except for ongoing collaboration with NSWC DD and joint conference presentation and joint experiments.

10. Products, Publications, Patents, License Agreements, etc.

Peer-reviewed publications acknowledging this grant:

1. a. Low Energy State Electron Beam in a Uniform Channel
   b. Plasma
   c. M.I. Fuks, D.A. Andreev, A. Kuskov, and E. Schamiloglu
   d. Keywords: high power microwaves; virtual cathode; magnetron with diffraction output; MDO; magnetic mirror
   e. Distribution Statement: Unlimited release
   f. Publication Status: published
   g. Publication Identifier Type: DOI
   h. Publication Identifier: https://doi.org/10.3390/plasma2020016
   i. Publication Date: 27 May 2019
   j. Volume: 2
   k. Issue: 2
   l. First Page Number: 222
   m. Publication Location: Basel, Switzerland
   n. Acknowledgement of Federal Support? Yes
   o. Peer Reviewed? Yes

2. a. Application of a Magnetic Mirror to Increase Total Efficiency in Relativistic Magnetrons
   b. Physical Review Letter
   c. M.I. Fuks and E. Schamiloglu
   d. Keywords: high power microwaves; virtual cathode; magnetron with diffraction output; MDO; magnetic mirror
   e. Distribution Statement: Unlimited release
   f. Publication Status: published
   g. Publication Identifier Type: DOI
   h. Publication Identifier: https://doi-org.libproxy.unm.edu/10.1103/PhysRevLett.122.224801
   i. Publication Date: 7 June 2019
   j. Volume: 122
   k. Issue: N/A
   l. First Page Number: 224801
   m. Publication Location: Ridge, NY, USA
   n. Acknowledgement of Federal Support? Yes
   o. Peer Reviewed? Yes

3.

a. A Multibeam Metamaterial Backward Wave Oscillator
b. Physics of Plasmas
c. H. Seidfaraji, A. Elfrgani, C. Christodoulou, and E. Schamiloglu
d. Keywords: high power microwaves; backward wave oscillator; metamaterials
e. Distribution Statement: Unlimited release
f. Publication Status: published
g. Publication Identifier Type: DOI
h. Publication Identifier: https://doi-org.libproxy.unm.edu/10.1063/1.5100159
i. Publication Date: 22 July 2019
j. Volume: 26
k. Issue: N/A
l. First Page Number: 073105
m. Publication Location: Melville, NY, USA
n. Acknowledgement of Federal Support? Yes
o. Peer Reviewed? Yes

4. a. Review of the Relativistic Magnetron (Featured Article)
b. Matter and Radiation at Extremes
c. D.A. Andreev, A. Kuskov, and E. Schamiloglu
d. Keywords: high power microwaves; virtual cathode; relativistic magnetron; magnetron with diffraction output; MDO
e. Distribution Statement: Unlimited release
f. Publication Status: published
g. Publication Identifier Type: DOI
h. Publication Identifier: https://doi-org.libproxy.unm.edu/10.1063/1.5100028
i. Publication Date: 11 October 2019
j. Volume: 4
k. Issue: N/A
l. First Page Number: 067201
m. Publication Location: Melville, NY, USA
n. Acknowledgement of Federal Support? Yes
o. Peer Reviewed? Yes

5. a. A ’Crab-Like’ 12-Cavity Relativistic Magnetron with Diffraction Output using Single-Stepped Cavities Driven by a Transparent Cathode
b. Physics of Plasmas
c. M. Liu, Q. Yang, E. Schamiloglu, J. Feng, Y. Teng, M.I. Fuks, W. Jiang, W. Wu, C. Liu, and P. Zhang
d. Keywords: high power microwaves; magnetron with diffraction output; MDO; transparent cathode
e. Distribution Statement: Unlimited release
f. Publication Status: published
g. Publication Identifier Type: DOI
h. Publication Identifier: https://doi-org.libproxy.unm.edu/10.1063/1.5097319
i. Publication Date: 23 October 2019
j. Volume: 26
k. Issue: N/A
l. First Page Number: 103301

    m. Publication Location: Melville, NY, USA
    n. Acknowledgement of Federal Support? Yes
    o. Peer Reviewed? Yes

6.
    a. A Multibeam Metamaterial Backward Wave Oscillator (Featured Article)
    b. Advances in Engineering
    c. H. Seidfaraji, A. Elfrgani, C. Christodoulou, and E. Schamiloglu
    d. Keywords: high power microwaves; backward wave oscillator; metamaterials
    e. Distribution Statement: Unlimited release
    f. Publication Status: published
    g. Publication Identifier Type: url
    h. Publication Identifier: https://advanceseng.com/multibeam-metamaterial-backward-wave-oscillator/
    i. Publication Date: 26 November 2019
    j. Volume: N/A
    k. Issue: N/A
    l. First Page Number: N/A
    m. Publication Location: Ottawa, Ontario, Canada
    n. Acknowledgement of Federal Support? Yes
    o. Peer Reviewed? Yes

Conference Papers

None

Conference Presentations

1. I. Chavez, E. Schamiloglu, K. Ilyenko, Y. Tetyana, and S. Portillo, “Design of a Long Pulse High Energy Water Transmission Line to Drive HPM Sources,” IEEE PPPS-2019 (Orlando, FL, June 23-28, 2019).

2. D. Andreev, A. Kuskov, D. Reass, A. Sandoval, E. Schamiloglu, Y.-J. Chen, J. Kreger, and J. Chaparro, “Rep-Rated Testing of a Compact Magnetron with Diffraction Output (MDO) and Plans for Testing the full MDO,” IEEE PPPS-2019 (Orlando, FL, June 23-28, 2019).

3. R. Beattie-Rossberg, A. Kuskov, S. Portillo, and E. Schamiloglu, “Investigation of Sterolithographic Laser Additive Manufacturing Resins for Pulsed Power Applications,” PPPS-2019 (Orlando, FL, 2019).

4. D. Andreev, A. Kuskov, and E. Schamiloglu, “50 Years of High Power Microwaves and 43 Years of the Relativistic Magnetron,” DEPS UK/US Directed Energy Workshop (Shrivenham, UK, July 22-26, 2019).

Books

J.W. Luginsland, J.A. Marshall, A. Nachman, and E. Schamiloglu, *Advances in High Power Microwave Sources and Technologies using Metamaterials* (IEEE Press/Wiley, New York, NY, 2020) (in preparation).

Theses

None

Websites

None

Patents

None

Other Products:

None

11. Point of Contact in Navy

NSWCDD – John Kreger and Jack Chen – we have periodic (at least quarterly) telecons and several (at least twice yearly) in person visits.

12. Acknowledgement/Disclaimer

This work was sponsored by the Office of Naval Research (ONR), under grant number N00014 - 19-1-2155. The views and conclusions contained herein are those of the authors only and should not be interpreted as representing those of ONR, the U.S. Navy or the U.S. Government.

Material Assessment for High Power RF Systems

Grant No. N00014-19-1-2599

Period of Performance: April 1, 2019 to September 30, 2019

Prepared by:
Dr. Somnath Sengupta, Principal Investigator
Powerhouse Consulting Group
3210 Boones Lane
Ellicott City, MD 21042-2138
Tel: (443) 820-7798
Email: somnath@powerhouseconsultinggroup.com

Powerhouse Consulting Group

DEPARTMENT OF THE NAVY • UNITED STATES MARINE CORPS

This work was sponsored by the Office of Naval Research (ONR), under grant number N00014 -17-1-2848. The views and conclusions contained herein are those of the authors only and should not be interpreted as representing those of ONR, the U.S. Navy or the U.S. Government.

Grant or Contract Number: N00014-19-1-2599
Date Prepared: January 31, 2020
Project Title: Material Assessment for High Power RF Systems
Annual Summary Report: CY 2019; 1 April 2019 to 30 September 2019
Principle Investigator: Somnath Sengupta, 443 820 7798;
somnath@powerhouseconsultinggroup.com, Powerhouse Consulting Group

Section I: Project Summary

1. Overview of Project

Abstract: This document contains the activities/accomplishments, findings/conclusions, and recommendations for future work in the field of low loss tunable dielectric ceramic for high power microwave applications

Objective: The overall objective of our work is to assess a class of low loss tunable dielectric materials for moderate to high (between 10 and 100 watts) RF incident power aimed for directed energy applications.

Introduction: High Power Microwave (HPM) sources may deliver 10s to 100s of GWs to a transmitting antenna. Actively controlling the antenna sidelobes is a method to avoid equipment fratricide while maintaining the maximum amount of power directed on a target is important for directed energy applications. A robust and inexpensive way to implement sidelobe control will benefit high-power Directed Energy (DE) implementation.

Low-loss, voltage tunable dielectric materials have been implemented in tunable device applications including filters, antennas and oscillators amongst others. Dielectric materials have an advantage in power handling over conventional tunable approaches like Monolithic Microwave Integrated Circuits (MMIC) and diodes. Additionally, they are low cost and can have tailored compositional variances that can enable multiple applications.

Tunable materials are attractive because of their potential for fast tuning speed (microseconds) and ability to optimize the electronic loss and tunability. Past uses of these tunable materials have shown that they can be fabricated in a variety of compositions to address applications from VHF to Ka-band. Phase steerable, true time-delay lines, tunable patch antennas, and tunable dielectric lenses are some of the examples of antenna designs that have been demonstrated; none of these components or subsystems have been demonstrated for high (100s of watts and above) incident RF power.

As for **naval relevance,** one of the applications concerns shipboard deployment of HPM systems on naval vessels. By reducing the antenna sidelobes, the probability of EMI/EMC (fratricide) may be further reduced, potentially resulting in increased gain of the main lobe. Sidelobe reduction is of interest in non-HPM system applications also. This technology will allow the Navy to pursue shipboard, high-power electromagnetic maneuver warfare while maintaining the ability to communicate. By reducing the sidelobes of antennas deployed in current and future HPM systems, we may be able to reduce time-out-of-action due to system blanking from other RF systems. Sidelobe emission reduction may also reduce the radar cross section (RCS) of Naval antennas. Development of this technology will assist in reducing EMI/EMC issues and assist in the transition of HPM DEW to the warfighter. These tunable dielectric materials may also have applications in moderate-to-high power, on-the-move communication systems for the Navy.

Background: This research aims to assess innovative tunable dielectric materials for implementation to reduce, on-command, sidelobes of antennas as the main lobe is steered. The approach includes the fabrication of tunable dielectric materials and the material's response functions (ε', ε'', tunability, intermodulation products (IP3), and breakdown voltages). Tunability is defined as the percentage change in dielectric constant of the material with applied electric field. There are two iterative tasks in this project: Task 1: Fabricate and characterize the material properties of the tunable dielectric material and Task 2: Measure the RF/Microwave properties of the selected tunable dielectric materials.

2. Activities and Accomplishments

The performance start date for this contract is August 1, 2019. So, accomplishments reported here are from August 1, 2019 through September 30, 2019.

a. The kickoff was held on July 31st at the ONR offices. Technical experts from NRL and NSWCDD participated along with the ONR team led by Mr. Ryan Hoffman. Dr. Sengupta and Dr. Mandelbaum attended from Powerhouse. Powerhouse presented its plan for execution that was well received. The consensus was to monitor the progress of the fabrication of the ceramics and its repeatable performance in the low RF power regime before delving deeply into high RF power performance.

b. Prior to the kickoff,

- Powerhouse had ordered the necessary ceramic materials for fabricating the tunable dielectric ceramics. Barium Strontium Titanate (BST) will be investigated under this program.
- RF measurement equipment was also ordered prior to the kickoff.
- X-ray characterization facilities were identified. X-ray characterization of each ceramic material is necessary for phase confirmation after calcination and sintering.
- Two polishing facilities were contacted to discuss the price and turnaround time for the polished ceramics prior to electrical and RF measurements; one polishing facility was selected.
- We executed all necessary paperwork for our consultant, Dr. Mandelbaum.

c. In August,

- We initiated the ceramic fabrication process. BST (Ba=0.6; Sr=0.4) composition was chosen as the first composition to try out the entire process before increasing the number of samples. The calcined powder has been sent to the X-ray laboratory to determine the phase of the powder. The results showed that we were attaining the ceramic phase of the material during calcination.
- We also procured commercial Barium Titanate (BT) samples and used one of our older BST samples (made from commercial BST powder) for the polishing test run. The samples were polished on both sides to thicknesses of 1 mm and 0.5 mm. At the rate of an electric field of 2V/micron, that would result in a total bias voltage of about 1000 V maximum keeping it at a reasonable level without worrying about spark gaps or sample damages.
- The electrical measurements were divided into 3 steps
    a. Capacitance (and therefore epsilon) and dissipation factor measurement with an LCR meter to evaluate the metallic contacts on the samples.
    b. Same measurements as (a) above with an applied bias field of 1000 V (maximum) to determine the electrical contacts under bias and any other ancillary issues like shorting due to material imperfections, etc.

c. Measurement of low power RF propagation up to 1 GHz through the device setup described in item (b) above to study the capacitance, insertion loss, self-biasing and thermal heating issues.

With regards to the first step of measuring the capacitance, dielectric constants, and dissipation factor of known samples to verify the measurement system, we have performed preliminary measurements. Our measurements at 1 KHz produces acceptable vales for dielectric constants of both the Barium Titanate and the Barium Strontium Titanate. We then measured capacitance at 1 KHz. The measured values of BT and BST were similar to the published values thereby giving us confidence in our measurement methodology.

3. Findings and Conclusions

The objective of this program is to assess a class of low loss tunable dielectric materials for moderate to high (between 10 and 100 watts) RF incident power aimed for directed energy applications. To accomplish that, we must establish verifiable ad repeatable methods of fabricating the material and means of measuring them. In the August- September time frame, we have been able to verify the compositional formula of the ceramics and shown that our low frequency measurement method is reliable.

4. Plans and Upcoming Events

The next major steps (milestones) of the program are

a. Demonstrate a ceramic fabrication process that will produce ceramic materials of the same composition (over a wide molar ratio range of Ba:Sr) with similar X-ray, density, and grain morphology results.
b. Measure the RF and electrical properties of all the ceramic material samples reliably to establish a pattern of dielectric properties
c. Once (a) and (b) above are accomplished, then repeat the above steps for BST/oxide composites to examine the electrical and RF properties of even lower loss electronic ceramics.
d. Measure the influence of high RF power on all BST compositions.

Recommendations for Future Work: Beyond the four milestones described in the previous section, we recommend that these materials are measured under higher incident RF power (especially pulsed RF power) to determine their characteristics and viability for components for directed energy systems.

5. Transitions and Impacts

No information to report

6. Collaborations

No information to report

7. Personnel

Principal investigator- Somnath Sengupta, PhD (0.75 person month effort)
Business Contact- Somnath Sengupta
Subs- Idan Mandelbaum, PhD (consultant)

8. Students

Not Applicable

9. Technology Transfer

Not Applicable

10. Products, Publications, Patents, License Agreements, etc.

No information to Report

11. Point of Contact in Navy

Joseph Croman (NRL); last contact date January 15, 2020
Victor Gehman (NSWCDD E13); last contact date December 31, 2019
Matthew Laskoski (NRL); last contact date January 16, 2020

12. Acknowledgement/Disclaimer

This work was sponsored by the Office of Naval Research (ONR), under grant (or contract) number N00014-19-1-2599. The views and conclusions contained herein are those of the authors only and should not be interpreted as representing those of ONR, the U.S. Navy or the U.S. Government.

Theory and Experiments on Magnetically Insulated Line Oscillator (MILO)

Grant No. N00014-19-1-2262

Annual Report for Fiscal Year 2019

Period of Performance: May, 1, 2018 to September 30, 2019

Prepared by:
Professor Ronald Gilgenbach, Principal Investigator
University of Michigan
Department of Nuclear Engineering and Radiological Sciences
2355 Bonisteel Blvd
1905 Cooley Building
Ann Arbor, MI 48109-2104
Tel: (734) 763-1261
Email: **rongilg@umich.edu**

This work was sponsored by the Office of Naval Research (ONR), under grant number N00014 -17-1-2848. The views and conclusions contained herein are those of the authors only and should not be interpreted as representing those of ONR, the U.S. Navy or the U.S. Government.

Grant or Contract Number: N00014-19-1-2262
Date Prepared: 1/14/2020
Project Title: Theory and Experiments on Magnetically Insulated Line Oscillator (MILO)
Annual Summary Report: FY2019
Principal Investigator:

Ronald M. Gilgenbach
(734) 763-1261
rongilg@umich.edu
University of Michigan, Ann Arbor, MI, US

Section I: Project Summary

1. Overview of Project

Abstract: In the first 5 months of this project, the University of Michigan has made progress on the development of novel MILO concepts, which may address the previous low efficiency and narrow bandwidth of MILOs. We have performed simulations using Microwave Studio CST to investigate the feasibility of MILO operation with applied magnetic fields in several configurations, and have observed a decrease in the required current for magnetic insulation when a transverse magnetic field is externally applied to a smooth-bore, planar MILO. We have constructed the complete solution of the Brillouin flow in planar MILO or planar Relativistic Magnetron, or some combination of the two, in cylindrical geometry with axial electron flow (as in cylindrical MILO), in cylindrical geometry with azimuthal electron flow (as in cylindrical magnetron and cylindrical RM), and in the radially converging flow in MITL (as in a linear transformer driver (LTD)).

Objective: This project aims to improve understanding of the fundamental science of Magnetically Insulated Line Oscillators (MILO) through improvements in computational modeling and analytic theory verified by experimental results. This improved understanding will be applied to the development of efficient, multi-tone MILOs, and (with the aid of the University of New Mexico) transitioned to Naval Surface Warfare Center Dahlgren Division (NSWCDD) for testing on high-value targets of interest.

Introduction: The MILO is a crossed-field device, basically, a linear magnetron, in which the magnetic field is self-generated by the electron current, thereby eliminating or reducing the need for external magnets or magnetic field coils. This means that the MILO is more compact, and lighter, than other high power microwave (HPM) sources, including the relativistic magnetron.

Background: The goal of this research program is to generate multi-spectral, high power microwaves from the Magnetically-Insulated-Line Oscillator (MILO). The topic of MILO was investigated extensively throughout the 1990's with excellent results, particularly at the Air Force Research Laboratories. However, since that time there have been major developments in: 1) low impedance, high current pulsed power (Linear Transformer Driver, LTD); 2) 3-D EM particle-in -cell codes; and 3) innovative manufacturing techniques (e.g., additive manufacturing/ 3D printing) that justify a new examination of MILO in the USA. It should be mentioned that several Chinese institutions have extensively investigated MILO and LTD in recent years, so it is crucial that the US conduct theory, simulations, and experiments on MILO to reduce the chances technological surprises.

Previous ONR research at the University of Michigan, demonstrated that the Multi-frequency Recirculating Planar Magnetron (MFRPM) concept could generate 10's MW, high power microwaves in two different frequency bands, simultaneously. It is expected that the MILO could generate even higher power levels at single or multiple frequencies. This research program consists of analytic theory (e.g., MILO Buneman-Hartree condition), 3-D EM PIC simulations and experiments.

The primary thrusts of this research include: a theoretical analysis of the Buneman-Hartree condition for MILO; analysis of MILO efficiency, gain, and startup; the viability of multi-frequency MILO; the effects of a modest external magnetic field; the compatibility of new low impedance drivers (such as LTD) for MILO; opportunities for additive manufacturing of MILO; and technology transfer for NSWC Dahlgren.

The first year of this research program is concentrating on fundamental research to develop the scaling laws (e.g., Buneman-Hartree condition), computational modeling, and moderate-current, single frequency experiments on the MILO. The second and third year will become more applied MILO research with technology transfer to the Naval Surface Warfare Center at Dahlgren. UM will collaborate closely with University of New Mexico (UNM) as well as NSWC-Dahlgren.

MILOs were intensively investigated in the USA (1980's-2000), but recently, substantial research and development is underway by potential competitor countries. The fundamental research undertaken in this project addresses some of the critical problems facing Navy operations. Enhanced HPM capabilities are an important part of the toolkit to address electronic threats, and can provide a non-lethal response to the approach of unknown or undeclared vessels, as well as small airborne drones.

2. Activities and Accomplishments

While we are only 7 months into this research project (reporting on 5 months), we have designed and simulated a variety of potential MILO prototypes, primarily focusing on methods of lowering the required current and increasing efficiency. Additionally, we made significant strides in the analytic theory of MILO.

Analytic Theory of MILO:

MILO and relativistic magnetron (RM) are both crossed-field devices capable of generating high-power microwaves. The RM is basically the kilowatt-class microwave source that powers the microwave ovens, but upgraded in power exceeding a million times. The MILO is similar to RM but does not require an external magnetic field. These two are thus very different, yet similar, devices. RM possesses a moderately high efficiency (like the microwave oven). The MILO has a much lower efficiency, but has a tremendous system advantage because of its substantial reduction in size and weight (no external magnet) compared with RM.

The theoretical foundation for MILO was amazingly weak (even non-existent strictly speaking), though this device has been in existence for more than 30 years. One can find numerous erroneous statements, and grossly inadequate scaling formulas, in the MILO literature. This poor understanding of the MILO, in comparison with the RM, greatly hindered an effort to find an optimal crossed-field configuration, if one exists, that would combine the advantages of MILO and RM.

This forced us to provide a foundational study of Brillouin flow that is applicable to both MILO and RM. This is important because the Brillouin flow is now generally regarded as the prevalent equilibrium state in crossed-field devices, from which the Hull-cutoff condition (HC) and the Buneman-Hartree condition (BH) can be derived. The urgency of this problem may be understood if one notes that BH has never appeared in the open literature for a cylindrical MILO with an axial electron flow (which is the most common MILO configuration). Our intensive study of the Brillouin flow led to the following novel results. They are being written up for archival publication.

1. It is found that the most appropriate description of HC and BH, for both MILO and RM, is in terms of the AK voltage drop (V_a) and the total magnetic flux (A_a) within the crossed-field gap. The traditional use of the magnetic field (B) is inconvenient because the self-magnetic field could be strong and difficult to account for. The use of the current (I) is also inconvenient because there are three (3) components of currents in the Brillouin flow: the current on the anode, the current on the cathode, and the current carried by the electrons in the Brillouin hub.

2. In terms of V_a and A_a, we have found an analytic, closed form solution of the Brillouin flow and the associated HC and BH. This is applicable to both MILO and RM, or some combination of the two, as in the case where the total magnetic flux (A_a) is partially provided by an externally imposed magnetic field, and partially provided by the wall currents on the MILO.

3. Once the Brillouin flow solution, and the associated HC and BH are established (at a given combination of V_a and A_a), the mechanism for spoke formation and for conversion of the potential energy to RF, then become identical in MILO and in RM, or some combination of the two, as pointed out in Item 2.

4. In addition to the planar RM and MILO, we have also constructed the HC and BH for a cylindrical MILO with axial electron flow, whether the diode voltage V_a is relativistic or not. This analysis is important to explore the possibility of a low voltage MILO.

5. Our general analysis has been successfully extended to the radially converging Brillouin flow that would exist, for example, in the linear transformer driver (LTD), which has become the basic building block for the architecture in modern pulsed-power technology. Our complete characterization in the Brillouin flow (once V_a and A_a, and the geometry are given) allows a ready evaluation of the severity of the diocotron instability, which has long been suspected to cause the leakage current observed in the deeply insulated (or not so deeply insulated) region of MITL.

6. In summary, our group has now constructed the complete solution of the Brillouin flow in planar MILO or planar RM, or some combination of the two, in cylindrical geometry with axial electron flow (as in cylindrical MILO), in cylindrical geometry with azimuthal electron flow (as in cylindrical magnetron and cylindrical RM), and in the radially converging flow in MITL (as in a LTD).

Simulation and Experiment:

Using CST Microwave Studio, initial simulation work explored the effects of axial magnetic fields on MILO performance. After re-evaluating the task of achieving operation of a MILO on MELBA (at approximately 500 kV and 10 kA), it was decided to design a planar MILO. To simplify initial simulations, a "smooth bore" MILO was designed, shown in Figure 1, which lacks a slow wave structure in the anode. The cathode voltage is applied in coaxial geometry, giving rise to an electric field in the interaction space pointing from the planar anode inward to the planar cathode. An emitting strip is placed on the cathode to allow for liberation of electrons into the AK gap. Downstream of the planar diode is a cylindrical diode (also set as an emitting surface) and a collector, which exists to draw current and consequently generate a transverse magnetic field inside the interaction space. This is the self-generated magnetic field, which provides the crossed-field flow in MILO devices.

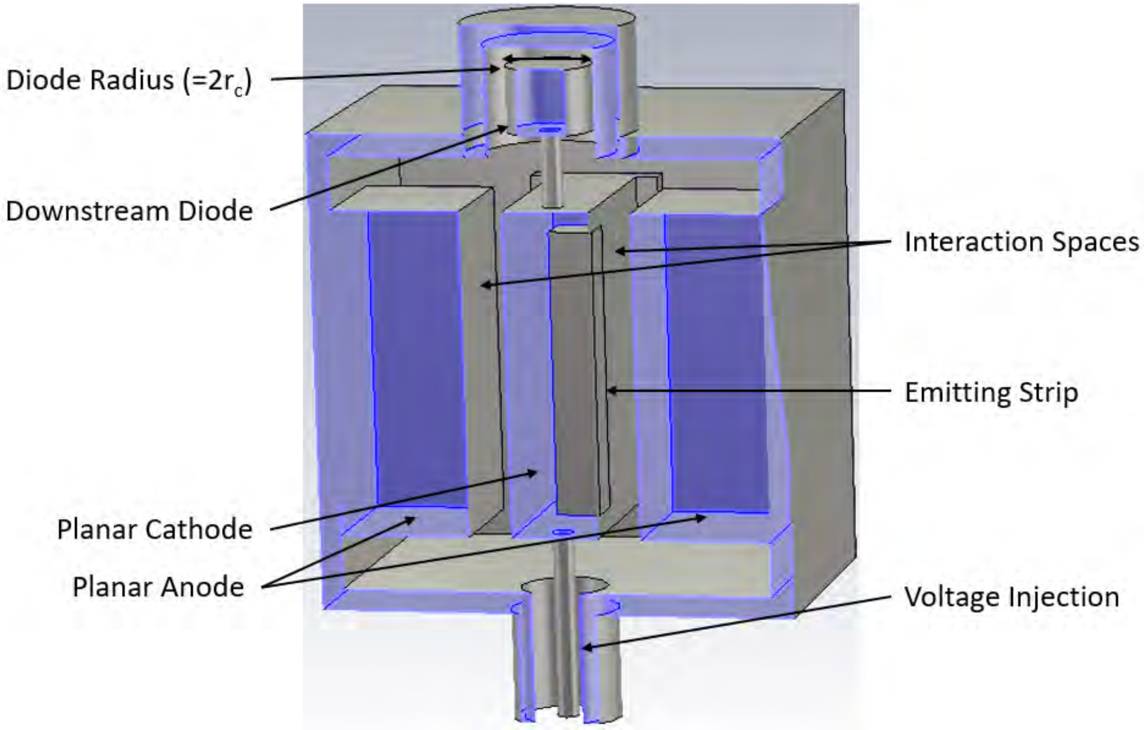

Figure 32: Planar, smooth-bore MILO cross section, demonstrating geometry and components.

The planar MILO geometry avails itself of many of the advantages the Recirculating Planar Magnetron (RPM) geometry holds over conventional magnetrons. Various extraction mechanisms can be applied to this structure and higher current could be drawn into the interaction space. The most important advantage for this application is that the transverse magnetic field generated by the downstream diode current can be assisted by an applied magnetic field, potentially reducing the current required for MILO operation and increasing its efficiency.

To analyze this device, we simulated the required magnetic field for magnetic insulation by varying the diode impedance, and thus the resulting current and self-generated magnetic field. As shown in Figure 2, the current collected by the planar anode, I_p, falls to zero as the total current, I_c, increases to 50 kA, indicating magnetic insulation (Hull cutoff) is achieved. The electron distribution can be observed directly in Figure 3. These simulations indicate that a transverse magnetic field of approximately 0.15 T is required to achieve Hull cutoff.

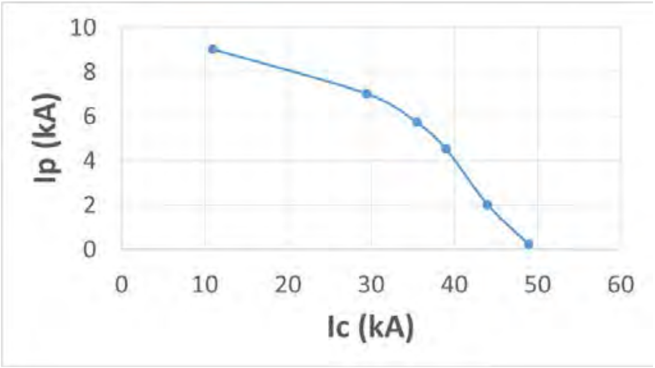

Figure 33: Current collected on the planar, smooth bore drift region as a function of I_c. Low values of I_p indicate good magnetic insulation.

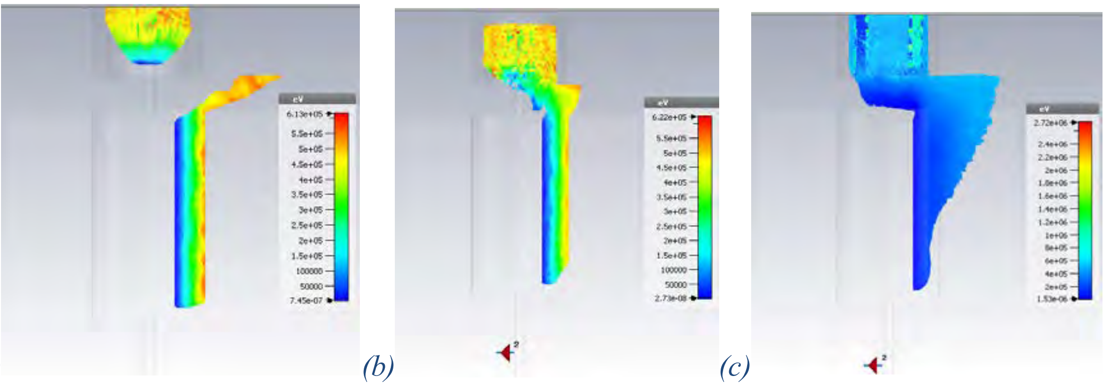

(a) *(b)* *(c)*

Figure 34: Flow of electrons as a function of I_c, which is 10 kA, 30 kA, and 50 kA in (a), (b), and (c), respectively.

As we are designing a MILO with lower current requirements, we next explored the feasibility of operating the planar MILO with only 10 kA. This was shown to produce an azimuthal magnetic field of 0.05 T. Consequently, we expect that applying a roughly 0.1 T external B field should produce magnetic insulation. This value is realistically achievable using an external electromagnet, and possibly even using permanent magnets placed within the chamber.

After establishing that the required external B field was reasonable, we next simulated the planar magnetron operation using a variety of applied external magnetic field values, and observed very little change in the self-generated B field. These simulations showed that an applied magnetic field of 0.11-0.12 T was sufficient, paired with the 0.05 T self-generated B field, to achieve magnetic insulation. Refinements of this design are currently under investigation.

Building from these simulations, which show the possibility of reducing the applied current by applying an external magnetic field, we used CST Microwave Studio to evaluate possible mechanisms for generating that field in a planar MILO. To explore the viability of generating a transverse magnetic field using permanent magnets, a set of plate magnets were procured and tested by undergraduate student Emma Guerin. CST simulations of this geometry, are in general agreement with the experimental testing.

3. Findings and Conclusions

Our group has now constructed the complete solution of the Brillouin flow in planar MILO or planar RM, or some combination of the two, in cylindrical geometry with axial electron flow (as in cylindrical MILO), in cylindrical geometry with azimuthal electron flow (as in cylindrical magnetron and cylindrical RM), and in the radially converging flow in MITL (as in a LTD). This will improve our understanding of the MILO, and assist the effort to find an optimal crossed-field configuration, if one exists, that would combine the advantages of MILO and RM.

Our simulations of applied magnetic fields show promise in reducing the required current for magnetic insulation and improving the operational efficiency. The application of a modest transverse magnetic field to a planar MILO, for example, can reduce the required current by a factor of 5.

4. Plans and Upcoming Events

In the coming months, we will perform initial tests of the smooth-bore planar MILO on the MELBA pulsed power generator, varying the application of external transverse magnetic fields and observing the current emission and distribution.

5. Transitions and Impacts

Nothing to report.

6. Collaborations

Air Force

We have several active HPM efforts with the Air Force Office of Scientific Research (AFOSR), Office of Naval Research and the Air Force Research Lab (AFRL).

- "High-Power Microwave Generation by Compact Linear Transformer Driver Technology", Ryan McBride ONR Young Investigator, 6/2018 – 5/2021
- "Multipactor and Breakdown Susceptibility and Mitigation in Space-based RF Systems", Multi-University Research Initiative (MURI), AFOSR #FA9550-18-1-0062, 8/2017 – 7/2022
- "High Power Recirculating Planar Amplifiers", AFOSR #FA9550-15-1-0097, 3/2015 – 8/2020.

AFOSR student training and research on these efforts has substantial overlap with ONR-sponsored research, serving to both increase student capability and develop techniques which can be applied to MILO improvements.

We are currently participating in an AFOSR MURI grant for "Multipactor and Breakdown Susceptibility and Mitigation in Space-based RF Systems". This project studies the basic physics of multipactor breakdown, with a focus on multipactor events in systems using multi-frequency, modulated signals. Consequently, the results are quite relevant for future HPM systems where high microwave power levels could result in multipactor breakdown events.

Building off our collaboration with UNM for this MILO project, we are also teaming with them for an AFOSR MURI proposal titled "Exploration of Fundamental Limits to High Power Electromagnetic (HPEM) Amplification".

Navy

Another member of our research group, Prof. Ryan McBride, has been awarded a Young Investigator award by ONR, for research on "High-Power Microwave Generation by Compact Linear Transformer Driver Technology". This project explores the use of compact linear transformer driver (LTD) technology to drive various high-power microwave (HPM) sources for the Navy's directed energy program. We anticipate that lessons learned on the LTD-MILO will be applied to this project, and vice versa.

DARPA

One member of our research group, Prof. Y. Y. Lau, under support of the DARPA-INVEST program (through subcontract from Leidos), made a breakthrough in the understanding of the emission characteristics of thermionic cathodes with active, semi-active, and non-emitting regions [D. Chernin, Y. Y. Lau, et al., "Effect of nonuniform emission on Miram curves," IEEE Trans. Plasma Sci., vol. 48, pp. 146-155 (2020)]. He is invited to give a Plenary Talk at the 2020 IEEE International Conference on Plasma Science [ICOPS, 24-28 May 2020, Singapore]

- Y.Y. Lau, "Integrated model for design optimization and manufacturing tolerance analysis for vacuum electron devices", DARPA # HR0011-16-C-0080, 4/21/16 - 4/13/20.

7. Personnel

Principal investigator
Ronald M. Gilgenbach, 0.27 person months, National Academy Member (N)

Co-PI
YY Lau, 0.27 person months, National Academy Member (N)
Nicholas M. Jordan, 2 person months, National Academy Member (N)

8. Students

3 graduate (1 funded from this ONR grant) and 2 undergraduate students assisted work on this project.

9. Technology Transfer

In concert with Prof. McBride's ONR YIP "High-Power Microwave Generation by Compact Linear Transformer Driver Technology", we are organizing a visit with John Kreger and Matt McQuage from NSWC Dahlgren. In the coming months, we will be showing them our facility and research progress, and discussing how this best fits with the Navy's current needs.

We have also collaborated with Air Force Research Laboratory in Albuquerque to acquire several components of the GW-class MILO designed and tested at AFRL. We have frequent discussions with AFRL and NRL scientists on a variety of HPM topics.

10. Products, Publications, Patents, License Agreements, etc.

Packard, Cooleybeck, Jordan, Sporer, Mazarakis, Lau, Gilgenbach, McBride, "HFSS and CST Simulations of a GW-Class MILO", IEEE Transactions on Plasma Science: Special Issue on HPM Generation, 2019. [Under review]

N.M. Jordan, D.A. Packard, C. Swenson, Y.Y. Lau, R.M. Gilgenbach, "Axial Magnetic Field Effects on Magnetically Insulated Line Oscillators (MILO)", 61st APS-DPP, Ft. Lauderdale, FL, Oct 2019.

Drew A. Packard, Christopher J. Swenson, Anna Cooleybeck, Brendan J. Sporer, Alexander E. Mazarakis, Nicholas M. Jordan, Y. Y. Lau, Ryan D. McBride, and Ronald M. Gilgenbach, "Simulations and Experiments on Magnetically Insulated Line Oscillators at the University of Michigan", International Vacuum Electronics Conference 2020, Monterey, CA, April 2020. [Submitted]

11. Point of Contact in Navy

Kreger, John D CIV NSWCDD, E13

Date of last contact: January 8, 2020.

12. Acknowledgement/Disclaimer

This work was sponsored by the Office of Naval Research (ONR), under grant (or contract) number N00014-19-1-2262. The views and conclusions contained herein are those of the authors only and should not be interpreted as representing those of ONR, the U.S. Navy or the U.S. Government.

NAWCWD High Power Capacitor SBIR Testing Support

Annual Summary Report for Fiscal year 2019

Grant Number N0001419WX00126, PR# 1400738220

1. Period of Performance: October 1, 2018 to September 30, 2019

Prepared by:
Shawn Higgins, Principal Investigator
Naval Air Warfare Center Weapons Division
China Lake, CA
Tel: (760) 939-1047
Email: shawn.higgins1@navy.mil

This work was sponsored by the Office of Naval Research (ONR), under grant number N00014 -17-1-2848. The views and conclusions contained herein are those of the authors only and should not be interpreted as representing those of ONR, the U.S. Navy or the U.S. Government.

Annual Report Format and Research Performance Progress Reports Information

Grant or Contract Number: N0001419WX00126, PR# 1400738220
Date Prepared: January 31, 2020
Project Title: NAWCWD High Power Capacitor SBIR Testing Support
Annual Summary Report: CY2019

Principle Investigator: Shawn Higgins, 760-939-1047, shawn.higgins1@navy.mil
Naval Air Warfare Center Weapons Division, China Lake

Section I: Project Summary

1. Overview of Project

High voltage temperature stable capacitors are required for pulse discharge applications where a high energy density with little capacitance change over temperature will enable lower costs, smaller applications, and circuits that are more reliable. Empirically, it has been found that NP0 rated capacitors with a tolerance of 0 ± 30 PPM/℃ and a capacitance variance, ΔC, of ±0.3% within the temperature range -55 ℃ to +125 ℃ respond with minimal degradation and damage to high speed and high voltage pulse discharges due to a stable dielectric.

An ONR led SBIR contract, N142-123, was awarded to promote technology advancement in energy dense capacitors meeting the NP0 specification for high power microwave (HPM) pulse discharge applications. Ballistic Devices Inc., produced several variants with specific capacitance and voltage ratings but lack the means to perform environmental and high current discharge measurements to validate the manufacture approach.

Previous work in fiscal year 2018 (FY18) showed the performance of Ballistic Devices' capacitors in ambient temperature as measured through a Keysight LCR meter measuring series capacitance and resistance (Cs-Rs) up to 2 MHz. This project continues the validation of the data associated with the capacitors through environmental stressing as well as evaluation under pulsed discharge conditions. The analysis includes Cs-Rs measurements up to 2 MHz in environmental conditions appropriate with NP0 capacitance rating (up to -55 ℃ and +125 ℃), as well as pulsed DC high-current discharge cycles measuring internal inductance and capacitance (LC) with low resistance oscillation ring down testing.

<ins>Abstract:</ins>

Naval Air Warfare Center Weapons Division (NAWCWD) China Lake performed measurements on Ballistic Devices Inc. high energy density capacitors in ambient temperatures and in an environmental conditioning oven from -55 ℃ to 120 ℃ in several increments in temperature, and measured at various frequency steps up to 2 MHz to determine parts per million (PPM) difference in capacitance. Capacitors placed in the environmental conditioning oven were selected from the ambient temperature testing based on their performance and where applicable: best, average, and worst performing. Damage was found in the form of fractures in the epoxy make up of several of the capacitors, developed during the low temperature cycle, as well as tacky epoxy at high temperatures.

After informing Ballistic Devices Inc. of the damage to the epoxy after exposure to low temperature, the manufacturer corrected its manufacturing method to improve upon the cure time of the epoxy coating. Ballistic Devices Inc. then sent out new sample to China Lake where they were applied to MIL-Spec environmental conditions. The results showed a lower percentage of epoxy damaged capacitors. Analysis by the Composites Engineering Laboratory at NAWCWD China Lake showed deltas in the capacitor materials coefficients of thermal expansion (CTE) that would contribute to epoxy failure. Specifically that the CTE of the epoxy used was twice that of copper and dielectric.

Capacitors exposed to MIL-Spec environmental conditions were then tested on high potential (HIPOT) measuring equipment up to rated voltage or the limit of the HIPOT equipment, 20kV. While the majority of the capacitor samples passed the test, it was found that varieties of capacitors in the environmental conditioning as well as capacitors that had been sitting on the shelf failed HIPOT measurements up to their rated voltage levels. A higher failure rate was observed on the capacitors subjected to MIL-Spec environmental condition.

Capacitors were placed in a custom fixture to measure a high current discharge through the capacitor via a 0.002 Ohm current viewing resistor (CVR). Findings, with measurements up to 2000 amps peak current, showed similar performance to a baseline capacitor.

Objective:

Using a custom test fixture created in FY18, which accommodates large capacitor housings of various thicknesses, measure Ballistic Devices Inc. capacitors' Cs-Rs with LCR meter from 100 Hz to 2 MHz in environmental conditioning oven from -55 °C to +125 °C. Calculate the PPM rating of the capacitors using the measurements obtained from the environmental conditioned capacitor testing. Perform a second round of environmental testing for newly manufactured capacitors.

Perform a high potential (HIPOT) test of all sample capacitors from Ballistic Devices Inc. to determine any failures at rated voltages.

Create a test circuit and evaluate high current, low impedance, pulse discharge through a baseline capacitor of known performance as well as Ballistic Devices Inc. capacitors. Utilize this data to compare pulsed measurements through capacitors and current capability.

Introduction:

Figures:

Tables:

Background:

Testing will be conducted at the DE HPM laboratory as well as the China Lake Fuze Assessment and Components Branch environmental conditioning chamber. Measurement focus is on the Cs-Rs measurements under variance of frequency and temperature and current through a small resistance. Cs-Rs measurements will be conducted on the capacitor samples from Ballistic Devices Inc. using an Keysight E4980A 20 Hz-2 MHz LCR meter where a custom 4-port fixture was created to minimize influence on the device under test.

Using environmental chambers available at China Lake, LCR measurements will be made under MIL-Spec environmental conditions for NP0 capacitors bounding -55 °C to +125 °C. Influence of the test fixture will be measured with open, short, and loaded conditions to gate out the equipment variance in the Cs-Rs measurements.

Pulsed discharged conditions will be applied through a high current solid state switch, model S33B, rated at 12 kV and manufactured by Silicon Power, and current is measured across a T&M Research 0.0025630 Ohm current viewing resistor (CVR), model W-2-0025-4FC.

2. Activities and Accomplishments

Previous Fiscal Year LCR Measurements and Testing, Recap

In FY18, a custom 4-port test fixture was designed and evaluated to conduct accurate measurements of the capacitors with a Keysight E4980A 20 Hz to 2 MHz Precision LCR Meter. This test fixture was used for all FY19 testing. The fixture accommodated a 6 inch diameter capacitor, could be adjusted for various capacitor thicknesses, and had minimal self-resonance below 2MHz. Utilizing the Keysight 16048A Test Lead kit, a custom fixture was created with variable height adjustment and precision clamping torque to 8in-lbs as shown in Figure 1. This test fixture was evaluated with a known NP0 rated capacitor made by Novacap. The results showed there was some unexpected variance in capacitance above 500 kHz, but this was resolved when placing a larger capacitor on the fixture to minimize field lines from one side of the test fixture to the other.

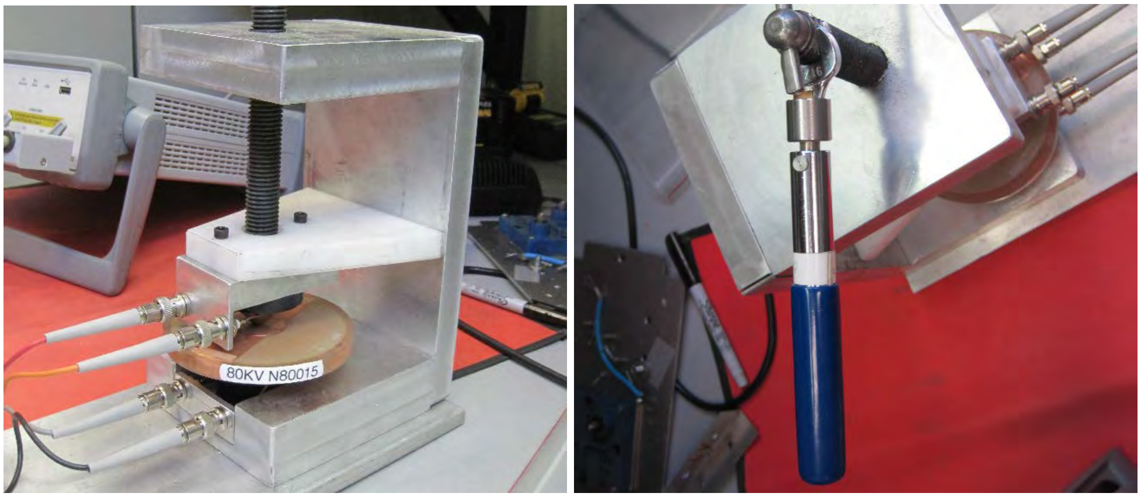

Figure 35: Capacitor Test Fixture and Consistent Clamping Torque Setting

Data was collected on Ballistic Devices Inc. capacitors in ambient temperature environmental conditions and the data analyzed. The results showed a frequency stability in the 80kV rated and 16kV rated capacitors. Based on this data and the capacitors available, three capacitors from each voltage rating were selected based on their performance: best, worst, and average performing. The selected capacitors were placed in an environmental conditioning oven located at the China Lake Propulsion Laboratory Fuze Assessment and Components Branch for measurements from -55 °C to +125 °C in 8 temperature steps: -55, -25, 0, 10, 30, 50, 100, 125 °C. Each capacitor was soaked at each temperature increment for 1 hour before measuring on the LCR meter. As the results from the ambient temperature data showed more consistent results at 100kHz, an analysis of the temperature stability was performed at 100 kHz. The results showed a wide variance of PPM depending on the temperatures selected, and an even wider variance still if frequency was varied in the analysis. Ballistic Devices Inc. provided their analysis of several capacitors during temperature testing at 50, 30, and 10 ℃. Correlating this data and the data collected from the China Lake several of the capacitors were similarly measured. Some of the analysis is shown in Figure 2.

PPM was calculated by the formula $PPM_{\Delta f} = \frac{\frac{C1-C2}{2}}{Cn(F1-F2)}$, where $PPM_{\Delta f}$ is the parts per million calculation based on frequency change, C1 is the capacitance measured at F1, C2 is the capacitance measured at F2, Cn is the nominal capacitance, F1 is the frequency at which C1 was measured, and F2 is the frequency at which C2 was measured.

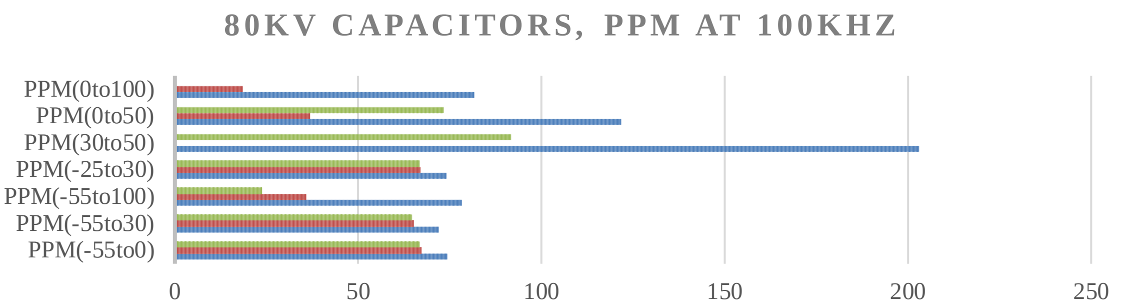

	PPM(-55to0)	PPM(-55to30)	PPM(-55to100)	PPM(-25to30)	PPM(30to50)	PPM(0to50)	PPM(0to100)
🟩 N80021	67	65	24	67	92	73	0
🟥 N80011	67	65	36	67	0	37	18
🟦 N80001	74	72	78	74	203	122	82

Figure 36: 100kHz PPM Analysis for Selected 80kV Capacitors

Environmental LCR Measurements

Due to the feedback supplied in FY18, newly manufactured capacitor samples were delivered by Ballistic Devices Inc. to include manufacturing improvements over the previous capacitors through a longer duration cure time for the epoxy coating. LCR measurements in environmental conditions were performed on 16 old and new Ballistic Devices Inc. Capacitors in environmental conditioning ovens from -55 ℃ to +125 ℃. To minimize thermal shock to the capacitors, the testing was performed from 0 ℃ to -55 ℃, and then from 0 ℃ to +125 ℃ allowing the capacitors to soak in each temperature range for 1 hour. PPM measurements for these capacitors followed the trend from previous testing with good performance.

When applying temperatures below -40 ℃ the encasement epoxy was damaged on several capacitors. Failure was observed on 13 capacitors including two newly manufactured capacitors. No failure was observed on 16 kV. Figure 3 shows epoxy encasement failures.

After testing the capacitors were measured on HIPOT equipment up to the equipment limit, or 6 kV. All of the capacitors exhibiting broken epoxy failed HIPOT below 1 kV. This result is expected in the failed capacitors as the epoxy encasement provides voltage standoff between the edges of the capacitor legs.

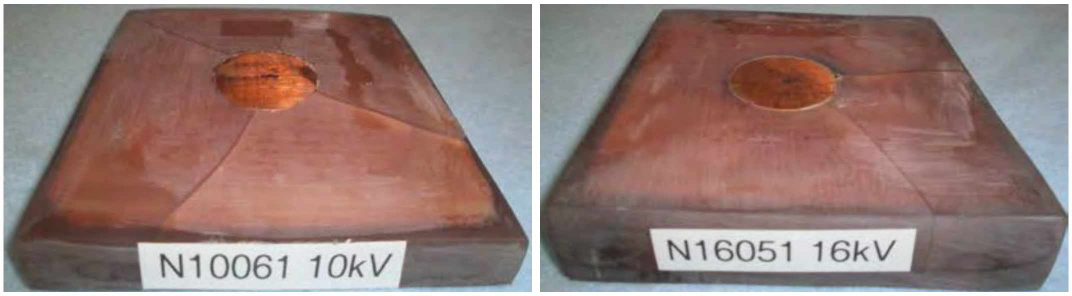

Figure 37: Several Capacitors Showing Failed Encasement

HIPOT Testing

New HIPOT equipment was made available with the capability to perform HIPOT analysis up to 20 kV. This test held pass/fail criteria that was bound by the rated voltage of the capacitors and the amount of leakage current at a voltage potential. The voltage was set to ramp up, dwell, and then discharge as seen in Figure 4. During this time, if the HIPOT equipment measured a leakage current exceeding 5000 uA, the test would fail.

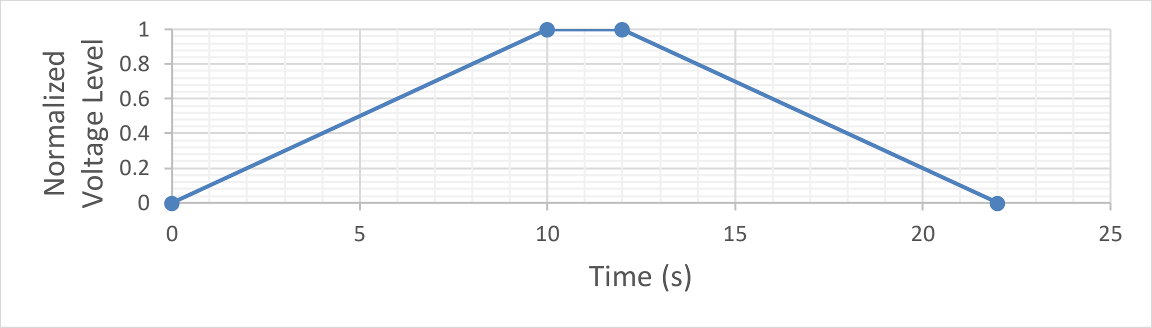

Figure 38: HIPOT Test Setup Criteria

Capacitors were placed into a custom holder, as seen in Figure 5, and tested to their rated voltage. Out of the 64 capacitors tested in this configuration there were 9 failures. Several of the failed capacitors had been previously tested in a MIL-Spec environment that lead to the breakdown of the epoxy coating. Any capacitor showing a visible break in the epoxy coating was rejected before HIPOT testing, and is not included in the failed capacitor results

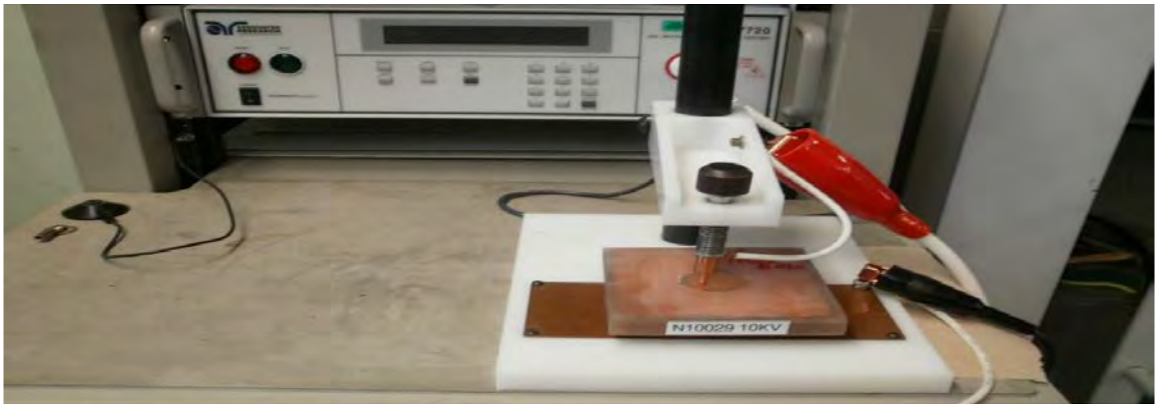

Figure 39: High Potential Test Setup

Pulsed Discharge Testing

To measure the discharge performance of the capacitors, a low impedance ring down circuit was developed and evaluated. As shown in Figure 6, the test circuit is comprised of a solid state closing switch manufactured by Silicon Power model S33B rated at 12 kV and 14 kA (blue circle), a high voltage inductor (110 nH), a T&M Research 0.0025630 Ohm CVR model W-2-0025-4FC (green circle), and a custom adjustable width capacitor holder (red circle). This circuit was connected to a high voltage power supply (HVPS) (purple), and a digital delay generator (DDG) (orange).

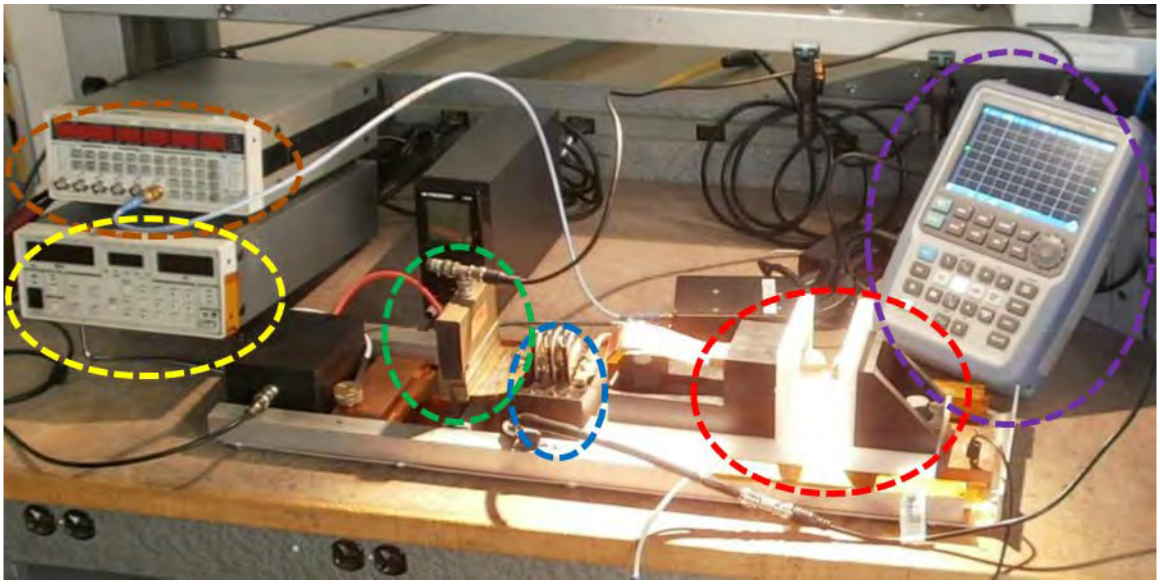

Figure 40: Test Circuit: Capacitor Holder (Red), HV Switch (Blue), CVR (Green), DDG (Orange), HVPS (Yellow), and Oscilloscope (Purple).

The HVPS applied a user specified voltage across the capacitor under test, and when triggered by the DDG, the capacitor would discharge through the switch and CVR. This allowed a high current ring down measurement for each capacitor under test at various charges. The oscilloscope measured the ring down created by the resistance, inductance, and capacitance (RLC) of the circuit. To ensure consistent results, each voltage level was repeated a minimum of 3 times. Performance of the capacitors is very consistent as shown in the consistency of the waveforms in Figure 7.

While the performance of the capacitors is relatively consistent, capacitor N10032 contained a visible arc on the inside of the epoxy during high current discharge. This arc created high frequency distortion in the data measured, shown as ripples at the peak voltage (Figure 7, top, black line). As it passed HIPOT testing and there is minimal performance degradation, it is speculated that this arc occurred at the output of the capacitor where the output lead makes two 90° bends. This added inductance creates resistance at high frequencies, creating a potential not present during DC tests.

Capacitor N16008 shows a higher frequency and a lower peak to peak voltage (Figure 7, middle, red line) due to 10 nF less capacitance than the other 16 kV capacitors tested. Capacitors numbered N16116-N16120 were the newest capacitors developed, and so a change in the manufacturing process that increased their capacitance is speculated.

Due to the limited voltage potential allowable and the low capacitance of (5.5 nF) the test setup did not apply enough energy to measure the current of the 80 kV rated capacitors. The measured current indicated that there was only 115 amps going through the CVR during ring downs, which produced a non-ideal waveform through the solid-state switch (Figure 7, bottom).

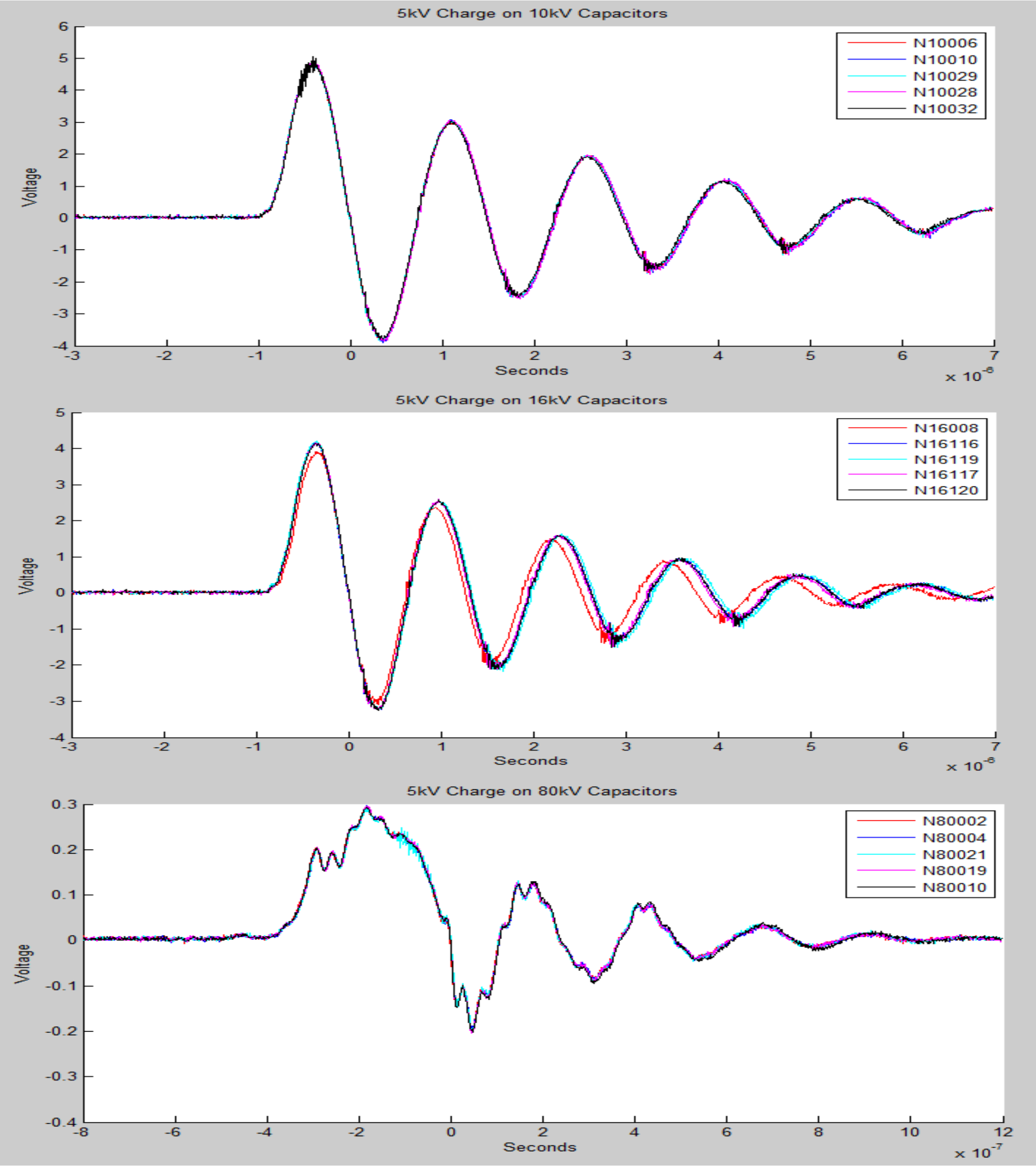

Figure 41: Ring Down of 10, 16, and 80 kV Capacitors

Table 1 lists the peak current through the CVR as well as the calculated inductance. This inductance includes both the capacitor and system inductances. As stored energy is different for the 16 kV rated and 10 kV rated capacitors due to their capacitance (120 nF vs. 154 nF respectively), the peak current levels and frequencies were different.

Table 1: Data from 10 and 16 kV Capacitor Tests

Capacitor	Max Current [Amps]	Peak to Peak [V]	Capacitance [nF]	Inductance [nH]	Frequency [kHz]
N10029	1920	8.7843	153	385	654
N10032	1970	8.8471	148	387	665
N16008	1520	7.00	110	380	776
N16116	1630	7.40	121	359	762

Comparison with Baseline

As the baseline capacitors were rated at 4 kV and 39 nF, a parallel and series combination of baseline capacitors was created to equal 117 nF, or equivalent capacitance to one 16 kV rated capacitor. At a 5 kV charge voltage, the capacitance energy of each capacitor is the similar. The measured waveforms are shown in Figure 8. The baseline test (red) has a very similar ring down in comparison to the 16 kV rated capacitors. Inductance is slightly higher in the baseline testing, which is attributed to the change in shape of the test circuit due to greater length.

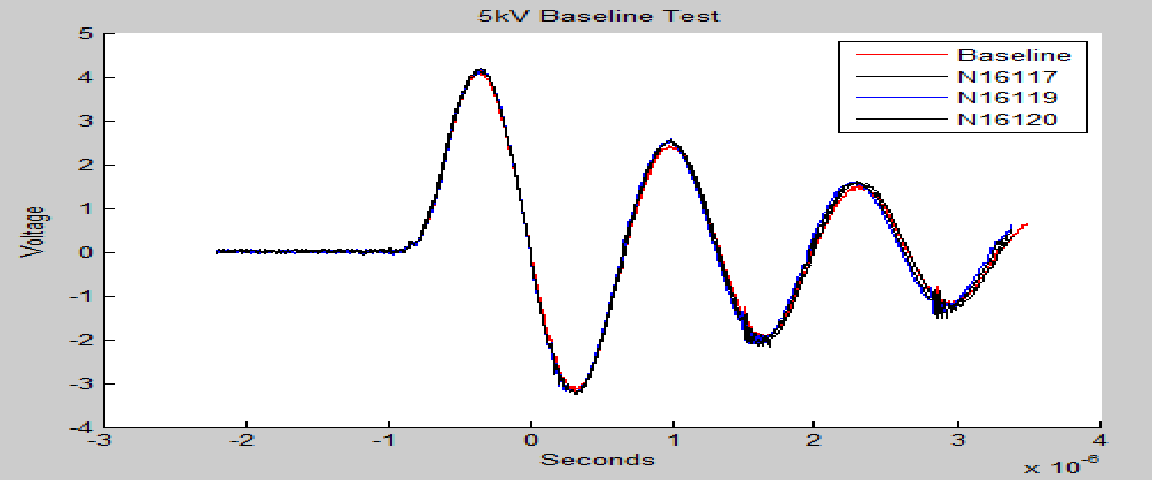

Figure 42: 5 kV Baseline Capacitor Test (12 Baseline Capacitors)

Higher Frequency Pulsed Discharge

An effort to increase resonant frequency to the megahertz range was performed due to a desire to operate at a higher frequency and observe any mechanical or electromechanical stresses. From previous testing, the average system inductance was calculated to be 380 nH. As the high voltage inductor measured 110 nH on an LCR meter, the inherent system inductance is calculated to be 270 nH. Reaching a higher resonant frequency could be achieved through a series combination of capacitors and a decrease in high voltage inductor value.

The high voltage inductor was changed from 110 nH to a 40 nH, but as this change would only increase resonant frequency by 100 kHz, from 750 kHz to 850 kHz, a capacitance value less than 82 nF is needed to reach MHz frequency resonance. By arranging three 10 kV rated capacitors in series (Figure 9) the equivalent capacitance is decrease from 154 nF to 51 nF. These changes result in a calculated resonant frequency to 1.27 MHz. Figure 10 shows the waveform measured while utilizing these new test conditions. A frequency of 1.28 MHz was calculated from this configuration, matching the theoretical value.

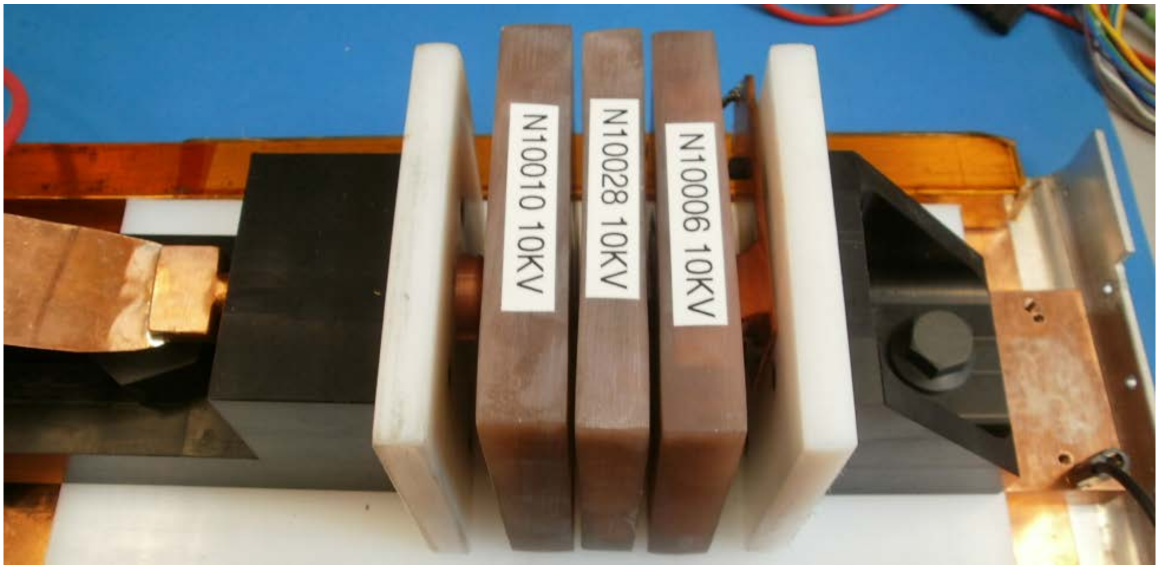

Figure 43: Three 10 kV Capacitors in Series in the Test Circuit

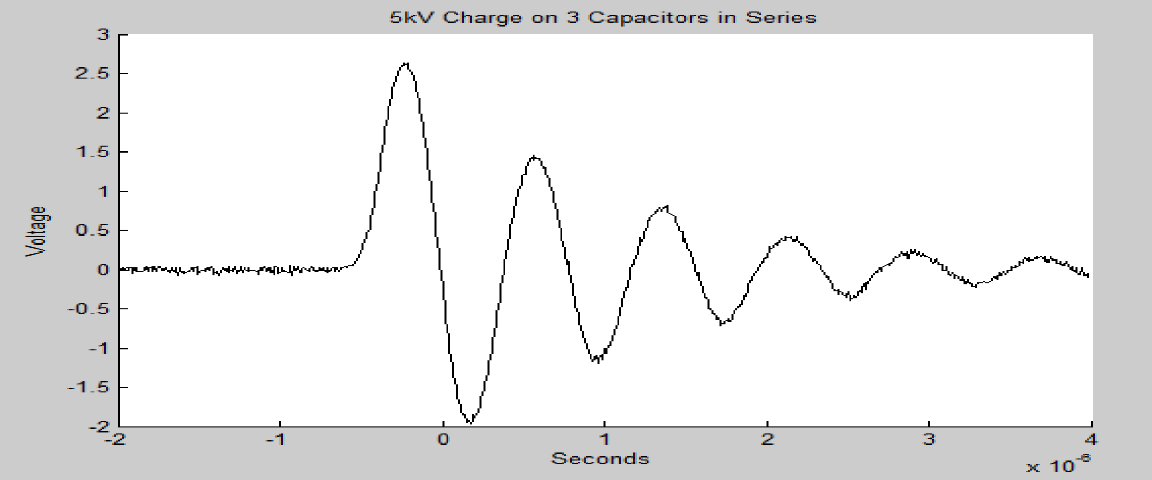

Figure 44: High Frequency Ring Down, Capacitors in Series

3. Findings and Conclusions

The findings from data analysis suggests that the performance of the Ballistic Devices Inc. capacitors perform with marginal difference to the baseline capacitors in both capacitance variance over temperature and in pulsed discharge scenarios. Differences to baseline were seen only in extreme cold and hot conditions where the epoxy became brittle and tacky respectively. Through corrective approaches to manufacturing suggested by China Lake these issues can be mitigated. Though similar in performance, the main difference between the baseline and capacitors under test becomes apparent in their respective energy densities. The potential limit in capacitor energy can be calculated by $E = 0.5CV^2$, and the energy density can then be calculated by the division of capacitor energy by the capacitor volume. The capacitor energy densities will be represented in joules per cubic inches (J/in^3). Table 2 presents the energy density calculations made through measuring the outer dimensions of each capacitor, the voltage rating, and the capacitance.

Table 2: Capacitor Energy Densities

Cap Type	Length [in]	Width [in]	Thickness [in]	Voltage [kV]	Capacitance [nF]	Volume [in^3]	Energy [J]	Energy Density [J/in^3]
Baseline	0.75	0.65	0.30	4	39	0.15	**0.31**	2.1
16kV	4.25	4.25	1.00	16	117	18	**15.0**	0.8
10kV	4.25	4.25	0.78	10	153	14	**7.7**	0.5
80kV	3.90	3.90	0.53	80	5.5	8	**17.6**	2.2

Improvements to manufacturing improved encasement damage likelihood in low temperature environmental conditions. It was found that CTE deltas between materials was likely the cause for epoxy damage.

The ring down curves at 1-5 kV charge voltage were very consistent and all the capacitors held within a similar max current and frequency relative to their rating. There are still a few faults that arose while testing, such as N10032 contained arcing within the capacitor and N16118 not being able to hold a charge. Most of the capacitors were able to hold a high charge and were able to be discharged at damping that lined up with baseline capacitors.

A variance in capacitor types, baseline vs. Ballistic Devices Inc. can be visualized when evaluating energy density. The capacitors under test excel in energy density at much higher breakdown voltages: greater than 80 kV. As the high voltage was the initial path of the project, the advantages of this style of capacitors is evident.

4. Plans and Upcoming Events

NAWCWD China Lake has supplied Ballistic Devices Inc. with information to further improve their manufacturing process through keeping the CTE of materials similar, which will improve the longevity of the capacitors both in operation and shelf life. This can be either through the addition of fiber wrapping in the epoxy or a change of epoxy to one of similar CTE to the other materials used. Given the results of the pulsed discharge testing, the capacitors are a cost effective solution to high voltage temperature stable energy storage and supply an alternative solution to traditional capacitor solutions. As the energy density of the Ballistic Devices Capacitors is good at higher voltage capacity, it is anticipated to be a solution for future high voltage pulse generator products.

5. Transitions and Impacts

None.

6. Collaborations

Analysis and results were shared with Ballistic Devices Inc. that led to manufacture improvements to the capacitor encasement, which was then tested for improvements.

The Composites Engineering Lab at NAWCWD China Lake collaborated with the HPM team at China Lake and Ballistic Devices Inc. to analyze encasement issues with the capacitors under extreme cold conditions. Determining the coefficient of thermal expansion (CTE) of multiple materials and proposing encasement epoxy with similar CTE benefited future development of high voltage temperature stable capacitors.

7. Personnel

Name and Org	Title/Role	Email	Phone
Shawn Higgins NAWCWD 47M500D	DE HPM Lead / Principal Engineer and Lead Engineer	Shawn.Higgins1@navy.mil	760-939-1047
Stan Byrd NAWCWD 478700D	Electronics Technician, Lead Technician	stanley.byrd@navy.mil	760-939-1308
Jamey Pryor NAWCWD 418300D	Mechanical Technician, Lead Fabricator	jamey.pryor@navy.mil	760-793-7879
Andrew Hernandez NAWCWD 479800D	Physicist, ESDP	andrew.hernandez4@navy.mil	760-371-5070
Caroline Paciaroni NAWCWD 472200D	Physicist, ESDP	caroline.paciaroni@navy.mil	760-939-2047
Paul McDaniels NAWCWD 47M500D	Aerospace Engineer, ESDP	kenneth.mcdaniels@navy.mil	760-939-2649

8. Students

None.

9. Technology Transfer

None.

10. Products, Publications, Patents, License Agreements, etc.

None.

11. Point of Contact in Navy

Mr. Shawn Higgins, NAWCWD/NAVAIR DE HPM Lead

12. Acknowledgement/Disclaimer

This work was sponsored by the Office of Naval Research (ONR), under grant (or contract) number N0001419WX00126, PR# 1400738220. The views and conclusions contained herein are those of the authors only and should not be interpreted as representing those of ONR, the U.S. Navy or the U.S. Government.

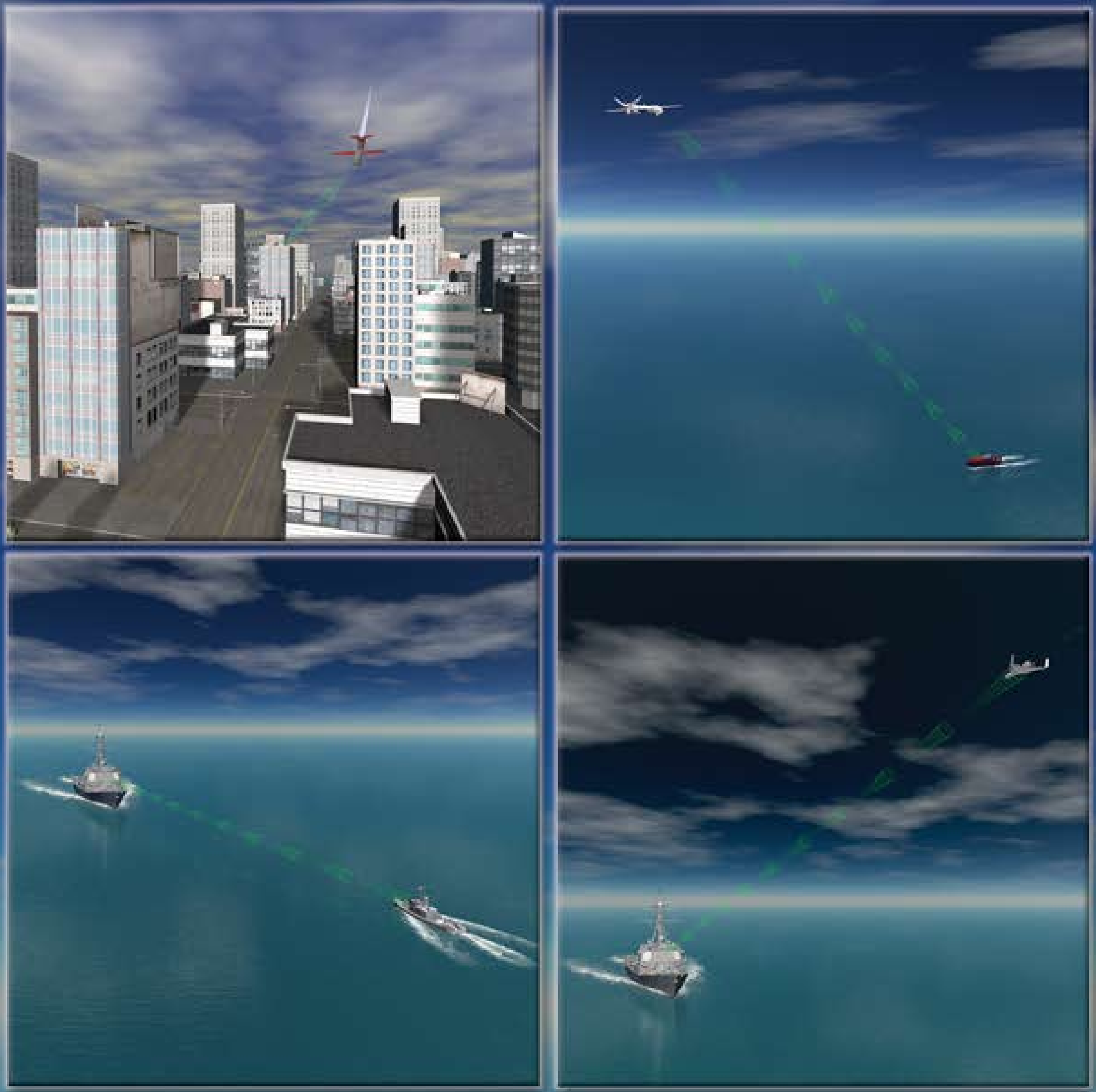

Office of Naval Research
875 N. Randolph Street
Arlington, VA 22203-1995
www.onr.navy.mil

OFFICE OF NAVAL RESEARCH